Measurement of the QED Compton Scattering Cross Section with the H1 Detector at HERA

Vom Fachbereich Physik
der Universität Dortmund
zur Erlangung des akademischen Grades
eines Doktors der Naturwissenschaften
genehmigte

DISSERTATION

von
M. Sc. Victor Lenderman
aus Kiew

Dortmund
Dezember 2001

Contents

Preface

Quantum Chromodynamics, the gauge quantum field theory of the strong interaction, is nowadays together with the electroweak theory a well established part of the Standard Model. This fact seems to be really impressive if one bears in mind that the fundamental particles in QCD, gluons and quarks, have not been observed in a free state. Moreover, according to this theory they can never be detected as isolated particles due to the non-abelian structure of the theory that leads to the asymptotic freedom and quark confinement.

The successful development of QCD became possible essentially owing to the series of spectacular experiments on high energy lepton–hadron scattering. The idea of these experiments, namely probing a hadron target by a high energy lepton beam, is based on Heisenberg's uncertainty relation, according to which one can resolve the target structure in a scattering process down to the scale $\lambda \sim \hbar/p$, where p is the projectile momentum. Thus, the higher the energy in the centre of mass of the interacting particles that can be achieved, the finer the structure that can be studied. Therefore historically these experiments were developed towards continuous increase of the centre of mass energy.

The first experiments began in the early fifties of the twentieth century with the building of the linear accelerator MARK III in Stanford, at which HOFSTADTER et al. [hof56, mah56] studied elastic scattering of electrons with an energy of 400 MeV on fixed target nuclei, and in particular, protons. In these experiments a proton was found not to be point-like but to have a charge distribution concentrated within a sphere with a radius of about 0.85 fm [yh58]. The elastic *ep* scattering cross section was well described by the electric and magnetic form factors, as it was proposed shortly before by ROSENBLUTH [ros50].

A further increase of the electron beam energy up to 17 GeV was achieved at the Stanford Linear Accelerator put into operation in 1967. The SLAC–MIT collaboration was the first to study the deep inelastic electron–proton scattering (DIS) and to observe the scale invariance of the proton structure function F_2 [pan68, slac69] in the limit of inifinite momentum transfers — an effect predicted by BJORKEN [bjo68] and expected for the scattering off point-like objects. This result was explained by FEYNMAN in 1968 within his parton model [fey69]. In this model a proton consists of point-like *partons*, on which electrons scatter incoherently. In 1969 BJORKEN and PASCHOS [bp69] associated partons with quarks.

The history of quarks began 1961 when GELL-MANN [gel62] and NE'EMAN [nee61] proposed *The Eightfold Way* — based on SU(3) group classification of all mesons and baryons known at that time according to their spin, charge and strangeness. In 1964 GELL-MANN [gel64] and ZWEIG [zwe64] showed that this classification comes about by assuming all mesons to be built of a quark and an anti-quark and all baryons to be composed of three quarks. However, although the quark model was very successful in classifying hadrons, the existence of quarks was considered questionable for many years until the SLAC experiments had been done.

Later, a number of newer fixed target experiments with substantially extended kinematic range coverage observed significant deviations from the Quark Parton Model predictions. In particular, it was found that quarks carry only about a half of the proton momentum [per75]. An explanation for that was given by Quantum Chromodynamics, which stated that the remaining part is carried by the strong force gauge bosons called *gluons*. QCD explained also another observation made in μN scattering experiments [fnal74], namely the violation of the structure function F_2 scaling behaviour.

As a continuation of this series of successful experiments a new type of machine — the electron–hadron collider HERA — started operating at the end of 1991 at DESY in Hamburg. In two experiments, H1 and ZEUS, electrons or positrons with an energy of 27.5 GeV collide with protons accelerated to an energy of 820 GeV until 1997 and 920 GeV starting from 1998 onwards. The usage of colliding beams has enabled an additional large extension of the kinematic range and allowed much more extensive tests of QCD.

One of the first important results of the H1 [h193] and ZEUS [zeus93] measurements was the observation of a steep rise of the proton structure function F_2 towards low values of the Bjorken variable x. This phenomenon has been successfully described by perturbative QCD calculations [grv92]. Moreover, pQCD appeared to give a very good description of the F_2 behaviour down to low values of momentum transfers squared, Q^2, of the order of a few GeV^2.

A matter of special interest today remains the regime of even lower Q^2, *i.e.*, the transition region between DIS and real photoproduction. Perturbative QCD methods are no longer applicable in this domain, and phenomenological models must be employed.

One way to study this region is by means of QED Compton events (QEDC). These are *ep* scattering events with additional hard photon radiation having a characteristic signature: both the outgoing lepton and the photon are detected under large polar angles almost back-to-back in azimuth. The diffential cross section of the QED Compton process is measured in the framework of this analysis and is used to gain information about the behaviour of the structure function F_2 at low Q^2.

A further subject of the present analysis is an experimental test of the so called *collinear approximation*, which has been used by several authors for the calculation of the QED Compton scattering cross section. In this approach the transverse momentum of the exchanged photon is neglected and thus it can be treated as a parton of the proton. The photon–parton content of the proton is described by the structure function γ. The latest theoretical calculation of this function has been carried out by DE RÚJULA and VOGELSANG [rv98]. A comparison of their predictions with the results of the cross section measurement presented here is performed.

This thesis is organised as follows. The chapter 1 serves as a theoretical introduction into the scope of research. In the chapter 2 the experimental facility used to collect the data — the H1 detector — is described. Afterwards, basic issues of the QEDC cross section measurement are discussed in chapter 3. The chapter 4 is devoted to the details of the experimental data analysis. Finally in chapter 5, the results of the measurements are presented and compared to the theoretical predictions. The thesis is completed by a short summary of results and an outlook.

Chapter 1

QED Compton Events in *ep* Scattering

The theoretical basis of *ep* scattering in general and QED Compton scattering in particular is the topic of this chapter. In the beginning the inclusive *ep* scattering cross section is given in terms of the standard Lorentz invariant kinematic variables. The presented formalism embraces the domains of elastic, resonance and continuum inelastic scattering. The discussion is further concentrated on the theoretical interpretations of the continuum region, which is of main interest for HERA experiments.

Afterwards, radiative *ep* scattering is considered and the QED Compton event topology is defined. Subsequently, an exact computation of the QED Compton scattering cross section using helicity amplitudes is presented, followed by a study of the kinematic range of the QEDC events at HERA. It is shown that the continuum inelastic QEDC events lie in the kinematic range not accessible by the HERA DIS measurements.

Finally, a simplified approach to the cross section calculation — the collinear approximation — is introduced and the possibility of measuring the photon parton content of a proton is discussed.

1.1 Inclusive *ep* Scattering Cross Section

The inclusive electron proton scattering can be described in the lowest order of perturbation theory as an exchange of a virtual gauge boson between the electron and the proton. The Feynman diagram for this process is shown in fig. 1.1. In case of the exchange of a neutral boson, γ or Z^0, the electron is scattered off the proton and some hadronic final state is produced. If a

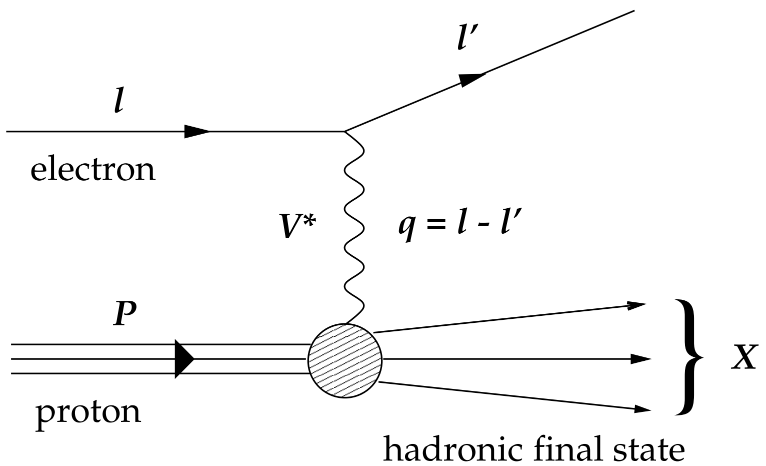

Figure 1.1: *Lowest order Feynman diagram for inclusive ep scattering.*

charged boson, $W^{\pm}$, is exchanged, then an electron neutrino, ν_e, appears in the final state instead of an electron. The measurement presented here concerns only neutral current processes, therefore the charged current reactions will not be discussed in the following.

The inclusive *ep* cross section can be conveniently expressed in terms of only three Lorentz invariant kinematic variables (see, *e.g.*, [cdr98]):

- The centre of mass energy squared:

$$s = (l + P)^2 \tag{1.1}$$

  where l is the four-momentum of the incident electron and P is that of the incident proton, as depicted in fig. 1.1. Neglecting electron and proton masses one obtains: $s = 4E_{e0}E_{p0}$, where E_{e0} and E_{p0} are the energies of the electron and proton beams. In a typical collider or fixed target experiment, in which the incident electron and proton momenta are fixed, s remains constant.

- The negative of the invariant mass squared of the exchanged boson

$$Q^2 = -q^2 = -(l - l')^2 = -(X - P)^2 \tag{1.2}$$

  where l' and q are the four-momenta of the scattered electron and the virtual boson, respectively, and X is the total four-momentum of the hadronic final state.

- The Bjorken scale variable

$$x = \frac{Q^2}{2P \cdot q}, \qquad 0 < x < 1\,. \tag{1.3}$$

  In the quark parton model, in which particle masses and parton transversal momenta are neglected, x corresponds to the fraction of the proton momentum carried by a struck parton before entering the scattering process.

Furthermore, two additional (also Lorentz invariant) variables, which are rather useful for the cross section description, are defined as follows:

- The "inelasticity" variable

$$y = \frac{P \cdot q}{P \cdot l}, \qquad 0 < y < 1\,, \tag{1.4}$$

  which corresponds to the fraction of the incident lepton energy carried by the exchanged boson in the proton rest frame. By neglecting particle masses the relation between y and the previously defined quantities is given by:

$$Q^2 = xys\,. \tag{1.5}$$

- The invariant mass of the hadronic final state M_X which can be calculated according to the formula

$$M_X^2 = (P + q)^2 = Q^2\frac{1-x}{x} + m_p^2\,, \tag{1.6}$$

  where m_p is the (not negligible here) proton mass.

The fact, that at a fixed centre of mass energy there are only two degrees of freedom, can be illustrated in the following example: If the parameters of the scattered lepton are employed for the measurement, then its energy E_e and polar angle θ_e fully constrain the event kinematics. The third degree of freedom, namely the azimuthal angle ϕ_e, provides no new information about the underlying physics of the interaction. Therefore the inclusive cross section is usually written in double differential form.

In the range where $Q^2 \ll M_Z^2$, as considered in this analysis, the Z^0 exchange can be neglected and the *ep* scattering can be treated as the interaction of a virtual photon flux with the proton. The differential *ep* cross section can be then given in Born approximation as:

$$\frac{d^2\sigma}{dx\,dQ^2} = \Gamma(\sigma^T_{\gamma^* p} + \epsilon\sigma^L_{\gamma^* p}) \ , \tag{1.7}$$

where $\sigma^T_{\gamma^* p}$ and $\sigma^L_{\gamma^* p}$ are the cross sections of transversely and longitudinally polarised virtual photon absorption by a proton, Γ is the flux factor and ϵ is the virtual photon polarisation.

The definition of the flux factor includes some arbitrariness which can be absorbed in the definition of the cross section for virtual photons on protons. It should just yield the correct real photon flux as $Q^2 \to 0$. In the convention of Hand [han63] it is given by the expression

$$\Gamma = \frac{\alpha}{2\pi}\frac{y(1-x)}{sx^2(1-\epsilon)} \tag{1.8}$$

with the polarisation parameter defined via

$$\epsilon^{-1} = 1 + 2\frac{Q^2 + 4m_p^2x^2}{Q^2}\left[\frac{s(xs-Q^2)}{xm_p^2Q^2} - 1\right]^{-1} \ . \tag{1.9}$$

To determine the virtual photon absorption cross sections $\sigma^T_{\gamma^* p}$ and $\sigma^L_{\gamma^* p}$, one must distinguish three kinematic domains — those of elastic, resonance and continuum inelastic scattering, all of which are described in the following.

1.1.1 Elastic Scattering

In the elastic scattering $ep \to ep$ the proton remains intact with $M_X = m_p$. The cross sections $\sigma^T_{\gamma^* p}$ and $\sigma^L_{\gamma^* p}$ are usually expressed in terms of the proton electric (G_E) and magnetic (G_M) form factors:

$$\sigma^T_{\gamma^* p} = \frac{4\pi^2\alpha}{Q^2}G_M^2(Q^2)\frac{\delta(1-x)}{1-x} \ , \tag{1.10}$$

$$\sigma^L_{\gamma^* p} = \frac{4\pi^2\alpha}{Q^2}\frac{4m_p^2}{Q^2}G_E^2(Q^2)\frac{\delta(1-x)}{1-x} \ . \tag{1.11}$$

The inclusive elastic scattering possesses obviously only one non-trivial degree of freedom. In this formalism it is Q^2, while x is eliminated from equation 1.7 by the δ-functions. Physically, this reflects the fact that the elastic process is a coherent scattering of the electron on the proton as a whole, where no parton structure of the proton can be resolved consequently leading to $x \equiv 1$.

Since the first Hofstadter experiments the electromagnetic form factors of the proton were extensively measured at SLAC and other accelerators at the end of 60th – beginning of 70th

Table 1.1: *Characteristics of the three most prominent resonances [car74, pdg00].*

	m_R (GeV)	σ_R (µb)	Γ_R (GeV)	Q^2_R (GeV^2)	Main Decay Modes
Δ	1.236	550	0.12	2.5	$N\pi$
N^*	1.520	280	0.12	3.0	$N\pi$, $N\pi\pi$
N^*	1.688	220	0.12	3.0	$N\pi$, $N\pi\pi$

[slac73]. Measurements at higher Q^2 continued also later [slac92]. In these measurements the form factors were found to be very well described by the *dipole fit*:

$$G_E(Q^2) = \frac{G_M(Q^2)}{2.79} = \left[1 + \frac{Q^2}{Q_E^2}\right]^{-2} \tag{1.12}$$

with $Q_E^2 = 0.71\,\mathrm{GeV}^2$. It follows from equations 1.10 – 1.12 that the elastic cross section rises rapidly as $Q^2 \to 0$. It dominates over other contributions already at $Q^2 \sim 0.1\,\mathrm{GeV}^2$.

In the measurement of the inclusive *ep* scattering cross section at HERA the elastic component plays only a minor role. At very low Q^2 where it dominates it is not detected, since both particles escape into the beam pipe. At higher Q^2 its contribution becomes negligible compared to the inelastic part of the cross section. However the elastic events make an essential contribution to the cross section of specific processes, in particular QED Compton events.

1.1.2 Inelastic Scattering in the Resonance Region

In the region, in which the invariant mass of hadronic final state M_X is just above the proton mass, the scattering is dominated by the production of several resonances. These are excited nucleon states with a very short lifetime of typically: $\tau \sim 10^{-23} - 10^{-24}$ s. The most prominent of them are concentrated in the mass range $m_p + m_\pi \gtrsim M_X \gtrsim 1.8\,\mathrm{GeV}$ and less noticeable ones have been observed with masses up to 2.5 GeV. Their production was extensively studied in many experiments during the last three decades (see an overview in [pdg00]), and several parameterisations of the photoabsorption cross sections are available in this region. Following [car74] which used the data from [dre71], it can be approximately described as a sum over all resonant states:

$$\sigma^T_{\gamma^* p} = \sum_R \sigma_R \frac{m_R^2 \Gamma_R^2}{(M_X^2 - m_R^2)^2 + m_R^2 \Gamma_R^2} \left[1 + \frac{Q^2}{Q_R^2}\right]^{-2}, \tag{1.13}$$

$$\sigma^L_{\gamma^* p} = 0\,. \tag{1.14}$$

The various parameters for the most significant resonances and their dominant decay modes are listed in table 1.1. Alternative more complex and more accurate parameterisations can be found, *e.g.*, in [bra76] or [bod79].

Similar to the elastic scattering, the resonance production at HERA is essential only for the description of some semi-inclusive processes like the QED Compton scattering.

1.1.3 Inelastic Scattering in the Continuum Region

With further increase of M_X one enters the region of continuum inelastic scattering. At $Q^2 \gtrsim 1$ GeV^2 it is usually named *deep inelastic scattering (DIS)*. In this regime the photoabsorption cross sections are expressed in terms of the proton structure functions F_2 and F_L (see, *e.g.*, [cdr98]):

$$\sigma^T_{\gamma^* p} = \frac{4\pi^2\alpha}{Q^2(1-x)}\left[\left(1+\frac{4m_p^2x^2}{Q^2}\right)F_2(x,Q^2) - F_L(x,Q^2)\right], \tag{1.15}$$

$$\sigma^L_{\gamma^* p} = \frac{4\pi^2\alpha}{Q^2(1-x)}F_L(x,Q^2), \tag{1.16}$$

and the differential ep cross section is written as:

$$\frac{d^2\sigma}{dx\,dQ^2} = \frac{2\pi\alpha^2}{Q^4x}[Y_+F_2(x,Q^2) - y^2F_L(x,Q^2)], \tag{1.17}$$

where $Y_\pm = 1 \pm (1-y)^2$. In the region, in which $Q^2 \gg 4m_p^2x^2$, *i.e.*, at sufficiently small x or large Q^2, the expression 1.9 can be simplified, so that:

$$\epsilon = \left[1+\frac{y^2}{2(1-y)}\right]^{-1}, \tag{1.18}$$

and the differential DIS cross section can be transformed to:

$$\frac{d^2\sigma}{dx\,dQ^2} = \frac{2\pi\alpha^2}{Q^4x}Y_+\left[\frac{1+\epsilon R}{1+R}\right]F_2(x,Q^2), \tag{1.19}$$

where

$$R = \frac{\sigma^L_{\gamma^* p}}{\sigma^T_{\gamma^* p}} = \frac{F_L}{F_2 - F_L} \tag{1.20}$$

is a commonly utilised measure of the relative probability of photon absorption with different polarisations.

From equations 1.15, 1.16 it can easily be seen that $0 \leq F_L(x,Q^2) \leq F_2(x,Q^2)$, since the cross sections $\sigma^T_{\gamma^* p}$ and $\sigma^L_{\gamma^* p}$ cannot be negative, and the term $4m_p^2x^2/Q^2$ in eq. 1.15 can be neglected in almost the entire kinematic domain. And from the formula 1.18 it follows, that at not very large y the polarisation ϵ is close to 1, and hence the DIS cross section practically does not depend on R (or F_L) but only on F_2.

The measurement of the inclusive scattering cross section, or equivalently, the proton structure functions in the DIS regime is one of the main goals of the HERA experiments H1 and ZEUS. The theoretical treatment of this domain is the subject of the following sections.

1.2 Quark Parton Model

The Quark Parton Model (QPM) has been the first approach to provide a reasonable interpretation of the SLAC results of the structure function measurement. In the QPM a proton is composed of quasi-free point-like partons with spin 1/2 that can be identified with quarks. The interaction is considered in the "infinite momentum frame", where the quark transverse momenta are neglected and $Q^2 \gg m_p^2$. The DIS process is treated as an incoherent elastic scattering of an electron on one of the quarks in the proton, as displayed in fig. 1.2, and the differential cross section is then written as a sum of eq scattering cross sections:

$$\frac{d^2\sigma}{dx\,dQ^2} = \sum_i \int d\zeta q_i(\zeta)\frac{d^2\sigma^{eq_i\to eq_i}}{dx\,dQ^2}, \tag{1.21}$$

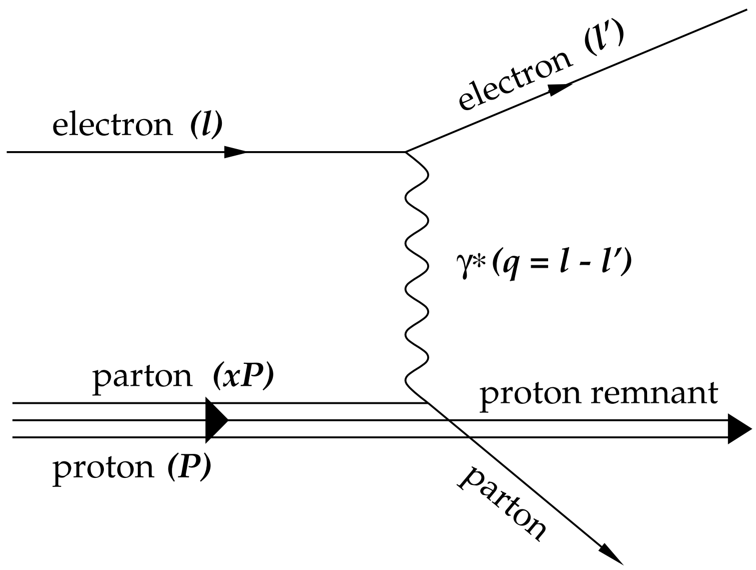

Figure 1.2: *Deep inelastic ep scattering in the Quark Parton Model. Letters in braces denote particle four-momenta.*

where $q_i(\zeta)$ is the probability to find a quark i in the proton and the Nachtmann variable ζ is the fraction of the proton momentum carried by the struck quark before entering the scattering process. The quantities ζ and x become approximately equal at large Q^2 where the proton mass can be neglected:

$$\zeta \approx \frac{Q^2}{2P \cdot q} \equiv x \,. \tag{1.22}$$

The subprocess cross section is then written as:

$$\frac{d^2\sigma^{eq_i \to eq_i}}{dx\, dQ^2} = \frac{2\pi\alpha^2}{xQ^4} Y_+ e_i^2 \delta(x - \zeta) \,, \tag{1.23}$$

and the structure functions F_2, F_L read:

$$F_2(x) = \sum_i e_i^2 x q_i(x) \,, \tag{1.24}$$

$$F_L(x) = 0 \,. \tag{1.25}$$

Thus, according to QPM the structure function F_2 must be scale invariant, *i.e.*, it does not depend on Q^2 but only on x. This so called *Bjorken scaling* was observed in the first SLAC DIS experiments at $x \approx 0.25$ [pan68, slac69]. Equation 1.25 was derived by CALLAN and GROSS [cg69] from the helicity conservation for massless spin 1/2 partons. In 1969 it was used in a combined analysis of SLAC and DESY data to prove that partons have spin 1/2 [desy69, tay69].

1.3 Proton Structure in QCD

As already pointed out in the preface, the naïve Quark Parton Model was able to successfully describe DIS only in the limited kinematic region of the first SLAC experiments. In addition it provided no answer to the fundamental question of why the quarks are not observed as free particles? The full picture of the proton structure could only be obtained in the framework of Quantum Chromodynamics (for a recent review see, *e.g.*, [esw96]).

In this theory quarks are assigned one more quantum number *colour*. Each quark possesses one of three colours: red, green or blue. The introduction of the concept of colour [gre64, hn65] also solved other difficulties of the Quark Model, for example, a seeming violation of Fermi statistics by the Δ^{++} resonance consisting of three u quarks.

In the theory of strong interaction colour plays the role of the charge. The colour interaction is mediated by eight massless gluons, that arise out of SU(3) internal colour symmetry. Thus, gluons play the same role for the strong interaction, as photons do for the electromagnetic force. An important difference between them is that due to the non-abelian SU(3) symmetry gluons themselves are "coloured" and therefore interact with each other by exchanging other gluons.

This selfcoupling of gluons leads to an increase of the strong force with the distance between coloured objects and thus forbids the existence of isolated quarks and gluons. For this reason they are observed only *confined* within colour neutral bound states called hadrons[1].

Vice versa, at small distances the strong force vanishes, so that quarks can be considered as quasi-free. This feature of the strong interaction referred to as *asymtotic freedom* [gw73, pol73] allows one to conduct perturbative calculations in QCD at large Q^2, corresponding to small distances according to the Heisenberg's uncertainty relation. Quantitavely this behaviour is described by the running of the strong coupling constant α_s, given in the leading logarithmic approximation by:

$$\alpha_s(Q^2) = \frac{12\pi}{(33 - 2N_f)\ \ln(Q^2/\Lambda^2)}\,, \tag{1.26}$$

where N_f is the number of quark flavours with the mass $m_q^2 < Q^2$, and $\Lambda \approx 200 - 300\,\mathrm{MeV}$ determines the energy scale, at which α_s becomes large. The rise of α_s with decreasing Q^2 causes perturbative calculations to break down at some point, since a perturbative expansion in α_s becomes impossible.

In the framework of QCD a proton consists of three *valence* quarks interacting via gluon exchange. The gluons can produce virtual quark–antiquark pairs, so called *sea* quarks, and, due to their selfcoupling, other gluons. The gluon radiation explains the F_2 scaling violation, *i.e.*, the F_2 dependence on Q^2. As in the QPM, the virtual photon is scattered off a quark in QCD and not off a gluon, since gluons bear no electromagnetic charge. Thus, equation 1.24 holds. The higher the photon virtuality Q^2, the smaller space and time structure is resolved, and, consequently, the higher is the probability of striking a quark just after it emitted a gluon loosing a part of its momentum, or of striking a sea quark. The sea quarks carry on average smaller fractions of the proton momentum than the valence quarks, therefore at lower Bjorken x the probability for a photon to strike a sea quark is higher than at higher x. As a result of these effects the structure function F_2 is expected to rise with increasing Q^2 at low x and to fall at high x.

A quantitave description of this behaviour is given in terms of quark and gluon parton distribution functions (PDF) $q_i(x, Q^2)$ and $g(x, Q^2)$ using the DGLAP evolution equations named

[1] At present there is only a qualitative but no quantitative description of the quark confinement in QCD.

after DOKSHITZER, GRIBOV, LIPATOV, ALTARELLI and PARISI [gl72, dok77, ap77]:

$$\frac{\partial q_i(x,Q^2)}{\partial \ln Q^2} = \frac{\alpha_s(Q^2)}{2\pi}\int_x^1 \frac{d\zeta}{\zeta}\left[q_i(\zeta,Q^2)P_{qq}\left(\frac{x}{\zeta}\right)+g(\zeta,Q^2)P_{qg}\left(\frac{x}{\zeta}\right)\right], \tag{1.27}$$

$$\frac{\partial g(x,Q^2)}{\partial \ln Q^2} = \frac{\alpha_s(Q^2)}{2\pi}\int_x^1 \frac{d\zeta}{\zeta}\left[\sum_{i=1}^{N_f} q_i(\zeta,Q^2)P_{gq}\left(\frac{x}{\zeta}\right)+g(\zeta,Q^2)P_{gg}\left(\frac{x}{\zeta}\right)\right], \tag{1.28}$$

where the *splitting functions* $P_{ij}(z)$ give the probability for a parton j to emit a parton i with the momentum fraction z of the parent parton. These splitting functions are calculable by perturbative expansion. In the leading order they are given by:

$$\begin{aligned} P_{qq}(z) &= \frac{4}{3}\frac{1+z^2}{1-z}, & P_{gq}(z) &= \frac{4}{3}\frac{1+(1-z)^2}{z}, \\ P_{qg}(z) &= \frac{z^2+(1-z)^2}{2}, & P_{gg}(z) &= 6\left(\frac{z}{1-z}+\frac{1-z}{z}+z(1-z)\right). \end{aligned} \tag{1.29}$$

The parton distribution functions, however, cannot be calculated "from first principles" in pQCD. The above evolution equations are solved by inserting certain analytical functions at some starting scale Q_0^2 and evolving them up to higher Q^2. The structure function F_2 found as a result of this procedure is adjusted to the experimentally measured one. This adjustment allows then a determination of PDFs at the starting scale Q_0^2.

Another consequence of the gluon exchange is that the longitudinal structure function F_L differs from zero. Since quarks can have a non-negligble virtuality before scattering on the probing photon, the helicity may not be conserved in this process, and hence the coupling of a quark on a longitudinally polarised photon becomes possible.

1.4 Low Q^2 Region

Perturbative QCD allows a calculation of the structure functions only at $Q^2 \gtrsim 1\,\mathrm{GeV}^2$, since at lower Q^2 values the strong coupling constant α_s becomes too large, such that higher orders of the perturbative expansion cannot be neglected. A reasonable description of this transition region between DIS and quasi-real photoproduction (γp) remains one of the biggest challenges of QCD. Presently the best description of this region could be obtained only by using phenomenological approaches.

These models provide a smooth fit of the structure functions or equally the photoabsorption cross sections, such that in the limit $Q^2 \to 0$ these cross sections reach their well-known total photoproduction values:

$$\sigma^T_{\gamma^* p} \to \sigma_{\gamma p}, \qquad \sigma^L_{\gamma^* p} \to 0\,. \tag{1.30}$$

According to equations 1.15, 1.16 this implies that the structure functions F_2, F_L become equal to zero in this limit, a feature resulting from the general requirement of gauge invariance. To realise this behaviour, the F_2 parameterisations in all the approaches include a damping factor of the type:

$$F_2 \propto \frac{Q^2}{Q^2+c}\,. \tag{1.31}$$

Since low Q^2 values also imply low y almost in the whole accessible x range, the F_L contribution to the cross section is usually negligible and therefore not considered here.

In order to obtain a correct description of the cross section, one has to take into account that at very low Q^2, where the exchanged photon becomes almost real, it exhibits hadronic structure. This occurs, because the photon can fluctuate into a virtual quark–antiquark pair, and at small Q^2 the lifetime of this $q\bar{q}$ state becomes large and comparable to the photon–proton interaction time. In this regime photon–proton scattering can be thus interpreted as hadron–hadron interaction.

Among the models based on this interpretation, the REGGE type approach [reg59, cfm62] appeares to give the most successful description of the scattering process. In this model the proton and the hadronised photon interact by exchanging colour neutral particles, all of them having the same quantum numbers except for their spins. The spin is proportional to the particle mass squared t. The straight line describing this dependence is called a *Regge trajectory* and the mass values corresponding to the integer and half-integer spins are called *Regge poles*.

Using this approach DONNACHIE and LANDSHOFF [dl92, dl94] have proposed the F_2 parameterisation:

$$F_2 \propto A(Q^2)x^{-\lambda_1} + B(Q^2)x^{\lambda_2} \; , \tag{1.32}$$

where $A(Q^2)$ and $B(Q^2)$ include functions of the form 1.31. The first term in this equation that rises towards lower x values corresponds to the exchange of a *pomeron*, a Regge trajectory of quantum states with vacuum quantum numbers. In QCD it is attempted to consider the pomeron exchange as two–gluon exchange. The second term that rises as x increases describes the exchange of a *reggeon*, *i.e.*, mesons ρ, ω, f_2 etc. The fixed parameters $\lambda_1 = 0.0808$ and $\lambda_2 = 0.4525$ define the axis intercepts at $t = 0$ for the respective trajectories.

In this form the fit is applicable for not very large x values: $x < x_0 \sim 0.07$. At higher x the fit should guarantee that F_2 falls down to zero as x approaches one. Usually it is done by using quark counting rules [gun74, bb74] which predict, that in the limit $x \to 1$ the parton distribution functions must vanish as $(1-x)^{2n_s-1}$ with the number of spectator quarks $n_s = 2$ for a valence struck quark and $n_s = 4$ for a sea quark. Each x-dependent term of eq. 1.32 has to be thus subsitituted by a term of the form $x^{\pm\lambda}(1-x)^m$. In somewhat modified form these rules have been applied to the fit above, assuming that the pomeron trajectory corresponds to the sea quarks and the reggeon to the valence quarks.

The Donnachie–Landshoff parameterisation could successfully describe the data at $Q^2 \sim 0$. However it failed to reproduce the DIS data. To achieve a better description of the entire Q^2 region, this method was further elaborated by several authors. In particular, in the model of ABRAMOWICZ, LEVIN, LEVY and MAOR [allm91] F_2 is composed of a pomeron $F_2^{\mathcal{P}}$ and a reggeon $F_2^{\mathcal{R}}$ contributions with a common Q^2 damping factor:

$$F_2 = \frac{Q^2}{Q^2 + m_0^2}(F_2^{\mathcal{P}} + F_2^{\mathcal{R}}) \; . \tag{1.33}$$

The pomeron and reggeon terms are parameterised in a way similar to that of Donnachie and Landshoff but the fit parameters are assumed to be functions of Q^2. The actual form of the ALLM parameterisation was obtained in 1997 [allm97] by fitting DIS data of the HERA and fixed target experiments together with the total pp and γp cross sections measured. This parameterisation is employed in the present analysis.

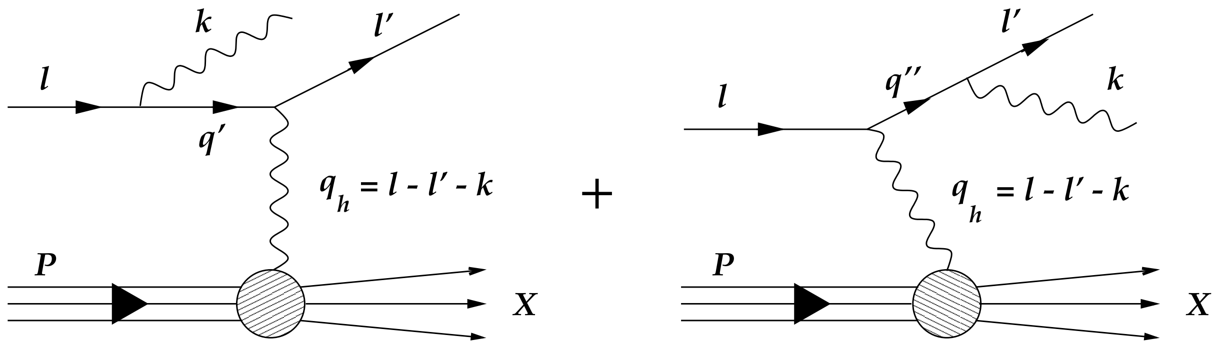

Figure 1.3: *Lowest order Feynman diagrams for the process $ep \to e\gamma X$ with the photon emission from the electron line.*

1.5 Radiative *ep* Scattering

In the perturbation theory of QED the Born contribution to the *ep* scattering is completed by higher order effects, such as real photon emission, multiple boson exchange, loop diagrams and vacuum polarisation. Among those only the real photon emission can be experimentally distinguished, provided the photon energy is above the detector acceptance threshold. The lowest order Feynman diagrams for photon emission from the lepton side are depicted in fig. 1.3 with the notation for the particle four-momenta. The photon radiation from the proton side is considered as background in this analysis. Its most prominent channel will be discussed in paragraph 3.2.5. The amplitudes given by both diagrams in fig. 1.3 and the interference between them contribute to the scattering cross section, so that there is no possibility for any particular event to determine whether it corresponds to the first or second diagram. The amplitudes for the first and second diagram are reversely proportional to the terms $(q'^2 - m_e^2)q_h^2$ and $(q''^2 - m_e^2)q_h^2$ respectively, therefore the differential cross section has several peaks when one or both these terms tend to zero. These peaks correspond to the following experimental configurations:[2]

- either $q'^2 \simeq 0$ or $q''^2 \simeq 0$, but q_h^2 is finite: the outgoing photon is emitted either along the incident or the final electron line. These events belong to the class of *radiative corrections* to the inclusive deep inelastic scattering.

  In the first case, as pictured schematically in fig. 1.4 a, the cross section is dominated by the contribution given by the first Feynman diagram, and this kind of events is called *Initial State Radiation (ISR)*. This process can be interpreted as DIS at lower electron beam energies, therefore they allow to measure F_2 at lower Q^2 values than can be reached using the non-radiative deep inelastic scattering. In the H1 detector the outgoing photon is measured by the photon arm of the luminosity system. Details of a recent H1 F_2 measurement with ISR events can be found in [işs01].

  In the second case, as depicted in fig. 1.4 b, the main contribution to the cross section is given by the second Feynman diagram in fig. 1.3, and such events are classified as *Final State Radiation (FSR)*. These events usually cannot be separated experimentally from non-radiative deep inelastic scattering, since both the outgoing electron and the photon build a common energy cluster in a calorimeter.

[2]The classical work by Mo and Tsai [mt69] played a major role in the analysis of different peaks in the radiative *ep* scattering at fixed target experiments. A review of radiative physics at HERA can be found in [spi91].

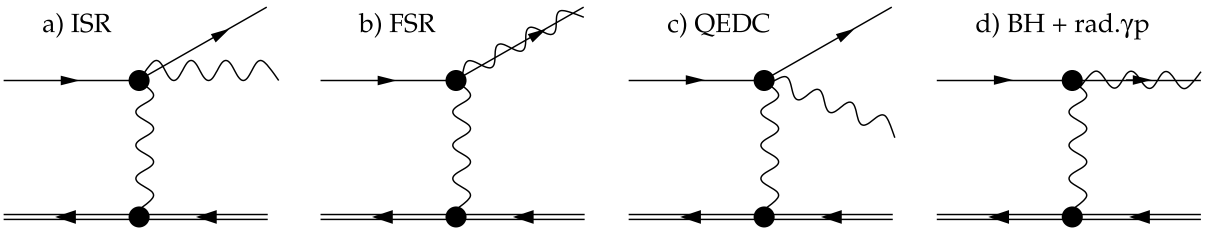

Figure 1.4: *Schematic representation of a) ISR, b) FSR, c) QED Compton and d) Bethe–Heitler and radiative photoproduction configurations.*

- $q_h^2 \simeq 0$, but q'^2 and q''^2 are finite: both the outgoing electron and the final photon are detected under large polar angles and almost back-to-back in azimuth, so that their total transverse momentum $p_{t,e\gamma} = |\vec{p}_{t,e} + \vec{p}_{t,\gamma}|$ (which is equal to the transverse momentum of the exchanged photon p_{t,γ^*}) is close to zero (see fig. 1.4 c). This configuration is referred to as *QED Compton Scattering (QEDC)*, since it involves the scattering of a quasi-real photon on an electron. The QEDC process is thus singled out by imposing a cut on the total transversal momentum or, almost equivalently, on the acoplanarity

$$A = 180^\circ - \Delta\phi \,, \tag{1.34}$$

where $\Delta\phi$ is the angle between the transverse momenta $\vec{p}_{t,e}$ and $\vec{p}_{t,\gamma}$. These events are the main topic of this thesis. Their detailed theoretical treatment will be discussed in the next paragraphs.

- both $q_h^2 \simeq 0$ and $q'^2 \simeq 0$: the final electron and photon have very small polar angles and therefore escape through the beam pipe (see fig. 1.4 d). They can be detected only by special low angle detectors like the electron and the photon arm of the luminosity system. The dominant elastic part of the cross section represents the BETHE–HEITLER (BH) *bremsstrahlung process* [bh34] utilised in H1 for the luminosity measurement (see paragraph 2.2.5). The inelastic contribution constitutes the radiative photoproduction.

1.6 QED Compton Scattering Cross Section

An exact computation of the differential QEDC scattering cross section has been conducted by COURAU and KESSLER [ck92] using the helicity amplitude technique [car74, ckp76]. "Exact" refers here to the fact that no approximation has been introduced a priori in the calculation of the Feynman graphs of fig. 1.3.

Because of an additional photon in the final state of QED Compton events, the kinematic variables describing the inclusive *ep* scattering have to be modified. The exchanged photon momentum is given as: $q_h = l - l' - k$, and formulae for the calculation of all other quantities on the lepton vertex change accordingly:

$$\begin{aligned} Q_h^2 &= -q_h^2 = -(l-l'-k)^2 \,, & x_h &= \frac{Q_h^2}{2P\cdot q_h} \equiv \frac{Q_h^2}{2P\cdot(l-l'-k)} \,, \\ y_h &= \frac{P\cdot q_h}{P\cdot l} \equiv \frac{P\cdot(l-l'-k)}{P\cdot l} \,, & M_X &= (P+q_h)^2 = Q_h^2\frac{1-x_h}{x_h} + m_p^2 \,. \end{aligned} \tag{1.35}$$

The expressions for these variables remain the same as in DIS if one computes them on the hadron vertex: $q_h = X - P$ etc., therefore they are referred to as *hadronic variables* and carry the subscript h. These variables have the same physical meaning as the usual ones in the inclusive ep scattering.

In comparison to the inclusive scattering, three additional independent variables have to be used to allow for a full description of the differential QEDC scattering cross section. For instance, if the event kinematics is determined by means of outgoing particle momenta, then apart from the electron energy and polar angle one has to measure also the same parameters of the final photon. Furthermore, the azimuthal angle is no more a trivial degree of freedom, but on the contrary, the acoplanarity is an essential event property.

In the formalism presented here the following variables are utilised apart from Q_h^2 and x_h to write the differential cross section:

- The Lorentz invariant scale variable x_γ:

$$x_\gamma = \frac{q_h \cdot l}{P \cdot l} = \frac{W^2 + Q_h^2 - m_e^2}{s - m_p^2 - m_e^2} \approx \frac{W^2 + Q_h^2}{s} \,, \tag{1.36}$$

  where

$$W^2 = (l - q_h)^2 = (l' + k)^2 \tag{1.37}$$

  is the invariant mass squared of the $e\gamma$ system.

- The scattering solid angle Ω^* in the centre of mass frame of the virtual Compton process. This quantity comprises two degrees of freedom: $d\Omega^* = du^* d\phi$, with $u^* = \cos\theta^*$, θ^* and ϕ^* being the corresponding polar and azimuthal scattering angles.

With these variables the differential QED Compton scattering cross section reads:

$$\frac{d^4\sigma^{ep\to e\gamma X}}{dx_h\, dx_\gamma\, dQ_h^2 d\Omega^*} = f^T_{\gamma^*/p}(x_h, x_\gamma, Q_h^2) \left[\frac{d\sigma}{d\Omega^*}\right]^T + f^L_{\gamma^*/p}(x_h, x_\gamma, Q_h^2) \left[\frac{d\sigma}{d\Omega^*}\right]^L \tag{1.38}$$

with

$$\left[\frac{d\sigma}{d\Omega^*}\right]^T = \frac{d\sigma_T}{d\Omega^*} + \epsilon\frac{d\sigma_L}{d\Omega^*} + \sqrt{2\epsilon(\epsilon+1)}\frac{d\sigma_{TL}}{d\Omega^*}\cos\phi^* + \epsilon\frac{d\sigma_{TT}}{d\Omega^*}\cos 2\phi^* \,, \tag{1.39}$$

$$\left[\frac{d\sigma}{d\Omega^*}\right]^L = \frac{d\sigma_L}{d\Omega^*} + \frac{1+\epsilon}{2\epsilon}\frac{d\sigma_L}{d\Omega^*} + \sqrt{\frac{1+\epsilon}{\epsilon}}\frac{d\sigma_{TL}}{d\Omega^*}\cos\phi^* - \frac{d\sigma_{TT}}{d\Omega^*}\cos 2\phi^* \,, \tag{1.40}$$

where the superscripts T and L denote the transversal and longitudinal polarisation of the virtual photon at the hadron vertex, while the subscripts T, L, TL and TT refer to its polarisation at the lepton vertex, *i.e.*, define the transverse and longitudinal cross sections and also the transverse-transverse and transverse-longitudinal interference terms of the virtual Compton scattering process $e\gamma^* \to e\gamma$.

The virtual photon spectra $f^T_{\gamma^*/p}$ and $f^L_{\gamma^*/p}$ in the expression 1.38 are given by:

$$f^T_{\gamma^*/p} = \frac{1-x_h}{4\pi^3 x_h x_\gamma} g^T(x_h, x_\gamma, Q_h^2)\sigma^T_{\gamma^* p} \,, \tag{1.41}$$

$$f^L_{\gamma^*/p} = \frac{1-x_h}{4\pi^3 x_h x_\gamma} g^L(x_h, x_\gamma, Q_h^2)\sigma^L_{\gamma^* p} \tag{1.42}$$

with

$$g^L(x_h, x_\gamma, Q_h^2) = g^T(x_h, x_\gamma, Q_h^2) - \frac{x_\gamma^2}{2x_h^2} = \frac{(1 - x_\gamma/x_h)Q_h^2 - x_h^2 m_p^2}{Q_h^2 + 4x_h^2 m_p^2} . \tag{1.43}$$

The polarisation parameter ϵ is given by $\epsilon = g^L/g^T$. The various polarisation terms for the virtual Compton scattering read:

$$\begin{aligned}
\frac{d\sigma_T}{d\Omega^*} &= \frac{\alpha^2}{W^2 + Q_h^2}\left[\frac{W^2}{(W^2 + Q_h^2)}\frac{1}{(1 + u^* + \eta)} + \frac{(W^2 + Q_h^2)}{4W^2}(1 + u^*)\right. &(1.44)\\
&\qquad \left. + \frac{Q_h^2}{W^2}\frac{(1 - u^*)}{(1 + u^* + \eta)} + \frac{Q_h^2}{2(W^2 + Q_h^2)}(1 - u^*)\right] ,\\
\frac{d\sigma_L}{d\Omega^*} &= \frac{\alpha^2}{W^2 + Q_h^2}\left[\frac{Q_h^2}{W^2 + Q_h^2}(1 - u^*)\right] , &(1.45)\\
\frac{d\sigma_{TL}}{d\Omega^*} &= \frac{\alpha^2}{W^2 + Q_h^2}\left[\frac{QW}{2(W^2 + Q_h^2)}\sqrt{1 - u^{*2}}\left(1 + \frac{Q_h^2}{W^2}\frac{1 - u^*}{1 + u^* + \eta}\right)\right] , &(1.46)\\
\frac{d\sigma_{TT}}{d\Omega^*} &= \frac{\alpha^2}{W^2 + Q_h^2}\left[\frac{Q_h^2}{2(W^2 + Q_h^2)}(1 - u^*)\right] &(1.47)
\end{aligned}$$

with the quantity η given by $\eta = 2m_e^2 W^2/(W^2 + Q_h^2)^2$.
As will be shown in the following sections, significantly lower M_X values than in the DIS measurements can be reached in QED Compton events at HERA, therefore one has to take into account not only the continuum inelastic but also the elastic and resonance contributions. The virtual photon absorption cross sections $\sigma^T_{\gamma^* p}$ and $\sigma^L_{\gamma^* p}$ for all three scattering processes have been given in paragraphs 1.1.1 – 1.1.3.

1.7 Monte Carlo Event Generator COMPTON

The Monte Carlo event generator COMPTON [cckk91, ker94] created on the basis of the above calculation is used in the present analysis. The original version 2.0 has lacked several important features, which are implemented into the new version 2.1 in this work. This will be discussed here and in sect. 3.4.

The program generates specific QED Compton events, *i.e.*, events with the final electron and photon observed at finite angle in the detector nearly back-to-back in azimuth. The limitations on acoplanarity and polar acceptance entail $Q_h^2 < W^2$ and $\eta \ll 1 + u^*$. To select relatively small Q_h^2 values, the following cuts on the acoplanarity and the transverse momentum of the $e\gamma$ system are imposed:

$$A < 45^\circ , \qquad p_{t,e\gamma} < 20\,\mathrm{GeV} . \tag{1.48}$$

The limit of 45° for the acoplanarity is used in the analysis chain, therefore in the upgraded version of the generator the limit has been extended up to 50° in order to avoid losses at the phase space boundary. The $p_{t,e\gamma}$ values are far below the cut value in the acceptance region of the present analysis. The elastic, resonance and continuum inelastic QEDC events are generated simultaneously by the program.

For the simulation in the resonance region the cross section parameterisation given by eq. 1.13 is employed. However, this is a relatively crude approximation of the real cross section in this region. Therefore the generated resonance events have been reweighted with the more accurate parameterisation by BRASSE *et al* [bra76] (also cited in paragraph 1.1.2).

To generate the continuum inelastic events, some proper structure function parameterisations have to be chosen. The continuum region is the least investigated kinematic domain of the QEDC scattering, hence there is a significant uncertainty in the choice of parameterisations.

The choice of F_L is not very important, since the differential cross section is almost insensitive to F_L. The authors have chosen:

$$F_L(x,Q^2) = \frac{4m_p^2x^2}{Q^2}F_2(x,Q^2) \tag{1.49}$$

which is, in particular, compatible with the SLAC measurements [dre71]. This F_L choice leads to the following simplification of the eq. 1.15 – 1.16:

$$\sigma^T_{\gamma^* p} = \frac{4\pi^2\alpha}{Q^2(1-x)}F_2(x,Q^2)\,, \tag{1.50}$$

$$\sigma^L_{\gamma^* p} = \frac{4\pi^2\alpha}{Q^2(1-x)}F_L(x,Q^2) = \frac{4\pi^2\alpha}{Q^2(1-x)}\frac{4m_p^2x^2}{Q^2}F_2(x,Q^2)\,. \tag{1.51}$$

To determine F_2, the authors have implemented several simple scale invariant parameterisations into the original version 2.0 of the program, which allowed a relatively fast event generation. The default parameterisation [kr78] based on the counting rules is:

$$F_2^x(x) = \frac{35}{32}\sqrt{(x)}(1-x)^3 + 0.2(1-x)^7\,. \tag{1.52}$$

To ensure that F_2 vanishes as Q^2 approaches zero, a damping factor of the form similar to eq. 1.31 is applied, such that the resulting $F_2(x,Q^2)$ is given by the expression

$$F_2(x,Q^2) = \frac{Q^2F_2^x(x)}{Q^2 + m_c^2F_2^x(x)} \tag{1.53}$$

with $m_c^2 = 1\,\mathrm{GeV}^2$. With this form of the damping factor the cross sections $\sigma^T_{\gamma^* p}$ and $\sigma^L_{\gamma^* p}$ become in the limit $Q^2 \to 0$:

$$\sigma^T_{\gamma^* p} \to \frac{4\pi^2\alpha}{m_c^2} \simeq 100\,\mu\mathrm{b}\,, \qquad \sigma^L_{\gamma^* p} \to 0\,. \tag{1.54}$$

The limit for $\sigma^T_{\gamma^* p}$ has a typical size of the photoproduction cross section [pdg00].

In order to illustrate the F_2 behaviour in the low Q^2 range, the default parameterisation employed in the COMPTON generator and the ALLM97 fit are depicted in fig. 1.5 as functions of Q^2 at a constant value $x = 10^{-2}$. It is seen that both models include a smooth transition to zero as Q^2 tends to zero, but there is a significant discrepancy between the two models. This discrepancy increases at lower x values, as demonstrated in fig. 1.6, in which both parameterisations are plotted as functions of x at a constant value $Q^2 = 1\,\mathrm{GeV}^2$. The discrepancy occurs, because the COMPTON $F_2^x(x)$ parameterisations do not include terms like $x^{-\lambda}$, and hence they don't rise rapidly with decreasing x. Therefore they can be expected to work only at relatively high x values.

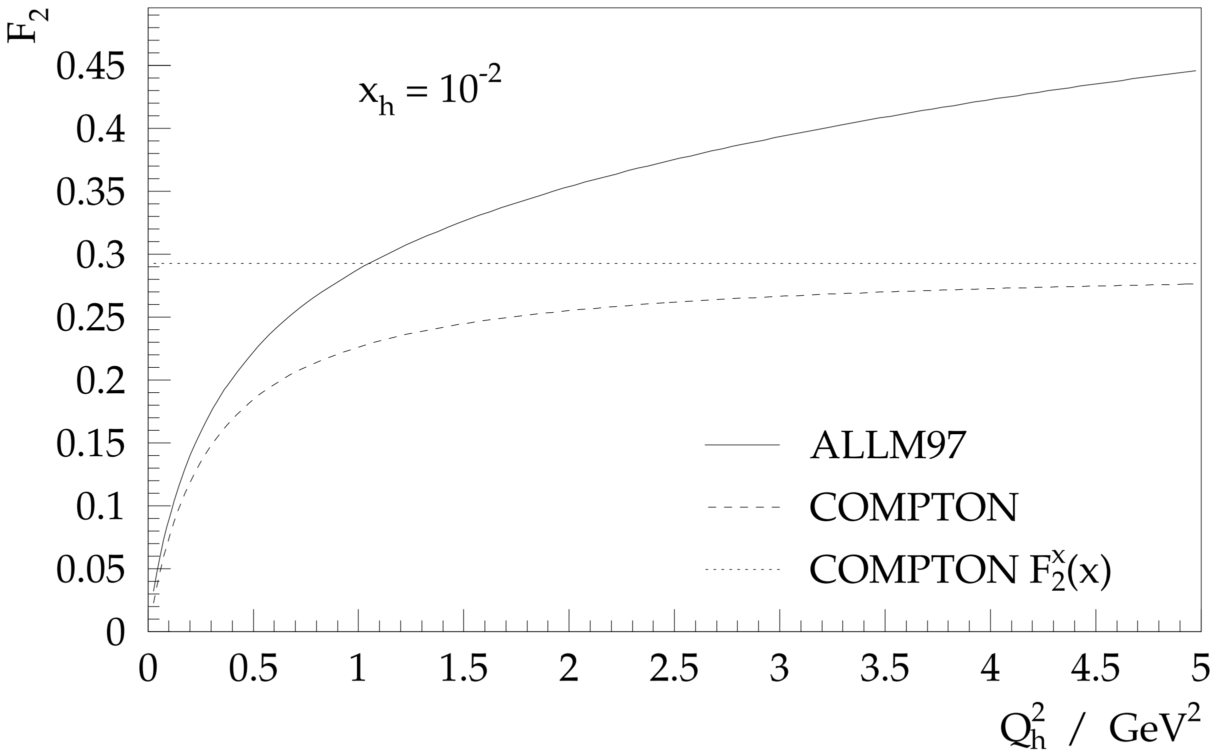

Figure 1.5: *The ALLM97 fit and the default COMPTON F_2 parameterisation in the continuum region as functions of Q^2 at $x = 10^{-2}$.*

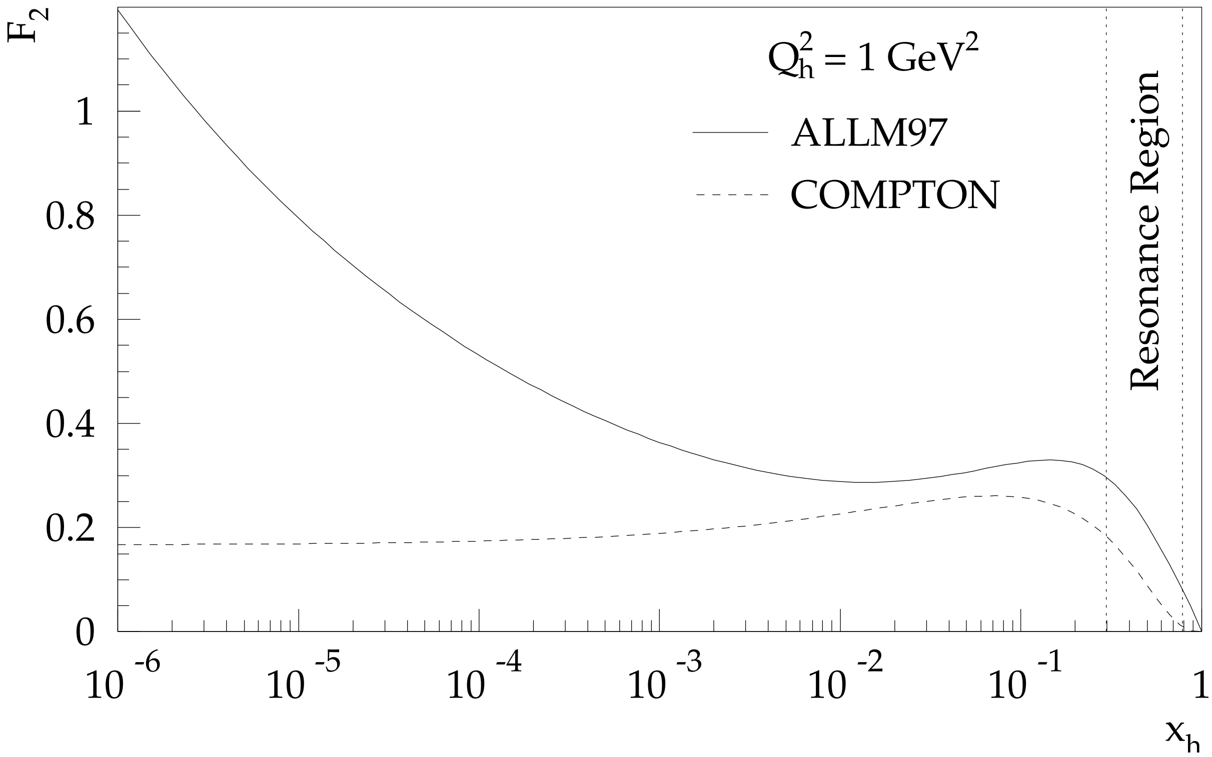

Figure 1.6: *The ALLM97 fit and the default COMPTON F_2 parameterisation in the continuum region as functions of Bjorken x at $Q^2 = 1\,\mathrm{GeV}^2$.*

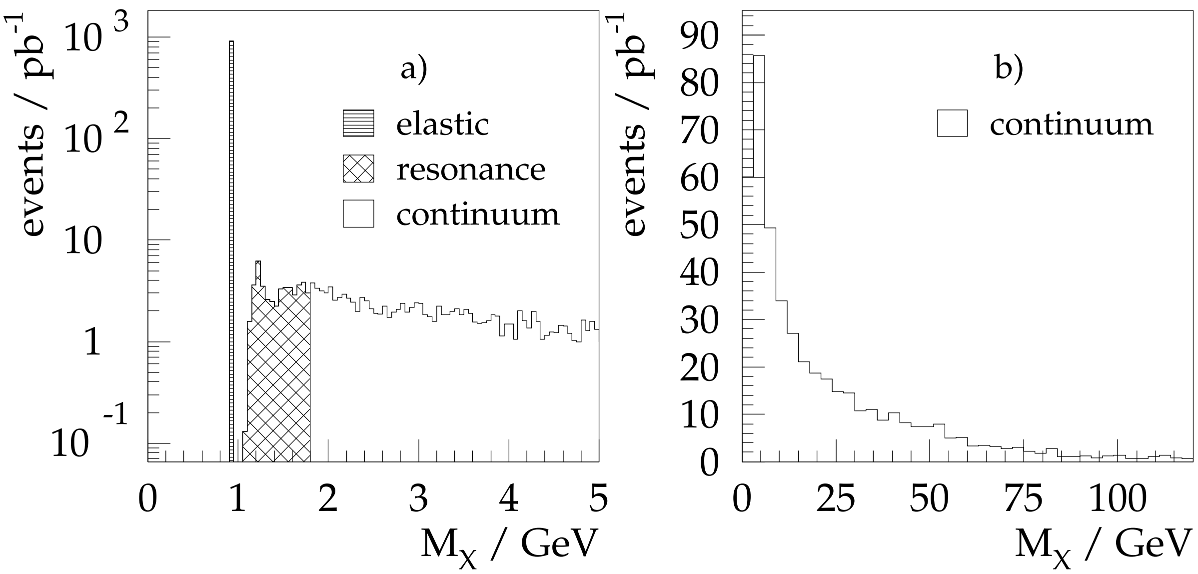

Figure 1.7: *Invariant mass of hadronic final state M_X in QEDC events as generated by the COMPTON program: a) three contributions to the QEDC cross section in the low M_X region, b) all continuum inelastic events.*

In the framework of this analysis the ALLM97 fit has been implemented in the new version 2.1 of the generator. A simulation with this fit is used in all plots of COMPTON events throughout this thesis.

A comparison of simulations with different F_2 parameterisations to real QEDC data is one of the main goals of this work. The results of this comparison are described in sect. 5.2. It is however important to understand first, in what kinematic region QED Compton events are concentrated. This is discussed in the next section.

1.8 Kinematic Range of QED Compton Events

The kinematic domain of QED Compton events at HERA is illustrated by a sample of events produced by the COMPTON generator. The distributions shown in figures of this section correspond to the experimental event selection in the present measurement.

The relative contributions of elastic, resonance and continuum inelastic channels to the QEDC scattering cross section are displayed in fig. 1.7, in which the M_X distributions are plotted. The low mass range where all contributions are visible is drawn in the left picture. It is seen that elastic scattering makes up a big fraction of QEDC events in contrast to inclusive ep scattering at HERA. The right picture shows all continuum inelastic events. Their distribution peaks at low masses, but has a long tail up to more than 100 GeV.

Figure 1.8 shows the distributions of the QEDC events in the hadronic variables x_h and Q_h^2. All types of events are concentrated in the low Q_h^2 region between zero and several GeV^2. However there is a difference between the elastic and inelastic events. The former are characterised by typically much lower Q_h^2. They reach down to less than 10^{-8} GeV^2, whereas the latter are distributed mostly between 10^{-1} and 10 GeV^2. The reason for this difference is that the structure functions that describe the inelastic scattering vanish at $Q_h^2 \to 0$, whereas the proton form factors which determine the elastic scattering don't fall to zero but even rise, see

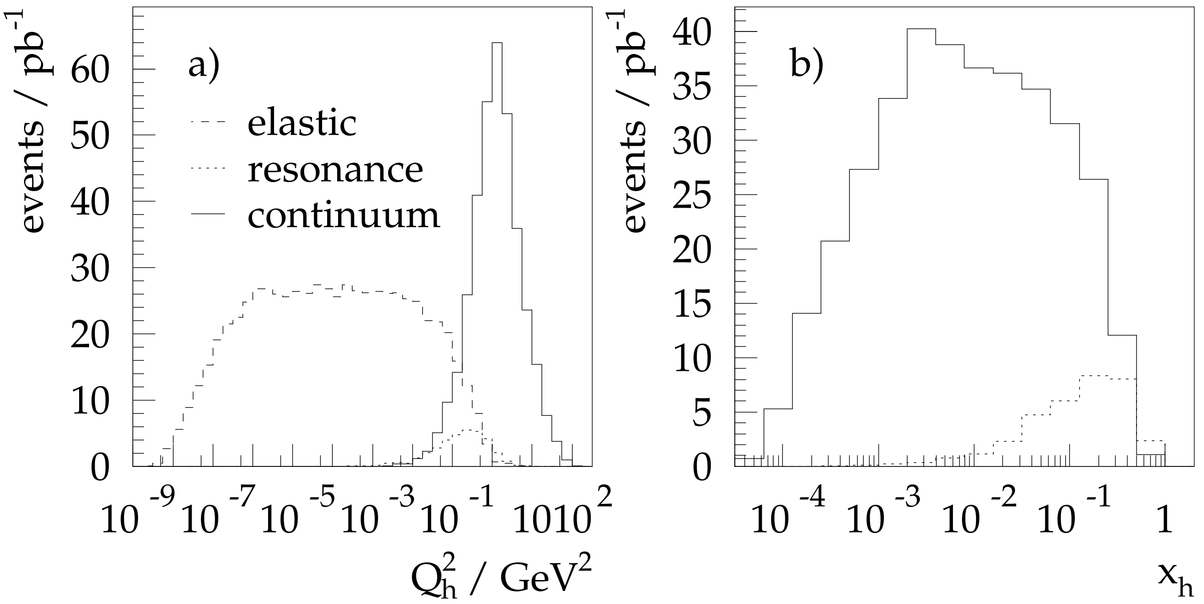

Figure 1.8: *Kinematic range of QEDC events after the experimental selection. The distributions of the generated hadronic variables a) Q_h^2 and b) x_h are plotted. Three reaction channels are depicted by different line styles. The trivial distribution $x_h \equiv 1$ of the elastic events is omitted in fig. b.*

eq. 1.12. The lower Q_h^2 limit of the elastic events is thus determined only by the very low phase space boundary.

The x_h distribution of the elastic events is trivial: $x_h \equiv 1$. The inelastic events are spread in the broad range of medium to high x between 10^{-4} and 1.

The continuum inelastic part of the cross section is of special interest in this analysis. It is given by the proton structure functions F_2 and F_L, with the F_L contribution being almost negligible. Thus, measuring QEDC cross section provides us with information about the F_2 behaviour in the low M_X region, *i.e.*, the domain of low Q_h^2 and medium to high x_h.[3]

In order to contrast the kinematic range of continuum inelastic QED Compton events with those of inclusive DIS measurements, the regions of both HERA and fixed target exeriments are shown in fig. 1.9. Only the ranges of experiments and analyses with presently most significant results, *i.e.*, with the results used for the theoretical F_2 fits are depicted. The experiments with neutrino beams, where F_2 is measured only in the charge current scattering, are not included.

For the comparison the kinematic domain of continuum inelastic QED Compton events is shown in a similar figure 1.10 overlaying the DIS regions. The points depict the same generated events as plotted in fig. 1.8. As seen from this figure, QED Compton events allow us to reach the region of low Q^2: $10^{-1}\,\mathrm{GeV}^2 \lesssim Q^2 \lesssim 10\,\mathrm{GeV}^2$ and wide range of x: $10^{-4} \lesssim x \lesssim 0.5$, inaccessible in inclusive ep scattering at HERA. One can see, that this region was partially covered by the fixed target experiments and partially not measured at all in the neutral current lepton–hadron scattering.

A direct measurement of F_2 in this region implies a measurement of the double differential QEDC cross section in terms of hadronic variables x_h and Q_h^2. However, in this analysis the

[3]The possibility to study the proton structure in this kinematic domain using QED Compton events was first pointed out in [bls91].

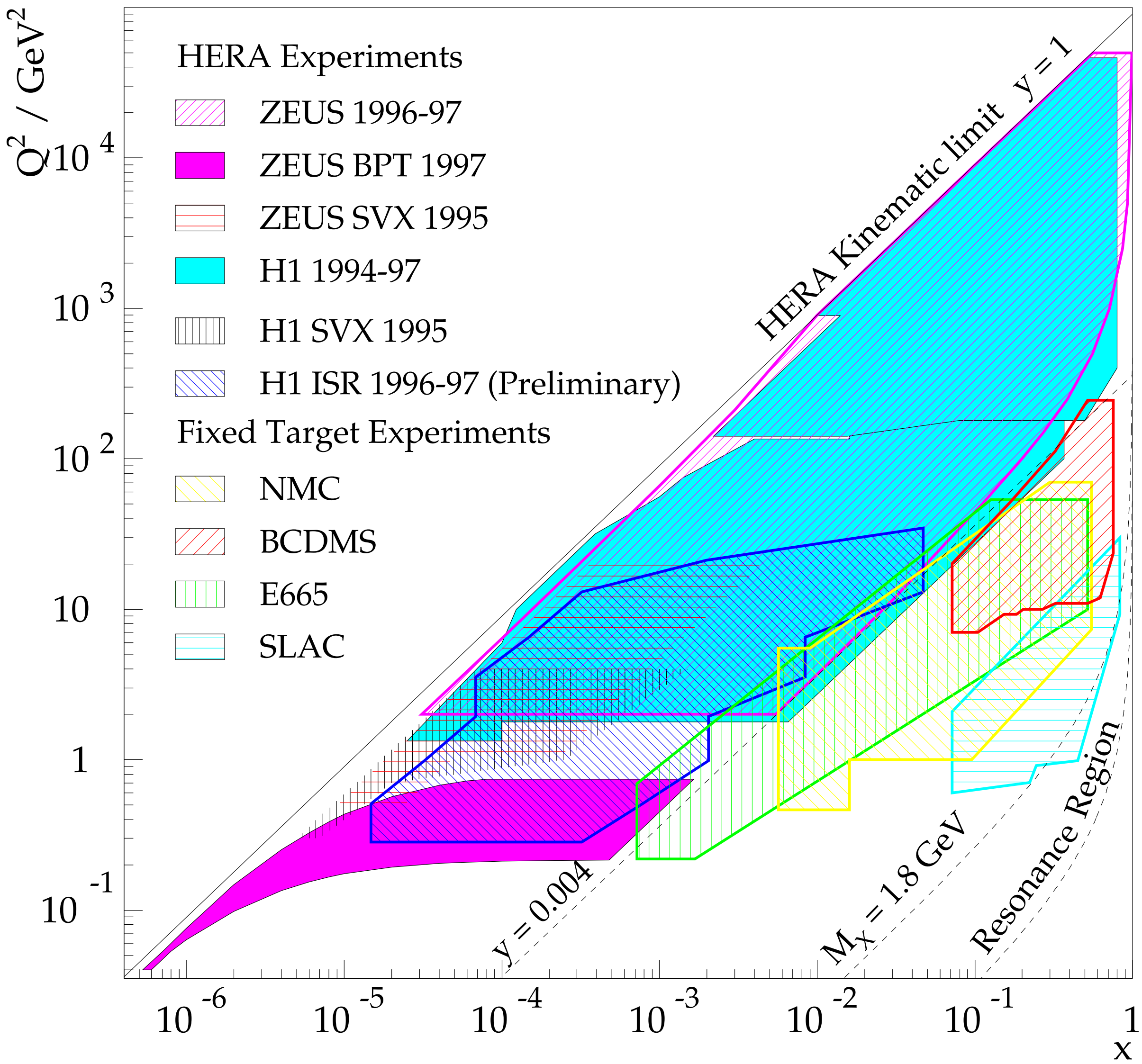

Figure 1.9: *Kinematic regions of F_2 measurement in lepton–hadron experiments. Out of HERA results, the domains of H1 low [h100] and high Q^2 [h101], ZEUS standard [zeus01] and BPT [zbpt00], H1 [h197] and ZEUS [zeus96] shifted vertex, and H1 ISR [işs01] measurements are drawn. The fixed target experiments shown are SLAC electron beam experiments [whi92], and CERN BCDMS [bcdms], NMC [nmc97] and FNAL E665 [e665] experiments on muon–nucleon scattering.*

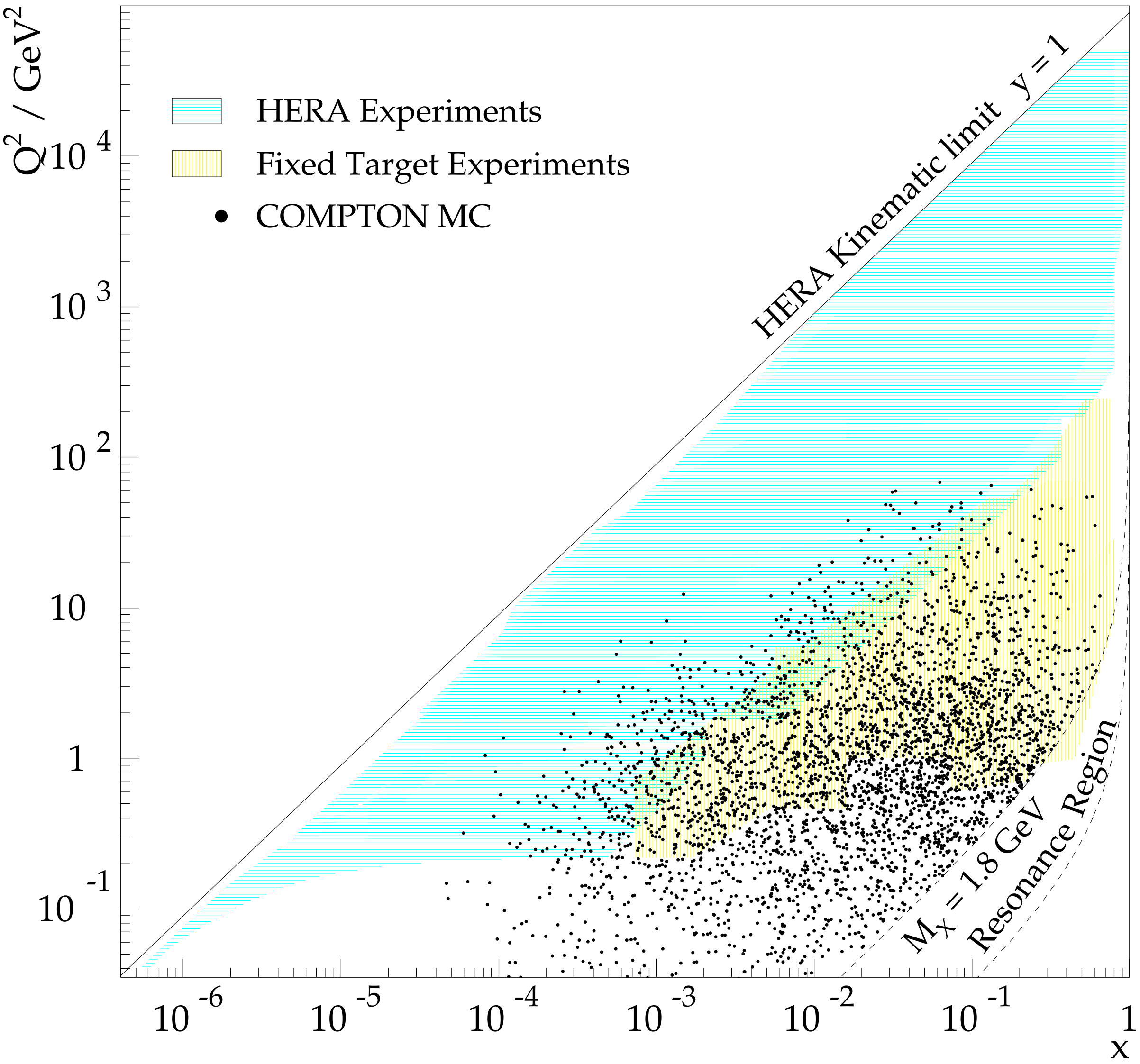

Figure 1.10: *Kinematic domain of continuum inelastic QED Compton events in contrast to the regions of inclusive DIS measurements at HERA and fixed target experiments.*

measurement is performed in terms of so called *leptonic* variables. These quantities are introduced for an approximative computation of the scattering cross section, as discussed in the following section.

1.9 QED Compton Events in Collinear Approximation

The calculation of the QEDC cross section given above is an accurate but rather complex treatment of the scattering process. In such cases it is often desirable to employ simpler and more transparent expressions which exhibit basic features and the underlying physics of the reaction, provided such formulae supply an acceptable degree of accuracy. An often used approach of this kind has been originally conceived by WEIZSÄCKER [wei34] and WILLIAMS [wil34] who demonstrated that the field of a rapidly passing charged particle can be well approximated by a beam of photons having the same energy spectrum as this field. In a properly generalised form this technique was applied to *ep* scattering by many authors. The formalism reviewed in this chapter refers to the latest theoretical publications related to the HERA experiments (see [rv98] and references therein).

In this ansatz, usually referred to as the *equivalent photon approximation* or *collinear approximation*, the transverse component of the exchanged photon momentum is neglected, *i.e.*, it is assumed to be emitted collinear to the incident proton. This permits the treatment of the exchanged photon as a parton in the proton, similar to gluons and quarks. The entire QEDC scattering process is then considered as probing the photon in the proton by a virtual lepton, as schematically shown in fig. 1.11. The outgoing photon plays the role of the struck quark in DIS. Like the Quark Parton Model in DIS, this picture is valid only in the infinite momentum frame, where the transverse momentum of the exchanged photon is negligible. Due to this analogy to the conventional DIS the QEDC process in this representation is called *Deep Inelastic Compton Scattering (DICS)* .

The kinematic variables used to describe the event are formally the same as calculated in DIS

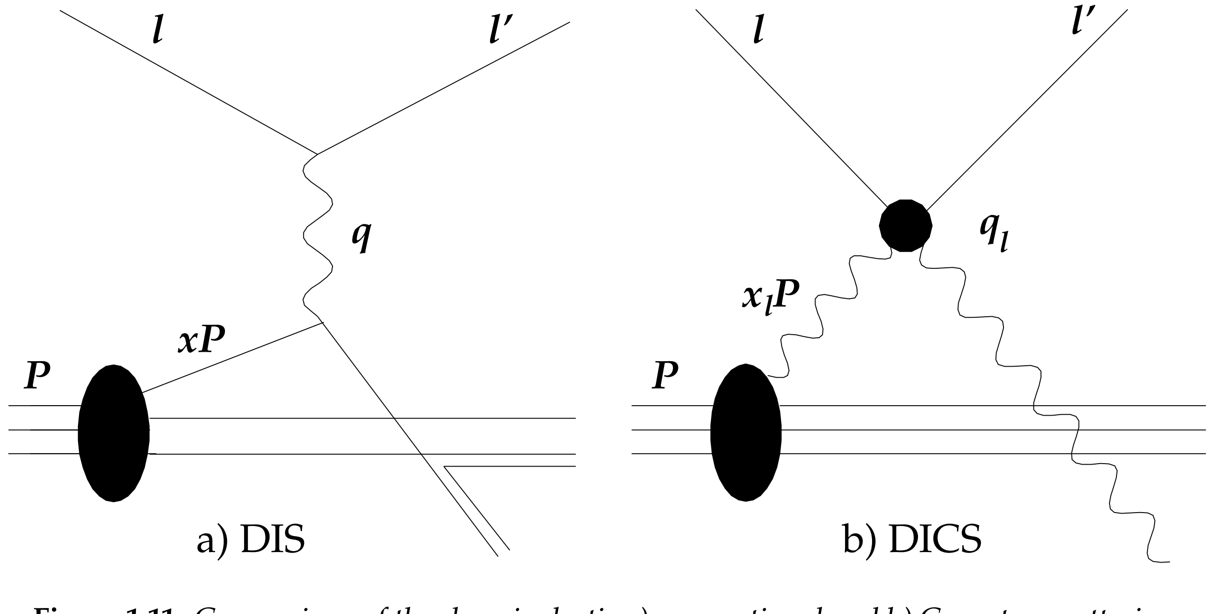

Figure 1.11: *Comparison of the deep inelastic a) conventional and b) Compton scattering.*

on the lepton vertex:

$$Q_l^2 = -q_l^2 = -(l - l')^2 \,, \qquad x_l = \frac{Q_l^2}{2P \cdot q_l} \equiv \frac{Q_l^2}{2P \cdot (l - l')} \,, \qquad y_l = \frac{P \cdot q_l}{P \cdot l} \equiv \frac{P(l - l')}{P \cdot l} \,, \quad (1.55)$$

therefore they are called *leptonic variables* and carry subscript l. Their physical meaning however differs from that of standard DIS variables. Instead, it is similar to DIS in the interpretation given here. To be specific, the variable x_l is treated as the fraction of the proton momentum carried by the emitted photon in the infinite momentum frame:

$$-q_h \simeq x_l P \,, \quad (1.56)$$

where $-q_h$ is the four-momentum of the exchanged photon, if one treats it as *emitted by the proton*. Q_l^2 is in this interpretation a hard resolving scale similar to the usual Q^2 in DIS. One should stress, that expression 1.56 is only approximately valid for the components of the four-momenta in the infinite momentum frame, but it doesn't hold, *e.g.*, for the squared four-momenta: $Q_h^2 \neq x_l^2 m_p^2$. In contrast, the relation $Q_h^2 \gg x_l^2 m_p^2$ holds in all events. Q_h^2 becomes of the same order of magnitude only as it approaches its lower kinematic limit:

$$Q^2_{h\,\min} = \frac{x_l^2 m_p^2}{1 - x_l} \quad (1.57)$$

where the cross section vanishes. In fact, it is only in this limit that the transverse momenta of the final electron and photon *exactly* balance each other. In general, the smaller Q_h^2, the better this method describes the data.

The following relations between the hadronic and the leptonic variables are always valid:

$$0 \leq Q_h^2 \leq Q_l^2 \,, \qquad x_l \leq x_h \leq 1 \,. \quad (1.58)$$

The variables x_l and x_γ are almost equal in real events. In the collinear approximation they are exactly equal: $x_l \equiv x_\gamma$. Again, the smaller the exchanged photon virtuality, the better this equation holds in practice.

In the collinear approximation the event kinematics is constraint by only two variables like in the inclusive ep scattering. The differential DICS cross section is given as a convolution of the probability $\gamma(x_l, Q_l^2)$ to find a photon "inside" the proton by probing it at the scale Q_l^2 and the cross section of the Compton process $e\gamma \to e\gamma$:

$$\frac{d^2\sigma^{\rm DICS}}{dx_l\, dQ_l^2} = \int_0^1 \frac{dz}{z}\, \gamma(z, Q_l^2)\, \frac{d^2\hat{\sigma}^{e\gamma\to e\gamma}}{d(x_l/z)\, dQ_l^2} \quad (1.59)$$

with

$$\frac{d^2\hat{\sigma}^{e\gamma\to e\gamma}}{d\hat{x}\, dQ_l^2} = \frac{2\pi\alpha^2}{W^2} \frac{1 + (1 - y_l)^2}{1 - y_l} \delta(1 - \hat{x}) \,. \quad (1.60)$$

The "structure" function $\gamma(x_l, Q_l^2)$ determines, thus, the *photon–parton content* of the proton or its *equivalent photon flux*[4].

After the integration over z in eq. 1.59 using eq. 1.60 the differential DICS cross section reads:

$$\frac{d^2\sigma^{\rm DICS}}{dx_l\, dQ_l^2} = \frac{2\pi\alpha^2}{W^2} \frac{1 + (1 - y_l)^2}{1 - y_l}\, \gamma(x_l, Q_l^2) \,. \quad (1.61)$$

[4] In some publications this function is also denoted as $f_{\gamma|p}$ or $D_{\gamma|p}$.

According to this expression, an experimental determination of the double differential QED Compton scattering cross section $d^2\sigma/dx_l\,dQ_l^2$ can be interpreted in the collinear approximation as a measurement of the photon–parton density function $\gamma(x_l, Q_l^2)$.
To work out a theoretical description of this function behaviour, one has to distinguish the elastic, resonance and continuum inelastic contributions.

1.9.1 Elastic Contribution

Like in the exact calculation given above, the elastic cross section in the equivalent photon approximation is written down in terms of the electric G_E and magnetic G_M form factors given by eq. 1.12. The elastic contribution to $\gamma(x_l, Q_l^2)$ reads [kni91]:

$$\gamma_{\mathrm{el}}(x_l) = \frac{\alpha}{\pi x_l}\int_{Q_{h1}^2}^{Q_{h2}^2}\frac{dQ_h^2}{Q_h^2}\left[\left(1 - x_l - \frac{x_l^2 m_p^2}{Q_h^2}\right)\frac{G_E^2(Q_h^2) + \tau G_M^2(Q_h^2)}{1+\tau} + \frac{x_l^2}{2}G_M^2(Q_h^2)\right], \tag{1.62}$$

where $\tau = Q_h^2/4m_p^2$ and the integration limits are given by:

$$Q_{h1,2}^2 = \frac{1}{2s}\left[(s+m_p^2)[s(1-x_l)+m_p^2] \mp (s-m_p^2)\sqrt{[s(1-x_l)+m_p^2]^2 - 4sm_p^2}\right] - 2m_p^2\,. \tag{1.63}$$

The small m_p^2 expansion ($m_p^2 \ll s(1-x_l)$) of this expression yields:

$$Q_{h1}^2 \simeq Q_{h\,\mathrm{min}}^2 \equiv \frac{x_l^2 m_p^2}{1-x_l}\,, \qquad Q_{h2}^2 \simeq Q_{h\,\mathrm{max}}^2 \equiv s(1-x_l)\,. \tag{1.64}$$

From eq. 1.62 follows that the elastic part of $\gamma(x_l, Q_l^2)$ does not depend on Q_l^2.

1.9.2 Inelastic Contribution

The inelastic scattering in collinear approximation was first worked out by BLÜMLEIN, LEVMAN and SPIESBERGER [bls93]. The γ function in this region is given by the expression

$$\gamma_{\mathrm{in}}(x_l, Q_l^2) = \frac{\alpha}{2\pi}\int_{x_l}^{1}dz\int_{Q_{h\,\mathrm{min}}^2}^{Q_l^2}\frac{dQ_h^2}{Q_h^2}\frac{z}{x_l}\left[\frac{1+(1-z)^2}{z^2}F_2\left(\frac{x_l}{z}, Q_h^2\right) - F_L\left(\frac{x_l}{z}, Q_h^2\right)\right], \tag{1.65}$$

where the F_L contribution can be neglected in practice. To get a theoretical prediction of the γ behaviour in this region, an F_2 parameterisation defined for $Q_h^2 \to Q_{h\,\mathrm{min}}^2 \approx 0$ has to be chosen. This can be in particular one of the parameterisations described in section 1.4.
To calculate $\gamma(x_l, Q_l^2)$ in the resonance region, one can rewrite the equations 1.15 – 1.16 as:

$$F_2 = \frac{Q^2(1-x)}{4\pi^2\alpha}\frac{Q^2}{Q^2+4m_p^2x^2}(\sigma_{\gamma^*p}^T + \sigma_{\gamma^*p}^L)\,, \tag{1.66}$$

$$F_L = \frac{Q^2(1-x)}{4\pi^2\alpha}\sigma_{\gamma^*p}^L \tag{1.67}$$

and make use of the expressions 1.13 – 1.14 or alternative fits for the cross sections $\sigma_{\gamma^*p}^T$ and $\sigma_{\gamma^*p}^L$ cited in paragraph 1.1.2. Equivalent F_2 and F_L parameterisations determined in this manner can then be put into eq. 1.65.

1.10 pQCD Based Calculation of the γ Function

The latest theoretical computation of the function $\gamma(x_l, Q_l^2)$ has been performed by DE RÚJULA and VOGELSANG [rv98] based on a perturbative QCD approach. In pQCD the structure function F_2 is defined as an incoherent sum of parton density functions (1.24), and, neglecting F_L, equation 1.65 is rewritten as follows:

$$\frac{\partial \gamma(x_l, Q^2)}{\partial \ln Q^2} = \frac{\alpha}{2\pi} \int_{x_l}^{1} \frac{dx_h}{x_h} \sum_{i=1}^{N_f} q_i(x_h, Q^2) P_{\gamma q}\left(\frac{x_l}{x_h}\right) , \tag{1.68}$$

where the quark-to-photon splitting function is:

$$P_{\gamma q}(z) = \frac{1 + (1-z)^2}{z} \equiv \frac{3}{4} P_{gq}(z) \tag{1.69}$$

and the subscript of Q^2 plays no role in this differential form. The expression 1.68 can be called the "QED evolution equation" similar to the QCD gluon evolution equation 1.28. It is in principle valid only in the region where F_2 can be represented in terms of parton distribution functions, *i.e.*, at Q^2 beyond some typical lower pQCD scale μ_0^2. Like the QCD evolution equations it can be solved starting from some quark distribution at $Q^2 = \mu_0^2$ and evolving it to higher Q^2 values. The authors have used $\mu_0^2 = 0.25\,\mathrm{GeV}^2$ as the start scale [vog01] and the most recent parton density functions by GLÜCK, REYA and VOGT [grv98].

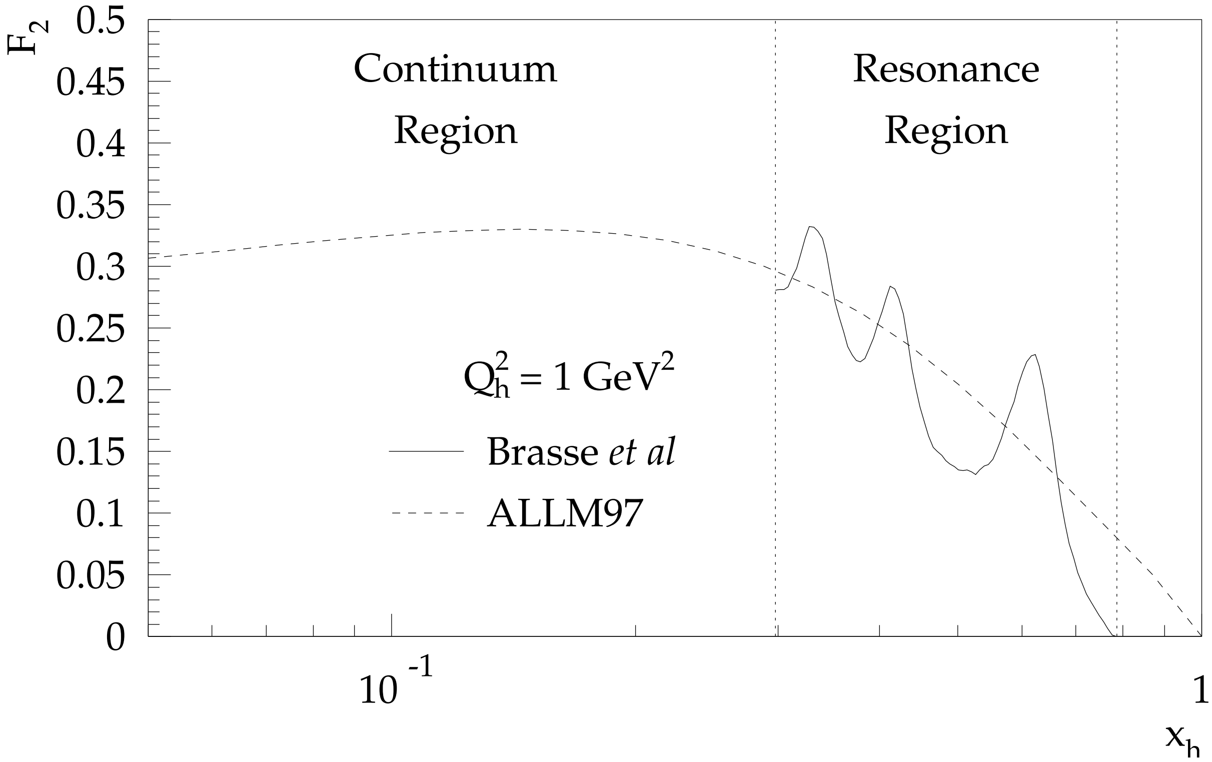

Figure 1.12: *Comparison of the ALLM97 F_2 (dashed line), extended into the resonance region, and the parameterisation of the resonance domain by Brasse et al (solid line). Both fits are plotted as functions of x_h at $Q_h^2 = 1\,\mathrm{GeV}^2$.*

The same parton distributions have been used also in the resonance region instead of the real resonance parameterisations. This approach is based on the *local duality* [bg71, kob75, rgp77] observed in the first SLAC experiments. Namely, it was found that the structure functions, extended from the continuous to the resonance domain, go through the resonance bumps, agreeing with the data averaged over each resonance. This feature of the function F_2 is illustrated in fig. 1.12, where the ALLM97 F_2, extended into the resonance domain, is contrasted to the parameterisation of the resonance region by Brasse *et al*. Similar to the F_2 parameterisations in fig. 1.6, both fits are plotted as functions of x_h at a constant Q_h^2 value of $1\,\mathrm{GeV}^2$.

The most essential difference between equations 1.28 and 1.68 is the self-coupling of gluons P_{gg} arising from their non-abelian nature. Consequently these two equations predict strikingly different Q_l^2 evolutions of γ and g functions.

One should note, that there is no elastic contribution to the gluon density function. But the elastic contribution to γ is independent on Q_l^2, *i.e.*, it doesn't change its Q_l^2 behaviour. Besides, the elastic scattering cross section is very well known. It is calculated with 1–2% precision. It was utilised, in particular, to cross-check the H1 luminosity measurement [ker94, fm98]. For these reasons there is no need to separate only the inelastic contribution in order to investigate its dependence on Q_l^2 and compare to the gluon content.

The proposal of the authors was, thus, to measure the total photonic function of the proton and contrast its Q_l^2 evolution to that of its gluonic counterpart. The expected Q_l^2 behaviour of the γ function at some constant x_l values accessible at HERA is depicted in fig. 1.13 in comparison to the leading order gluon distribution function by Glück, Reya and Vogt [grv98].

The cross section measurement in terms of the leptonic variables has been carried out in this work. One should stress that it can be interpreted as a measurement of the function γ only if the collinear approximation is applicable in the studied kinematic region. Therefore a study of the accuracy of this approach has also been performed. It will be discussed in sect. 5.3.

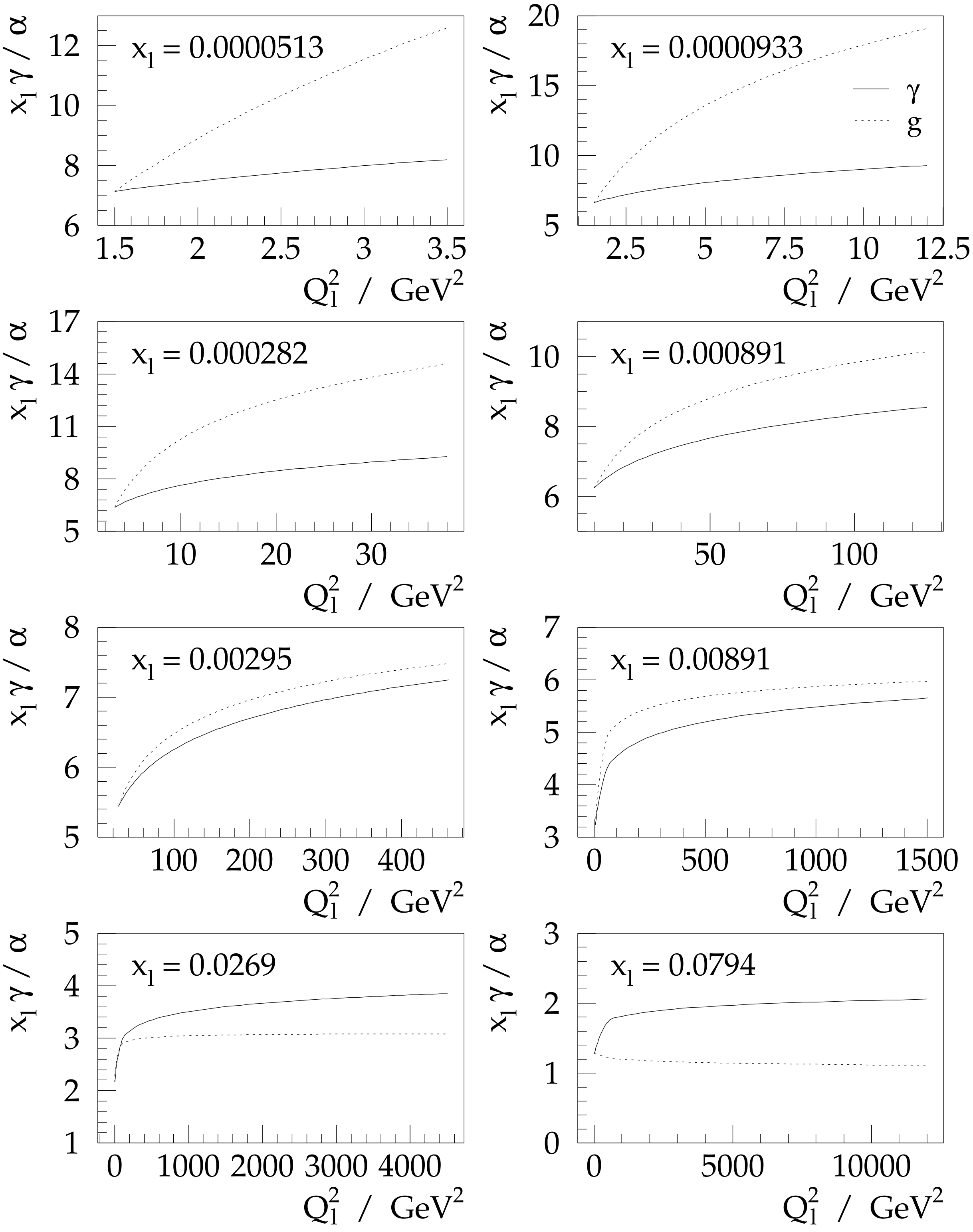

Figure 1.13: *Q_l^2 evolution of the γ function plotted as $x_l\gamma/\alpha$ in different x_l-bins as predicted by De Rújula and Vogelsang. The dotted line displays the Q^2 dependence of the LO GRV [grv98] gluon density, which has been normalised in each plot so as to coincide with $x_l\gamma/\alpha$ at the lowest accessible Q^2 value. The data for the curve drawings have been provided by W. Vogelsang.*

Chapter 2

The H1 Detector at HERA

The data for this analysis were collected with the H1 detector in the year 1997. After a brief overview of the accelerator HERA, the H1 experimental setup is described. Special attention is payed to the detector components relevant for the presented measurement of the QED Compton scattering cross section.

2.1 HERA Storage Ring

The *Hadron–Elektron–Ring–Anlage* HERA [vw94] at DESY is the first ever constructed storage ring to collide positrons or electrons[1] with protons. A schematic layout of the acceleration facility together with the injection system is presented in fig. 2.1.

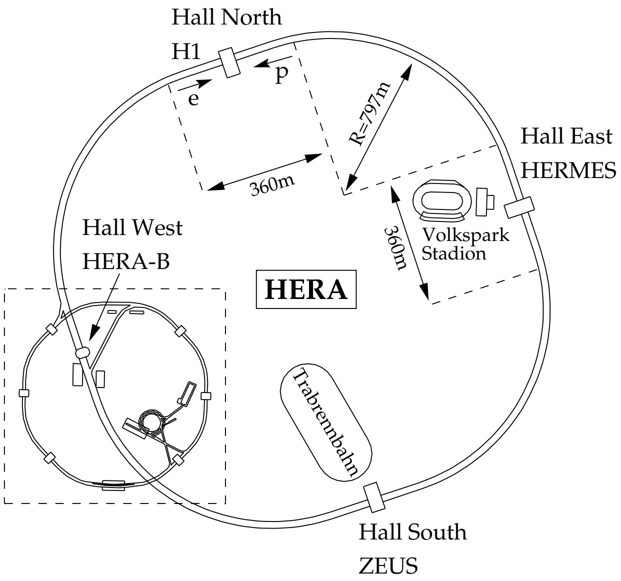

Figure 2.1: *Schematic view of HERA (left) and its preaccelerator complex (right).*

The proton injection complex includes the 50 MeV linac, the DESY II ring and the modified PETRA II ring where protons are accelerated up to the energy of 40 GeV. The electrons go through the 500 MeV linac, DESY III and then PETRA II to reach the energy of 12 GeV. Further

[1]The generic name "electron" will be used throughout this thesis to denote both electrons and positrons. The name "positron" will be used only in the discussion of those parts of the presented analysis where the particle charge is relevant.

the electron and proton beams are injected into HERA, where they are stored in two independent accelerators placed in a 6.3 km long tunnel. Inside the tunnel the electron beam is steered by a warm magnet system of 0.165 T and the proton beam is guided by 4.68 T superconducting magnets. The counter rotating beams collide head-on at the North and South interaction regions, where the general purpose detectors H1 and ZEUS are installed. In the years 1994, 1996 and 1997 the HERA collider was operating with 27.5 GeV positrons and 820 GeV protons at a centre of mass energy of 300 GeV. The HERA particle beams are split into 220 bunches with 96 ns bunch crossing intervals corresponding to a rate of 10.4 MHz. In a typical run there are in average 174 colliding bunches. The remaining bunches are either not filled or have no filled counterpart. The maximum beam currents achieved in 1997 were 74 mA for the proton beam and 28 mA for the electron beam.

2.2 H1 Experimental Facility

The H1 detector [h1d97] is a multiple purpose experimental apparatus designed to measure particles produced in high energy electron–proton scattering. It is a complex arrangement of subdetectors built around the nominal interaction point IP of colliding electron and proton beams. Figure 2.2 is a schematic three-dimensional view of the main setup. Figure 2.3 shows a longitudinal cut through the detector along the beam line. The main detector is a cylindrically symmetric installation with nearly 4π coverage in the laboratory frame except for the backward and forward region, where the colliding beams enter the facility. Because of the substantially higher energy of the proton beam compared to the electron beam the centre of mass frame is boosted into the direction of the proton beam. Consequently, the H1 detector has a more massive and higher segmented instrumentation in this direction.

The right handed coordinate system is chosen so that the z axis points into the direction of the protons, called therefore “forward direction”. The origin of the coordinate system is placed at the nominal interaction point.

The interaction point is situated inside the beam pipe which is enclosed in the tracking systems. The tracking device is used for the measurement of charged particle momenta and their identification. The particle energies are measured by the calorimeters surrounding the tracker. The time-of-flight system consists of three scintillators positioned along the beam axis. The superconducting cylindrical solenoid sourrounds both the tracking system and the calorimeters and produces an almost uniform magnetic field of 1.16 T parallel to the beam axis. The next layer is formed by the iron return yoke, instrumented with streamer tubes for muon detection and recording of residual particles that leak out of the calorimeters. Muons going in the forward direction are also registered by the forward muon spectrometer. The influence of the magnetic field on the beam circulation in HERA ring is neutralised by a superconducting compensation coil. The H1 main detector is complemented by the luminosity system installed downwards the electron beam line in the HERA tunnel. The data delivered by the detector components are processed by the trigger and data acquisition system. In the present work the following subdetectors are used:

- the backward spaghetti calorimeter in conjunction with the backward drift chamber to detect the scattered electron and photon and measure their energies and momenta,
- components of the central tracking detector, primarily the backward silicon tracker and the central inner multiwire proportional chamber to identify the scattered electron, measure the interaction point z position and the electron’s scattering angle,

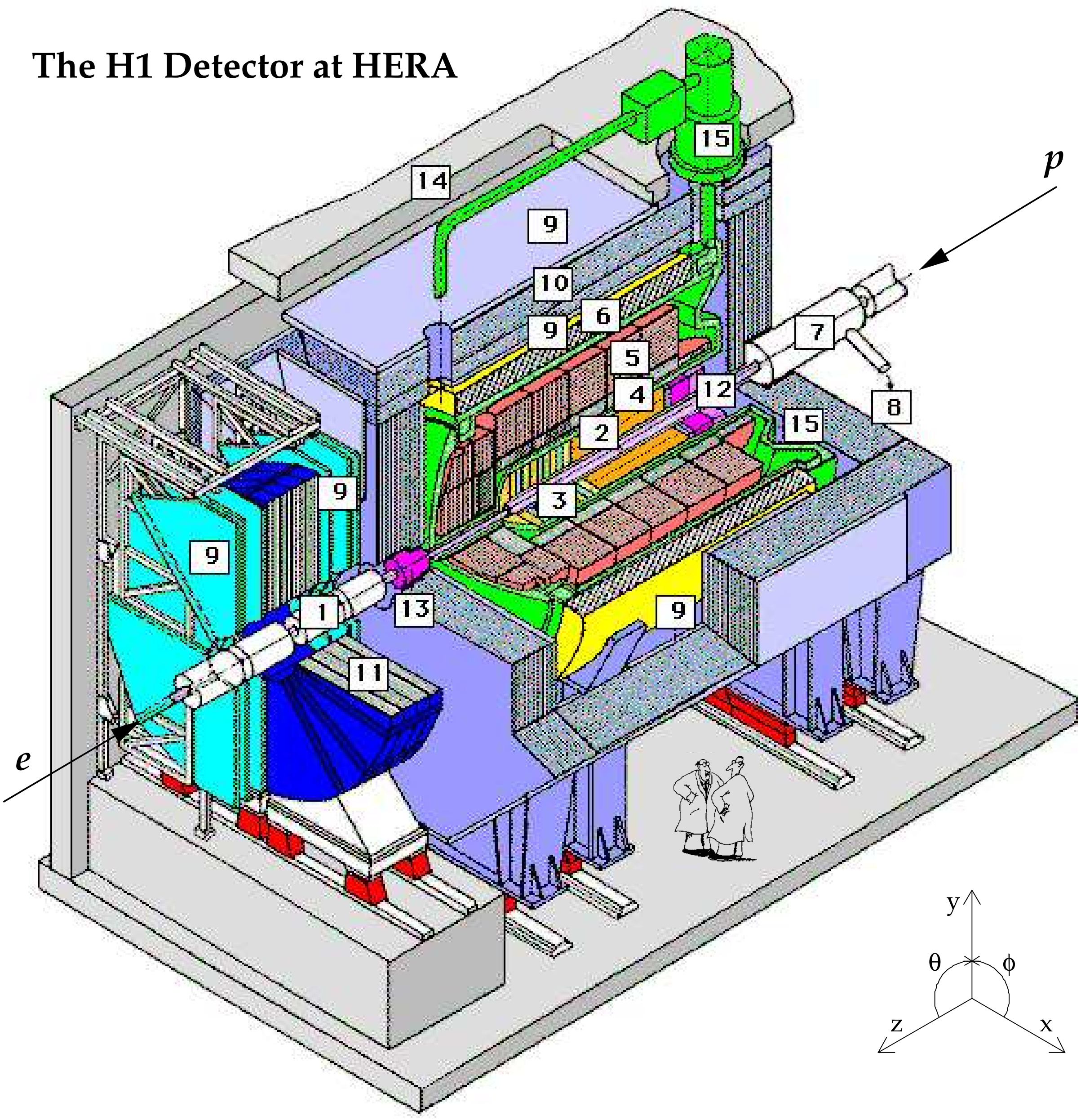

Figure 2.2: *3D view of the H1 Detector. The numbers denote:*

1	*Beam pipe and beam magnets*	9	*Muon chambers*
2	*Central tracking chambers*	10	*Instrumented iron yoke*
3	*Forward tracking chambers*	11	*Forward muon toroid*
4	*Electromagnetic LAr calorimeter*	12	*Backward calorimeter SpaCal and backward drift chamber*
5	*Hadronic LAr calorimeter*		
6	*Superconducting coil (1.16 T)*	13	*Forward plug calorimeter*
7	*Compensating magnet*	14	*Concrete shielding*
8	*Helium supply for* 7	15	*Liquid argon cryostat*

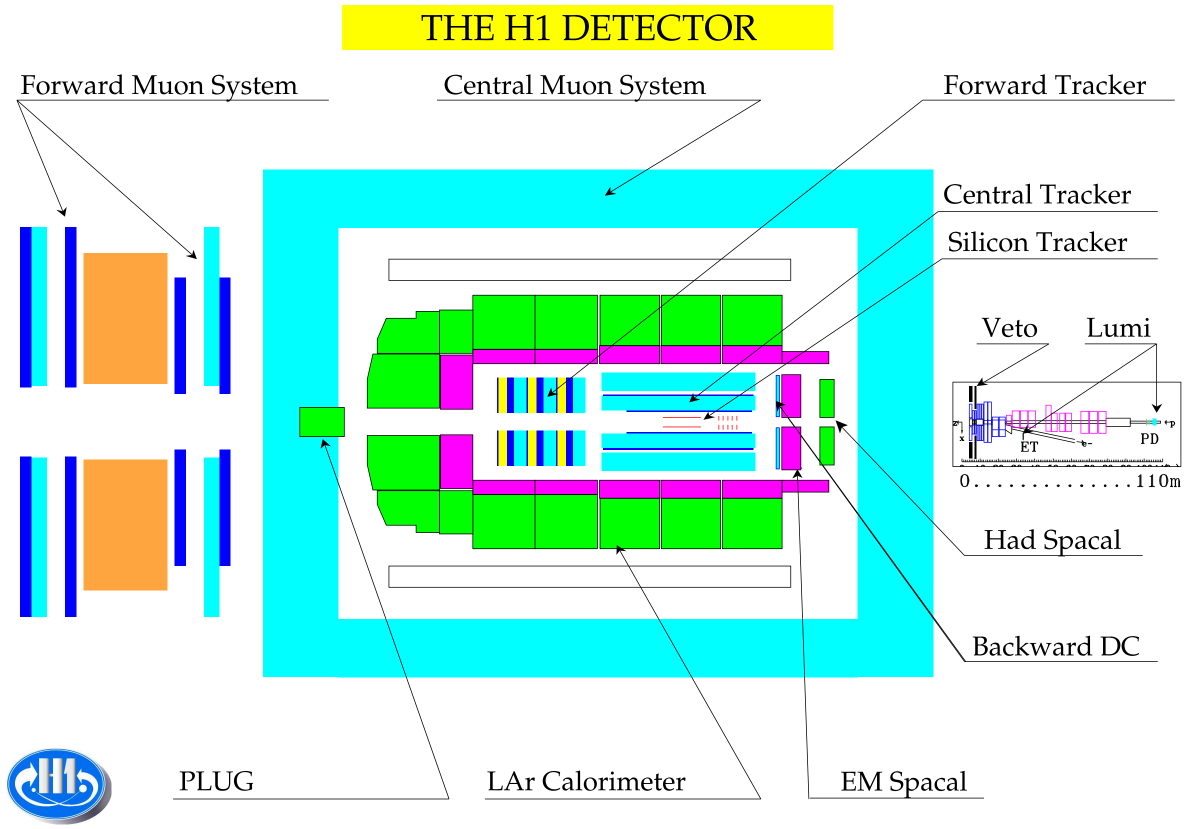

Figure 2.3: *Longitudinal cut through the H1 detector along the beam line. The electron beam comes from the left and the proton beam comes from the right in this picture.*

- the liquid argon calorimeter to measure the hadronic final state,
- the luminosity system to perform the luminosity measurement,
- and the time-of-flight and trigger systems to select an event.

These subdetectors are now described in more detail.

2.2.1 Backward Spaghetti Calorimeter (SpaCal)

The lead/scintillating–fibre sampling calorimeter SpaCal [h1sp] facilitates the energy measurement in the backward region of the H1 detector. The device covers the angular range of $153^\circ < \theta < 177.5^\circ$. It is composed of an electromagnetic and a hadronic section with the inner radius of 5.7 cm and the outer radius of 80 cm. Both parts are fabricated of scintillating fibres embedded in a lead matrix with the fibre diameter of 0.5 mm and 1.0 mm for the electromagnetic and hadronic part respectively. The scintillation light is converted into electrical pulses by photomultiplier tubes [jan94].

The front view of the electromagnetic section is displayed in fig. 2.4. It consists of 1192 cells with a cell cross section of $40.5 \times 40.5\,\mathrm{mm}^2$. This cross section is well matched to the Molière radius of 25.5 mm to ensure a good spatial resolution of $\sigma = (6.3 \pm 0.4)\,\mathrm{mm}/\sqrt{E/\mathrm{GeV}} \oplus (1.7 \pm 0.1)\,\mathrm{mm}$ [poe96], where $\oplus$ denotes the quadratic summation. This allows, in particular, a good

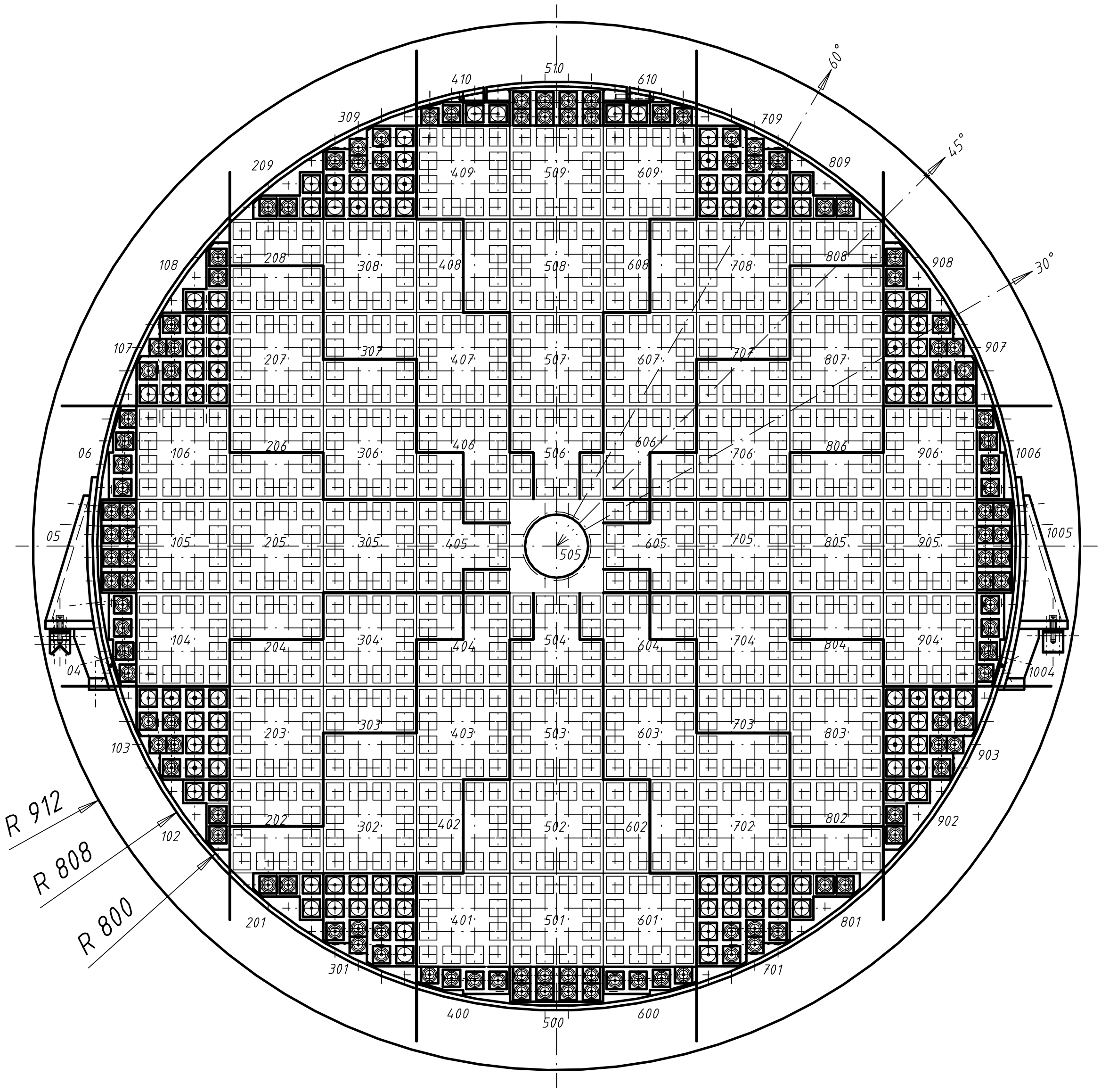

Figure 2.4: *Front view of the backward Spaghetti Calorimeter. The cells are grouped into super-modules with* 4×4 *cells in each module.*

electron/hadron separation by measuring transverse shower profiles. The cell depth of 25 cm in the z direction corresponding to 27.47 radiation lengthes is sufficient for electromagnetic showers to deposit their whole energy up to 30 GeV inside the section. The uncertainty of the energy scale is studied, in particular, in the framework of this analysis and lies within 0.5% at cluster energies above 17 GeV and increases up to 2.5% at 5 GeV (see sect. 4.6). The calorimeter excels with an energy resolution of $\sigma/E = (7.1 \pm 0.2)\%/\sqrt{E/\mathrm{GeV}} \oplus (1.0 \pm 0.1)\%$. and a low noise level of about 3 MeV. A high time resolution of less than 1 ns permits suppression of the beam induced background.

The hadronic section is assembled out of 136 cells of $119.3 \times 119.0\,\mathrm{mm}^2$ cross section and 25 cm depth providing one nuclear interaction length. It is used for a coarse hadronic energy

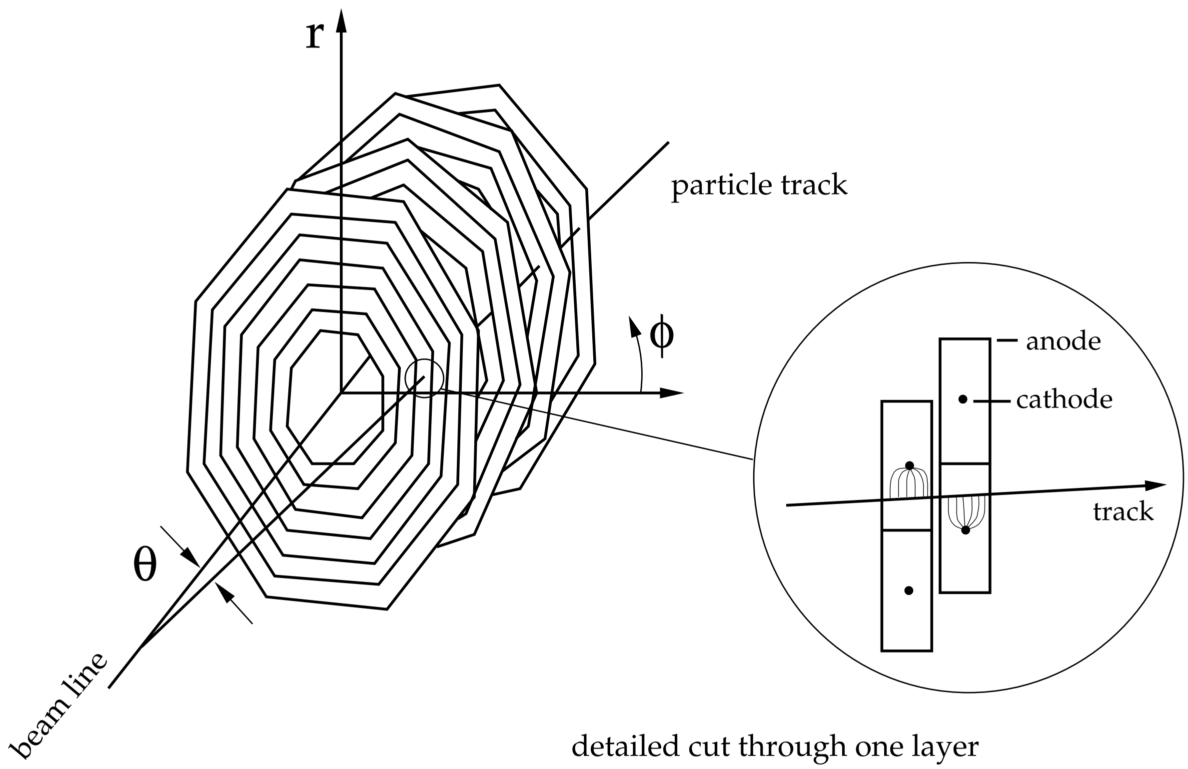

Figure 2.5: *Schematic layout of the signal wire orientation in the Backward Drift Chamber.*

measurement and to distinguish between hadronic and electromagnetic showers. The electromagnetic energy resolution is $\sigma/E = (13.0 \pm 0.2)\%/\sqrt{E/\mathrm{GeV}} \oplus (3.0 \pm 0.1)\%$, while the hadronic resolution amounts to $(56.0 \pm 3.0)\%$.

2.2.2 Backward Drift Chamber (BDC)

The backward drift chamber [sch96] has been designed as a supplement to the SpaCal to improve the measurement of the polar angle of the scattered electron. In this analysis the photon polar angle is also measured by BDC in the events, in which the photon converts into an electron–positron pair while passing the inactive material in front of the chamber. The device is installed in front of the Spaghetti Calorimeter covering the same angular range of $153^\circ < \theta < 177.5^\circ$ as SpaCal. The chamber is built out of four double layers, which are divided into eight octants. Each octant comprises 32 drift cells with sense wires. A schematic layout of the signal wire orientation is depicted in fig. 2.5. The wires are strung in azimuthal direction in order to optimise θ resolution. The wire radial spacing is 1 cm for the inner 16 cells in an octant and 3 cm for the outer cells. The wires in neighbouring planes of a double layer are shifted by half the cell size in order to resolve the left–right ambiguity of the drift origin. The double layers are revolved by 11.25° to allow a coarse measurement of the azimuthal angle ϕ. The chamber provides an average resolution of 0.57 mrad for the θ measurement [kel98].

2.2.3 Central and Forward Tracking Detectors

The H1 tracking system serves for track triggering, reconstruction, measurement of charged particle momenta and particle identification. The reconstructed tracks are also used to deter-

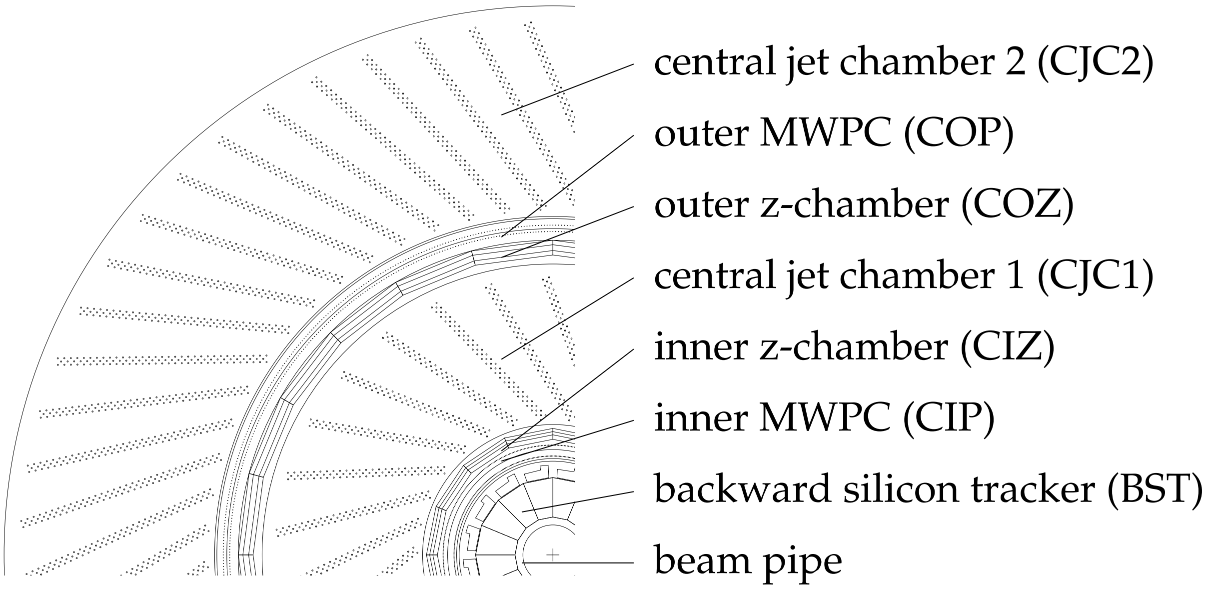

Figure 2.6: *Transversal Layout of the H1 Central Tracking System.*

mine the interaction point of the event, the so called event vertex. The H1 tracker has been designed to provide maximum efficiency and acceptance for the specific topology of the HERA ep reactions. Due to the boost of the hadronic final state in forward direction it is divided into two separate modules: the central tracking device (CTD) and the forward tracking device (FTD).

The schematic transversal layout of the central tracking system is depicted in fig. 2.6. It includes several coaxial tracking chambers settled in the z range between -1.5 and 1.5 m. These are the jet chambers CJC1 and CJC2, the multiwire proportional chambers (MWPC) CIP and COP, the drift z-chambers CIZ and COZ and the silicon detectors BST and CST.

The **Backward Silicon Tracker (BST)** [ark00] has been designed for an exact measurement of the polar angle of the scattered electron. Furthermore it allows the standalone event vertex determination on the basis of the reconstructed electron track. In 1997 the BST was a telescope of four planes arranged concentrically around the beam pipe with an angular coverage of $171.5^\circ < \theta < 176.5^\circ$. A 3-dimensional sketch of the BST with its readout electronics is shown fig. 2.7. The active planes were placed at z =-73.20, -80.03, 87.50 and -95.66 cm ensuring the largest possible plateau of the polar angle acceptance. Each plane is made up of 16 identical wedge shaped silicon detectors with the inner and outer radii of 5.9 and 12.04 cm. The resolution provided by the BST is better than 0.33 mrad for the polar angle measurement and better than 0.36 cm for the z coordinate of the reconstructed vertex.

The **Central Inner Proportional Chamber (CIP)** immediately surrounds the silicon trackers. It has an average radius of 161.5 mm and an angular acceptance of $9^\circ < \theta < 171^\circ$. The chamber is composed of two concentrical layers CIP1 and CIP2. Each layer has 6 mm thickness in radius and consists of 480 pads: 60 pads in the z direction and 8 pads in azimuth, collecting the charge induced by the crossing charged particles. A 3-dimensional view of the chamber is presented in fig. 2.8. The construction of the **Central Outer Proportional Chamber (COP)** is similar to the CIP. Two layers COP1 and COP2 are divided into 18 sectors of 12.1 cm length along the z axis and 16 sectors in azimuth. Its angular coverage is $25^\circ < \theta < 155^\circ$.

The primary goal of the multiwire proportional chambers in H1 is to provide a fast timing

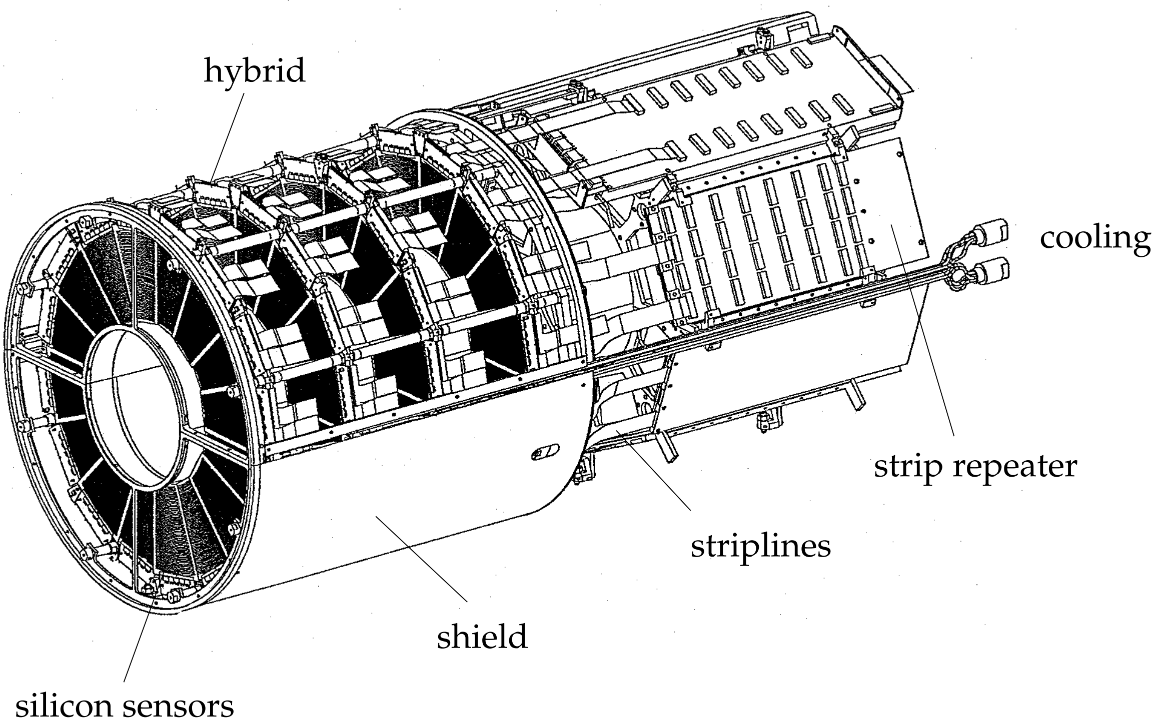

Figure 2.7: *3D sketch of the Backward Silicon Tracker with the front-end electronics.*

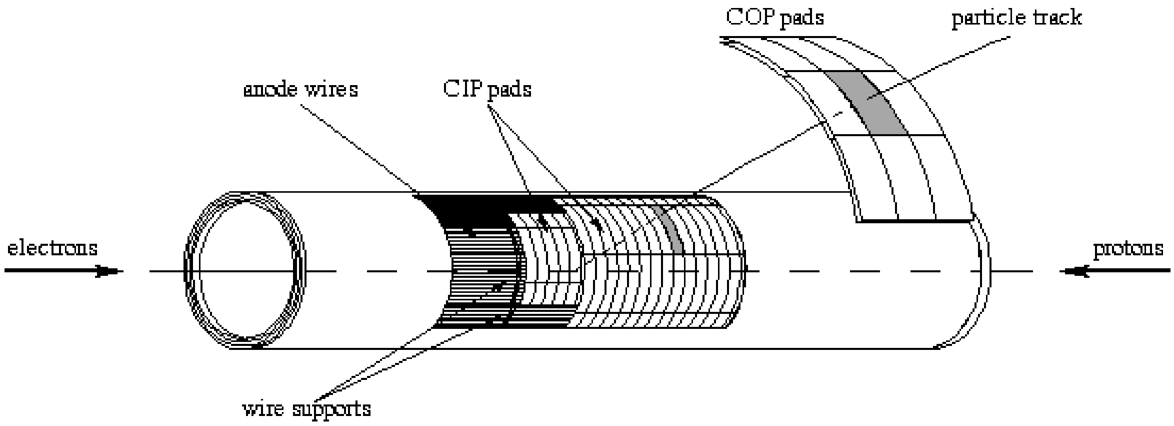

Figure 2.8: *3D sketch of the Central Inner Proportional Chamber.*

signal between consecutive HERA bunch crossings. Furthermore a combination of hits in different chambers is used to trigger on tracks coming from the nominal interaction vertex. In addition, the CIP is applied in some H1 analyses, in particular in this work, for the electron validation and vertex reconstruction.

The **Central Jet Chambers (CJC)** are the largest track reconstruction devices of the H1 detector. These are two coaxial drift chambers with an active length of 2200 mm and the inner and outer radii of 203 and 452 mm for CJC1 and 530 and 844 mm for CJC2. The CJC1 consists of 30 cells of 24 sense wires each and the CJC2 of 60 cells of 32 wires each. The orientation of the wires is parallel to the z direction. To maintain an optimum track resolution and to get rid of the usual drift chamber ambiguity, the drift cells are inclined by about 30° with respect to the radial direction. Both chambers achieve a 170 µm resolution in the $r - \phi$ plane and about 22 mm in the z direction.

The **Central Inner Z-Chambers (CIZ)** and the **Central Outer Z-Chamber (COZ)** are thin drift chambers with sense wires perpendicular and drift direction parallel to the beam axis. They complement the measurement of charged track momenta and detemine the z coordinates with an accuracy of typically 300 µm. The z-chambers are located just inside and outside CJC1.

The forward tracker is formed by three identical supermoduls strung along the beam axis. Each supermodul is composed of three planar drift chambers, a forward multiwire proportional chamber for fast triggering, a transition radiation detector for particle identification and a radial wire drift chamber.

The QED Compton events studied in the present work are characterised by absent or typically very low hadronic activity. Therefore, only those informations provided by the tracking detectors, which are used to identify the scattered electron, to measure its polar angle and to reconstruct the event vertex position from the parameters of the electron, are employed for the QEDC cross section measurement. These informations are provided only by the central tracker components. However, there were several intermediate steps in the data analysis, where the tracking of hadronic final state particles had to be dealt with.

2.2.4 Liquid Argon Calorimeter (LAr)

The Liquid Argon Calorimeter, the largest calorimeter in the H1 detector, covers the angular range between 4° and 153°. Its design criteria are clear identification and precise energy measurement of electrons, photons and hadronic jets with high particle densities. The device is placed inside the superconducting coil in order to minimise the amount of dead material in front of it and the overall size and weight of the calorimeter. It is segmented in z direction in eight self-supporting "wheels" of about 60 cm length, which in turn are divided in azimuth into eight octants. Figure 2.9 shows a schematic side view of the device.

The calorimeter is composed of an inner electromagnetic and an outer hadronic section. The electromagnetic part comprising lead absorber plates has a total depth varying between 20 and 30 radiation lengths and between 1.0 and 1.4 nuclear interaction lengths. The hadronic part with stainless steel absorber boards is about 4.7 to 7 absorption lengths deep. The orientation of sampling layers in each segment is sketched in fig. 2.9. In order to optimise the energy measurement, it has been chosen such, that the angle between the direction of particles coming from the nominal interaction point and the normals of the layer surface is smaller than 45°.

The fine segmentation of the LAr calorimeter leads to 44352 readout channels: 30884 in the electromagnetic section and 13568 in the hadronic one. Calibrated charges for each readout cell serve as the input to the energy reconstruction software. The reconstruction program converts charges to energies, corrects for dead material efects, eliminates noise and forms clusters from cell groups. The scaling from charge to energy involves a charge to energy calibration factor and a correction for the charge collection efficiency [bor92, bab94, bes96, nau98].

The calorimeter is non compensating. The charge output for hadrons is about 30% smaller than for electrons. The exact value depends on the incident particle energy. A special offline weighting procedure [wel94, işs96] is applied to reconstruct the energy deposited by hadrons. The technique makes use of the difference in the development of the electromagnetic and hadronic constituents of hadronic showers.

The energy resolution measured using test beams is $12\%/\sqrt{E} \oplus 1\%$ for the electromagnetic

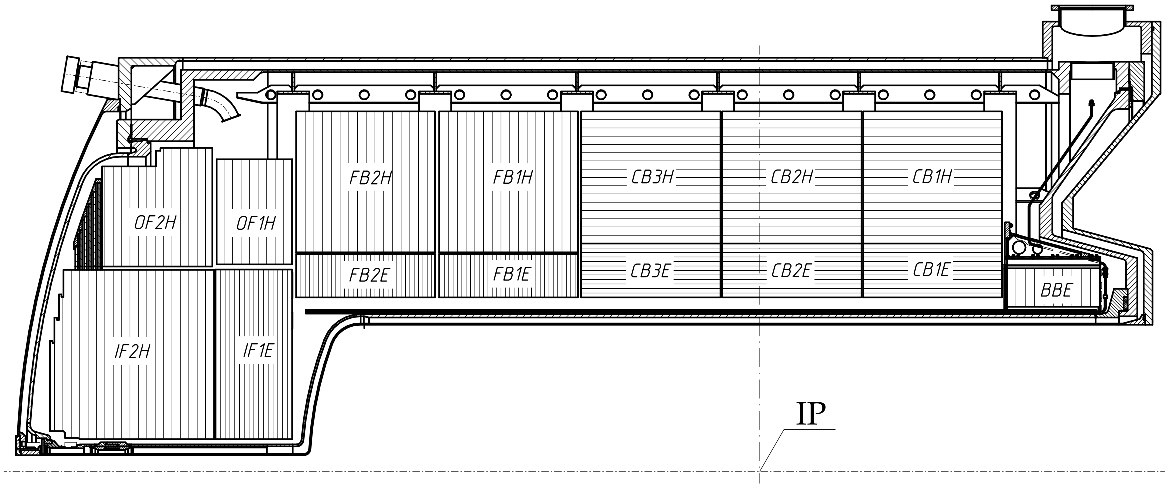

Figure 2.9: *Side view of the Liquid Argon Calorimeter.*

and $50\%/\sqrt{E} \oplus 2\%$ for the hadronic section. The absolute energy scale is reconstructed by the standard tools with uncertainty up to 3% for the electromagnetic and up to 4% for the hadronic part. A 2% precision for the hadronic energy scale can be achieved by applying additional recalibration software in the analysis step.

2.2.5 Luminosity System

The H1 luminosity system is made up of two electromagnetic calorimeters: the Electron Tagger (ET) and the Photon Detector (PD). The components are located close to the beam pipe in the HERA tunnel at $z_{ET} = -33.4\,\text{m}$ and $z_{PD} = -102.9\,\text{m}$ respectively. Both devices are assembled of thallium chlorid / thallium bromid (KRS–15) crystal cells serving as total absorption Cherenkov counters. Each cell is read out by a photomultiplier over an optical contact.

The electron tagger is compounded of 7×7 crystalls with a total area of $154 \times 154\,\text{mm}^2$. Its angular acceptance amounts to 1 mrad. The electrons scattered at low angles with an energy different from the beam energy are deflected by the HERA focusing magnets and leave the beam tube. At $Q^2 < 0.01\,\text{GeV}^2$ they can be tagged by the electron calorimeter if their energy is between 10 and 20 GeV.

The photon detector comprises 5×5 cells covering a total area of $100 \times 100\,\text{mm}^2$. The average θ acceptance varies within 0.5 mrad depending on the run vertex position and the angular beam tilt. Photons coming from the ep interaction region leave the proton beam pipe through the photon exit window at $z = -92.3\,\text{cm}$. The photon calorimeter is protected from the low energy synchrotron radiation by a lead–copper filter (F) of two radiation lengths followed by a water Cherenkov veto counter (VC) of one radiation length. The VC is utilised to detect particles interacting with the lead–copper absorber. The setup of the photon detector and the veto counter is referred to as *the photon arm* of the luminosity system.

The schematic layout of the system is drawn in fig. 2.10. The luminosity measurement is carried out by counting the rate of the bremsstrahlung events $ep \to ep\gamma$ [bh34] because of their distinct signature and the high and precisely calculable cross section. In the on-line procedure the luminosity is determined by the *coincidence method*, where the outgoing electron and the photon are detected simultaneously. In the more careful off-line analysis [gl96] only the

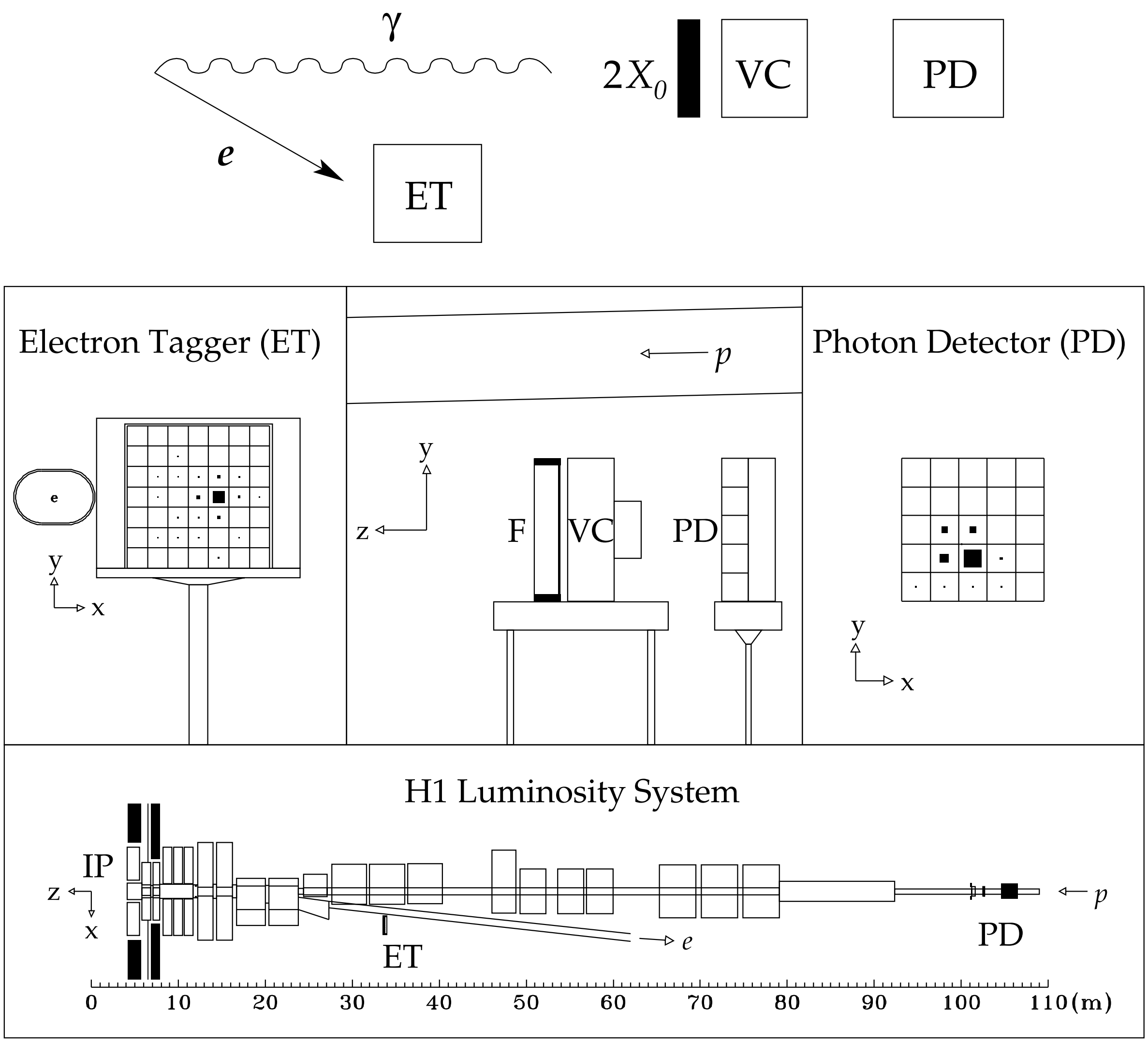

Figure 2.10: *Layout of the H1 luminosity system.*

photon measurement is used. The resulting uncertainty of the measured luminosity is within 1.5%.

2.2.6 Time-of-Flight (ToF) System

The Time-of-Flight detectors consist of scintillator devices mounted perpendicularly to the beam pipe: FToF at $z = +7.0$ m, PToF at $z = +3.5$ m, BToF at $z = -3.2$ m and the veto walls at $z = -6.5$ m and $z = -8.1$ m. Detailed descriptions of the the ToF system can be found in [fla92, wis98, bbfw98]. The devices measure the particle time of flight with respect to the bunch crossing time provided by the HERA machine. For each device an interaction time window (IA) depending on the detector position is defined so that particles originating from a region around the nominal *ep* interaction vertex reach the device inside the IA window. A big part of background events arising from unwanted collisions of the beam particles with the residual gas particles or with the beam pipe walls is thus rejected, since their arrival time lies outside the IA window. The decision to accept or reject the event is made by the trigger system, that reads, in particular, the ToF information at the on-line event processing.

2.2.7 Trigger System

Background events make up an overwhelming part of the statistics registered by the H1 detector. The typical background rate at the design luminosity $\mathcal{L} = 1.5 \times 10^{31}\,\mathrm{cm}^{-2}\mathrm{s}^{-1}$ is of the order of 1000 times higher than, *e.g.*, the rate of deep inelastic scattering reactions.

The task of the trigger system is to select events of physics interest out of this huge data flow. Four levels of event filtering undertake this duty: L1, L2, L4 and L5 (L3 is currently bypassed).

The first level trigger makes a decision for each bunch crossing. The fully pipelined system runs deadtime free at 10.4 MHz, whereby the trigger decision is ready after 2.5 μs. Up to 256 different trigger signals of different subdetectors, the so called trigger elements (TE), are logically combined into 128 subtrigger elements (ST). If at least one of the subtrigger conditions is fulfilled in the event the corresponding “raw” subtrigger bit is set. Any subtrigger rate can be downscaled in order to meet the bandwidth constraints. If the event is selected after possible prescaling, then the corresponding “actual” subtrigger bit is set. The L1 trigger decision is the logical OR of all actual subtriggers. In case of a positive L1 decision the pipeline is frozen causing the primary deadtime of 1–2 msec per event.

The second level trigger operates during the primary deadtime. It validates the L1 decisions using more complex algorithms within 20 μs. The L2 alogrithms are the realisations of two concepts: the topological trigger L2TT [biz92] and the neural network trigger L2NN [kr91, kra98].

Once a positive L2 trigger decision is reached, the event information is read and transferred to the fourth level trigger, which is a software filter farm made up of 30 parallel processors. Fast algorithms designed specifically for the filter farm or parts of the standard offline reconstruction program run at this level, employing more detailed event information than on the previous trigger levels. The event processing on the level 4 is done in two steps. During the L4 *trigger verification* step the L1 subtrigger decision is checked on the basis of more accurate and more detailed detector informations. In case of a positive trigger verification the event has to fulfill the requirements of at least one of the L4 *finders* dedicated to special physics signatures. Otherwise it is downscaled according to a Q^2 *dependent scheme*. For a more detailed description of this trigger level see [pro95].

The level 5 is an offline processing step, where the full event reconstruction is done and the events are assigned to one or more predefined physics classes. Unclassified events are rejected. The selected ones are collected on so called Data Summary Tapes (DST), which are read by physics analysis programs.

Chapter 3

Essentials of QEDC Cross Section Measurement

In this chapter the basic issues of the QEDC scattering cross section measurement are discussed. In the beginning the characteristic signature of QED Compton events in the H1 detector is described that serves as a basis for the experimental event selection in this analysis.

The cross section measurement can be essentially affected by diverse background processes which can mimic the QEDC events. The following background sources are considered in this analysis: di-lepton production, deep inelastic scattering, photoproduction, diffractive vector meson production, deeply virtual Compton scattering, pseudoscalar meson production in $\gamma\gamma$ fusion and odderon exchange and finally beam induced reactions. A description of these background contributions continues the chapter. Afterwards, the higher order radiative corrections, which can also have a significant influence on the measured cross section, are discussed.

One of the most significant background sources is formed by DIS events, in which one of the hadronic final state particles fakes the outgoing photon. To reduce this background, a limitation on the angular distribution of outgoing hadrons must be imposed. This cut can only be made if a correct modelling of the hadronic final state is guaranteed by the Monte Carlo program. However, the hadron production has not been included into the original version 2.0 of the COMPTON generator. Therefore, hadronisation packages were implemented into the generator within the framework of this analysis.

Further discussion is devoted to the reconstruction of kinematic variables. The Lorentz invariant variables used for the theoretical description of the studied process have to be computed from the measured quantities. Different ways of calculation of the hadronic and leptonic variables are considered here.

Finally, the kinematic intervals used for the differential cross section measurement are defined and the technique of the measurement and of a possible structure function extraction is discussed.

3.1 QEDC Event Signature

The basic signature of a QED Compton event as used in the experimental event selection is given by two high energetic clusters detected in the H1 backward calorimeter and reconstructed nearly back to back in azimuth. In a QEDC event one of these clusters is produced by the scattered electron and the other one by the outgoing photon. A schematic image of a real H1 event fulfilling all selection criteria is shown in fig. 3.1 together with the corresponding theoretical interpretation of this event.

The hadronic final state is boosted in the forward direction. Due to usually low masses of the hadronic final state all hadrons are concentrated in the forward part of the detector, where they are measured by the Liquid Argon calorimeter. At very low masses, in particular in elastic or resonance scattering, the hadronic final state is not detected at all.

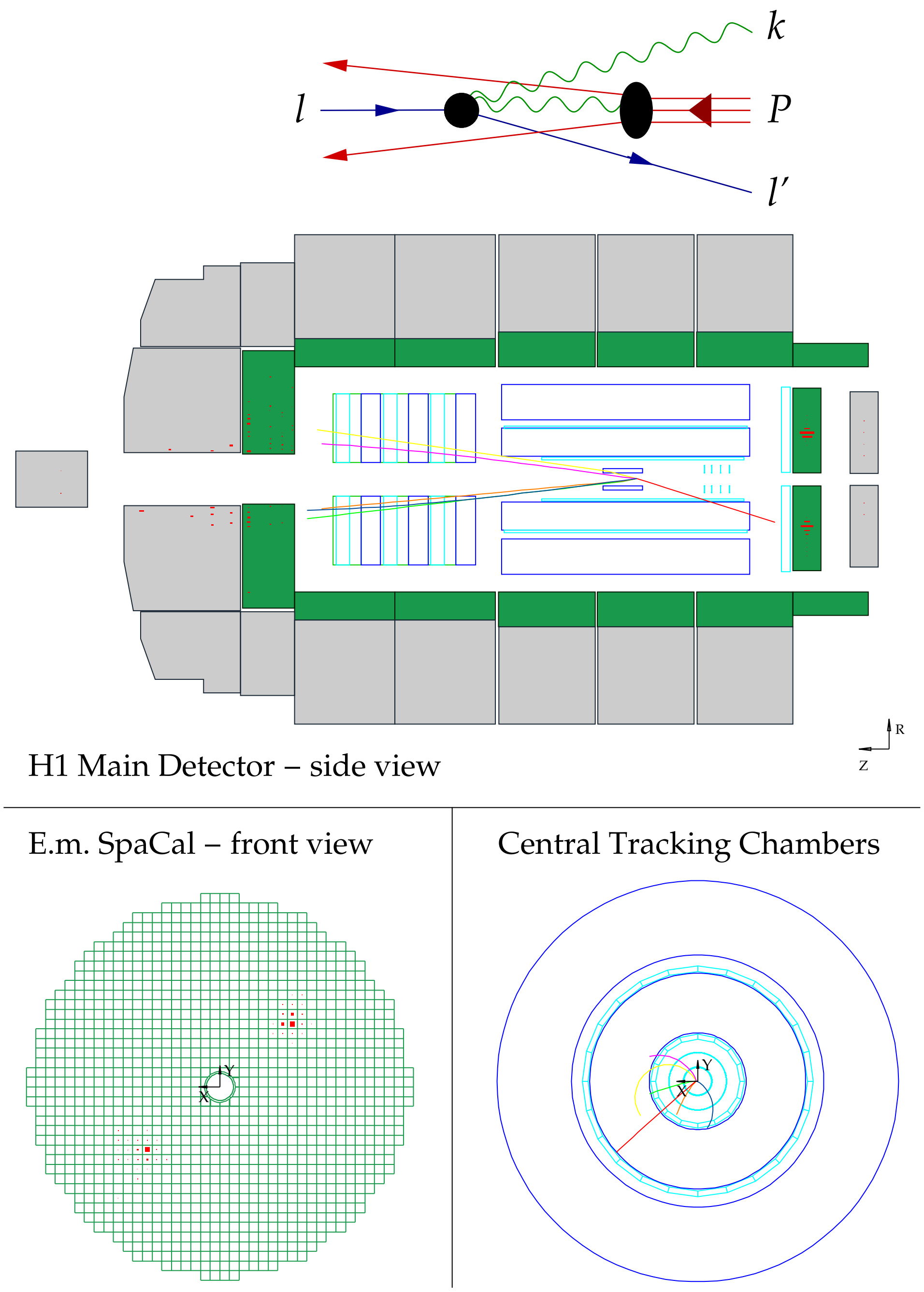

Figure 3.1: *QED Compton event in the H1 detector. The spots in the electromagnetic part of the SpaCal represent energy depositions in cells, which form two clusters. One of the clusters is produced by the outgoing electron and the other one by the final state photon, as depicted in the upper schematic picture. The clusters are reconstructed nearly back-to-back in azimuth, as can be seen in the front view of the SpaCal. The cluster corresponding to the scattered electron is validated by the CIP and the CJC in this event. In the side view of the detector and in the transversal layout of the central tracker the CJC track is depicted by the line directed from the event vertex to the SpaCal cluster. The spots in the forward part of the LAr calorimeter represent clusters produced by outgoing hadrons. Also shown are tracks left by the outgoing hadrons in the central and forward trackers.*

Electron and photon are identified using the central tracking chambers. Depending on its radial position a SpaCal cluster falls into the acceptance of either BST or CIP. At high radii $r \gtrsim 45$ cm the CJC can be used in addition to CIP. While passing through the chamber active volumes an electron produces hits in these chambers. The hits are combined into tracks in BST and CJC or clusters in CIP, as described in sect. 4.4. If such a track or a cluster is associated with one of the two SpaCal clusters, then this SpaCal cluster and the track or the cluster in the central tracker are considered to be produced by the scattered electron. The other SpaCal cluster is assumed to be created by the photon, since a photon does not produce a signal in the tracking chambers. A detailed description of the particle identification algorithm is given in sect. 4.4.

For the calculation of polar and azimuthal angles of detected particles the knowledge of the interaction vertex coordinates is necessary. In the H1 analyses, in which there is a large hadronic activity in the central part of the detector, the vertex position is determined using tracks produced by hadrons in the central tracking device (CJC, CIZ, CST). However in the QEDC analysis the CTD vertex reconstruction is either impossible or has a very large uncertainty, because the hadronic final state is either absent or concentrated mostly in the forward part of the detector. Fortunately the electron validation procedures in the tracking chambers also involve the reconstruction of the interaction vertex coordinates.

3.2 Background Processes

A number of other reactions can imitate the QEDC signal and thus lead to wrong values of the measured cross section. In order to correct for their effects, the contributions of these processes are estimated in this analysis by either corresponding Monte Carlo simulations or analytical calculations or direct determination from the data. These background sources and their treatment are discussed in this section.

3.2.1 QED Dilepton Background

The electron–positron pair production is one of the prominent background sources for QEDC scattering. Three types of Feynman diagrams for this process are depicted in fig. 3.2. To reject the events with all three leptons detected in the SpaCal, a cut on the residual energy in SpaCal, *i.e.*, the energy measured in the SpaCal apart from the two most energetic clusters, is made. However, the QED Compton event signature can be faked by two leptons, whereas the third one escapes the main detector through the beam pipe or has an energy below the residual energy cut threshold. Most of such events are rejected in the analysis chain by requiring the electron/photon identification in the central tracker. Nevertheless, some events survive the validation procedure due to the inefficiency of the tracking chambers.

Similar to the QED Compton process lepton pairs can be produced in the elastic, resonance and continuum inelastic ep scattering. For the simulation of all three contributions to this process the MC generator GRAPE [abe99] is used in this analysis.

Since these events lie in the same kinematic range as the QED Compton events, the systematic error of their cross section is estimated from the theoretical QEDC cross section uncertainties studied in this analysis. For the well known elastic scattering cross section a systematic error of 2% is assumed. Like the inelastic Compton events, the inelastic dilepton events are situated in the low Q^2 / high x kinematic domain, in a part of which F_2 has not been measured. As a typical theoretical uncertainty of the cross section in this region, an average difference between

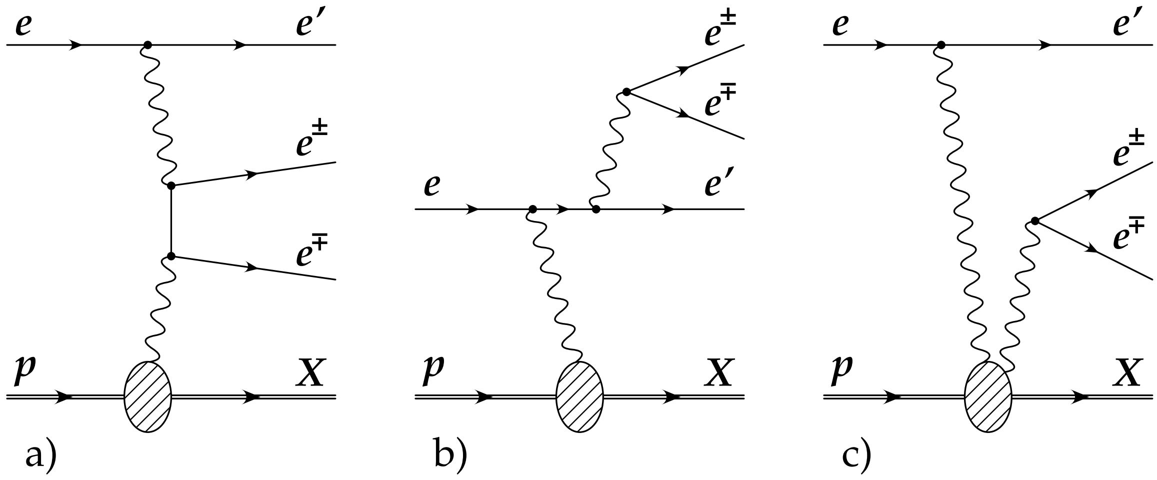

Figure 3.2: *Three types of leading order Feynman diagrams for electron pair production: a) $\gamma\gamma$ process, b) radiation from the electron line, c) radiation from the proton line. Figure taken from [hf99].*

the ALLM97 and the COMPTON F_2 parameterisations, amounting to about 30%, is taken. This uncertainty is assumed as a systematic error of the inelastic dilepton production cross section.

3.2.2 DIS Background

In the H1 low Q^2 DIS events the scattered electron is measured as a cluster in the backward calorimeter SpaCal. At high enough y values the hadronic jet is also detected in the backward region of the detector. In such events the second SpaCal cluster can be produced by one or more particles of hadronic final state. In a typical case a high energetic π^0 decays into two photons, and one or both of them together make a cluster in the electromagnetic part of SpaCal. To suppress this background, the cut on the residual energy in the SpaCal and the cut on the space distribution of particles in the Liquid Argon calorimeter have to be imposed (see sect. 4.2), *i.e.*, a gap between the hadronic and the leptonic final states is required. Obviously, these cuts will also reject some part of the QEDC signal. Therefore a complete generation of the hadronic final state must be performed by the MC program in order to control the influence of these cuts.

The DIS events used in this work were simulated by the DJANGO [ss91] generator, which includes both QED and QCD radiative effects. The DJANGO package consists of several parts. The program LEPTO [ing91] is employed to calculate the QCD matrix elements and generate the hadronic final state on the parton level. Parton cascades are generated by ARIADNE [lön92] using the Colour Dipole Model (CDM). The subsequent fragmentation is performed by the JETSET package [sjo94] that implements the Lund string model [agis83]. The generator HERACLES [ksm92] takes into account the complete one-loop electroweak radiative corrections and order $O(\alpha)$ radiative scattering. In particular, inelastic QED Compton events enter as an inherent part into the radiative cross section computation. To avoid double counting with the COMPTON generator signal, DJANGO events with a radiative photon emitted into the SpaCal area are rejected in the analysis chain.

An unexpected problem, encountered in the course of the analysis, has been an extremely high rate of DJANGO events surviving the selection procedure. These events are characterised by very low hadronic multiplicity at high invariant hadronic masses: $120\,\mathrm{GeV} < M_X < 270\,\mathrm{GeV}$.

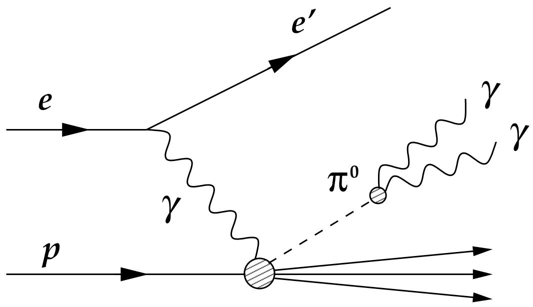

Figure 3.3: *DIS background to QED Compton Events.*

A typical event of such kind has the scattered electron and one high energetic hadron, mostly π^0, in the SpaCal area. The Feynman diagram for such events is depicted in fig. 3.3. The rate of these events in some kinematic bins reaches about one third of that of the QED Compton events, which seemed to be very unlikely. Therefore a special investigation of DIS background events is carried out in this work, where the event rate is estimated from real data. This study is described in sect. 4.7.

3.2.3 Photoproduction

In photoproduction events the scattered electron leaves the main detector through the beam pipe. The QEDC signal can be imitated by two particles from hadronic final state which create two clusters in the backward calorimeter.

For the generation of γp events the Monte Carlo program PHOJET [eng96] is used. The generator is based on the Dual Parton Model (DPM) [cstt94]. The fragmentation of the parton configurations is done by JETSET. The program includes also the elastic and proton dissociative production of light vector mesons ρ, ω and ϕ. The systematic uncertainty of the cross section calculation amounts to about 20%.

3.2.4 Diffractive Vector Meson Production

The Feynman diagram for vector meson production as described by the Regge model is depicted in fig. 3.4. A vector meson can be produced in a diffractive process as a result of an interaction between a pomeron and a (hadronised) photon. Such reactions occur both in deep inelastic scattering and in photoproduction. The produced mesons decay subsequently into lighter hadrons.

A cluster in the SpaCal can be made by one of the decay products, while the other cluster is produced by the scattered electron in DIS or another hadron in case of photoproduction. A special case is the photoproduction of J/ψ mesons, which decay into an electron–positron pair with 6% branching ratio. Due to the high mass of J/ψ the angle between the electron and positron produced in its decay is large, such that the two leptons create separate clusters in the SpaCal leaving a QEDC event signature. Thus, the photoproduction of J/ψ mesons makes up a background signal similar to the previously discussed QED dilepton production.

As pointed out above, the photoproduction of light vector mesons ρ, ω and ϕ is generated by PHOJET. Their production in DIS is performed by the generator DIFFVM [lis93]. The J/ψ event samples produced both in DIS and γp and decayed into an e^+e^- pair is also simulated by this program. Except for the ρ production samples, realistic cross section values have not been provided for the generation, therefore the effective luminosities of all samples are estimated

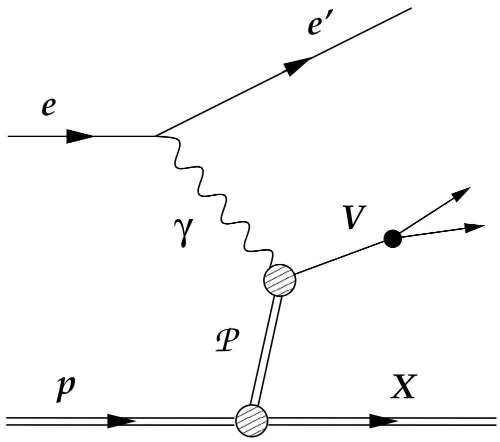

Figure 3.4: *Feynman diagram for vector meson production in Regge model.*

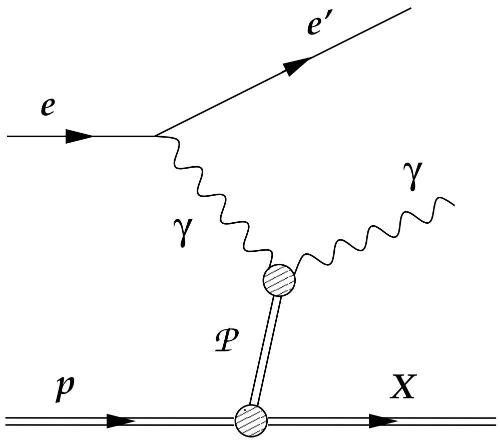

Figure 3.5: *Feynman diagram for the DVCS process in Regge model.*

by using published cross section values [zeus00, h1j99][1]. A 30% systematic uncertainty of the cross section determination is assumed for all samples.

3.2.5 Deeply Virtual Compton Scattering (DVCS)

Deeply Virtual Compton Scattering [ffs98] is a diffractive process of photon radiation from the proton side. The corresponding Feynman diagram in the Regge model is shown in fig. 3.5. This reaction constitutes the most significant background contribution to the QED Compton process.

Since the same final state is created as in the QEDC scattering, there is no way to separate DVCS from QEDC events experimentally. Both reactions differ only in the kinematic distributions of the outgoing electron and photon. The indistinguishable final state causes also interference effects between the two processes. Mercifully, in the leading twist approximation these effects do not influence the energy and polar angle distributions of the final state particles, so that it is possible to use separately generated Monte Carlo samples of both processes for the differential cross section measurement.

DVCS events have been generated in this work by the MC program TINTIN developed in [sta01]. Up to now, only the elastic contribution has been measured [h1d01] with both the statistical and the systematic errors of approx. 15%. The TINTIN generator thus produces only elastic events. At present there is no theoretical prediction for the inelastic channel cross section. The ratio of the inelastic to elastic scattering cross section is however experimentally estimated in [sta01] to be of the same order of magnitude as for diffractive vector meson production. For the generated DVCS events a systematic uncertainty of 50% is assumed.

3.2.6 Two Photon Resonance and Odderon Production

As a potential background source, exclusive pseudoscalar meson production in photon–photon fusion (PRIMAKOFF effect) is also considered in this analysis. The Feynman diagram of this re-

[1]The luminosities of the J/ψ photoproduction samples were estimated by D. SCHMIDT [sch00]. He also provided the photon flux factors for the bins used in [h1j99], which relate the $\gamma^* p$ cross section values published to the ep cross sections required for the calculation of the DIS J/ψ sample luminosities.

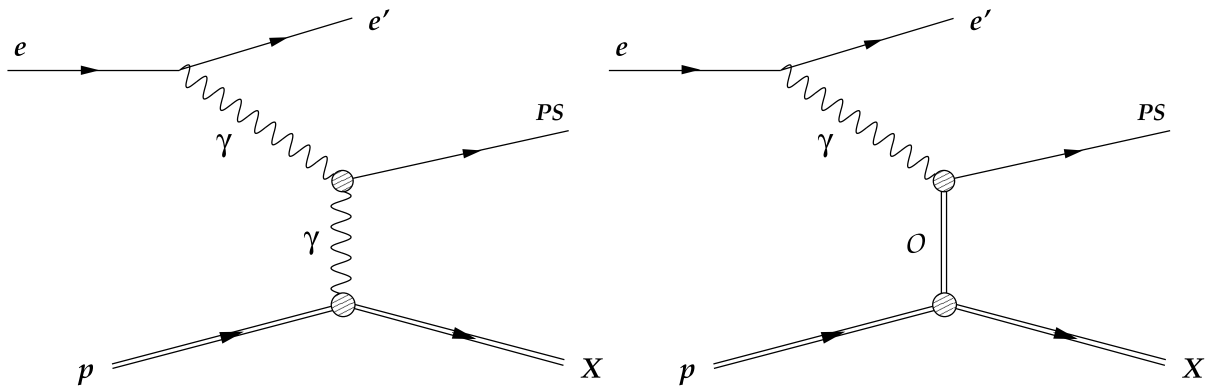

Figure 3.6: *Feynman diagrams for pseudoscalar meson production through a) photon and b) odderon exchange.*

action is shown in fig. 3.6 a. Similarly to QEDC and QED dilepton production this process is characterised by low masses of the hadronic remnant system X. For the cross section calculation elastic, resonance and continuum inelastic $\gamma^* p$ interaction have to be taken into account.

The angular distribution of the produced mesons has a strong peak in the electron beam direction, such that one or two photons resulting from π^0 or η decay can make a cluster in the backward calorimeter. In the DIS region the other cluster can be produced by the scattered electron.

The cross section values for all relevant mesons have been computed in [kn98, ber99]. In the DIS range they are all of the order of 0.5 pb. These are negligible contributions with respect to the QEDC cross section, therefore these reaction have not been considered in the further analysis.

In some theoretical models [kn98, ber99] it is supposed, that the same resonances can also be produced by *odderon* exchange as depicted in fig. 3.6 b. The hypothetic quantum state odderon [ln73, jlnl75] is similar to the pomeron $\mathcal{P}$ but differs in its quantum numbers. The pomeron carries charge and space parities $C = P = +1$, while the odderon should bear $C = P = -1$. In QCD this contribution corresponds to the three–gluon exchange. The odderon exchange is searched for at HERA but up to now has not been observed [h1o01].

The odderon exchange cross sections, estimated in the previously cited works, are of the same order of magnitude in the DIS region as those for the $\gamma\gamma$ fusion. Likewise, these processes are neglected in the present measurement.

3.2.7 Beam Induced Background

Despite high vacuum in the beam pipe, interactions of the proton and electron beam particles with the residual gas molecules (and also with the beam tube walls) create a huge background to the ep interactions studied at HERA. Most of it is rejected immediately during the data taking by various timing and minimum energy deposit requirements imposed by the trigger system. Further reduction of the background rate is achieved after applying cuts in the physics analysis, first of all the cut on the z position of the interaction vertex (see sect. 4.2).

The remaining small contribution has been estimated by using so called *pilot bunches* of the HERA beams. These bunches have no matching bunch in the counter beam to collide with, so that particles in these bunches can enter only into the beam–gas and beam–wall interactions. The amounts of events $N_{e-\text{pilot}}$ and $N_{p-\text{pilot}}$ recorded in the pilot electron and proton bunch

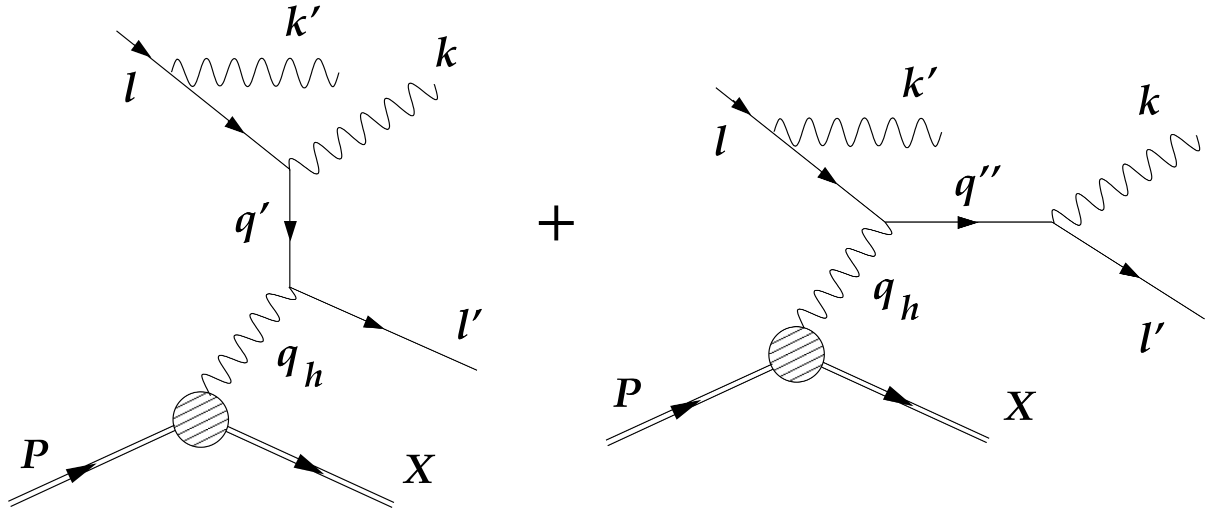

Figure 3.7: *Radiative corrections on the incident electron line for QEDC events.*

interactions, respectively, and which survived all QEDC selection criteria have been renormalised to obtain the total number of beam induced background events N_b according to the formula

$$N_\mathrm{b} = N_{e-\mathrm{pilot}} \frac{I_{e-\mathrm{collide}}}{I_{e-\mathrm{pilot}}} + N_{p-\mathrm{pilot}} \frac{I_{p-\mathrm{collide}}}{I_{p-\mathrm{pilot}}}\,, \tag{3.1}$$

where $I_{e-\mathrm{collide}}$, $I_{p-\mathrm{collide}}$, $I_{e-\mathrm{pilot}}$ and $I_{p-\mathrm{pilot}}$ are the sums of currents of all colliding or pilot electron and proton bunches, respectively. The resulting value is very small: $(0.5 \pm 0.2)\%$ of the total number of data events used for the cross section measurement.

3.3 Higher Order Radiative Corrections

Radiation of additional photons can substantially change the measured leading order cross section. Although emission of each photon is suppressed by the factor $\alpha \approx 1/137$, the corrections become large in some corners of the phase space. An exact calculation of all next order QED corrections to the Compton scattering is a complex and time consuming theoretical task, because interference effects between the two final photons have to be taken into account. A simplified approach has been implemented into the COMPTON generator and will be discussed below.

The major correction to the measured QEDC cross section is due to photon emission from the electron side collinear to the electron beam direction. This process can be approximately treated as a radiation from the incident electron line as depicted in the Feynman diagrams in fig. 3.7. It is simulated by COMPTON in the so called *peaking approximation* [ept67, pan69]. In this technique the photons are emitted exactly collinear to the incident electron beam. Due to the large angular separation between the scattered and the radiative photon in the final state, the interference terms between them are suppressed. The energy spectrum of the emitted photons is generated according to a probability law given by the semiclassical formula:

$$dP(z) = \beta z^{\beta-1} \left(1 - z + \frac{z^2}{2}\right) dz \tag{3.2}$$

with

$$\beta = \frac{2\alpha}{\pi}\left(\ln\frac{2E_{e0}}{m_e} - \frac{1}{2}\right) \tag{3.3}$$

and defining $z = E'_\gamma/E_{e0}$, where E'_γ is the radiated photon energy. After the photon emission the event is considered as a normal QEDC event at lower electron beam energy.

The hard photon tail of the radiation spectrum has a low emission probability, but on the other hand it leads to smaller values of the invariant $e\gamma$ mass W, thus resulting in an increase of the QEDC cross section (see eq. 1.44–1.47). To diminish the influence of hard radiation effects, the hard photon tail can be eliminated by imposing a lower limit on the total energy of the $e\gamma$ system. Such a cut is applied by default in the COMPTON generator and made in this analysis (see sect. 4.2).

Several comparisons of the simulated corrections with the real data and an estimation of the remaining systematic uncertainty in the measured cross section shall be discussed in sect. 4.8.

3.4 Generation of the Hadronic Final State

The original version 2.0 of the COMPTON generator does not include the generation of the hadronic final state. The primary purpose of the program considered by the authors was the application of QED Compton events for studies, in which the elastic component plays a major role, like detector alignment, energy calibration and luminosity measurement. Besides, at that time the implementation of hadronisation was a complicated task, since the standard approaches, like the Lund string model, had been optimised for the jet production, *i.e.*, presuming high particle multiplicities and the validity of the parton model. For instance, the hadronic mass limit set in DJANGO, below which the Lund fragmentation is not performed, is $M_X = 5\,\mathrm{GeV}$.

Since then several models have been developed or tuned to produce hadronic final state also for low hadronic masses. So far, no thorough comparison of the packages was published, so that it was not clear, what approach better reproduces real data. Therefore three of these models — those used by the DIFFVM, EPSOFT and SOPHIA generators — were implemented into the COMPTON program in this work. In the actual version 2.1 of the program the user can choose any of the three models to generate a QEDC event sample. Thus the upgraded program allows for a direct comparison of different approaches. In the present QEDC cross section measurement event samples generated with the tuned EPSOFT package are used. A detailed comparison with the competing models is still to be done in future analyses.

In the kinematic range, where the quark parton model is valid, *i.e.*, at Q_h^2 larger than several GeV^2, and at high enough M_X, where large particle multiplicities are expected, the well established Lund fragmentation by PYTHIA/JETSET can be run. This option was also implemented into the new version of COMPTON. The parton configuration is defined by the quark parton model. The user can set the lower limits of M_X and Q_h^2, beyond which the Lund model is employed. The default values, used also in the present measurement are: $M_{X,\mathrm{lim}} = 5\,\mathrm{GeV}$, $Q^2_{h,\mathrm{lim}} = 2\,\mathrm{GeV}^2$. The Lund hadronisation option is used only if both conditions: $M_X > M_{X,\mathrm{lim}}$ and $Q_h^2 > Q^2_{h,\mathrm{lim}}$ are satisfied in the event. Otherwise one of the aforementioned packages is run. Such splitting of the kinematic range is the standard approach for MC programs, which generate mostly low M_X / low Q^2 events, and in which deep inelastic events form only a relatively small fraction of the event sample.

While running the new version of the COMPTON generator, the user can choose not only between the electron and positron beam, as it was in the previous version, but also between the proton and antiproton beam.

In the following paragraphs the implementation of different hadronisation models is discussed in detail.

3.4.1 DIFFVM Model

The low mass hadronisation done in the DIFFVM generator is a simplified approach, in which the final state consists of one proton or neutron and a number of pions. No other hadrons are produced. Because of baryon number conservation there must be a nucleon in the final state. Assuming isospin symmetry, twice as many charged pions are generated in average as neutral pions.

The charged particle multiplicity $n_\pm$ is given according to the KOBA, NIELSEN, OLESEN *(KNO) scaling* [kno72]. This term denotes the fact, experimentally observed in diffractive high energy hadron collisions [coo82], that the average number of charged particles $N_\pm$ depends only on the invariant hadronic mass M_X and the actual multiplicities in events are spread normally around this value. The package employs formulae 46 – 48 from [gou83] for the probability $P_\pm$ that $n_\pm$ charged pions come into existence:

$$P(n_\pm) \propto \exp -\frac{(n_\pm - N_\pm)^2}{2\left(\frac{N_\pm}{2}\right)^2} \tag{3.4}$$

with

$$N_\pm = 2N_c\ , \qquad N_c = \begin{cases} \sqrt{M_r} & \text{for } M_r \leq 1\ , \\ a_1 + b_1 \ln M_r + c_1 \ln^2 M_r & \text{for } M_r > 1\ , \end{cases} \tag{3.5}$$

with parameters: $a_1 = 0.36$, $b_1 = 0.13$, $c_1 = 1$, where N_c is the mean multiplicity of charged pion pairs, and the residual mass variable M_r is given by

$$M_r = \frac{M_X - m_p}{1\,\text{GeV}}\ . \tag{3.6}$$

If $n_\pm$ is an even number, then one proton, $n_\pm/2$ positive and $n_\pm/2$ negative pions occur in the final state. In case of an odd $n_\pm$ one neutron, $(n_\pm + 1)/2$ positive and $(n_\pm - 1)/2$ negative pions are produced, *i.e.*, there is one more positive pion than negative pions.

The formulae 3.4 - 3.6 were obtained in [gou83] by fitting data from CERN experiments performed at pp colliders ISR with the centre of mass energy $\sqrt{s} = 60\,\text{GeV}$ and SPS with $\sqrt{s} = 540\,\text{GeV}$.

The average number of generated neutral pions N_n is half the mean number of charged pions. For this ratio to hold, the actual generation procedure chooses at first the total number of pions $n_t = n_\pm + n_n$ according to:

$$P(n_t) \propto \exp -\frac{(n_t - \frac{3N_\pm}{2})^2}{2\left(\frac{3N_\pm}{4}\right)^2}\ , \tag{3.7}$$

where the result must lie between one and the limit set by the total hadronic mass. Afterwards, if $n_t > 1$, the number of charged particles $n_\pm$ is determined from n_t by the binomial distribution with the parameter $p = 2/3$. The number of neutral pions is then $n_n = n_t - n_\pm$.
After the final state particles have been defined, a phase space decay of the hadronic mass M_X into these particles is executed by the package RAMBO *(Random Momentum Booster)* [kse86]. A well known problem of the phase space decay is that in case of a large M_X and a low number of pions it produces particles with too large transverse momenta that are not observed experimentally.
Both the phase space decay of the entire hadronic mass and the disregard of all hadrons other than pions are strong simplifications of the real fragmentation processes that are not made in the other programs. For this reason the DIFFVM model is not intended to be used as a default hadronisation package in the COMPTON program. It was implemented mainly for the purpose of testing and comparing with the competing approaches.

3.4.2 EPSOFT Model

EPSOFT [kas96] is a Monte Carlo generator for soft diffractive and non-diffractive photon–proton collisions. As the basis for hadronic final state modelling the HERWIG generator approach [cor01] has been implemented. The fragmentation of a low hadronic mass in EPSOFT is an optimised HERWIG procedure of the soft underlying event hadronisation, which, in turn, is based on the minimum bias event generator of the UA5 collaboration [ua587]. The parameters were tuned to reproduce the hadron–hadron and ZEUS photoproduction data. For the implementation in COMPTON the version, EPSOFT2 was used with parameters further retuned [inu01, abe01] compared to [kas96].
In the first step of fragmentation the charged pair multiplicity n_c is chosen. In the standard version of the generator it is spread according to the negative binomial distribution (NBD):

$$P(n_c) = \frac{{N_c}^{n_c} k^k}{(N_c + k)^{n_c + k}} \frac{\Gamma(n_c + k)}{n_c!\,\Gamma(k)} \tag{3.8}$$

with $1/k = 0.05$ around the mean value:

$$N_c = a_2 \ln^2 M_r + b_2 \ln M_r + c_2 \tag{3.9}$$

with $a_2 = 0.176$, $b_2 = 0.43132$ and $c_2 = 0.86224$. The total number of charged particles is $2n_c + 1$. At $M_r < 1$ n_c is set to zero, meaning that there is only one charged particle in the final state.
In a recent ZEUS study [ada99], focused at very low masses $M_X < 5\,\text{GeV}$, the negative binomial distribution in EPSOFT was replaced by the Gaussian, since the NBD was found to fail for hadron–hadron data in this region. With the Gaussian distribution:

$$P(n) \propto \exp - \frac{(n - N)^2}{2\left(\frac{N}{2}\right)^2} \tag{3.10}$$

and the mean multiplicity of neutral particles and charged pairs:

$$N_c = N_n = \sqrt{M_r} \tag{3.11}$$

EPSOFT employs thus almost the same model as used by DIFFVM.
However, for the present analysis a correct description of hadronic distribution at higher mass is an important issue for two reasons:

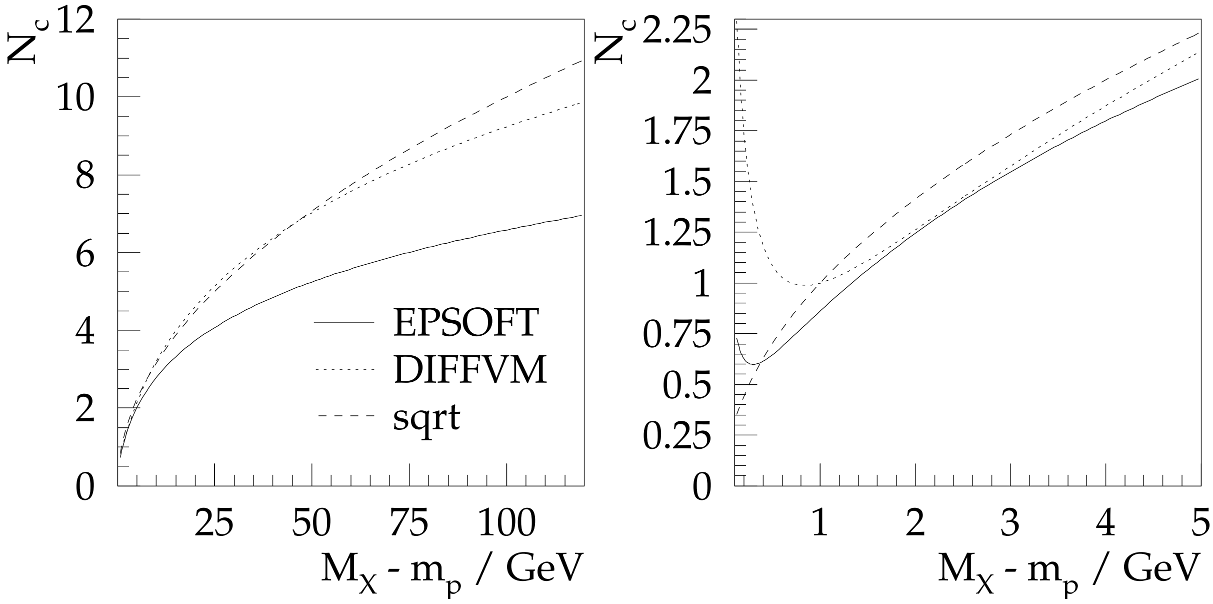

Figure 3.8: *Average multiplicity of charged particles as a function of the residual mass of the hadronic final state as used in different hadronisation packages. Both figures display the same parameterisations in different mass ranges.*

1. A cut on the energy distribution in the LAr calorimeter is imposed in the region of higher masses M_X;

2. The reconstruction of kinematic variables based on the hadronic final state opens new opportunities for the cross section measurement (see sect. 3.6, 3.8). To perform such a reconstruction, a reasonable simulation of hadronic final state must be guaranteed over the whole mass range.

Therefore it has been made possible to choose between different hadronic distributions in COMPTON depending on the mass M_r in the event. At masses below a given limit the Gaussian distribution is used, while above the limit the NBD is applied. The default limit value is set to 2 GeV. Like all other EPSOFT hadronisation parameters in the COMPTON program it can be changed via input steering cards.

The behaviour of various parameterisations of the average charged pair multiplicity N_c is contrasted in fig. 3.8 for two mass ranges. The solid line depicts the EPSOFT fit in eq. 3.9, the dashed line shows the square root function 3.11 used in the modified EPSOFT program and in DIFFVM at $M_r < 1$ GeV and the dashed line displays the lower expression in 3.5 used in the DIFFVM MC at $M_r > 1$ GeV. This last expression gives nearly the same result as $\sqrt{M_r}$ in the range $1 < M_r < 60$ GeV so as to describe the ISR data taken at $\sqrt{s} = 60$ GeV and becomes smaller at higher values to reproduce the SPS data at $\sqrt{s} = 540$ GeV [gou83]. The EPSOFT fit provides significantly lower values than the DIFFVM one, indicating lower multiplicities in ep reactions as measured by ZEUS with respect to those in pp interactions at the same mass M_r.

Assuming that the EPSOFT fit reproduces the ep data at high hadronic masses and that the low mass region is correctly described by eq. 3.5, the default mean charged pair multiplicity in the

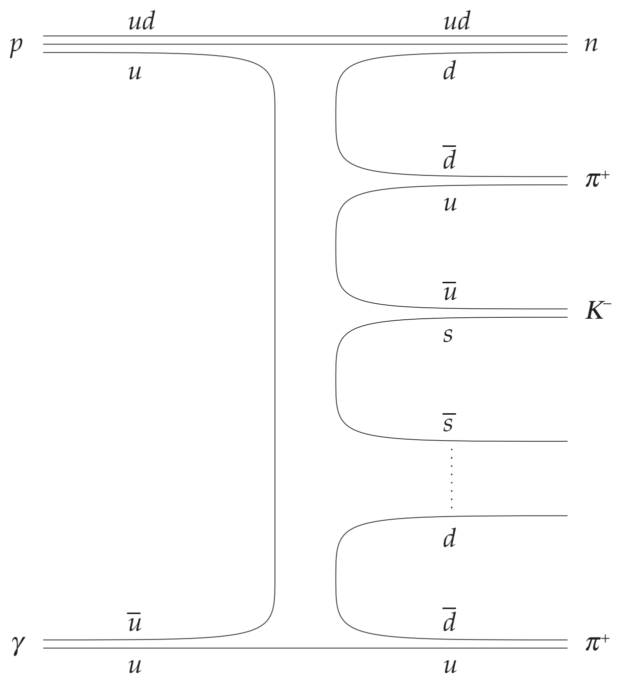

Figure 3.9: *Valence quark flavour generation in EPSOFT [kas96].*

COMPTON EPSOFT implementation is computed as:

$$N_c = \begin{cases} \sqrt{M_r} & \text{for } M_r \leq 1\ , \\ a_1 + b_1 \ln M_r + c_1 \ln^2 M_r & \text{for } 1 < M_r \leq 2\ , \\ a_2 + b_2 \ln M_r + c_2 \ln^2 M_r & \text{for } M_r > 2\ . \end{cases} \tag{3.12}$$

In the second step the particle content of the hadronic state is defined. The flavours of the valence quarks of final state hadrons are selected according to the scheme depicted in fig. 3.9 that automatically conserves charge, isospin and strangeness. In this algorithm adding a new hadron involves extending the quark flavour chain by one element that can be a light quark (u, d or s) or a diquark line. The flavours are picked randomly with probabilities adjusted so as to produce hadrons in ratios close to those measured in hadron–hadron interactions [mw88]. If the valence quark flavours do not define the hadron uniquely, the one with the smallest mass is chosen. The procedure is repeated until $2n_c + 1$ charged hadrons are determined.

After the hadron content is specified, the transverse momenta of particles are generated according to the probability distribution

$$\frac{dP}{dp_t^2} \propto \exp\left(-\kappa\sqrt{p_t^2 + m^2}\right) \tag{3.13}$$

where the slope parameter κ is computed as:

$$\kappa = \frac{d}{a \ln^2 M_r + b \ln M_r + c} \tag{3.14}$$

with $a = 0.00175$, $b = 0.00167$, $c = 0.353$ and $d = 2$. For strange particles κ is reduced by factor 0.6.

In the last step the generation of the longitudinal momenta is performed from the flat rapidity distribution with Gaussian shoulders based on the technique of JADACH [jad75].

3.4.3 SOPHIA Model

The EPSOFT model involves a much more elaborated particle production scheme than that of DIFFVM. However, it still lacks important features like, *e.g.*, generation of nuclear resonances and vector mesons. These disadvantages are absent in the newly developed generator SOPHIA *(Simulations of Photohadronic Interactions in Astrophysics)* [muc00]. The program provides a minimum bias description of photoproduction processes, which reproduces a large set of available data. To be specific, the production of major resonances, the direct pion production and the multiparticle generation including diffractive and non-diffractive production of light vector mesons ρ and ω are implemented. The choice of a particular process at a given mass M_X is made by sampling from the corresponding cross section fits. Decays of unstable particles are performed by a routine DECSIB from the SIBYLL package [fgls94].

The treatment of the non-diffractive multiparticle production is based on the Dual Parton Model. The string fragmentation is done by the Lund PYTHIA/JETSET routines. Several parameters of the fragmentation code have been tuned by the authors in order to obtain a reasonable description at small hadronic masses.

3.4.4 Generation at High M_X and High Q_h^2

For the generation in this kinematic domain parts of the hadronisation code of the DIFFVM, WABGEN [kan98] and PYTHIA generators have been used.

In the beginning of generation the four-momenta of the outgoing partons are determined according to the simple Quark Parton Model. In this approach the four-momenta of the proton remnant r and the struck quark j exiting the scattering process are given by

$$r = P(1 - x_h)\ , \qquad j = X - r\ , \tag{3.15}$$

where P and X are the four-momenta of the incoming proton and the hadronic final state, respectively, and x_h is the hadronic Bjorken x as defined in eq. 1.35.

Afterwards the flavour of the struck quark is generated by using a chosen parton distribution function set from the PDFLIB package [plo95]. By default the GRV LO parameterisation set is taken. Further treatment depends on whether a valence or a sea quark is selected.

If the struck parton is a valence quark, then the remnant part is a di-quark system, chosen so as to conserve isospin, and taking into account that the probability ratio to pick $(ud)_0$ or $(ud)_1$ state is 3:1. A colour string is then defined between the quark and the di-quark and the fragmentation by PYTHIA 6.1 is run[2].

Otherwise, the remnant part consists of four partons - three valence and one sea quark. The scattered sea quark cannot make a colour string with its remnant counterpart, since the sea pair could be produced only by a gluon emission, and hence it cannot be colour neutral. Therefore, to define a colour string a valence partner for the struck quark has to be chosen. The valence content uud is then split into a quark and a di-quark state. One of them is combined with the remainder sea quark into a colour neutral hadron depending on the sea quark flavour. A sea anti-quark composes a meson with the chosen valence quark. On the contrary, a sea quark builds with the valence di-quark a baryon. The total four-momentum of the remnant part is split between the meson and the di-quark jet or between the baryon and the quark-jet

[2] Actually, the routines which belonged earlier to the JETSET package are called. Since PYTHIA version 6.1 both generators have been merged into the single PYTHIA package.

according to the probability distribution:

$$\frac{dP}{d\chi} = 2(1-\chi)\ , \tag{3.16}$$

based on counting rules, where χ is the energy fraction taken by the meson or the quark jet. The two components can obtain also transverse momenta from the primordial $k_\perp$ distribution, which can be either a Gaussian (default) or an exponential one. After generating the parton momenta a colour string is defined between the struck quark and the remaining coloured object (quark or di-quark), as in the case of a struck valence quark, and the PYTHIA fragmentation is performed.

3.5 Detector Simulation

The extensive use of Monte Carlo simulations for the study of detector response demands that the simulation reproduces all effects influencing the measurement, such as detector acceptance, efficiency, noise and energy scale. To achieve this, all generated signal and background events pass a detailed H1 detector simulation and reconstruction. It is performed in several steps:

1. A simulation of passage of particles through all detector components is performed by the H1SIM package based on the GEANT [gea94] program. In order to save simulation time, shower propagation in the calorimeters is by default not simulated in detail. Instead, it is computed by the H1FAST [gpr90] program employing special shower parameterisations.
2. In the *digitisation* step the simulated subdetector responses are converted into data of the same form as collected from the real detectors components. Basic efficiency and noise corrections are applied in this step.
3. The fully simulated events are subject to the same reconstruction procedure as the real data. The reconstructed events are then used for the physics analysis.

3.6 Reconstruction of Hadronic Variables

Both the hadronic and the leptonic kinematic variables are modifications of the standard kinematic variables used in the inclusive DIS measurements. Consequently, for their reconstruction properly modified methods of the DIS analyses can be applied.
In the most part of the HERA DIS kinematic range the so called *electron method* provides the highest resolution among the available techniques. In the DIS event reconstruction by the electron method all quantities are calculated from the measured parameters of the scattered electron. However, in order to calculate the hadronic variables in QED Compton scattering by such a method one has also to take into account the outgoing photon as a part of the leptonic final state. Calculating the total transverse momentum of the $e\gamma$ system:

$$p_{t,e\gamma} = |\vec{p}_{t,e} + \vec{p}_{t,\gamma}|\ , \tag{3.17}$$

the hadronic kinematic variables are computed as:

$$y_{h,\mathrm{e}} = 1 - \frac{(E_e - p_{z,e}) + (E_\gamma - p_{z,\gamma})}{2E_{e0}} = 1 - \frac{E_e(1-\cos\theta_e) + E_\gamma(1-\cos\theta_\gamma)}{2E_{e0}}\ , \tag{3.18}$$

$$Q^2_{h,\mathrm{e}} = \frac{p^2_{t,e\gamma}}{1-y_{h,\mathrm{e}}}\ , \qquad x_{h,\mathrm{e}} = \frac{Q^2_{h,\mathrm{e}}}{s y_{h,\mathrm{e}}}\ . \tag{3.19}$$

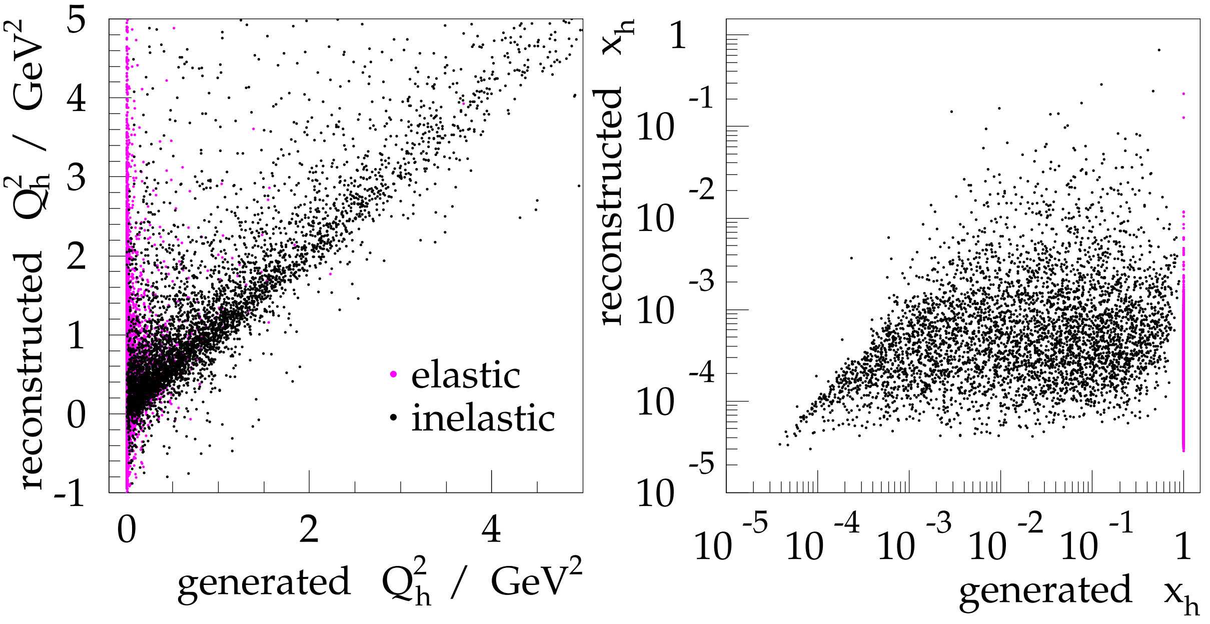

Figure 3.10: *Feasibility of the reconstruction of the hadronic kinematic variables Q_h^2 and x_h by the electron method. Distributions of the elastic (magenta dots) and inelastic (black dots) events generated by the COMPTON program are drawn. The generated variables are plotted along the x-axis, and those calculated by the event reconstruction chain are plotted along the y-axis.*

The formula for $Q^2_{h,\mathrm{e}}$ calculation can also be rewritten as follows:

$$Q_h^2 = -(l - l' - k)^2 = -(l - l')^2 - (l - k)^2 - (l' + k)^2 \tag{3.20}$$

and hence:

$$Q^2_{h,\mathrm{e}} = 2E_{e0}E_e(1 + \cos\theta_e) + 2E_{e0}E_\gamma(1 + \cos\theta_\gamma) - 2E_eE_\gamma(1 - \cos\upsilon_{e\gamma}) \,, \tag{3.21}$$

where $\upsilon_{e\gamma}$ is the opening angle between the electron and the photon in the laboratory frame. The last term in this expression gives the square of the invariant mass of the $e\gamma$ system, *i.e.*:

$$W = \sqrt{2E_eE_\gamma(1 - \cos\upsilon_{e\gamma})} \,. \tag{3.22}$$

The feasibility of the hadronic variable reconstruction by the electron method has been studied on the sample of events generated by the COMPTON program. In the scatter plots of fig. 3.10 the variables Q_h^2 and x_h generated by the program for each event are plotted versus their reconstructed counterparts. A reasonable correlation of Q_h^2 values is visible in the left graph down to about 0.1 GeV^2. In most elastic events the reconstruction fails, since they have much lower Q_h^2 values. Thus, in order to measure Q_h^2 one has to pre-select the events at $Q_h^2 \gtrsim 0.1\,\mathrm{GeV}^2$. This can be done by making a cut on the $e\gamma$ acoplanarity, as described in the next section. Mercifully such a selection means singling out the inelastic channel, which is actually required for the F_2 measurement.

On the contrary, the y_h and subsequently x_h reconstruction using the electron method fails completely, as can be seen in the right plot of fig. 3.10 for the example of x_h. This occurs because very low y_h values have to be reconstructed by subtracting a value very close to one from one in the y_h calculation in expression 3.18. This is also reflected in the $y_{h,\mathrm{e}}$ resolution that is dominated by the electromagnetic energy resolution:

$$\frac{\delta y_{h,\mathrm{e}}}{y_{h,\mathrm{e}}} \approx \frac{1}{y}\sqrt{\left(\frac{1-\cos\theta_e}{2E_{e0}}\delta E_e\right)^2 + \left(\frac{1-\cos\theta_\gamma}{2E_{e0}}\delta E_\gamma\right)^2} \tag{3.23}$$

and becomes very large at low y_h values.

Thus by using this method one can measure the cross section only in terms of Q_h^2 integrated over the whole x range. One can also test if the available F_2 parametersations describe the data in this kinematic range. However, an extraction of single $F_2(x_h, Q_h^2)$ values is not possible.

An alternative way of the *ep* event kinematics reconstruction, is by use of the hadronic final state. This method, originally introduced by JAQUET and BLONDEL [jb79], can in principle be applied to QEDC events in the same form as to inclusive DIS events. The formulae are obtained by making use of the energy and momentum conservation laws. To be specific, assuming the detector to have the complete 4π angular coverage one can write for the incoming and outgoing particle energies and longitudinal momenta:

$$(E_{p0} - p_{z,p0}) + (E_{e0} - p_{z,e0}) = (E_e - p_{z,e}) + (E_\gamma - p_{z,\gamma}) + \sum_{i=1}^{N_h}(E_i - p_{z,i})\,, \tag{3.24}$$

where the index i in the summation runs over all outgoing hadrons. Neglecting particle masses and defining:

$$\Sigma = \sum_{i=1}^{N_h}(E_i - p_{z,i}) = \sum_{i=1}^{N_h} E_i(1-\cos\theta_i)\,, \tag{3.25}$$

one obtains

$$2E_{e0} = E_e(1-\cos\theta_e) + E_\gamma(1-\cos\theta_\gamma) + \Sigma\,. \tag{3.26}$$

The requirement of transverse momentum balance gives

$$\vec{p}_{t,e} + \vec{p}_{t,\gamma} + \sum_i \vec{p}_{t,h} = 0 \qquad \text{or} \qquad p_{t,e\gamma} = p_{t,h} \qquad \text{with} \qquad p_{t,h} = |\sum_i \vec{p}_{t,h}|\,, \tag{3.27}$$

where the summation is also performed over all final state hadrons. Using the above equations, the hadronic variables are then calculated by:

$$y_{h,\mathrm{JB}} = \frac{\Sigma}{2E_{e0}}\,, \qquad Q^2_{h,\mathrm{JB}} = \frac{p^2_{t,h}}{1-y_{h,\mathrm{JB}}}\,, \qquad x_{h,\mathrm{JB}} = \frac{Q^2_{h,\mathrm{JB}}}{s\,y_{h,\mathrm{JB}}}\,. \tag{3.28}$$

In practice it is impossible to build a detector having a full 4π coverage. There is always some leakage of particles along the beam axis. For the DIS measurement at HERA the leakage of hadrons in the forward direction plays a more significant role due to the boost of the centre of mass. The $E - P_z$ and P_t balance for the variable reconstruction in DIS were chosen to minimise this effect. For the QEDC events this problem is even more important because of the very low mass and transverse momentum of the hadronic final state. In particular, the outgoing proton in elastic events practically never enters the main detector. The reconstruction of hadronic

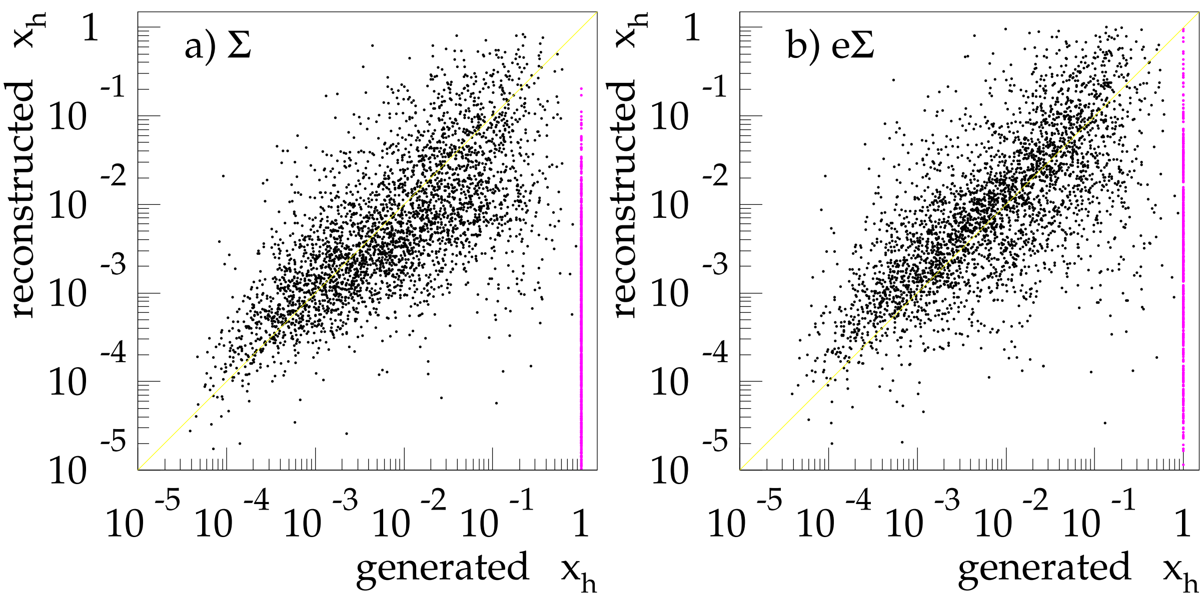

Figure 3.11: *Reconstruction of the hadronic variable x_h by the Sigma and eSigma method. Distributions of the elastic (magenta dots) and inelastic (black dots) events generated by COMPTON are plotted.*

variables by measuring outgoing hadrons can be done only in some part of the inelastic events where the hadronic mass M_X is not too small.

In eq. 3.24 the most prominent radiative correction, the initial state radiation is not taken into account. The Sigma method [bb95] allows to reduce this effect by using the sum over $E - p_z$ of all measured particles instead of $2E_{e0}$ in eq. 3.28:

$$\begin{aligned} y_{h,\Sigma} &= \frac{\Sigma}{\Sigma + E_e(1-\cos\theta_e) + E_\gamma(1-\cos\theta_\gamma)}\,, \\ Q^2_{h,\Sigma} &= \frac{p^2_{t,e\gamma}}{1-y_{h,\Sigma}}\,, \qquad x_{h,\Sigma} = \frac{Q^2_{h,\Sigma}}{s y_{h,\Sigma}}\,. \end{aligned} \tag{3.29}$$

The quality of x_h reconstruction by the Sigma method is demonstrated in fig. 3.11 a. A correlation between the the generated and reconstructed variables is clearly visible. The reconstruction can be also performed by using the combined eSigma method:

$$y_{h,e\Sigma} = y_{h,\Sigma}\,, \qquad Q^2_{h,e\Sigma} = Q^2_{h,e}\,, \qquad x_{h,e\Sigma} = \frac{Q^2_{h,e\Sigma}}{s y_{h,e\Sigma}}\,. \tag{3.30}$$

which provides an even better x_h resolution, as seen in fig. 3.11 b. An admixture of falsely reconstructed elastic events remains due to the noise in the LAr calorimeter. It can be cut off by imposing a limitation on the $e\gamma$ acoplanarity as discussed in the next section.

3.7 Separation of Elastic and Inelastic Channels

Singling out the inelastic QEDC contribution is necessary for the reconstruction of the hadronic variables. It is performed as follows:

1. Since x_h can be only reconstructed from the hadronic final state, at least one cluster in the Liquid Argon calorimeter with the energy above the noise threshold of 0.5 GeV is demanded. This requirement leaves however an approx. 7% admixture of elastic events due to the noise in the LAr calorimeter. A further reduction of the admixture is desirable, since these events are concentrated in the region of very low Q_h^2 values and hence they make a relatively high contribution in the range of lowest Q_h^2 accessible in inelastic scattering.

2. To remove the remaining elastic contribution, a cut on the $e\gamma$ acoplanarity A is imposed. The acoplanarity distribution is depicted in fig. 3.12 before and after applying the requirement of minimum hadronic activity described above. It is visible that elastic events have typically much lower acoplanarity values than inelastic ones. Even without constraints on the hadronic activity in LAr one can select a sample with a high fraction of inelastic events, *e.g.*, after the cut $A > 7^\circ$. Such a selection is sufficient for the Q_h^2 reconstruction, described in the prior section, but it still leaves an approx. 16% contribution of the elastic channel. In contrast, the requirement

$$A > 2^\circ \tag{3.31}$$

in conjunction with the condition that at least one LAr cluster exists reduces the fraction of elastic events below 2% and is also suitable for the reconstruction of both Q_h^2 and x_h.

Vice versa, by requiring that the $e\gamma$ acoplanarity does not exceed some value an almost pure sample of elastic events can also be set apart. Such a selection brings additional advantages to the experimental analysis, since elastic QEDC events are very well suitable for systematic studies and cross checks. The actual limit values have been chosen variably in different studies and will be given in corresponding sections of this thesis.

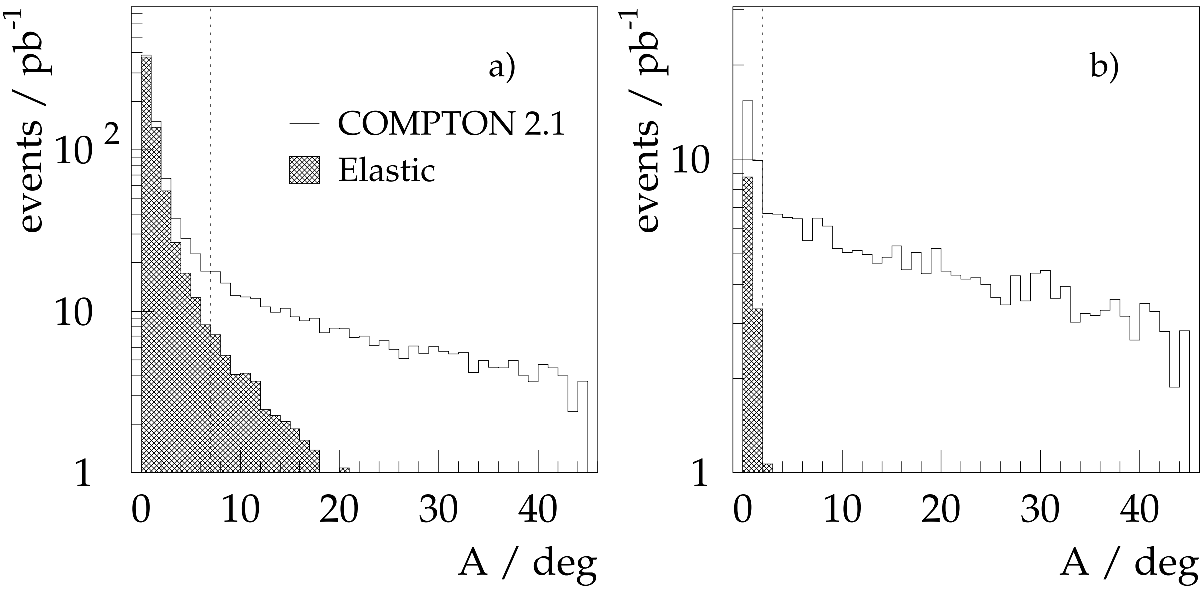

Figure 3.12: *Acoplanarity in COMPTON MC events selected a) without and b) with the requirement of the minimum energy deposition in the LAr calorimeter.*

3.8 Reconstruction of Leptonic Variables

The leptonic variables are calculated by similar methods, provided that now the final photon is treated as a part of the hadronic final state.

For the reconstruction with the electron method exactly the same expressions can be applied as used in the DIS analyses:

$$\begin{aligned} y_{l,\mathrm{e}} &= 1 - \frac{E_e - p_{z,e}}{2E_{e0}} = 1 - \frac{E_e(1-\cos\theta_e)}{2E_{e0}} \,, \\ Q^2_{l,\mathrm{e}} &= \frac{p^2_{t,e}}{1-y_{l,\mathrm{e}}} = \frac{E_e^2 \sin^2\theta_e}{1-y_{l,e}} = 2E_{e0}E_e(1+\cos\theta_e)\,, \\ x_{l,\mathrm{e}} &= \frac{Q^2_{l,\mathrm{e}}}{s y_{l,\mathrm{e}}} \,. \end{aligned} \tag{3.32}$$

In the methods employing hadronic final state the final photon energy and momentum have to be added to those of hadrons. Defining modified variables

$$\Sigma' = \sum_{i=1}^{N_h} E_i(1-\cos\theta_i) + E_\gamma(1-\cos\theta_\gamma)\,, \tag{3.33}$$

$$p'_t = |\sum_i \vec{p}_{t,h} + \vec{p}_{t,\gamma}|\,, \tag{3.34}$$

the reconstruction formulae read for the Jaquet – Blondel method:

$$y_{l,\mathrm{JB}} = \frac{\Sigma'}{2E_{e0}}\,, \qquad Q^2_{l,\mathrm{JB}} = \frac{p'^2_t}{1-y_{l,\mathrm{JB}}}\,, \qquad x_{l,\mathrm{JB}} = \frac{Q^2_{l,\mathrm{JB}}}{s y_{l,\mathrm{JB}}}\,, \tag{3.35}$$

and for the Σ method:

$$y_{l,\Sigma} = \frac{\Sigma'}{\Sigma' + E_e(1-\cos\theta_e)}\,, \qquad Q^2_{l,\Sigma} = \frac{E_e^2\sin^2\theta_e}{1-y_{l,\Sigma}}\,, \qquad x_{l,\Sigma} = \frac{Q^2_{l,\Sigma}}{s y_{l,\Sigma}}\,. \tag{3.36}$$

For the computation of the leptonic variable by any method the final electron and photon must be identified, *i.e.*, one has to distinguish experimentally, which cluster in the calorimeter was produced by the electron and which cluster by the photon. This can be done by associating a signal in one of the tracking chambers in front of the calorimeter with the electron cluster, as mentioned in sect. 3.1.

The y_l resolution of the electron, Jaquet – Blondel and Sigma methods is shown in the left plots of fig. 3.13. It is seen, that the Sigma method provides the best resolution among all methods in the whole kinematic range. Therefore it is used in the present QEDC cross section measurement in all bins of leptonic variables.

At this point there is an important difference to the DIS measurements, in which the electron method has a better y resolution at $y > 0.15$. In DIS this is caused by the large hadronic energy uncertainty that affects the reconstruction by the Jaquet – Blondel and Sigma methods. In contrast, the y_l calculation by these methods in Compton events is dominated by $E - p_z$ of the final state photon (see. eq. 3.36). Thus, their uncertainty due to the energy resolution is the same as that of the electron method. Like in DIS, at small y_l both hadronic methods work better due to the worsening y_l resolution of the electron method:

$$\frac{\delta y_{l,\mathrm{e}}}{y_{l,\mathrm{e}}} \approx \frac{1-y_{l,\mathrm{e}}}{y_{l,\mathrm{e}}}\frac{\delta E_e}{E_e}\,. \tag{3.37}$$

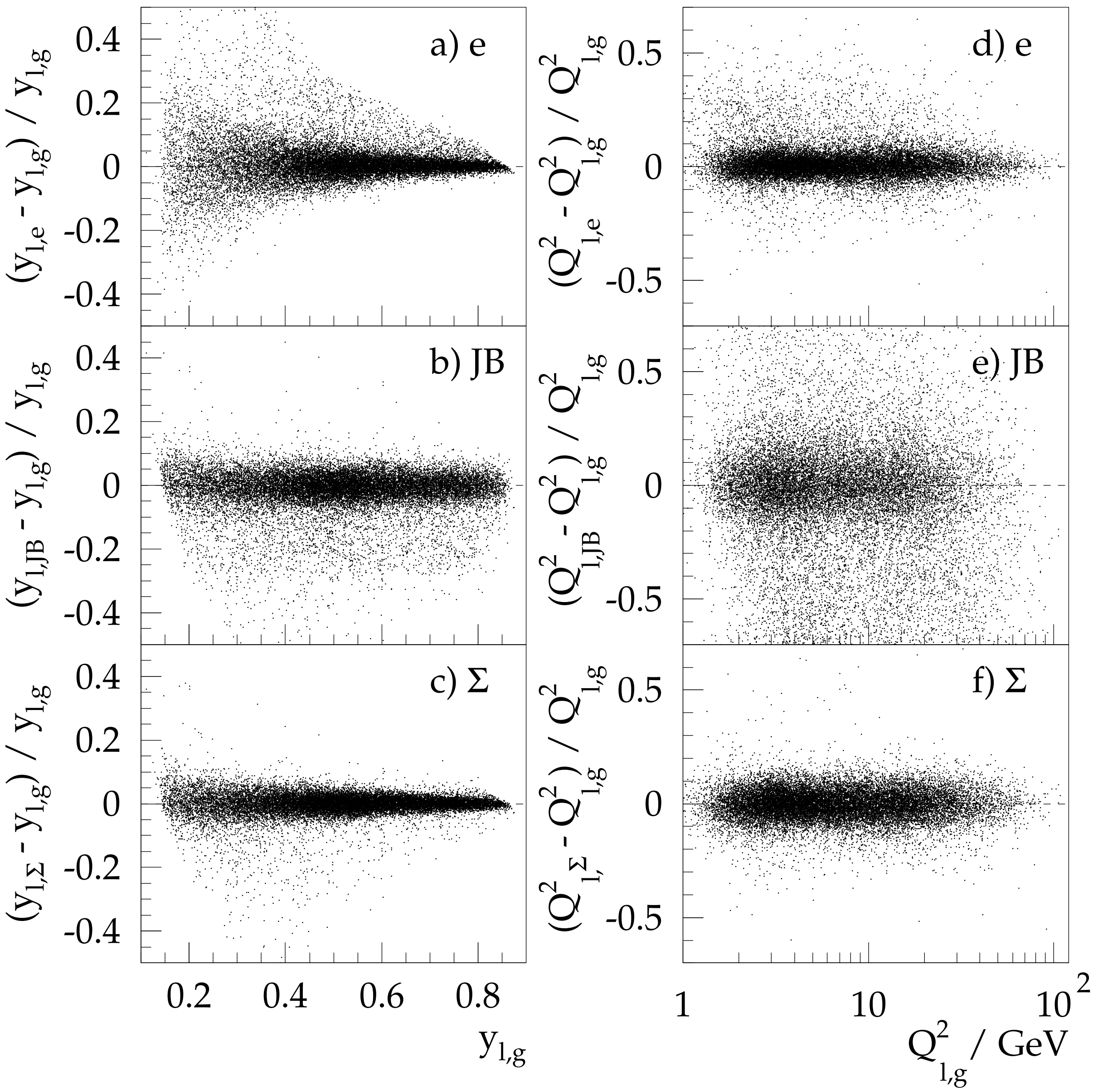

Figure 3.13: *Resolution of leptonic variables y_l and Q_l^2 in simulated COMPTON events. The dots in the scatter plots show the relative deviation of the reconstructed quantity from its generated value as a function of the corresponding generated variable. The left plots demonstrate y_l resolution of a) electron, b) Jaquet – Blondel and c) Sigma method. The right plots show Q_l^2 resolution of these reconstruction methods: d) electron, e) Jaquet – Blondel and f) Sigma method. Only such events are displayed, in which a correct electron/photon identification on the basis of the simulated central tracker response has been performed.*

Apart from that, the superiority of the Sigma method in the entire kinematic range can be traced back to its robustness against radiative corrections.

On the contrary, the transverse momentum reconstruction in QEDC events is influenced by the mediocre hadronic p_t reconstruction. This leads to the worse Q_l^2 reconstruction by the Jaquet – Blondel method, as displayed in the right plots of fig. 3.13. Therefore this method is not used in this analysis. The electron method is utilised to compare the measured cross section values and estimate the size of radiative corrections (see sect. 4.8).

3.9 Goal of the Analysis

From the theoretical description of QED Compton events given in chapter 1 it becomes clear that the major aim for an experimental analysis of QED Compton scattering is the investigation of the behaviour of the structure function F_2 in the region of low photon virtualities Q_h^2 and medium to high Bjorken scale variable x_h. However, the differential cross section measurement can actually pursue two different goals. The studies of the reconstruction of the hadronic and leptonic kinematic variables show that these two tasks necessitate essentially different analysis chains.

One goal is the direct measurement of F_2 in this kinematic range. This task implies singling out inelastic QEDC events and the subsequent double differential cross section measurement as a function of the hadronic variables x_h and Q_h^2. Actually, the possibility of measuring x_h in QED Compton events has been explored in the course of this analysis after the implementation of hadronic final state simulation into the COMPTON MC generator. Such a measurement demands a very good understanding of hadron production at low masses M_X and a thorough study of event reconstruction in the forward region of the LAr calorimeter.

The other goal is to measure the double differential cross section in terms of the leptonic variables x_l and Q_l^2 following the proposal of De Rújula and Vogelsang. The knowledge of the cross section should allow a determination of the structure function γ, provided that the collinear approximation holds. For this purpose the entire cross section of all QEDC channels has to be measured. The main uncertainty is in the continuum inelastic region, and the correct behaviour of the structure function F_2 must be found. Thus, this analysis also provides us with the information about F_2 behaviour in the given kinematic region. However, separate F_2 values cannot be measured in such an analysis, but instead parameterisations available from other measurements can be compared to the data. If a fit matching the data is found, the corresponding γ function can be calculated according to eq. 1.65. Furthermore, one has to check, if the Weizsäker – Williams approximation can be applied, *i.e.*, whether the factorisation given by eq. 1.59 holds. To do that, one can compute the cross sections according to this expression by employing the determined γ function and confront them to the measured values.

It is this goal that is pursued in the present work. The F_2 behaviour has been directly studied only as a function of Q_h^2. The task of a direct $F_2(x_h, Q_h^2)$ measurement remains for a future H1 analysis.

3.10 Kinematic Bins

The scattering cross section is measured in bins of leptonic variables x_l, Q_l^2 listed in table 3.1. The kinematic intervals chosen are close to those defined in the analytical calculation by De Rújula and Vogelsang, to allow for an easy comparison of their model to the experimental

Table 3.1: *Kinematic intervals and x_l bin "central" points used in the analysis. The Q_l^2 bins have been chosen for each x_l interval separately. Two Q_l^2 intervals have been defined for the first x_l bin and three for each other x_l interval. The x_l and Q_l^2 bins, where the QEDC cross section has been measured, are printed in bold face.*

x_l bin #	x_l interval	Q_l^2 intervals (GeV^2)	$x_{l,c}$
1	$\mathbf{1.78 \cdot 10^{-5} – 5.62 \cdot 10^{-5}}$	**1.5 – 2.5 – 3.5**	$5.13 \cdot 10^{-5}$
2	$\mathbf{5.62 \cdot 10^{-5} – 1.78 \cdot 10^{-4}}$	**1.5 – 5.0 – 8.5 – 12.0**	$9.33 \cdot 10^{-5}$
3	$\mathbf{1.78 \cdot 10^{-4} – 5.62 \cdot 10^{-4}}$	**3.0 – 14.67 – 26.33 – 38.0**	$2.82 \cdot 10^{-4}$
4	$\mathbf{5.62 \cdot 10^{-4} – 1.78 \cdot 10^{-3}}$	**10.0 – 48.33 – 86.67** – 125.0	$8.91 \cdot 10^{-4}$
5	$1.78 \cdot 10^{-3} – 5.62 \cdot 10^{-3}$	22 – 168 – 314 – 460	$2.95 \cdot 10^{-3}$
6	$5.62 \cdot 10^{-3} – 1.78 \cdot 10^{-2}$	0 – 500 – 1000 – 1500	$8.91 \cdot 10^{-3}$
7	$1.78 \cdot 10^{-2} – 5.62 \cdot 10^{-2}$	0 – 1500 – 3000 – 4500	$2.69 \cdot 10^{-2}$
8	$5.62 \cdot 10^{-2} – 1.78 \cdot 10^{-1}$	10 – 6005 – 12000 – 17995	$7.94 \cdot 10^{-2}$

Table 3.2: *Stability and purity of the electron and Sigma methods. Values in rows are given for Q_l^2 intervals, defined for each x_l bin separately, as pointed in table 3.1.*

x_l bin #	Electron method						Sigma method					
	Stability, %			Purity, %			Stability, %			Purity, %		
1	86	74		82	56		86	69		83	57	
2	89	88	82	93	85	76	90	87	79	92	85	75
3	85	90	83	89	89	79	86	89	80	89	89	79
4	88	90		91	84		88	87		91	85	

data. The cross section measurement is conducted in the bins populated by events with two clusters in the backward calorimeter. Higher x_l and Q_l^2 values shall be measured in another experimental analysis, involving cluster selection in the Liquid Argon calorimeter. Nevertheless, for the sake of completeness, comparisons between the theoretical model predictions are made in the whole kinematic range. In the rightmost column of table 3.1 the "central" values $x_{l,c}$ are listed, at which the function $\gamma(x_l, Q_l^2)$ has been calculated. These are average x_l values computed by De Rújula and Vogelsang for each x_l bin.

The choice of binning for the measurement is limited by the resolution of kinematic variable reconstruction and statistics available in each bin. Bad adjustment of the bin size to the resolution can cause large bin-to-bin migrations which can influence the results of the measurement. In order to control the migration effects, two quantities have been determined for each bin using simulated QEDC events which passed the entire analysis chain. These quantities are the stability S and the purity P defined as

$$S = \frac{\text{\# events generated and reconstructed in a bin}}{\text{\# events generated in a bin}}, \tag{3.38}$$

$$P = \frac{\text{\# events generated and reconstructed in a bin}}{\text{\# events reconstructed in a bin}}. \tag{3.39}$$

The values obtained by the electron and by the Sigma methods are summarised in table 3.2. Both methods give nearly the same very high values for all bins. The usual criterion, applied in DIS analyses, that both quantities must be larger than 30%, is thus far more than fulfilled. This

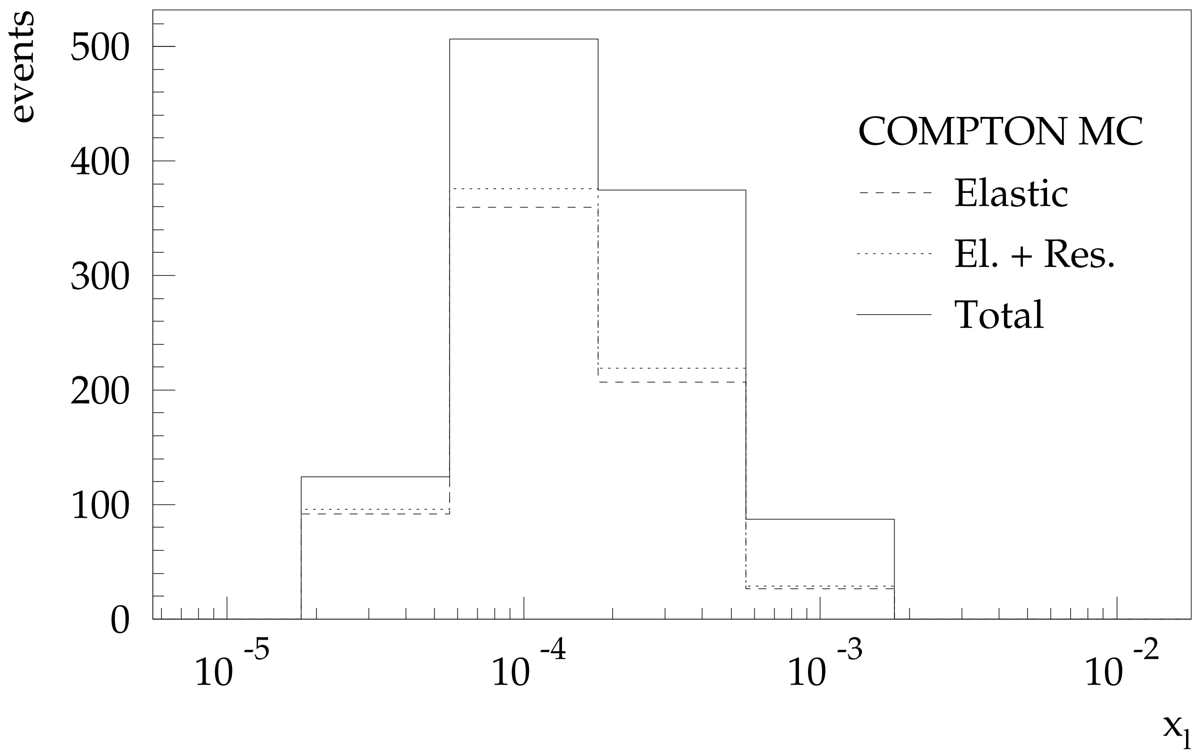

x_l-Bin #	1	2	3	4
Elastic, %	74	71	55	31
Resonance, %	3	3	3	2
Continuum, %	**23**	**26**	**42**	**67**

Figure 3.14: *Number of events in each x_l bin generated by COMPTON. The distributions of elastic (dashed line), elastic + resonance (dotted line) and all three channels together (solid line) are depicted in the histogram. The relative contributions of each channel are specified in percent in the table below.*

means, that from the experimental point of view a much finer binning could be in principle chosen.

A specific issue of this analysis is that the total cross section of QEDC scattering is measured in each bin, but the matter of special interest is the inelastic contribution. It is therefore important to understand how different channels are spread in leptonic variables. In fig. 3.10 the amount of generated events and relative contributions of the three QEDC channels in each x_l bin, in which the cross section measurement is performed, are shown. It is seen, that the resonance part is relatively small, so that it cannot affect significantly the total cross section. The fraction of continuum inelastic events becomes larger as x_l increases, therefore the total cross section of all QEDC channels is expected to be more sensitive to F_2 at higher x_l values.

3.11 Cross Section Determination

The QEDC cross section is determined in this analysis by counting the number of measured events in each kinematic bin $\Delta x_l \Delta Q_l^2$. This number corresponds to the integral of the double differential cross section over this kinematic interval. The QEDC scattering process is unambiguously defined only in the leading order, *i.e.*, under the assumption that only one high energetic photon is emitted. To confront the measurement to theoretical models, in particular to the computation by De Rújula and Vogelsang, the leading order cross section must be extracted. This is done according to the formula:

$$\sigma_{\square} = \frac{N_{\square}^{\mathrm{data}} - N_{\square}^{\mathrm{bg}}}{\mathcal{L}} \frac{1}{\epsilon \mathcal{A}(1+\delta)}, \tag{3.40}$$

where

- $N_{\square}^{\mathrm{data}}$ is the total number of events accumulated in a bin;
- $N_{\square}^{\mathrm{bg}}$ is the total number of background events surviving the selection procedure;
- $\mathcal{L}$ is the integrated luminosity of the event sample;
- $\mathcal{A}$ is the detector acceptance and efficiency computed using the full Monte Carlo simulation. It is given as the ratio of the number of reconstructed MC events to the number of generated events in the bin: $\mathcal{A} = N_{\square}^{\mathrm{MC}}/N_{\square}^{\mathrm{gen}}$;
- ϵ denotes additional efficiency corrections that have not been included in the simulation. They have been obtained from the data and applied in the data analysis chain (see chapter 4);
- δ designates higher order radiative corrections: $\delta = \sigma_{\square}^{\mathrm{full}}/\sigma_{\square}^{\mathrm{LO}} - 1$, where $\sigma_{\square}^{\mathrm{full}}$ is the full cross section including radiative corrections and $\sigma_{\square}^{\mathrm{LO}}$ is the leading order cross section.

If the radiative corrections are completely implemented in the simulation, the extraction of the leading order cross section can be simplified by using the following relation:

$$N_{\square}^{\mathrm{gen}} = \mathcal{L}^{\mathrm{MC}} \sigma_{\square}^{\mathrm{full}} \tag{3.41}$$

between the number of MC events $N_{\square}^{\mathrm{gen}}$ generated in the bin, the effective luminosity of the generated event sample $\mathcal{L}^{\mathrm{MC}}$ and the cross section $\sigma_{\square}^{\mathrm{full}}$ including radiative corrections. The QEDC cross section is then determined by the so called "Monte Carlo method":

$$\sigma_{\square} = \frac{N_{\square}^{\mathrm{data}} - N_{\square}^{\mathrm{bg}}}{N_{\square}^{\mathrm{MC}}} \frac{\mathcal{L}^{\mathrm{MC}}}{\mathcal{L}} \frac{1}{\epsilon} \sigma_{\square}^{\mathrm{LO}}, \tag{3.42}$$

where $\sigma_{\square}^{\mathrm{LO}}$ is the leading order cross section implemented in the simulation. In order to calculate it, a separate simulation without radiative corrections is performed.

The values calculated in this manner are the average cross sections for each x_l–Q_l^2 bin. They are compared in the present work to the analytical predictions of De Rújula and Vogelsang[3]. No bin centre corrections have been required for this comparison.

[3]The values for the final comparison have been provided by W. Vogelsang [vog01]. He recalculated them after adjustment of the kinematic binning and of the effective event selection cuts to those used in the present measurement.

In case the collinear approximation holds, the relation between the real and simulated cross sections can be interpreted as that between the γ functions calculated in effective bin centre points:

$$\gamma(x_c, Q^2_{l,c}) = \frac{N^{\mathrm{data}}_{\square} - N^{\mathrm{bg}}_{\square}}{N^{\mathrm{MC}}_{\square}} \frac{\mathcal{L}^{\mathrm{MC}}}{\mathcal{L}} \frac{1}{\epsilon} \gamma^{\mathrm{MC}}(x_c, Q^2_{l,c}) \ , \tag{3.43}$$

or

$$\gamma(x_c, Q^2_{l,c}) = \frac{\sigma_{\square}}{\sigma^{\mathrm{LO}}_{\square}} \gamma^{\mathrm{MC}}(x_c, Q^2_{l,c}) \ . \tag{3.44}$$

If the initial γ function of the simulation is close to the measured one, the above relation can be in principle employed at every point of the bin. Otherwise bin centre corrections are necessary. They can be performed by the iterative reweighting of the simulated sample.

The precision of the Monte Carlo method is essentially determined by the agreement between the real data and the simulation. The task of the experimental analysis is thus to understand in detail and minimise any remaining discrepancies between them. Deviations, which could not be understood, are included in the systematic error. The Monte Carlo method implies, thus, a thorough study of all experimental effects, just as it must be done for the direct measurement. The advantage of the Monte Carlo technique is that it greatly simplifies the unfolding of real cross section values from the measured ones.

Chapter 4

Data Selection and Treatment

This chapter is devoted to the data analysis procedure. At first the data samples chosen for the analysis are presented. Subsequently, the basic criteria of the QED Compton event selection are specified. Afterwards, the triggers used to collect QEDC events and the corrections of their efficiency are discussed.

The reconstruction of the leptonic variables necessitates the electron/photon separation. The particle identification procedure by means of tracking detectors is hence described next. A detailed description of the electron and photon identification efficiency is given. Since the validation algorithms involve the reconstruction of the event vertex, this is also considered in this part of the thesis.

Further discussion concerns the reconstruction of the polar angle and energy of the outgoing electron and photon. For an accurate measurement of the scattering angle an alignment of several subdetectors has been performed. A precise determination of the energy required extensive studies of the SpaCal energy scale and resolution and a subsequent energy calibration. In the framework of the analysis of the energy scale additional corrections to the measured polar angle have also been elaborated.

At the end of the chapter the estimations of the DIS background and the radiative corrections from real data (as mentioned in chapter 3) are given.

4.1 Experimental Data Selection

4.1.1 Data Samples

The present analysis is based on the data recorded by the H1 detector in 1997. The data are split into two samples with different trigger conditions. The first sample, here referred to as the "standard data range of 1997", contains the bulk of the data. Its luminosity, after the run selection and corrections mentioned below in this section, amounts to $9.25\,\mathrm{pb}^{-1}$. The QEDC cross section has been measured with this data sample. The second much smaller data set of $1.63\,\mathrm{pb}^{-1}$ corrected luminosity was collected at the end of the 1997 data taking period with so called "minimum bias trigger settings". The change of trigger requirements was caused by specific objectives of the inclusive DIS analyses. This second data sample has been employed for additional systematic studies. In particular, there were two main reasons for the use of the minimum bias sample:

1. An unfortunate setting of the QED Compton trigger in the standard 1997 running period has led to the rejection of a fraction of the inelastic QEDC events;
2. The BST electron validation efficiency in the standard 1997 run range could not be determined from DIS data, since a significant part of DIS events with the electron scattered within the BST acceptance was rejected by the DIS trigger.

The treatment of these problems in the current analysis is discussed in sect. 4.3 and 4.4. The minimum bias data sample is employed to cross-check that these problems were correctly solved.

4.1.2 Run Selection

H1 events are collected in so called *luminosity runs*. A run is a period of data acquisition with nearly constant experimental conditions. For each run its integrated luminosity value and other characteristic parameters are recorded in the H1 database. The runs taken in a time interval between the start of a HERA luminosity running and the dump or loss of one of the HERA beams form a *luminosity fill*. The standard and minimum bias 1997 data samples comprise the run ranges 176421 – 200431 and 200433 – 201519, respectively, corresponding to the luminosity fills 1220 – 1564 and 1565 – 1598.

The runs used for the present data analysis had to meet the following quality demands:

1. **Trigger phase 2, 3 or 4.** Different trigger phases during data taking within one luminosity fill correspond to different trigger prescale factors. There were four trigger phases in one fill during the standard 1997 running and two during the minimum bias running. In both cases the phase 1 with high prescale factors is set in the beginning of a luminosity fill, while the tracker high voltage is ramping up. The beam induced background is usually very large at this time, since the HERA machine keeps tuning the beams.

2. **Subdetector high voltage status.** Each hardware branch relevant for this analysis has to provide the full functionality for more than 80% of the total run time. Otherwise the run is rejected due to detector instability. To be specific, the HV status of the LAr calorimeter, the SpaCal, the BDC, the central tracking chambers (CJC, BST, MWPC, CIZ), the ToF and of the luminosity system was checked. Within accepted runs, events, in which one of the components was not operational, are rejected and the effective run luminosity is corrected accordingly.

3. **Medium or good run quality.** Each run is assigned a flag of good, medium or poor quality depending on the actual status of subdetector components. This is done first during the data taking by a shift crew and then in offline data quality checks.

4. **Pass an additional quality control** performed in the analysis step. A list of rejected runs together with the reasons for rejection is given in table 4.1. The run quality studies are partially based on results of checks done in previous analyses [kur99, ark00, işs01].

5. **Run luminosity of more than 1 nb^{-1}.** This condition is applied to ensure statistical significance of analysed data and also to avoid short time runs, which were terminated, as a rule, because of unstable running conditions.

In the run quality studies the stability of the rate of reconstructed events has been in particular considered. The average event rate per luminosity fill for the runs fulfilling the above criteria in the standard and the minimum bias data sample is depicted in fig. 4.1. The events passing the full selection and particle identication chain are used for the plots. A generally stable rate within each sample is observed. A closer look reveals however a small increase of the QEDC event rate within the standard 1997 sample around the luminosity fill 1470. This effect arises from the increase of the BST efficiency in summer 1997.

Table 4.1: *Run ranges excluded from the analysis.*

Runs	Reason for rejection
Standard range of 1997 data	
$<$ 185735	Low BST efficiency
187907 – 187908	BST readout problems
189790 – 189822	L2 T18 high rejection rate
190037 – 190055	BST readout problems
190057 – 190061	BST problems
190073 – 190776	BST problems
191512 – 191694	MWPC readout problems
191730	Data taking problems
191738 – 191745	BST readout problems
191749 – 192008	SpaCal IET problems
192521 – 192525	BST readout problems
192606	no DCRΦ trigger readout
192789 – 192906	SpaCal IET problems
192914 – 192916	no DCRΦ trigger readout
192980 – 192981	BST readout problems
193056 – 193253	SpaCal IET problems
193309	L2 T18 high rejection rate
193315	Data taking problems
193433 – 193462	SpaCal IET problems
193502 – 193526	SpaCal IET problems
193662 – 193672	DCRΦ trigger readout corrupted
194166 – 194255	L2 trigger problems
194247 – 194249	Raw data for BST
194643 – 194644	MWPC readout problems
194783 – 194785	MWPC readout problems
194827	Data taking problems
194832 – 194835	MWPC readout problems
195512	Data taking problems
195668 – 196377	SpaCal IET problems
197036	Data taking problems
197135 – 197143	BST readout problems
198345 – 198440	Unstable tracker performance
199318 – 199324	BST readout problems
200167	no DCRΦ trigger readout
200322 – 200324	BST readout problems
200407	BST readout problems
Minimum bias range of 1997 data	
201141	Lumi platform mistakenly moved
201142	Data taking problems
201281 – 201283	BST readout problems
201287 , 201293	BST readout problems
201439 – 201481	BST readout problems
201220	Pretest for L4 scheme 2000
201320 – 201383	Pretest for L4 scheme 2000

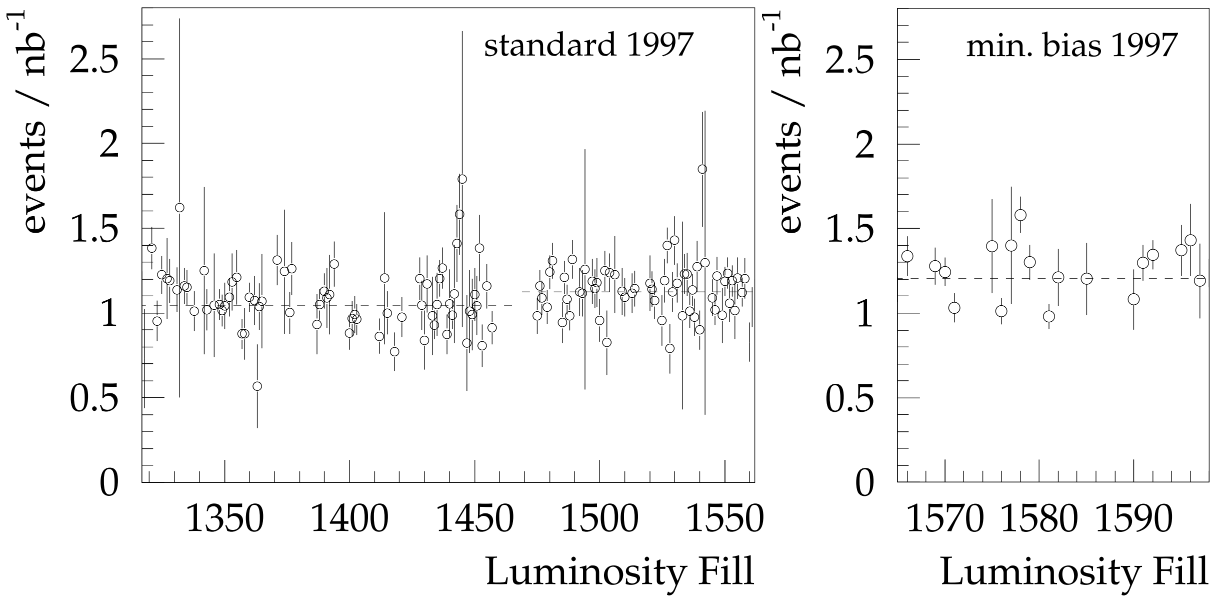

Figure 4.1: *Rate of the analysed events per luminosity fill after the QEDC event selection in the standard (left) and the minimum bias (right) run range of 1997.*

During 1997 much work was done by the BST group on the improvement of the BST readout [lah97, ark99], and the BST efficiency was hence not stable all the time. Therefore in the present study of the QEDC event rate stability a special emphasis is put on the BST validation rate. In the runs taken between the beginning of the running period in February and up to April 1997 a very low BST efficiency was found. This is the reason why the runs up to 185735 were removed from the analysis chain (see table 4.1). Afterwards, a stable acceptable QEDC event rate was observed. Furthermore, significant changes of the trailer electronics were implemented by the BST group in July – August 1997. These changes led to a further rise of the BST efficiency and consequently the increase of the QEDC event rate.

In the minimum bias sample the rate becomes even higher for another reason, namely, because of a relaxed cut on the angular distribution of hadrons. This cut is in general necessary in order to reduce the DIS background, as pointed out in paragraph 3.2.2. However the unfortunate trigger settings in the standard 1997 data, already mentioned in the previous section, required a significantly stronger limit of the maximum polar angle of hadrons. This will be discussed in detail in sect. 4.3.

4.2 QEDC Event Selection

In the beginning of this section a brief overview of the selection requirements is presented. Their detailed elucidation is given in the following paragraphs.

The QEDC event selection criteria are divided into two categories. At first the following *basic cuts* are imposed on the quantities measured in the backward detectors and the Liquid Argon calorimeter:

- QED Compton process selection cuts on

  - Energies E_1, E_2 of the highest and the second highest energy cluster in the electromagnetic SpaCal
$$E_1 > 10\,\text{GeV}\,, \qquad E_2 > 4\,\text{GeV}\,, \qquad 20\,\text{GeV} < E_1 + E_2 < 32\,\text{GeV}\,, \tag{4.1}$$
  - $e\gamma$ acoplanarity
$$A < 45^\circ\,, \tag{4.2}$$

- Background suppression cuts on
  - Maximum polar angle of a LAr cluster among all clusters with an energy above 0.5 GeV
$$\theta_{\text{LAr}} < 100^\circ\,, \tag{4.3}$$
  - Residual energy in the e.m. SpaCal
$$E_{\text{res}} < 1\,\text{GeV} \tag{4.4}$$
    defined as $E_{\text{res}} = E_{\text{tot}} - E_1 - E_2$, where E_{tot} is the total energy in the e.m. SpaCal,
  - Logarithmic radius of each of the two SpaCal clusters
$$\text{ECRA}_{\log,1} < 4.5\,\text{cm}\,, \qquad \text{ECRA}_{\log,2} < 4.5\,\text{cm}\,, \tag{4.5}$$
  - Energy in the hadronic SpaCal measured in the cells inside a circular area of a 15 cm radius behind each of the two clusters in the e.m. SpaCal
$$E_{\text{had},1} < 0.5\,\text{GeV}\,, \qquad E_{\text{had},2} < 0.5\,\text{GeV}\,, \tag{4.6}$$

- Cuts ensuring high detector and trigger efficiency:
  - Subtrigger s_{13} in the standard data range,
    Subtriggers s_0 and s_3 in the minimum bias data range
  - Stronger cut on the LAr cluster polar angle in the standard 1997 data range
$$\theta_{\text{LAr}} < 30^\circ\,, \tag{4.7}$$
  - Basic fiducial cuts.

In the next step of the analysis chain the electron/photon identification is performed, which also involves the measurement of the vertex coordinates. In doing so the following requirements are imposed:

- Selection of events with the identified electron and photon;
- Acceptance limits:
  - Cut on the vertex z coordinate
$$-30\,\text{cm} < z_{\text{vtx}} < 30\,\text{cm}\,, \tag{4.8}$$
  - Fiducial cuts on the BST and CIP acceptance.

Apart from the main purposes of the above requirements, the $e\gamma$ identification leads to a suppression of the dilepton backgrounds, while the z_{vtx} limit reduces the beam induced background.

In the rest of this section the basic criteria of the signal selection and background suppression are discussed in detail. Then the trigger selection and the $e\gamma$ identification together with the vertex reconstruction will be described.

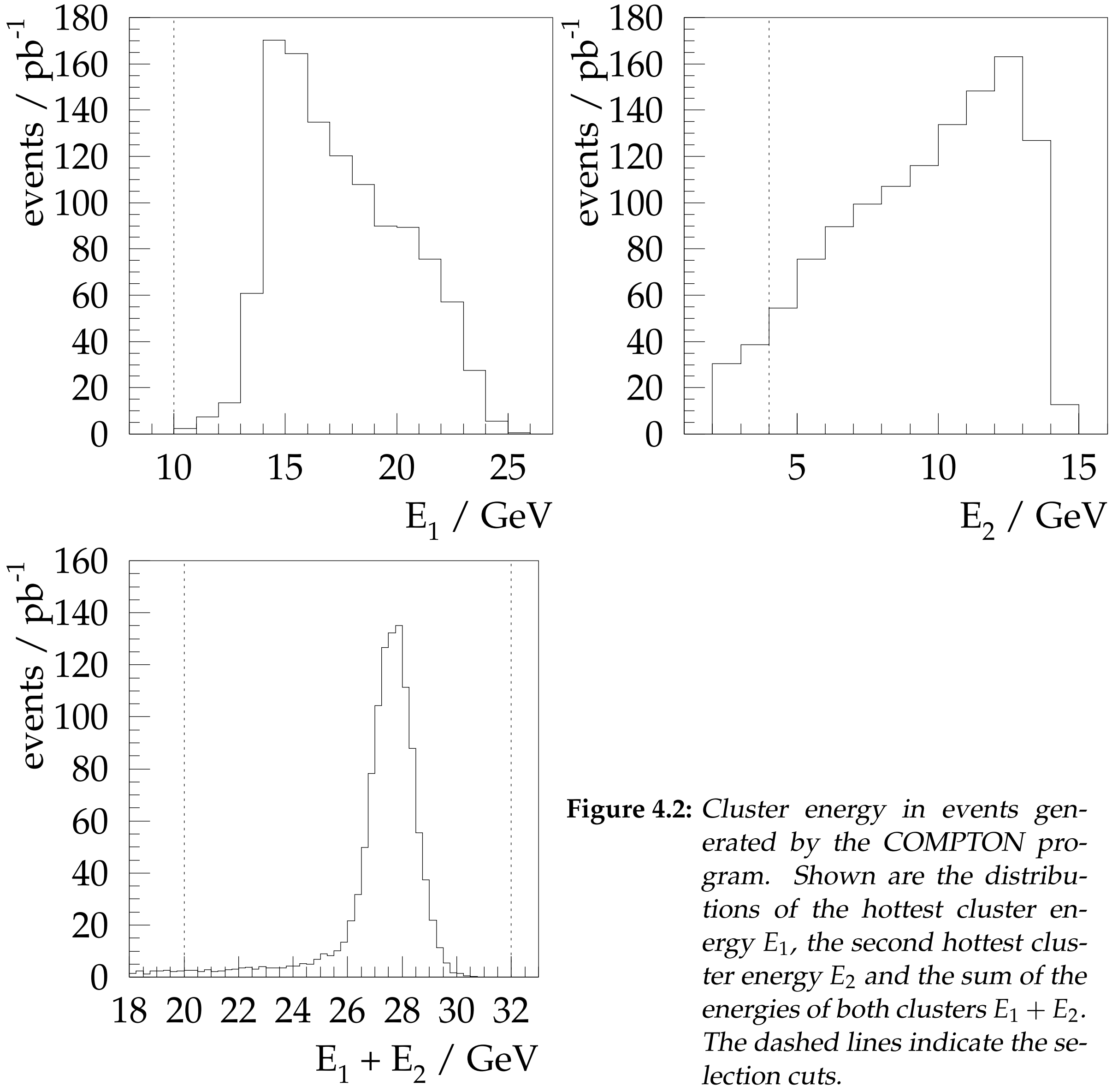

Figure 4.2: *Cluster energy in events generated by the COMPTON program. Shown are the distributions of the hottest cluster energy E_1, the second hottest cluster energy E_2 and the sum of the energies of both clusters $E_1 + E_2$. The dashed lines indicate the selection cuts.*

4.2.1 Cluster Energy Limits

The selection of the QED Compton process follows, in principle, the previous H1 QEDC analyses [mar98, sta98] and the proposal of De Rújula and Vogelsang [rv98].

The energy distributions of the final state electron and photon generated by the COMPTON program are depicted in fig. 4.2. The sum of the energies has a strong peak near the electron beam energy and a tail towards low energies. As pointed out in sect. 3.3, this tail has to be cut off in order to keep radiative corrections small.

After applying the cut on $E_1 + E_2$ the requirement of the minimum energy for the hottest cluster is fulfilled automatically.

The second cluster energy distribution falls towards low energies. The actual limit of the second cluster energy in the standard 1997 data is determined by the constraints of the QED Compton triggers on the second and fourth levels. The same cut value is also set for the minimum bias sample in order to select the same phase space in both data sets.

4.2.2 Acoplanarity

The acoplanarity cut is necessary to select the QED Compton phase space out of the whole ensemble of the leading order radiative corrections. The actual cut value is limited by the performance of the COMPTON generator.

A direct measurement of the $e\gamma$ acoplanarity leads to a systematic shift, because the scattered positron is deflected from its original azimuth by the magnetic field in the tracking chambers, as schematically depicted in fig. 4.3. An accurate reconstruction is however necessary, since stronger acoplanarity cuts are imposed at many steps of the analysis in order to separate elastic and inelastic QEDC channels. Therefore a correction of the azimuthal angle of the outgoing positron has been worked out using simulated QEDC events. The difference between the reconstructed and the generated ϕ of the outgoing positron and photon is shown in fig. 4.4 as a function of the particle energy. While there is no effect for the photon, the deviation of the positron's angle is visible. This deviation is fitted by a hyperbolic function

$$h(E) = a + \frac{b}{E + c} \tag{4.9}$$

with $a = -0.001$, $b = -0.24\,\mathrm{GeV}$ and $c = -0.3\,\mathrm{GeV}$. The main parameter b agrees well with a simple calculation based on the Lorentz force formula with a fixed value of 1.16 T for the magnetic field. The two other parameters are added to describe possible systematic effects like, *e.g.*, energy losses in dead material.

The $e\gamma$ acoplanarity distributions in the data and the simulation before and after the correction are displayed in fig. 4.5. After the correction their shape becomes narrow and corresponding to that of the generated acoplanarity distribution (cf. fig. 3.12 a).

4.2.3 Suppression of the DIS Background

The primary purpose of the cuts on θ_{LAr} and E_{res} is to create a gap between the outgoing electron–photon system and the hadronic final state and thus to suppress the DIS background.

The θ_{LAr} distribution is depicted in fig. 4.6, where the events without activity in the LAr calorimeter (elastic or low M_X inelastic events) are omitted in the plot. A strong peak of DIS signal is visible at high θ_{LAr} values. This peak represents DIS events with the hadronic jet directed backwards and reconstructed mainly in the backward part of the LAr calorimeter. However a fraction of the jet appears in the SpaCal acceptance faking the photon signature. Such events are suppressed with a cut denoted by the dashed line. A stronger cut, as illustrated by the dotted line, had to be made for the standard data sample due to the unfortunate trigger conditions, as discussed in sect. 4.3.

It can be seen that the original DJANGO signal relatively reasonably describes the inclusive DIS contribution at high θ_{LAr} values. However, as mentioned in paragraph 3.2.2, after the application of the θ_{LAr} cut the DJANGO contribution appeared to be unnaturally high. The DJANGO signal after all cuts was renormalised after the dedicated study described in sect. 4.7.

The size of the DIS peak strongly depends on the cut parameter for the residual energy E_{res} in the SpaCal. Vice versa, the E_{res} distributions strongly depends on the θ_{LAr} cut value, as shown in fig.4.7, where E_{res} is plotted before and after applying the θ_{LAr} cut. One can see, that DJANGO provides at least a partial description of the high energy tail. Nevertheless some problem with generated hadron multiplicity has led to a wrong DIS signal, especially at low E_{res}.

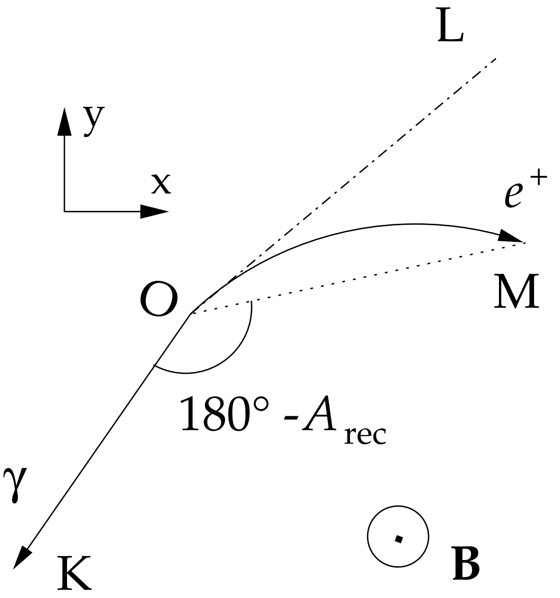

Figure 4.3: *Influence of the magnetic field on the azimuthal angle of the scattered positron, which leads to a wrong acoplanarity reconstruction. The measured value is determined from the angle KOM, while the true value is given by the angle KOL. Here, K and M indicate the SpaCal clusters and O denotes the vertex position in the xy plane.*

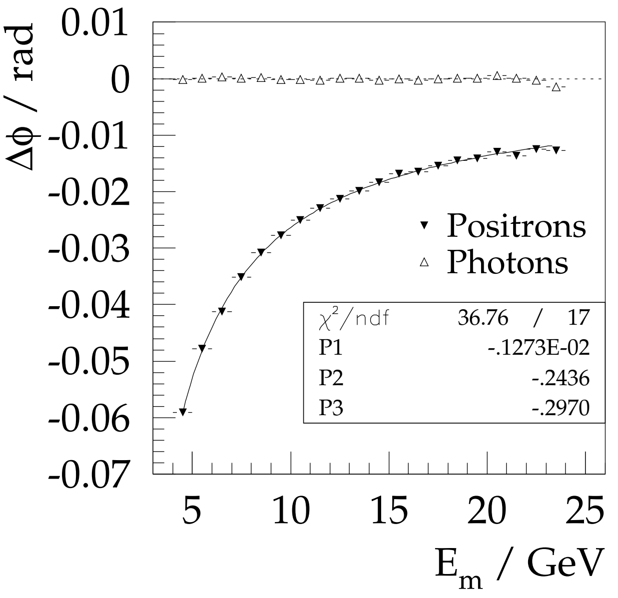

Figure 4.4: *Correction of the magnetic field influence on the positron ϕ measurement. Shown is the difference between the reconstructed and generated azimuthal angle as a function of particle energy in the simulation. Closed triangles depict positrons, while open triangles denote photons. The solid line displays the hyperbolic fit used for the correction.*

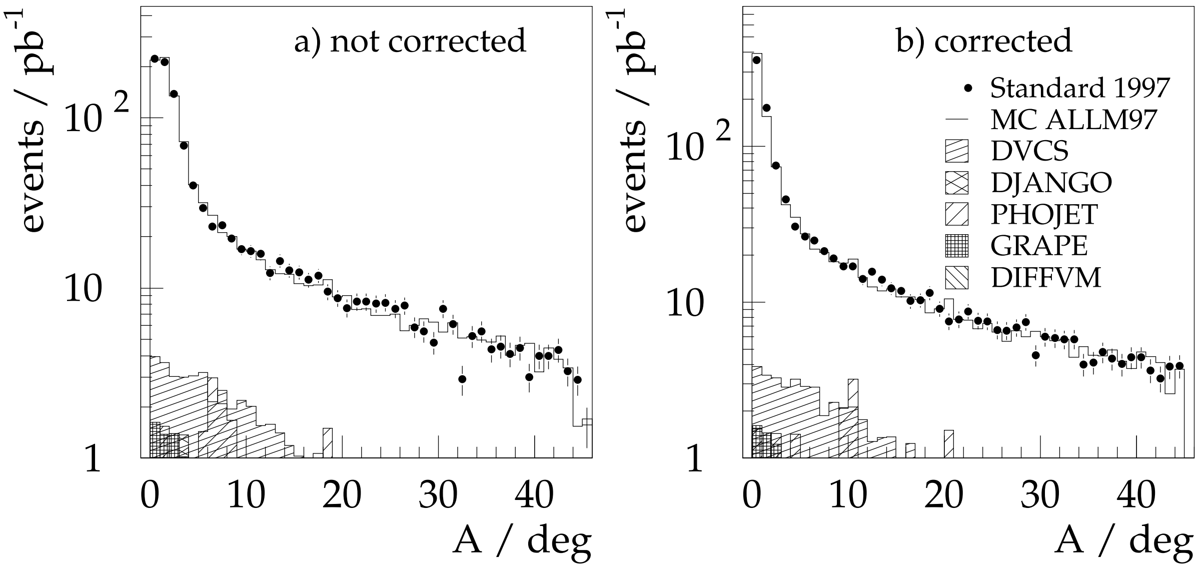

Figure 4.5: *Acoplanarity of two SpaCal clusters before and after the correction of the magnetic field effect. Shown are data of the standard 1997 sample (closed circles), COMPTON simulation with all background contributions added (solid histogram) and all simulated background sources (hatched histograms).*

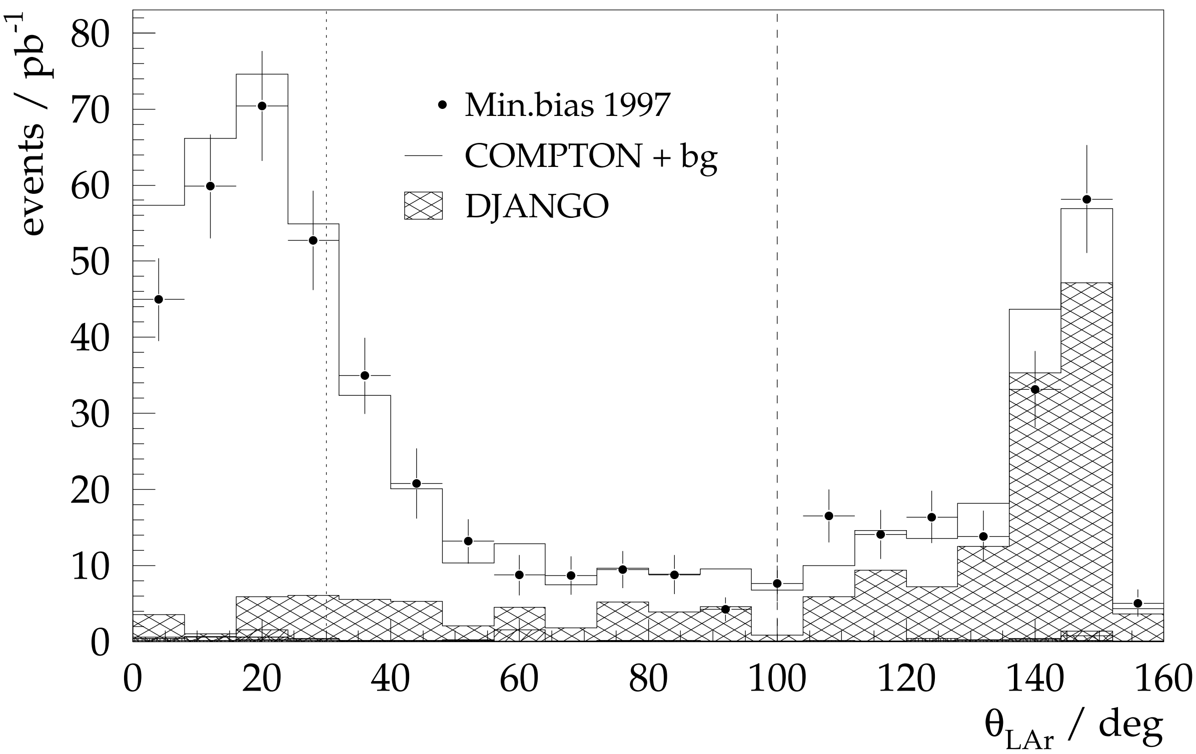

Figure 4.6: *Maximum polar angle of the LAr cluster in the data and the simulation. Only events with* $\theta_{\mathrm{LAr}} > 0$ *are depicted. Shown are data of the minimum bias 1997 sample (closed circle), COMPTON simulation with all background contributions added (solid histogram) and all simulated background sources (hatched histograms). In case of DJANGO the not renormalised distribution is depicted. The dashed line illustrates the cut imposed in the minimum bias event sample, while the dotted line denotes the limit set in the standard 1997 data.*

4.2.4 Characteristics of the Shower Profile

The transversal and longitudinal shapes of SpaCal showers provide a good possibility for distinguishing between electrons or photons and hadrons, since electrons and photons produce in average more compact showers than hadrons. Although the DIS background with a jet detected in the SpaCal is strongly suppressed by the requirements described above, the cuts on cluster properties allow us to eliminate also such events, in which several particles produce one common cluster, or events with only one hadron registered in the detector. The diffractive production of ρ mesons decaying into a $\pi^+\pi^-$ pair is a particular example of events, which can fall into one of these categories.

The characteristic measure of the lateral shower spread is the second moment, which is often given in H1 analyses by the *linear cluster radius*:

$$\mathrm{ECRA}_{\mathrm{lin}} = \frac{1}{E_{\mathrm{cl}}} \sum_i E_i \sqrt{(x_i - \hat{x})^2 + (y_i - \hat{y})^2} \tag{4.10}$$

with the summation performed over all cells in the cluster, and where x_i, y_i, E_i are cell coordinates and energies, and $\hat{x}$, $\hat{y}$, E_{cl} are the coordinates of the cluster centre of gravity (CoG) and the cluster energy, respectively.

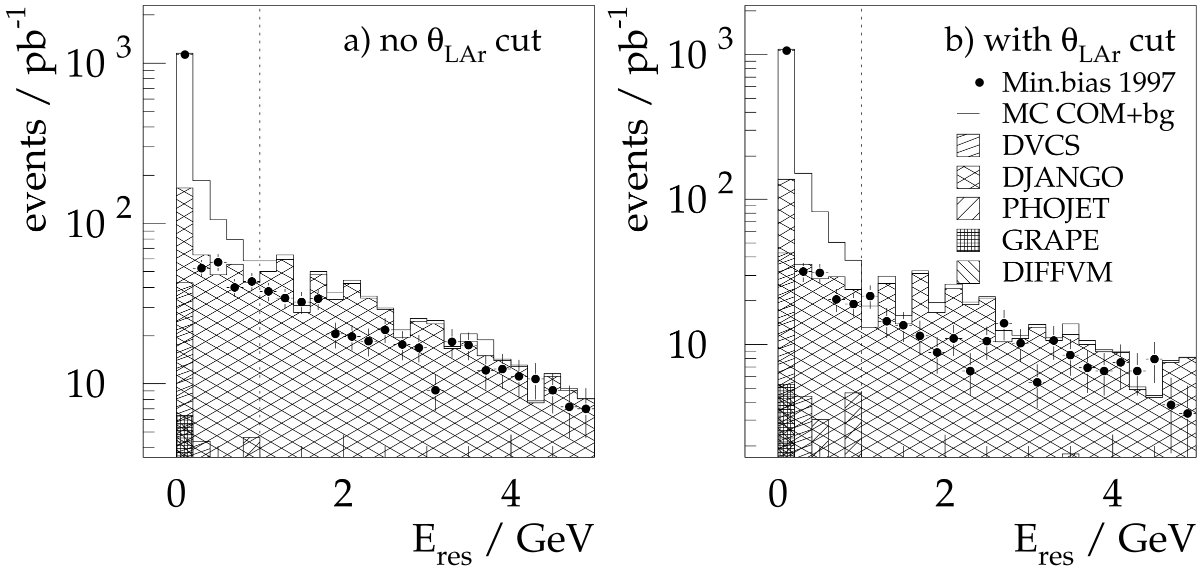

Figure 4.7: *Residual energy in the e.m. SpaCal. Shown are data of the minimum bias 1997 sample (closed circle), COMPTON simulation with all background contributions added (solid histogram) and all simulated background sources (hatched histograms). The not renormalised DJANGO contribution is depicted.*

In order to examine the quality of the shower profile simulation, the real and simulated $\mathrm{ECRA}_{\mathrm{lin}}$ distributions have been compared in the samples of elastic QEDC events, in which hadronic backgrounds are negligible. These distributions are displayed in fig. 4.8 a, where it is visible that the simulated profiles are in average narrower than the real ones. It is furthermore found that the reason for that is the limited performance of the H1 fast shower parameterisation package employed for the simulation of electromagnetic showers. In a special simulation, in which the complete GEANT running was enabled in the e.m. SpaCal[1], a very good reproduction of the real profile width is observed, see fig. 4.8 b.

Furthermore, it was shown in [gla98] that the linear cluster radius significantly depends on the particle impact point. To be specific, strong $\mathrm{ECRA}_{\mathrm{lin}}$ variations are observed between clusters with the centre of gravity reconstructed near the cell centre and those with the CoG at the cell edges. As an alternative measure the logarithmic cluster radius [awe92] was used in recent DIS analyses and also in this work, which is given by the expression

$$\mathrm{ECRA}_{\mathrm{log}} = \sqrt{\frac{\sum_i w_i[(x_i - \hat{x})^2 + (y_i - \hat{y})^2]}{\sum_i w_i}}\,, \tag{4.11}$$

where the weight factors are computed as

$$w_i = \max\left(0, W_0 + \ln\frac{E_i}{E_{\mathrm{cl}}}\right) \tag{4.12}$$

with W_0 being a cutoff parameter.

The difference between real and simulated profiles remains, of course, also in case of the logarithmic weighting, but it can be corrected for by applying different W_0 values for the calcula-

[1]This simulation consumes approx. 30 times more CPU time than a standard one.

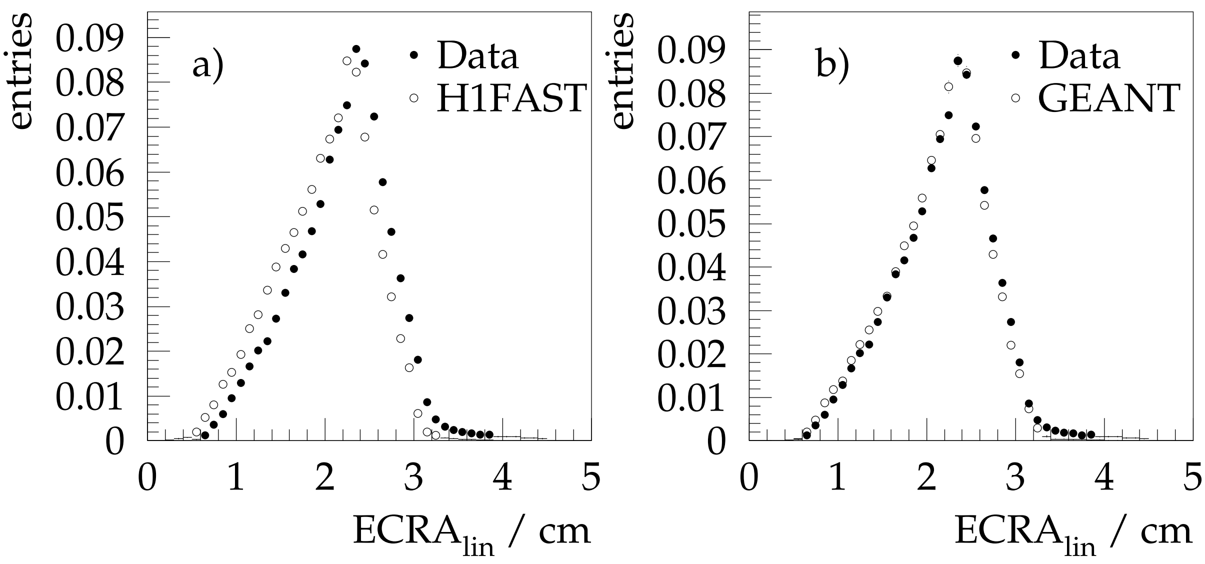

Figure 4.8: *SpaCal linear cluster radius in real and simulated elastic events. The simulation has been performed using a) the H1FAST and b) the GEANT package. Histograms are normalised so as to have the equal total contents.*

tion in data and MC simulation. As proposed in [gla98] the cutoff parameter is set to 4.85 in real events and 5.05 in simulated ones.

The ECRA$_{\text{log}}$ distributions for the hottest and the second hottest SpaCal cluster are presented in fig. 4.9. A reasonable agreement between the real and simulated radii, computed with different cutoff values, is visible. Furthermore one notices somewhat larger values for the second cluster compared to the first one. This effect reflects actually a dependence of the ECRA variable on the impact angle, namely, the higher the scattering angle (with respect to the electron beam direction) the bigger the cluster radius. The second hottest cluster in a typical QEDC event is reconstructed at a higher scattering angle than the hottest one.

The usual limit applied in H1 DIS measurements to separate the scattered electron from the hadronic background is ECRA$_{\text{log}} < 4\,$cm. In this analysis a more conservative cut at 4.5 cm is imposed, since the hadronic background is already suppressed to a large extent by the cuts on θ_{Lar} and E_{res}.

In addition to the cluster radius cut, the limit of E_{had} is imposed to reject hadronic showers. While electron and photon showers are completely absorbed in the e.m. SpaCal, hadrons produce showers of much bigger longitudinal size, since the nuclear interaction length is much larger than the electromagnetic one. A detection of energy behind the e.m. cluster is thus a sign of hadronic origin of the shower. The efficiency of the E_{had} cut has been studied in particular in [poe00] and found to be more than 99.5%.

4.2.5 Basic Fiducial Cuts

Several fiducial cuts are applied in the basic event selection in order to exclude inefficient areas of the detector components used for the measurement. The limits are imposed on the xy coordinates of each of the two particles in the backward region in the plane $z = -161.5\,$cm, which is the average z coordinate of a cluster centre of gravity in the electromagnetic SpaCal. An event is rejected if at least one of the particles falls into the excluded area. The following

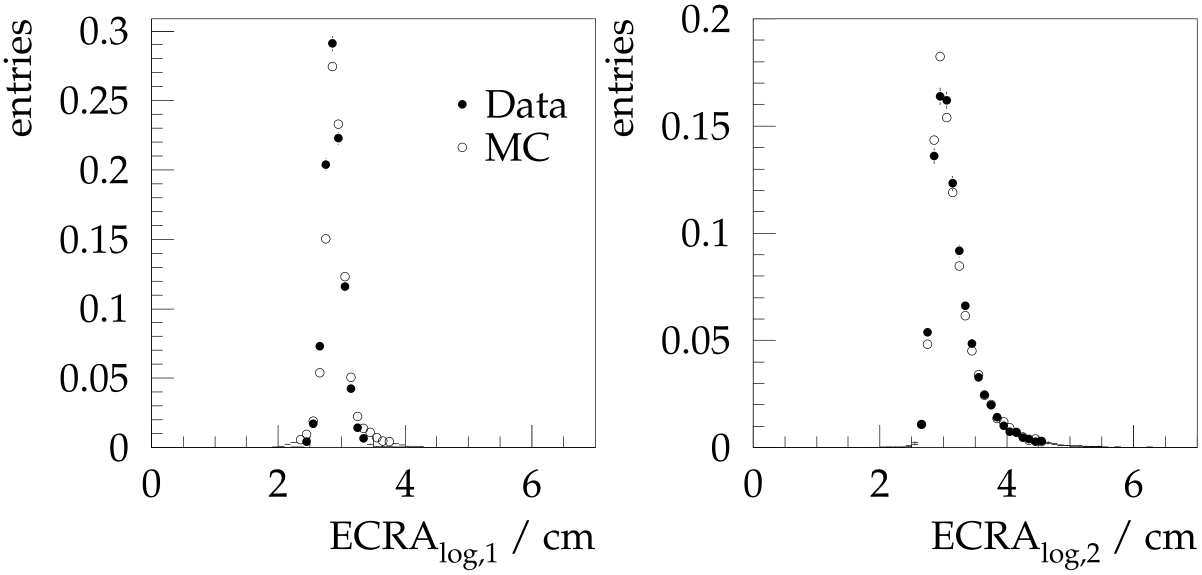

Figure 4.9: *Logarithmic cluster radius of the first and second SpaCal cluster in real and simulated elastic events. Histograms are normalised so as to have equal total contents.*

regions have been excluded:

- $r < 9$ cm or $r > 75$ cm — SpaCal and BDC acceptance limits;
- -33.5 cm $< x <$ -27.5 cm and 35.5 cm $< y <$ 41.5 cm — a broken cell in the e.m. SpaCal;
- -9.5 cm $< x <$ 9.5 cm and -5.5 cm $< y <$ 5.5 cm — a region of abnormally high trigger rate presumably induced by synchrotron radiation ("hot spot");
- 30 cm $< x <$ 42.5 cm and -42.5 cm $< y <$ 30 cm — an inefficient module in the e.m. SpaCal.

An additional geometrical cut is imposed to ensure high trigger efficiency in the minimum bias run range, as described in paragraph 4.3.2. Furthermore, fiducial cuts caused by the BST and CIP acceptance limits are applied in the electron/photon identification procedure. They will be discussed in paragraph 4.4.4.

4.3 Trigger Performance

The two data sets employed in the present analysis differ in the trigger requirements applied. Below the relevant trigger settings for each run range are described together with the corresponding data treatment in the course of the analysis presented.

4.3.1 Standard Trigger Conditions

In the standard trigger settings a special chain was used to record QED Compton events. Unfortunately, the physics potential of the inelastic QEDC scattering (in particular, the possibility of an F_2 analysis), was not considered in the development of the trigger. The primary purpose of triggering QEDC events was to select the elastic channel, which is used for various detector studies. For this reason a fraction of the inelastic events was lost during the data taking on the first and fourth trigger level. Nevertheless, an elaborated correction procedure allowed us to recover the original event rate.

Level 1

On the first level the QEDC subtrigger s_{13} is used as a master subtrigger, and events selected by other subtriggers but rejected by s_{13} are not employed for the cross section measurement. In the trigger phases 2 – 4 the s_{13} was not prescaled. This subtrigger is given by the following combination of trigger elements:

$$\mathrm{s}_{13} = (\mathrm{IET} > 2 \vee \mathrm{IET}_3^{\mathrm{Cen}}) \wedge \neg \mathrm{DCR}\Phi_{\mathrm{Tc}} \wedge \mathrm{ToF}_{\mathrm{E2}}^{\mathrm{eSp}} \wedge \mathrm{GLOBAL} \tag{4.13}$$

with

$$\begin{aligned} \mathrm{GLOBAL} = & \neg \mathrm{AToF}_{\mathrm{E1}}^{\mathrm{hSp}} \wedge \neg \mathrm{BToF}_{\mathrm{BG}} \\ & \wedge \neg \mathrm{VETO}_{\mathrm{BG}}^{\mathrm{inner}} \wedge \neg \mathrm{VETO}_{\mathrm{BG}}^{\mathrm{outer}} \\ & \wedge (\mathrm{FToF}_{\mathrm{IA}} \vee \neg \mathrm{FToF}_{\mathrm{BG}}) \ , \end{aligned} \tag{4.14}$$

where the trigger elements are defined as:

- $\mathrm{IET} > 2$ – Energy deposition detected by the inclusive electron trigger in the outer e.m. SpaCal is above the energy threshold 2 (see table 4.2);
- $\mathrm{IET}_3^{\mathrm{Cen}}$ – Energy deposition detected by the inclusive electron trigger in the central part of e.m. SpaCal is above the energy threshold 2;
- $\mathrm{ToF}_{\mathrm{E2}}^{\mathrm{eSp}}$ – Total energy deposition in the e.m. SpaCal within the interaction time window is above the second energy threshold which has been set to 12 GeV;
- $\mathrm{DCR}\Phi_{\mathrm{Tc}}$ – at least three tracks are reconstructed by the digital chamber $r\phi$ (dc$r\phi$) trigger;
- $\mathrm{AToF}_{\mathrm{E1}}^{\mathrm{hSp}}$ – Signal in the hadronic SpaCal is within the background time window;
- $\mathrm{BToF}_{\mathrm{BG}}$ – Signal in the backward ToF counters is within the background time window;
- $\mathrm{VETO}_{\mathrm{BG}}^{\mathrm{inner}}$ – Background signal is detected in the inner VETO wall;
- $\mathrm{VETO}_{\mathrm{BG}}^{\mathrm{outer}}$ – Background signal is detected in the outer VETO wall;
- $\mathrm{FToF}_{\mathrm{IA}}$ – Signal in the forward ToF counters is within the interaction time window;
- $\mathrm{FToF}_{\mathrm{BG}}$ – Signal in the forward ToF counters is within the background time window.

Previous studies have found the total losses caused by the GLOBAL condition to be far below 1% [hei99, wis98].

In order to eliminate the hot spot rate, the inclusive electron trigger (IET) elements are defined separately for the central and for the outer part of the e.m. SpaCal. In the standard data taking inclusive DIS subtriggers contain only the outer IET. On the contrary, the QEDC subtrigger involves both IET cards and thus selects events with clusters in the central SpaCal region. Therefore the inclusive DIS triggers have not been used for the QEDC event selection.

The efficiency ϵ_{IET} of the IET elements for all energy thresholds has been studied in several DIS analyses as a function of the electron cluster energy and shown a rather sharp rise at the

Table 4.2: *Energy thresholds for the inclusive electron trigger.*

Trigger elements	Standard running threshold, GeV	Minimum bias running threshold, GeV
IET > 0 and IET$_1^{\rm Cen}$	0.5	2
IET > 1 and IET$_2^{\rm Cen}$	2	5
IET > 2 and IET$_3^{\rm Cen}$	6	10

threshold value, such that at approx. 2 GeV above the threshold it achieves more than 99%. In this work the efficiency correction function from the ISR analysis [işs01] is employed. One should however note, that since two SpaCal clusters are detected by the IET trigger in a QEDC event, the resulting efficiency is given by

$$\epsilon_{\rm IET,QEDC} = \epsilon_{\rm IET}(E_1) + \epsilon_{\rm IET}(E_2) - \epsilon_{\rm IET}(E_1)\epsilon_{\rm IET}(E_2) \tag{4.15}$$

and is thus nearly 100%, considering the QEDC event selection requirements for E_1 and E_2.

The efficiency of the ToF$_{\rm E2}^{\rm eSp}$ element has been studied on the subsample of events selected by the inclusive DIS subtrigger s_0, which does not include this element. The overall efficiency is found to be (98.7 ± 0.2)%. No dependence of the efficiency on the total energy in the e.m. SpaCal is observed.

The DCR$\Phi_{\rm Tc}$ trigger element [ber95] fires in case at least three tracks with transverse momentum $p_t > 420$ MeV have been found by the dc$r\phi$ trigger in an event. Such events are thus rejected by the subtrigger s_{13}. The trigger searches for tracks by comparing signals in the $r\phi$ plane with programmed masks, called *roads*. Each road requires, in particular, a hit in the outer reference layer located at the radius 58.72 cm in the CJC2. A particle going from the nominal interaction point and making a hit in the CJC at this radius must have at least a polar angle of about 30°. The efficiency of the DCR$\Phi_{\rm Tc}$ has therefore been studied in dependence of the hadronic angular distribution. As a reference hadron angle in an event the maximum polar angle $\theta_{\rm LAr}$ of the LAr clusters is employed. The efficiency is determined using the minimum bias data, in which all inelastic QEDC events have been selected by inclusive DIS triggers (see paragraph 4.3.2). In fig. 4.10 a the DCR$\Phi_{\rm Tc}$ efficiency is shown as a function of $\theta_{\rm LAr}$. This distribution is fitted by a Fermi function

$$\epsilon_c(\theta) = \frac{\epsilon_{\rm max}}{1 + \exp\left[-\frac{\theta_{\rm LAr} - \theta_0}{\Delta}\right]} \tag{4.16}$$

with $\epsilon_{\rm max} = 0.424$, $\Delta = 7.30°$ and $\theta_0 = 40.47°$. The selected QEDC events in the standard 1997 run range are then reweighted by a factor $1/(1 - \epsilon_c)$. In order to avoid large statistical uncertainties arising from event rejection at high θ, a cut $\theta_{\rm LAr} < 30°$ is imposed in the standard 1997 data treatment. The cut value is depicted by a dotted line in fig. 4.10 a.

The efficiency correction procedure has been cross-checked by considering the DCR$\Phi_{\rm Ta}$ trigger element, that demands only one $r\phi$ trigger track. Its efficiency as a function of $\theta_{\rm LAr}$ is displayed in fig. 4.10 b. A similar fit by a Fermi function yields: $\epsilon_{\rm max} = 0.743$, $\Delta = 7.85°$ and $\theta_0 = 33.79°$. One can see that the distributions in fig. a and b agree very well under the simple assumption that at high $\theta_{\rm LAr}$ the efficiencies of the reconstruction of three tracks ϵ_c and one track ϵ_a are related as $\epsilon_c \approx \epsilon_a^3$.

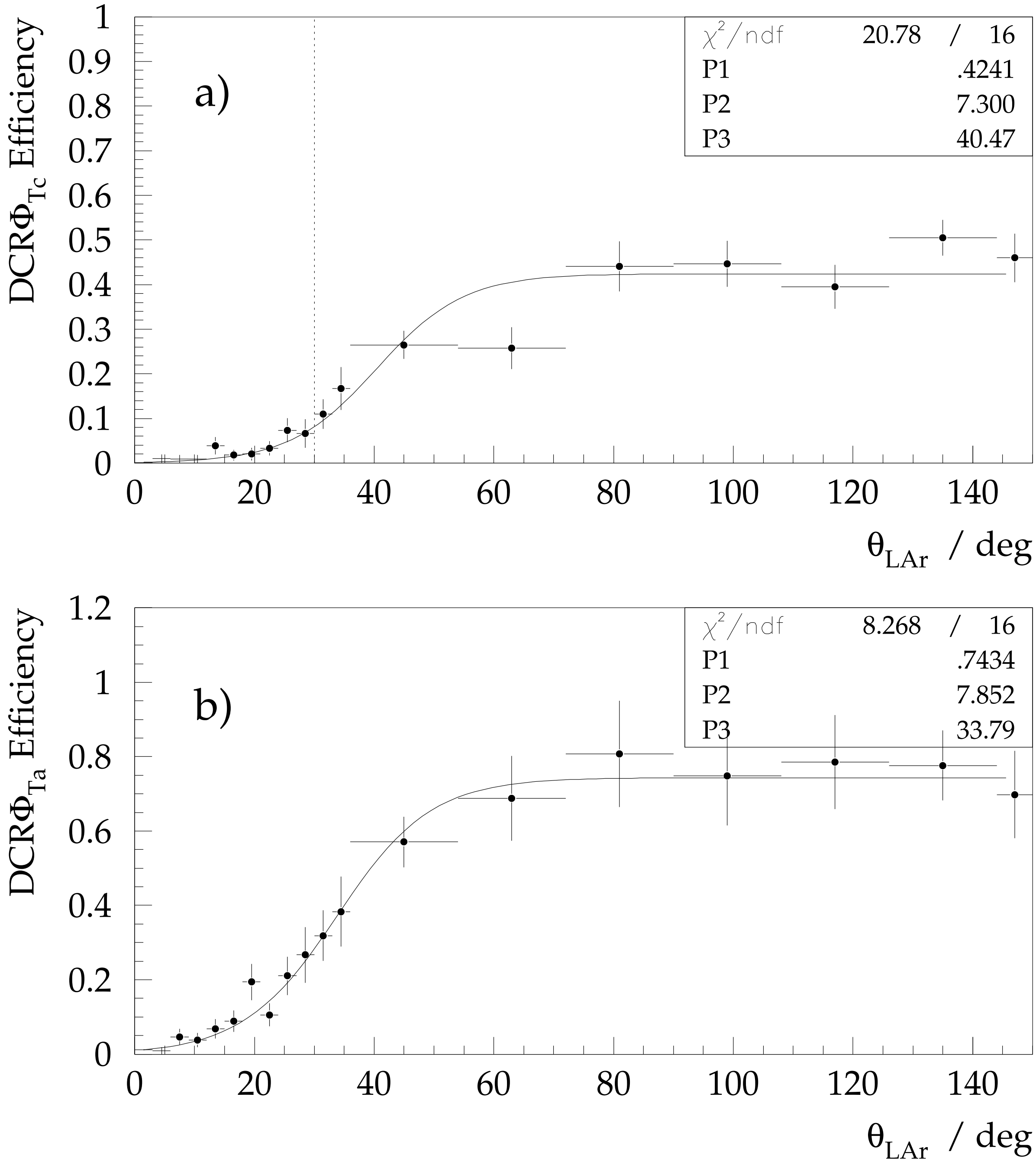

Figure 4.10: *Efficiency of the* DCRΦ *trigger as a function of the LAr cluster maximum polar angle: a)* DCRΦ_{Tc} *element, b)* DCRΦ_{Ta} *element. The solid lines illustrate the fit functions given by eq. 4.16. The dashed line demonstrates the* θ_{LAr} *cut applied in the analysis chain.*

Level 2

On the second level the topological trigger element t_{18} [biz92] is employed to select QED Compton events. This trigger searches for a specific QEDC event geometry — two energy depositions in the e.m. SpaCal with opposite ϕ coordinates.

The t_{18} efficiency has been studied in events collected in special L2+L4 transparent runs, in which the standard L2 and L4 event selection is performed, but all events, including those rejected on one or both trigger levels, are recorded by the data acquisition system. Out of 528 events fulfilling the basic QEDC selection criteria in these runs only one event was not selected by the L2 t_{18} element. The L2 efficiency is thus estimated to be (99.8 ± 0.2) %.

Level 4

The QEDC event selection on the fourth trigger level, as applied during the standard 1997 data taking period, involves the following criteria:

$$\begin{gathered} E_1 > 7\,\mathrm{GeV}\,, \qquad E_2 > 3.5\,\mathrm{GeV}\,, \\ 15\,\mathrm{GeV} < E_1 + E_2 < 32\,\mathrm{GeV}\,, \\ \mathrm{ECRA}_{\mathrm{lin},1} < 4\,\mathrm{cm}\,, \qquad \mathrm{ECRA}_{\mathrm{lin},2} < 4\,\mathrm{cm}\,, \\ \mathrm{s}_{13} \;+\; \mathrm{LOWMULT}: \;\#\,\mathrm{CJC\ tracks} \leq 4\,. \end{gathered} \tag{4.17}$$

All of these cuts except for the last one are superseeded by stronger limits in the analysis chain, so that no additional losses should appear. The QEDC data quality checks [sta97] have ensured a correct event processing in the L4 filter farm. A 0.5% uncertainty of the L4 event selection in the SpaCal has been determined in the inclusive DIS analysis [h100].

Similar to the $\neg\mathrm{DCR}\Phi_{\mathrm{Tc}}$ condition the low multiplicity requirement LOWMULT was applied in order to suppress the inelastic QEDC channel. It is corrected for in the same way as it is done for the level 1 selection. The efficiency is determined as a function of θ_{LAr} using events collected by the L4 inclusive DIS statements, which depend only on the SpaCal cluster energy. The efficiency distribution is depicted in fig. 4.11 together with the Fermi function fit with parameters $\epsilon_{\max} = 0.346$, $\Delta = 8.50^\circ$ and $\theta_0 = 32.82^\circ$.

4.3.2 Minimum Bias Trigger Conditions

The trigger settings for the minimum bias running [gkw98] allowed a collection of inclusive DIS events also in the central region of the SpaCal. QED Compton events were thus recorded as a subset of the inclusive DIS data. The bulk of the QEDC data was collected by the first level subtrigger s_0 composed of the following trigger elements:

$$\mathrm{s}_0 = (\mathrm{IET} > 1 \vee \mathrm{IET}_2^{\mathrm{Cen}}) \wedge \mathrm{GLOBAL}\,, \tag{4.18}$$

where higher IET energy thresholds were set for this run range (see table 4.2). This subtrigger was validated on the second trigger level, where an additional fiducial cut of 10 cm on the radial position was imposed.

The events with energy depositions detected at very low radii, in which the second level validation failed, were selected by the subtrigger s_3 defined as:

$$\mathrm{s}_3 = (\mathrm{IET} > 2 \vee \mathrm{IET}_3^{\mathrm{Cen}}) \wedge \mathrm{GLOBAL}\,. \tag{4.19}$$

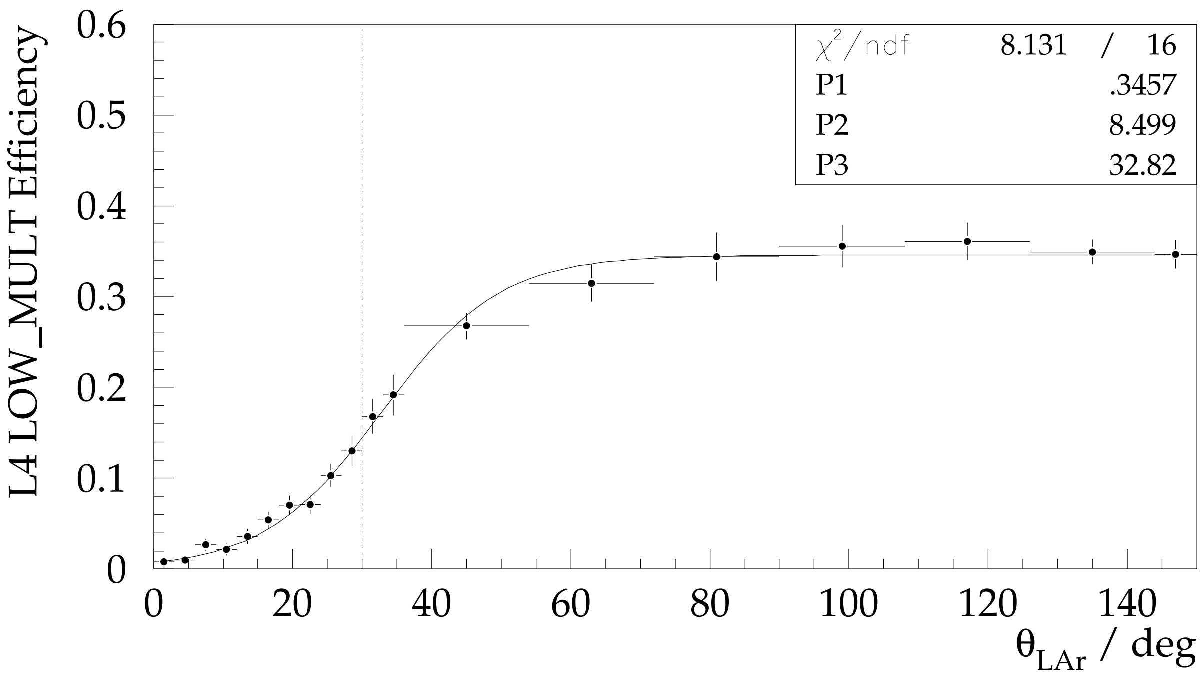

Figure 4.11: *Efficiency of the L4 LOWMULT condition as a function of the LAr cluster maximum polar angle. The solid line illustrates the fit function given by eq. 4.16. The dashed line demonstrates the θ_{LAr} limit applied in the analysis chain.*

To avoid uncontrollable losses, a fiducial cut is applied in the analysis chain which demands that at least one of the particles with an energy above 10.5 GeV is reconstructed outside the square: -10.5 cm $< xy <$ 10.5 cm in the plane $z = -161.5$ cm.

The subtriggers involved were downscaled by an automatic procedure [sc99], that adjusts prescaling factors depending on the beam currents and background rates in order to provide an optimum use of the delivered luminosity. A combined event weight, necessary for simultaneous use of two subtriggers with different downscaling factors, is computed as [egl97]:

$$w = \left[1 - \left(1 - \frac{r_0}{p_0}\right)\left(1 - \frac{r_3}{p_3}\right)\right]^{-1}, \tag{4.20}$$

where

$$r_0, r_3 = \begin{cases} 1 & \text{if the raw subtrigger } s_0,\, s_3 \text{ is set in the event,} \\ 0 & \text{otherwise,} \end{cases} \tag{4.21}$$

and p_0, p_3 are the prescaling factors of the subtriggers in the run in which the event was taken.

The events triggered by s_0 or s_3 were collected by the L4 filter farm if at least one of the SpaCal clusters met the following DIS selection requirements:

$$Q^2 > 0.5\,\mathrm{GeV}^2, \qquad E > 4\,\mathrm{GeV}, \qquad \mathrm{ECRA_{lin}} < 4\,\mathrm{cm}, \tag{4.22}$$

where Q^2 was calculated assuming the given cluster to be the scattered electron. These criteria are automatically fulfilled after the QEDC event selection in the analysis chain. The correctness of the L4 event processing has been justified in the data quality checks [wal97].

4.4 Particle Identification and Vertex Reconstruction

The electron/photon identification by means of the BST, the CIP and the CJC is performed in all events fulfilling the basic selection criteria. Events, in which the validation procedure fails are rejected from the further analysis. These are events in which both particles are identified either as electrons or as photons.

4.4.1 Usage of BST

The Backward Silicon Tracker is employed for the electron identification among particles detected in the inner part of the SpaCal. The validation procedure has been developed in [ark00] and was first employed for the F_2 measurement based on the low Q^2 DIS data 1997. It consists in the search for a track in the BST unambiguously linked to the SpaCal cluster.

The algorithmus can proceed in two modes depending on whether a well reconstructed CTD vertex exists. In [ark00] it is assured that both methods yield nearly identical efficiency and resolution. Since in QEDC events there is usually no central vertex or it is reconstructed with an unacceptably high uncertainty, the mode without prior knowledge of the vertex position has been forced. The track finding procedure in this mode is schematically depicted in fig. 4.12 and elucidated in the figure caption. It is based on the "two out of four" concept, *i.e.*, hits building the track must be found in at least two out of four BST planes. In case of several reconstructed tracks, they are first examined to have polar angles in the range $90° < \theta < 180°$ and then the one with a maximum number of assigned hits is chosen.

If a track is found, it is extrapolated forward in the rz plane until it crosses the electron beam line. The intersection point determines the reconstructed position of the interaction vertex.

4.4.2 Usage of CIP

The electron validation and vertex reconstruction by means of the Central Inner Proportional chamber has been developed in [pm93] for the application in DIS analyses. The original package includes two different procedures, one for the electron validation in case the central vertex exists and one for the CIP vertex finding. Since most of QEDC events have no central vertex, only the vertex reconstruction procedure is employed and the particle, for which the CIP vertex has been found, is considered to be the scattered electron.

The reconstruction is performed as shown in fig. 4.13. As an input the position of a BDC track is provided. The signals in the pads of the inner and outer CIP layer are searched for within a ϕ corridor around the given BDC track. Two adjacent or overlapping constellations of adjacent pads, one in each layer, are required to form a cluster.

In case several double layer clusters are found in the relevant ϕ sector the most backward is selected. There is normally no ambiguity in the cluster selection for QEDC events since the hadronic final state is either absent or concentrated in the forward region of the detector, so that the track density is relatively small. If there is no BDC track for the given SpaCal cluster or no CIP cluster has been found for the given BDC track, the procedure is performed with the centre of gravity of the SpaCal cluster as an input.

The vertex z coordinate is determined by prolonging the straight line, that connects the centre of gravity of the CIP cluster and the BDC track (SpaCal cluster), so as to intersect the beam line.

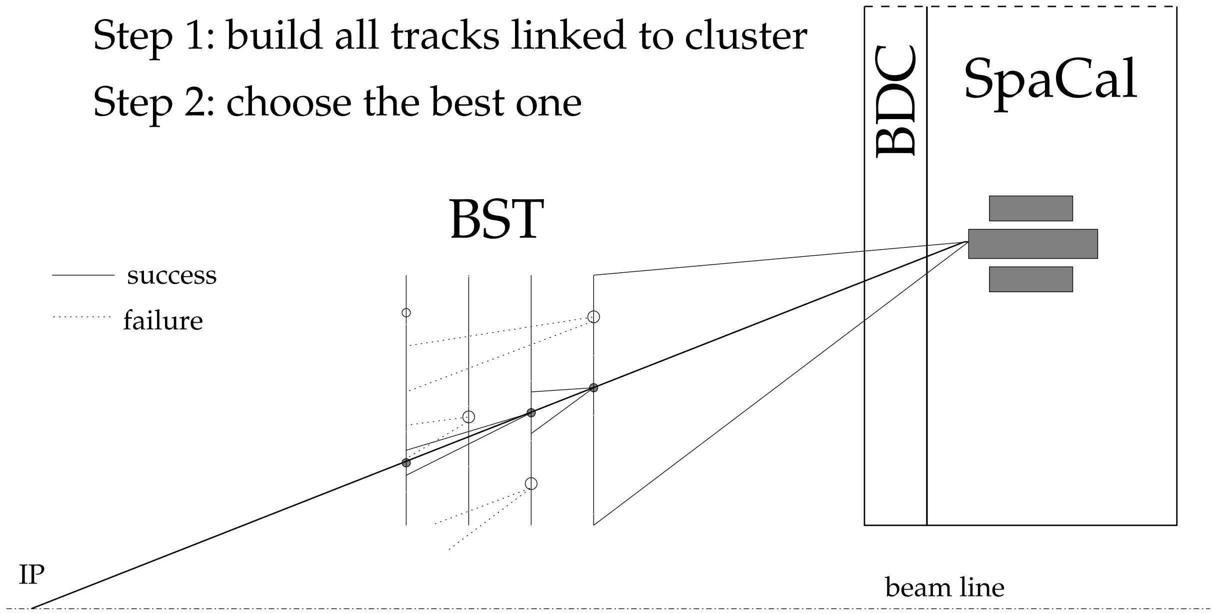

Figure 4.12: *Electron validation and vertex reconstruction procedure using BST [ark00]. The open circles in the BST represent rejected noise hits. The closed ones correspond to hits combined into the electron track, as indicated by the line connecting these hits and extrapolated forward to the interaction point and backwards to the SpaCal cluster. The opening angles denote the search corridors for the BST hits. The solid lines demonstrate the successful search, while the dashed lines depict failed searches.*

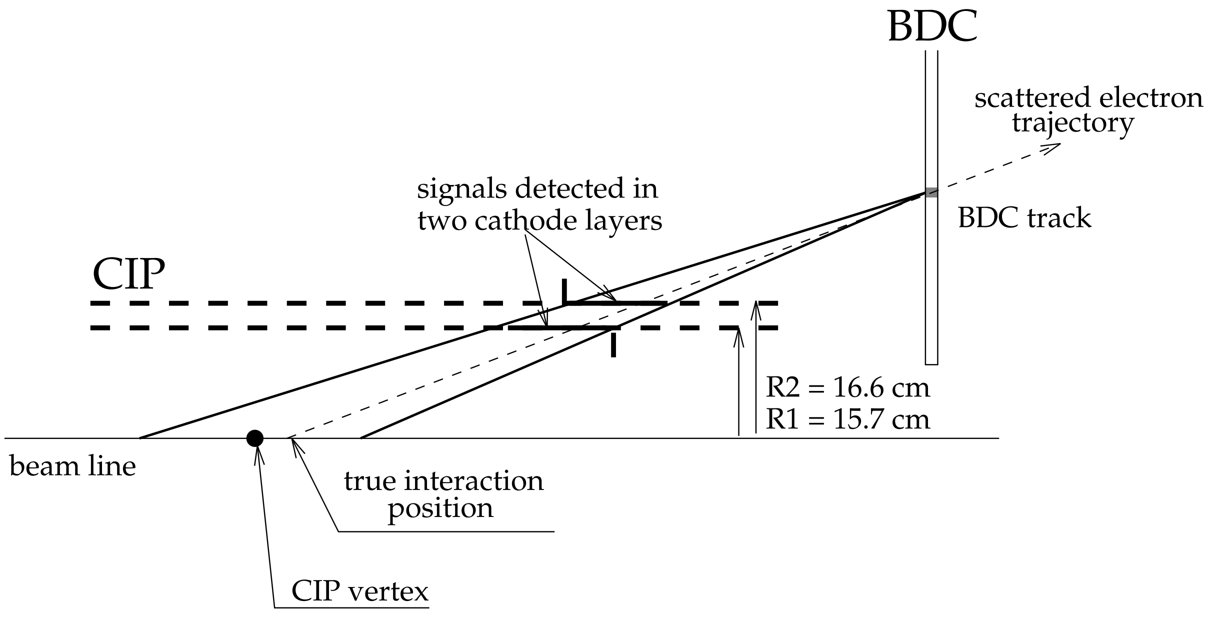

Figure 4.13: *Vertex reconstruction using the CIP and the backward detectors [pan96].*

4.4.3 Usage of CJC

The electron validation by means of CJC [gla98] is performed by linking a CJC track to a SpaCal cluster. Each track pointing to the backward direction is extrapolated up to the xy plane given by the cluster z coordinate. The electron validation is successful if the distance between the cluster and the track in this plane is smaller than a given value.

The CJC acceptance limits the applicability of this procedure to the outer SpaCal region. The clusters validated by the CJC are reconstructed mostly at $r \gtrsim 45\,\mathrm{cm}$. This region is however completely within the CIP acceptance. Due to the very high efficiency of the CIP procedure in 1997 the additional effect of the CJC appeared to be negligible. Therefore no further study of the CJC validation efficiency had to be performed.

4.4.4 Limits of BST and CIP acceptance

Additional fiducial cuts on the position of both particles in the backward region are applied in order to ensure that the acceptance of the BST and the CIP is the same in the data and the MC simulation. Otherwise siginificant discrepancies between the real and the simulated efficiencies may arise on the acceptance boundaries. It is especially important to control the acceptance effects at lower radial boundaries of the chambers due to the cross section rising rapidly towards low radii. Thus, if the electron/photon identification has succeeded in an event and the vertex is reconstructed, the trajectory of each particle is checked to fall into the acceptance of either the BST or the CIP.

For a correct BST acceptance description the limitations of the radial position of a track are imposed, similar to those proposed in [ark00]. The cuts

$$R_3^{\mathrm{BST}} > 5.95\,\mathrm{cm}\,, \qquad R_2^{\mathrm{BST}} < 12.0\,\mathrm{cm} \tag{4.23}$$

are applied at points R_2^{BST} and R_3^{BST}, where the particle trajectory intersects the second and the third planes of the detector, respectively. Within these limits the particle crosses at least two BST planes, which is demanded for a successful BST track reconstruction.

The limit of the CIP acceptance is defined as

$$R^{\mathrm{CIP}} > 16.6\,\mathrm{cm}\,, \tag{4.24}$$

where R^{CIP} is the radial coordinate of particle trajectory at $z_{\mathrm{last}} = -110.675\,\mathrm{cm}$. Here 16.6 cm is the radius of the outer CIP layer and z_{last} is the z coordiante of the centre of the last CIP pad on the backward side. This cut ensures that the particle traverses both the inner and the outer CIP layer, and thus a CIP cluster can be built.

Additional fiducial cuts are usually applied also in case there were dead regions in a detector. In the 1997 data taking there was a broken sector in the $+z$ region of the CIP chamber [ned00]. The $+z$ half of the chamber is situated in the range: -3 cm $< z <$ 106.5 cm. Fortunately, after imposing the cut on the vertex z coordinate this CIP region falls out of the acceptance zone required for the SpaCal cluster or the BDC track validation, so that additional fiducial cuts are unnecessary.

4.4.5 Efficiency of Electron Identification

The local efficiency of the electron measurement in a tracking chamber is generally determined in a subsample of events, in which some criteria independent of the chamber performance are fulfilled, which guarantee that the particle crossing the chamber at a given trajectory is really an electron. Since there are two particles, an electron and a photon, in the final state of the QED Compton process, the efficiency of the electron validation cannot be directly determined in QEDC events. The best way to study the efficiency is obviously provided by DIS events.

The efficiency of the BST electron validation in the minimum bias 1997 data has been investigated in the framework of the DIS low Q^2 analysis [ark00]. That very extensive study embraced several issues. At first, the "internal" efficiencies of hit recognition in all 64 subdetectors $\epsilon_{\rm int}$ were determined. The average efficiency was found to be about 92%. With the "two-out-of-four" procedure this value leads to an "external" efficiency of almost 100% in the angular region of common acceptance of all four planes, according to the binomial expression:

$$\epsilon_{\rm ext} = \epsilon_{\rm int}^4 + 4\epsilon_{\rm int}^3(1-\epsilon_{\rm int}) + 6\epsilon_{\rm int}^2(1-\epsilon_{\rm int})^2 \ . \tag{4.25}$$

However, additional "coherent losses" of the order of 4% were found in the BST readout chain leading to a reduction of the external efficiency. They were estimated separately in the 16 ϕ sectors. Furthermore, a fine tuning of the efficiencies was performed due to several broken preamplifier chips. As a result of the study the correction factors were acquired which were then applied to simulated DIS events.

These corrections are also applied to the simulated QEDC events in the present chain of the minimum bias 1997 data analysis. All corrections are performed on the event by event basis in the analysis procedure. This approach involves rerunning of the electron finder over the resimulated MC events.

Unfortunately, a similar efficiency study in the standard 1997 data sample could not be done due to the constraints of the inclusive DIS triggers, which rejected DIS events in a significant part of the BST acceptance. Therefore the common BST "external" efficiency has been estimated in this work using elastic QED Compton events. As mentioned above in sect. 4.1 the average BST efficiency in the standard 1997 data was somewhat lower than at the end of the 1997 data taking. In order to simulate the lower validation rate, a common damping factor is added to the values describing coherent losses in the minimum bias data.

For the study of the efficiency the acoplanarity cut $A < 4^\circ$ is applied, after which the fraction of elastic events in the sample amounts to approx. 93%. This value was chosen with the aim of maximum purity of the sample, sacrificing to some extent the efficiency of the event selection. The common damping factor is applied to the simulated events in order to achieve an optimum agreement between the radial distributions of the electrons in the region of the BST acceptance. These distributions are depicted in fig. 4.14. The radial coordinate is calculated in the plane $z = -161.5$ cm, which is the average z coordinate of a cluster CoG in the SpaCal. The BST acceptance corresponds approximately to the radial range $10\,\text{cm} \lesssim r \lesssim 24\,\text{cm}$. A dip in the distributions at $r \approx 24$ cm arises from the BST and CIP acceptance limitations. The optimum agreement is achieved by minimising the value of χ^2 given by

$$\chi^2 = \sum_{\rm bins} \frac{(n_{\rm data} - n_{\rm MC})^2}{\sigma_{\rm data}^2 + \sigma_{\rm MC}^2} \ , \tag{4.26}$$

where the sum is performed over all $N_{\rm bins}$ bins between 10 and 24 cm with $n_{\rm data}$, $n_{\rm MC}$ being the bin contents in the data and MC histograms, respectively, and $\sigma_{\rm data}$, $\sigma_{\rm MC}$ representing their statistical uncertainties. The value for the damping factor has been found to amount to $(6 \pm 1)\%$. One should remark that this radial distribution can also be affected by the photon conversion (both in the BST and the CIP), because it leads to the rejection of events in which both particles

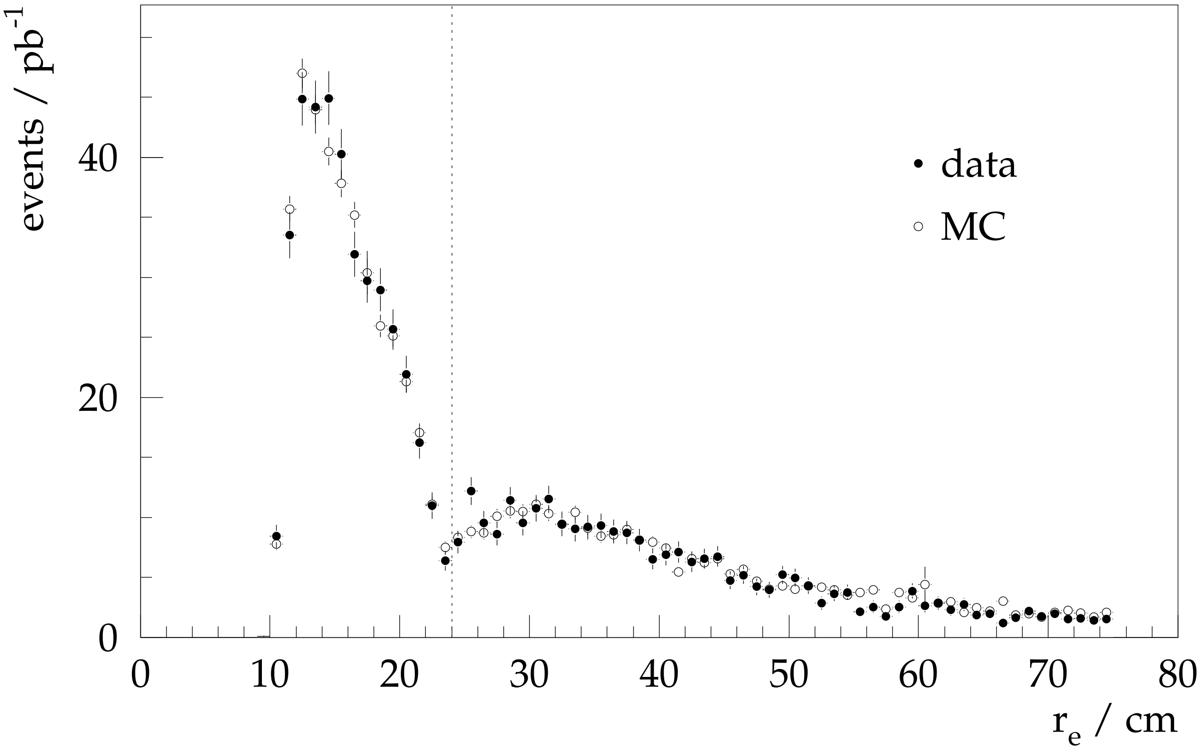

Figure 4.14: *Radial distribution of the scattered electrons in the plane $z = -161.5$ cm. The closed circle denote the data of the standard 1997 data sample, while the open circles depict the MC simulation with all background contributions added. The dotted line illustrates the average boundary between the BST and the CIP acceptance regions.*

are identified as electrons. Therefore this study was repeated several times together with the determination of the photon misidentification rate described in the following paragraph.

The efficiency of the CIP vertex reconstruction procedure for both the standard and the minimum bias 1997 data sample has been studied in the framework of the H1 DIS analyses as a function the electron's radial and azimuthal coordinates and energy. It was found to be higher than 98% in average both in the data and the simulation. The simulated and real efficiencies agree within 0.5%, so that no additional efficiency correction had to be performed.

4.4.6 Efficiency of Photon Identification

The photon identification is the operation opposite to the electron validation, namely, a particle is identified as a photon if it is anti-validated, *i.e.*, if no proper signal in the central chambers could be reconstructed for this particle. The issue of the photon identification is thus that of the wrong electron validation. Such misidentification can occur due to several reasons. The main factor is certainly the photon conversion into an electron–positron pair while passing through material of the beam tube and chamber walls. Another reason is electronic noise causing wrong hit reconstruction.

The photon misidentification rate has been determined using elastic QEDC events by counting the relative rate of the events, in which both particles were validated as electrons. The elastic selection is performed in order to reduce the uncertainty of dilepton background sources, such as J/ψ photoproduction and continuum dilepton production, whose elastic cross section is known better than the inelastic one. The elastic sample is selected by demanding that there was no cluster in the LAr calorimeter with an energy above 0.5 GeV and making a cut on the $e\gamma$ acoplanarity: $A < 8^\circ$.

An exact determination of the misidentifaction rate in a certain bin of a particular variable (like the radial coordinate of a particle) requires a selection of only such events in which both particles fall into the same bin. Otherwise a smearing of the differences between the bins appears, since in case both particles are validated as electrons there is no way to distinguish them and thus the photon conversion in one bin affects the rate in another bin. On the other hand, selecting events in which both particles have nearly the same radial coordinate leads to a significant reduction of the available statistics. In this study the misidentification rate is determined separately in two r regions, namely, for the BST and the CIP. Such splitting is necessary, since the two chambers may reveal significantly different noise levels. In each case only such events are selected in which both particles fall into the acceptance of the same chamber. The visible misidentification rate ρ is then defined via

$$\rho = \frac{\#\text{ events with both particles validated as an electron}}{\#\text{ events with at least one particle validated as an electron}} \,. \tag{4.27}$$

The radial and azimuthal ρ distributions for the BST in the data and the simulation are shown in the upper plots of fig. 4.15. As in paragraph 4.4.5 the radial coordinate is given in the plane $z = -161.5$ cm. One can see that the simulation significantly underestimates the data. The reason for this could not be clarified. One should also mention that the visible rate ρ differs from the actual rate κ due to the admixture of dilepton events. The fraction of the rate contributed by simulated dilepton events from the GRAPE and the DIFFVM J/ψ samples is also shown in fig. 4.15.

To produce these histograms, the radial and azimuthal coordinates of both particles in the event are plotted. One should note that an exact statement can only be made about the average rate shown by the dashed and dotted lines, since an accurate measurement in each r bin would require saving only such events in which both particles fall into the same r bin. Nevertheless it is still advantageous to calculate the correction factors bin by bin, because the differences between the bins at least partially reflect the real picture, and the bin-wise factors make a better estimation of the real rate than one common factor.

The correction procedure is performed as follows. All events are classified as either $e\gamma$ events (QEDC or DVCS) or dilepton ones, while other background contributions are negligible. All generated background samples are renormalised to have some common effective luminosity and so that the total number of selected real events be equal to that of the generated events. Furthermore the following quantities are introduced:
N_0 – # events with no signal in the chamber,
N_1 – # events with the electron validation for one particle,
N_2 – # events with both particles validated as electrons,
and this notation is used for real events, for generated $e\gamma$ events and for generated dilepton ones. The visible misidentification rates in data and simulation can then be written as

$$\rho^{\text{data}} = \frac{N_2^{\text{data}}}{N_1^{\text{data}} + N_2^{\text{data}}}\,, \qquad \rho^{\text{MC}} = \frac{N_2^{e\gamma} + N_2^{\text{dl}}}{N_1^{e\gamma} + N_2^{e\gamma} + N_1^{\text{dl}} + N_2^{\text{dl}}} \,. \tag{4.28}$$

The correction factor δ_κ is defined as the relative number of $e\gamma$ events with the correctly validated electron, in which the photon misidentification has to be resimulated in order to equalise

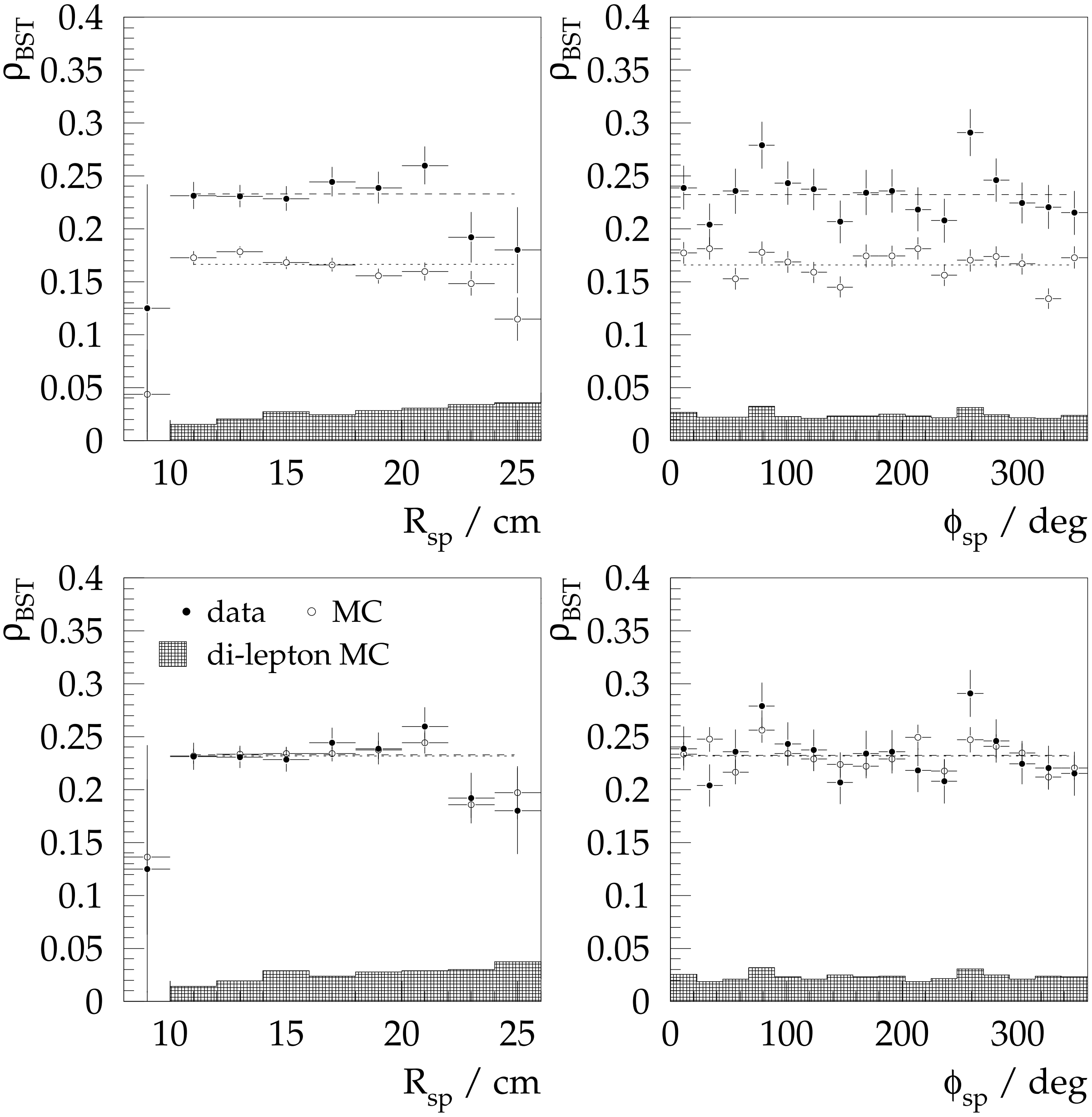

Figure 4.15: *Rate of the photon misidentication in the BST before the correction (upper plots) and after the correction (lower plots) as a function of the corresponding SpaCal cluster radial (left plots) and azimuthal position (right plots). Displayed are the real data (closed circles) and sum of all simulated signals (open circles). The dashed and dotted lines demonstrate the average values of the data and simulation rates, respectively. The hatched histogram shows the contribution of simulated dilepton events from the GRAPE and DIFFVM J/ψ samples.*

Table 4.3: *Correction factors δ_κ for the resimulation of the photon misidentification rate in the BST. In the upper row the centre of the bin of the particle radial coordinate in the plane $z = -161.5$ cm is specified.*

r_c, cm	9	11	13	15	17	19	21	23	25
δ_κ, %	5.6	9.2	7.3	7.9	12.6	11.6	14.7	5.1	7.0

the visible rates in the data and the simulation. Let us first assume that the chamber has a 100% efficiency of the electron validation. Then we can write:

$$\begin{aligned} N_0^{\mathrm{data}} &= N_0^{e\gamma} = N_0^{\mathrm{dl}} = N_1^{\mathrm{dl}} = 0\,, \\ N_2^{\mathrm{data}} &= N_2^{e\gamma} + N_1^{e\gamma}\delta_\kappa + N_2^{\mathrm{dl}}\,, \\ N_1^{\mathrm{data}} &= N_1^{e\gamma}(1-\delta_\kappa) + N_1^{\mathrm{dl}}\,. \end{aligned} \tag{4.29}$$

(Note that the total number of $e\gamma$ events with at least one particle validated $N_1^{e\gamma} + N_2^{e\gamma}$ does not change after the resimulation.) Consequently

$$\rho^{\mathrm{data}} = \frac{N_2^{e\gamma} + N_1^{e\gamma}\delta_\kappa + N_2^{\mathrm{dl}}}{N_1^{e\gamma} + N_2^{e\gamma} + N_2^{\mathrm{dl}}} = \rho^{\mathrm{MC}} + (1-\rho^{\mathrm{MC}})\delta_\kappa \tag{4.30}$$

and thus

$$\delta_\kappa = \frac{\rho^{\mathrm{data}} - \rho^{\mathrm{MC}}}{1-\rho^{\mathrm{MC}}}\,. \tag{4.31}$$

However, additional small corrections due to the limited efficiency of the electron validation ϵ make the expression for δ_κ much more complex and the correction factors slightly larger. To be specific, the number of $e\gamma$ events with one particle validated is given by

$$N_1^{e\gamma} = N_{1,\mathrm{true}}^{e\gamma} + N_{1,\mathrm{false}}^{e\gamma} = [\epsilon(1-\kappa) + \kappa(1-\epsilon)]N_{\mathrm{tot}}^{e\gamma} \tag{4.32}$$

with the total number of $e\gamma$ events $N_{\mathrm{tot}}^{e\gamma} = N_0^{e\gamma} + N_1^{e\gamma} + N_2^{e\gamma}$. The first term in the above equation gives the number of events with the correctly validated electron, while the second term gives the number of events with simultaneous wrong identification of both particles. The number of events, in which the additional simulation of photon conversion is performed, is equal to $\delta_\kappa N_{1,\mathrm{true}}^{e\gamma}$, instead of $\delta_\kappa N_1^{e\gamma}$ in the ideal case. Furthermore, the number $N_0^{e\gamma}$ of events with no particle validated is not equal to zero any more, but instead

$$N_0^{e\gamma} = (1-\epsilon)(1-\kappa)N_{\mathrm{tot}}^{e\gamma}\,. \tag{4.33}$$

During the resimulation the photons become validated in a fraction of these events $\delta_\kappa N_0$, and thus the number $N_{1,\mathrm{false}}^{e\gamma}$ and consequently $N_1^{e\gamma}$ rises. Both effects require an additional increase of δ_κ with respect to that given by eq. 4.31 in order to achieve equal rates in the data and the simulation.

The complete expression for δ_κ is not deduced here, since it is anyway difficult to determine the actual numerical values of the external BST efficiency ϵ in each radial bin. The BST efficiency is simulated in several steps, first in the H1 simulation program and then in the analysis chain, as described in paragraph 4.4.5. To find the correction factors, the correction procedure was performed several times employing eq. 4.31 until agreement has been reached. The acquired

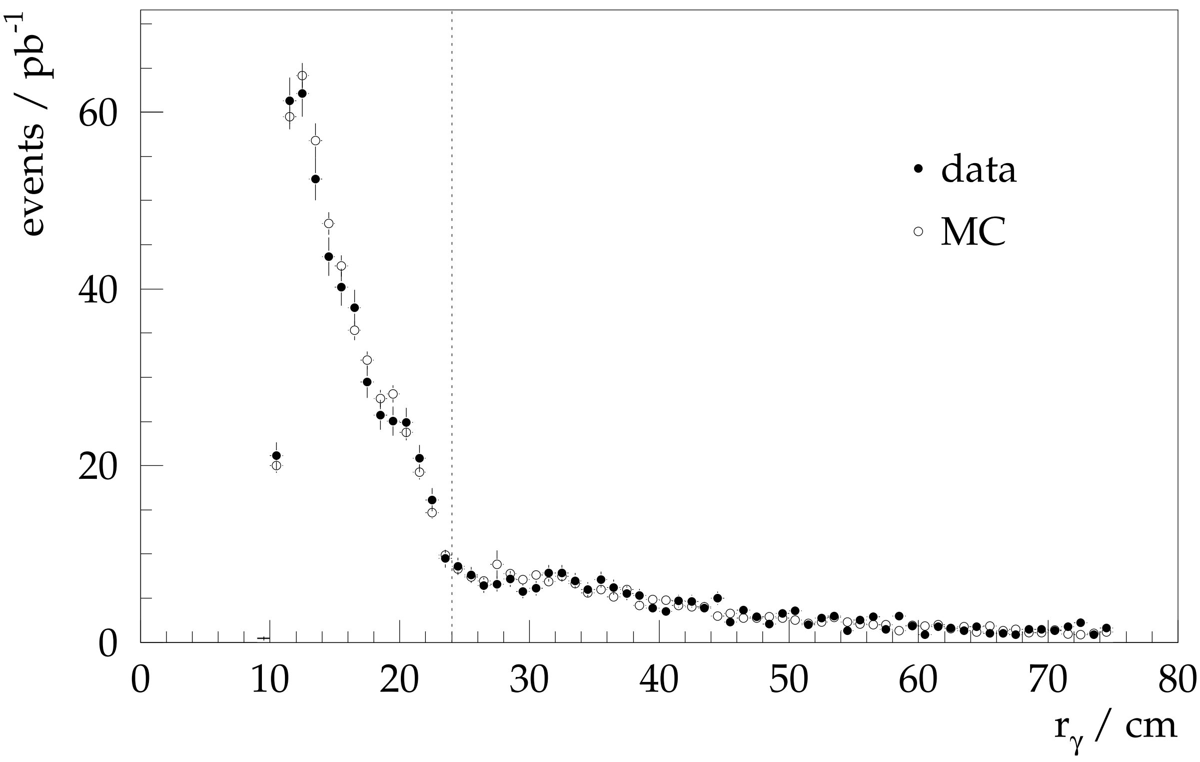

Figure 4.16: *Radial distribution of the final state photons in the plane $z = -161.5$ cm. The closed circle denote the data of the standard 1997 data sample, while the open circles depict the MC simulation with all background contributions added. The dotted line illustrates the average boundary between the BST and the CIP acceptance regions.*

correction factors are listed in table 4.3. An additional BST signal for the final state photons is resimulated with these factors event by event in the analysis chain using generated parameters of the outgoing photon and the resolution of the BST polar angle and vertex measurement, as given in sect. 2.2.3. The visible rate ρ in the resimulated events is contrasted to the real one in the lower plots of fig. 4.15. A good agreement between both distributions can be seen.

As pointed out in paragraph 4.4.5 the correction of the photon misidentification influences the results of the study of the electron validation efficiency. In order to determine the common systematic uncertainty of both procedures, the radial distribution of identified photons has been studied in the same way as that of the electrons in paragraph 4.4.5. This distributions is depicted in fig. 4.16. The maximum agreement between the real and the simulated events could be achieved by an additional 2% damping of the simulated signal compared to the result obtained for the electron validation efficiency. This value is taken as the uncertainty of the photon misidentification. The total error of both studies has been computed as the sum of both errors, equal to 3%, thus assuming full correlation between both procedures.

A similar investigation of the photon misidentification in the CIP has revealed a good agreement between data and simulation. As can be seen in fig. 4.17 the average rates in the data and the simulation agree within 1%, so that no additional correction had to be applied. The total error of the validation in the CIP has been taken to be 1.5%, *i.e.*, the sum of the uncertainties of the electron validation and the photon misidentification.

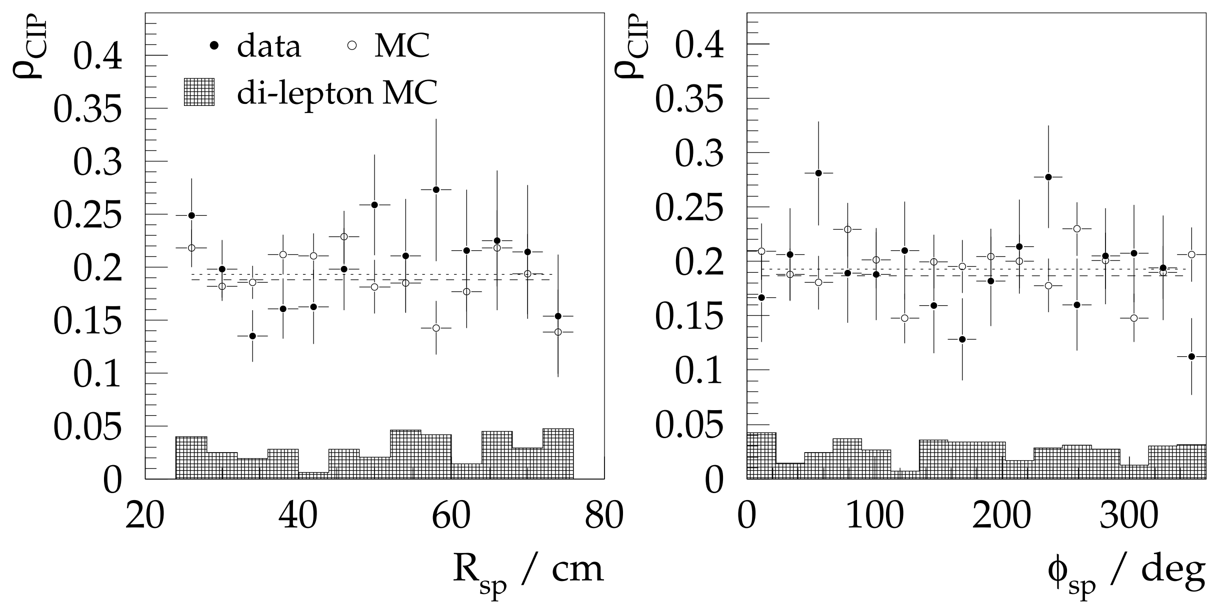

Figure 4.17: *Rate of the photon misidentication in the CIP as a function of the corresponding SpaCal cluster radial position (left plot) and azimuthal position (right plot). Displayed are the real data (closed circles) and sum of all simulated signals (open circles). The dashed and dotted lines demonstrate the average values of the data and simulation rates, respectively. The hatched histogram shows the contribution of simulated dilepton events from the GRAPE and DIFFVM J/ψ samples.*

4.4.7 Electron/Photon Identification Procedure

A special treatment is done for events in which one of the particles is identified as an electron by one of the chambers, BST or CIP, and as a photon by the other one. Such particles fall into the acceptance of both devices. The mixed validation can occur either due to the inefficiency of one of the chambers or a photon conversion in the other chamber. The rate of such events cannot be large anyway, since after the application of fiducial cuts the acceptance ranges of both chambers have a relatively small overlap area.

The particles with mixed validation are treated as if their kind is unknown and the identification of the other particles is used for the ultimate decision. If the second particle is validated as the electron then the first particle is assumed to be the photon and vice versa. To estimate the uncertainty of this procedure, the validation algorithm was also run in a simplified mode, in which such particles are validated as electrons. By this the cross section in most kinematic bins changed by no more than 0.5%. The differences in the cross section values are taken as systematic errors of the identification procedure.

4.4.8 Vertex Reconstruction

The reconstruction of the interaction vertex is performed according to the scheme "BST – CIP – CTD", *i.e.*, the BST vertex is used if it exists, otherwise the CIP vertex if it is found, and finally the central one if no other vertex is reconstructed. The BST vertex is preferred to that reconstructed with the CIP because of its better resolution. The need to choose between both vertices occurs only in the rare cases, when the electron falls into the acceptance of both chambers. In

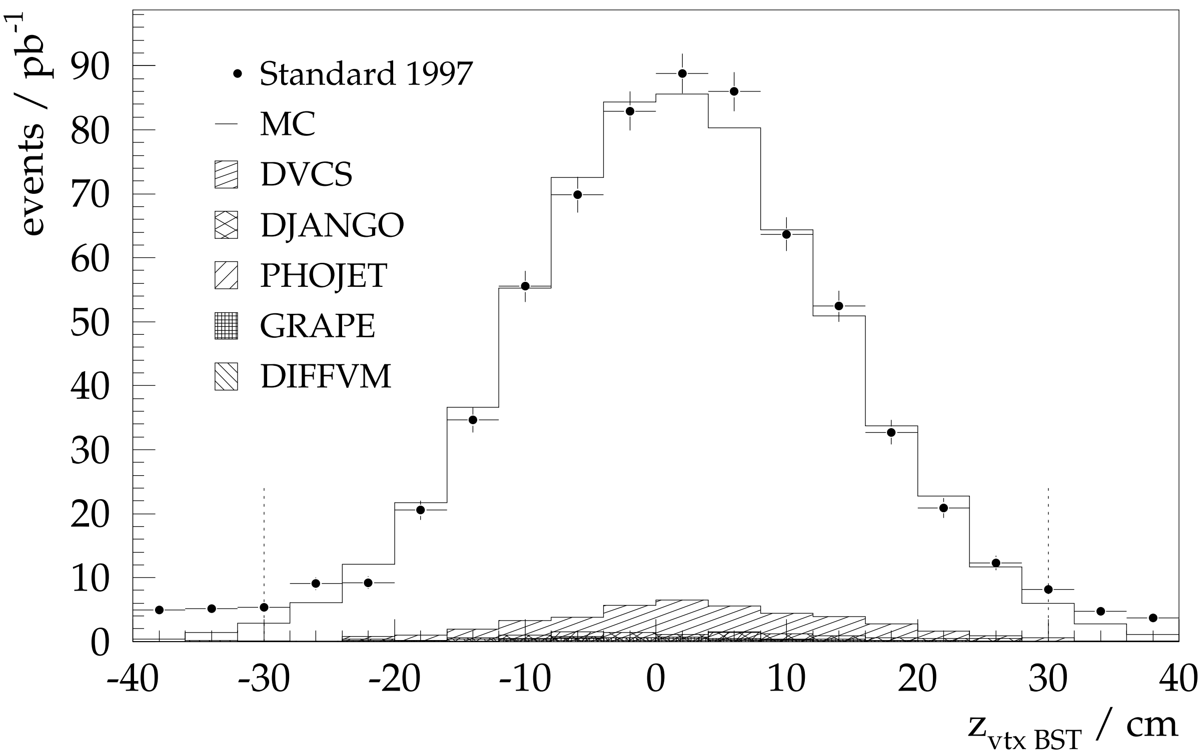

Figure 4.18: *BST vertex z position in the data and the simulation. The closed circles depict the data of the standard 1997 data sample, while the solid histogram stands for the COMPTON events with all background contributions added. The simulated background events are depicted by hatched histograms as denoted in the legend. The dotted lines illustrate the cuts at $|z| = 30$ cm.*

contrast, the choice between one of these vertices and the CTD vertex is not so rare. To be specific, it has to be often made in the events, in which the electron falls into the acceptance of both the CIP and the CJC and the CTD vertex is reconstructed from the electron track. Another case is represented by inelastic QEDC events, in which the central vertex is measured using tracks produced by hadrons. In both cases the central vertex provides usually a very bad resolution, since the tracks have relatively low polar angles. Therefore the CIP vertex is preferred to the central one. Since the vertex measurement is a part of the electron validation procedure, the efficiency of vertex reconstruction is automatically that of the electron identification.

The vertex z distributions have been studied separately for the BST and CIP vertices. The BST vertex z distribution in data and simulation is depicted in fig. 4.18. The collision points are spread around the nominal vertex position inside the H1 detector, at which the beams are focused by the HERA magnet optics. The Gaussian profile of the distribution arises from the longitudinal spread of the colliding bunches. The actual average z position and the width of the distribution can vary from run to run and are not exactly known during the Monte Carlo production. Therefore the simulated events are reweighted in the analysis chain to reproduce the centre and the width of the distribution observed in the data.

The CIP vertex z coordinate, which is plotted in fig. 4.19, reveals some discrepancies in shape between the real and simulated data. Their origin has not been clarified. Possibly they are related to the uncertainties of the CIP alignment discussed in the following section. The discrepancies correspond to an uncertainty of approximately 1 cm in the average z position, which

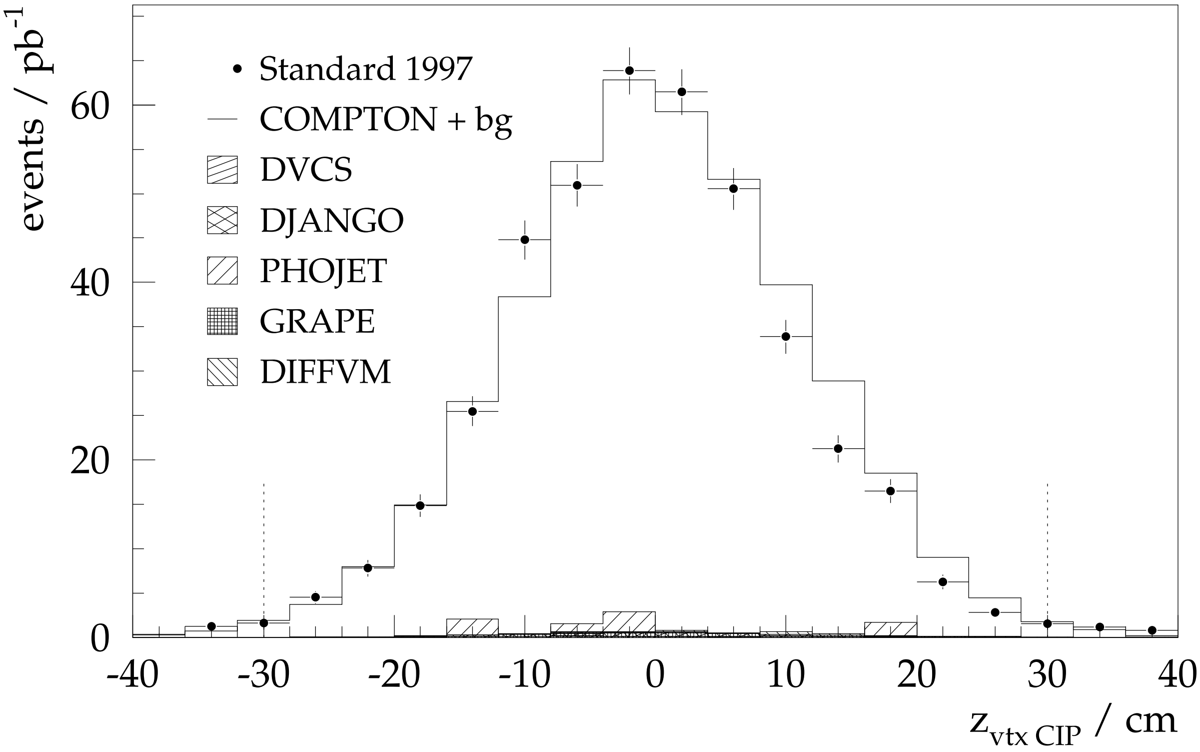

Figure 4.19: *CIP vertex z position in the data and the simulation. The closed circles depict the data of the standard 1997 data sample, while the solid histogram stands for the COMPTON events with all background contributions added. The simulated background events are depicted by hatched histograms as denoted in the legend. The dotted lines illustrate the cuts at* $|z| = 30\,\mathrm{cm}$.

has been taken as an additional systematic error influencing the polar angle reconstruction.

4.5 Polar Angle Measurement

For the main chain of the QEDC analysis a sophisticated algorithm for the θ measurement has been worked out. This procedure exploits the particle identification and vertex reconstruction routines provided for the central tracking chambers. For each of the two SpaCal clusters the following θ reconstruction scheme is applied:

1. If the associated BST track exists, its polar angle θ_{BST} is used. Obviously this method cannot be applied to the identified photons since the existence of the BST track means the electron validation;

2. Otherwise, if the BDC track exists, the polar angle θ_{BDC} is reconstructed from the BDC track and the vertex position. The BDCLEV routine [kel98] is employed for the BDC track reconstruction. This mode is used for electrons validated by the CIP or the CJC and for photons converted in front of the BDC;

3. If no BST and no BDC track exists, the angle θ_{Sp} is measured with the SpaCal cluster CoG and the vertex coordinates, where the logarithmic weighting is used to find the centre of

gravity [mur95, poe96]. This method is utilised mainly for the not converted photons, since almost all electrons (more than 97%) leave a track in the BDC.

The calculation is performed relative to the beam direction, taking into account the angular tilt of the beams with respect to the H1 coordinate system, which is defined by the Central Jet Chambers.

For an accurate θ reconstruction three issues have to be considered:

- The precise placement of all detectors involved must be known;
- Any systematic deviations of the measured angle from the true one must be corrected for. This point concerns especially the SpaCal, since it is supposed to provide a worse angle measurement than the tracking chambers;
- The relative number of particles measured by the BDC and the SpaCal must be the same in the data and the simulation, to avoid discrepancies caused by a different precision of angular reconstruction in these detectors.

In the remaining part of this section the first issue, namely, the alignment of the detectors, and the last issue, namely, the photon conversion rate in the BDC are discussed. The corrections of the systematic deviations have been worked out in the framework of the analysis of the SpaCal energy scale and will be described later in paragraph 4.6.3.

4.5.1 Detector Alignment

The BDC and the SpaCal have been aligned using very low Q_h^2 QEDC events, *i.e.*, an almost purely elastic QED Compton sample. Such events are selected by an acoplanarity cut $A < 10^\circ$. The alignment procedure, as discussed in [sta98], consists in the minimisation of the χ^2 parameter given by the expression

$$\chi^2 = \sum_{\text{events}} \frac{(180^\circ - A)^2}{\sigma_A^2} \tag{4.34}$$

with

$$\sigma_A^2 = \frac{y_1^2\sigma_x^2 + x_1^2\sigma_y^2}{(x_1^2 + y_1^2)^2} + \frac{y_2^2\sigma_x^2 + x_2^2\sigma_y^2}{(x_2^2 + y_2^2)^2}\,, \tag{4.35}$$

where x_1, y_1 and x_2, y_2 are the coordinates of the BDC tracks or of the SpaCal cluster centres of gravity with respect to the beam position on the SpaCal surface. The beam position is calculated taking into account the beam tilt. The average spatial resolution parameters σ_x, σ_y have been set to 0.1 cm for the BDC and 0.3 cm for the SpaCal. The χ^2 minimum is searched for by simultaneous systematic shifts of the xy coordinates of both clusters in all events. The obtained xy coordinates of the BDC and SpaCal central points in the H1 coordinate system are listed in table 4.4. For the z coordinates the values found in the analysis of the inclusive 1997 DIS data [wal99, zho99] are used.

The alignment procedure has been cross-checked on several samples of simulated COMPTON events and yields agreement with the simulated coordinates within 0.025 cm in all samples. This value corresponds to an error of approximately 0.17 mrad for the polar angle reconstruction, which is more than 3 times smaller than the BDC θ resolution.

Table 4.4: *BDC, SpaCal and CIP alignment parameters with respect to the nominal position of the detectors.*

x_{BDC}, cm	y_{BDC}, cm	x_{Sp}, cm	y_{Sp}, cm	x_{CIP}, cm	y_{CIP}, cm	z_{CIP}, cm
0.26	0.02	0.18	-0.11	0.02	0.19	0.20

In an independent analysis of the SpaCal space reconstruction [gar00] the differences between the SpaCal and the BDC xy coordinates were found to be: $x_{\mathrm{BDC}} - x_{\mathrm{Sp}} = 0.091$ cm and $y_{\mathrm{BDC}} - y_{\mathrm{Sp}} = 0.168$ cm. One can see that these values are consistent with those given in table 4.4.

An exact measurement of the BST track polar angle demands the radial alignment of the 64 silicon detectors with respect to the BST internal coordinate system and the alignment of the BST in relation to the H1 frame of reference. These procedures for the 1997 data were performed in [ark00] and the results are applied in the chain of the present analysis.

The CIP placement was determined after the alignment of the backward detectors had been performed. For this a sample of inclusive DIS events was used, in which the central vertex was well reconstructed. The CIP position was determined from the comparison of the CTD and CIP vertex z coordinates. The difference of these coordinates, $Z_{\mathrm{CTD}} - Z_{\mathrm{CIP}}$, is plotted versus the electron ϕ coordinate in the upper left graph of fig. 4.20. A sinusoidal dependence is visible, which arises typically from the relative misalignment of the detectors involved in the measurement. The distribution of $Z_{\mathrm{CTD}} - Z_{\mathrm{CIP}}$ was then fitted by Gaussian profiles separately in eight ϕ sectors. The medians of the fits are depicted in the upper right plot of the same figure. Apart from the sinusoidal shape a systematic z shift is also visible. The alignment was performed by shifting the xy coordinates of the CIP cluster used for the vertex reconstruction in order to achieve a flat ϕ distribution of the fit medians, and the z coordinate in order to shift them to zero. The resulting values are also listed in table 4.4 and the corresponding distributions after the alignment are presented in the lower plots of fig. 4.20.

It is, however, not clear if a 2 mm shift in y of the CIP could occur in reality, since the CIP is placed within the common central tracker installation. It is in principle possible that not a shift (or not only a shift) but also an angular tilt causes a misalignment. A similar problem occured, in particular, in the BDC alignment procedure performed in the framework of the DIS analysis mentioned above. The alignment was performed using two independent methods, where the procedure with QEDC events yielded nearly the same results as those found in the present analysis. However, the other method using tracks reconstructed in the central tracker[2] showed a 2 mm deviation in y. As a possible explanation a shift or a tilt of the CIZ chamber was considered. Since the CIZ and the CIP are neighbouring chambers in the central tracker, it is not excluded that both problems have the same origin.

4.5.2 Photons in BDC

The photon misidentification rate in the BDC has been studied with the same method as that in the BST and the CIP (see paragraph 4.4.6). The average rate in the data and the simulation is shown in the upper plots of fig. 4.21 as a function of the particle radial and azimuthal position. As in paragraphs 4.4.5–4.4.6 the radial position is calculated in the plane $z = -161.5$ cm. One can see that the simulation strongly underestimates the rate in the data. An additional photon conversion rate of 27.5% was therefore resimulated in the analysis chain on an event by event basis. The BDC signal was simulated using generated photon parameters and applying a polar

[2] A detailed description of this method can be found in [kat97].

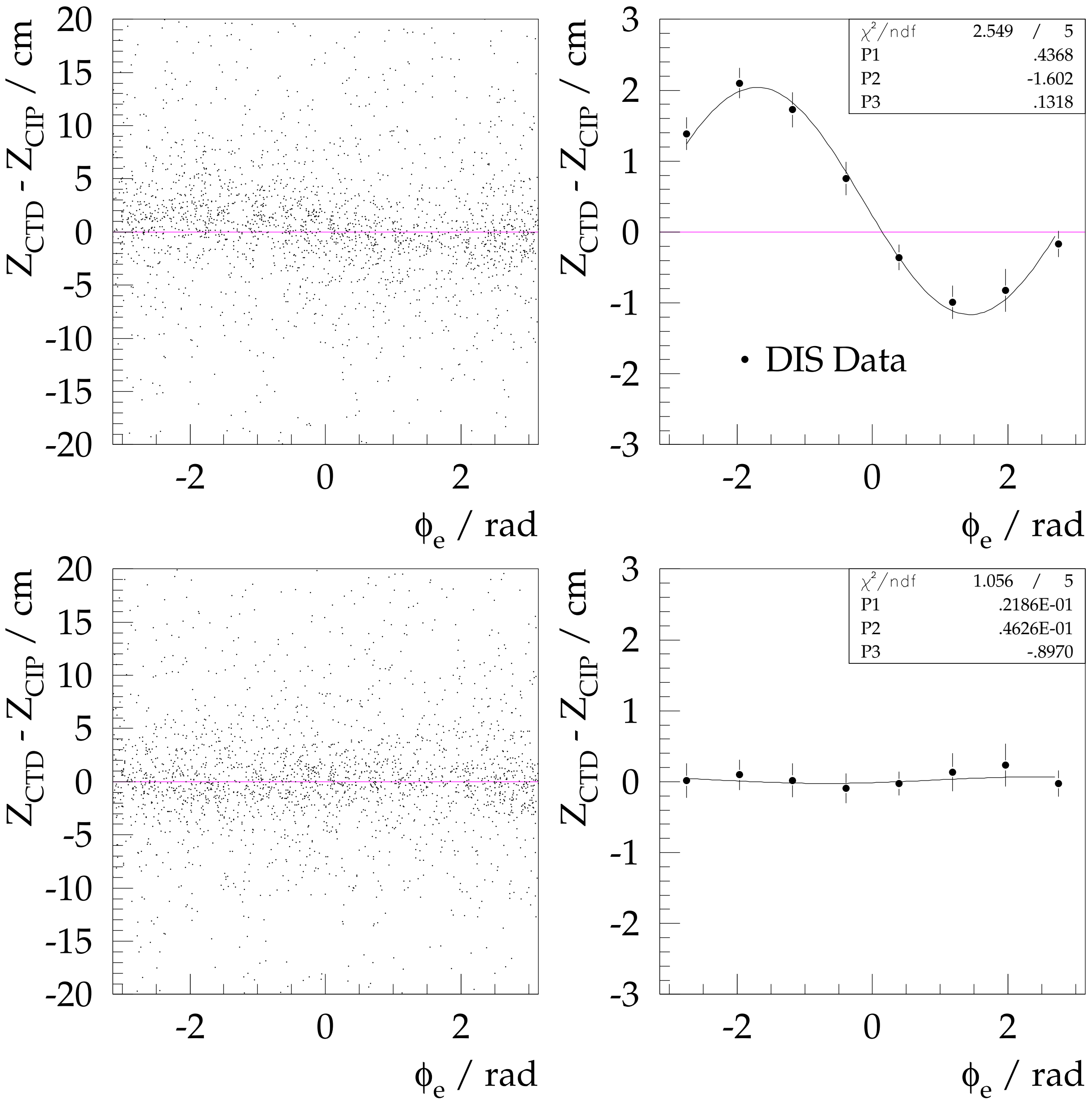

Figure 4.20: *Difference between the central tracker vertex coordinate z_{CT} and the CIP vertex position z_{CIP} as a function of the electron's azimuthal angle in DIS events. The upper (lower) plots are made before (after) the CIP alignment. In the left scatter plots general event distributions are depicted, while in the right figures the results of the octant fitting are presented.*

angle smearing of 0.57 mrad. The simulated rate after the correction is contrasted to the one in the data in the lower plots of fig. 4.21.

4.6 Energy Measurement in Spaghetti Calorimeter

The initial energy scale of the SpaCal, as used during the data taking, is maintained by a light-emitting diode (LED) system [jan96, mey96], supplying amplification gains for the 1192 photomultiplier tubes. Three methods have been developed for the pre-calibration, which make use of the shape of the kinematic peak of the ep interaction [jsm95], cosmic muons [dir96] or muons from the beam halo [arn95]. For the 1996 – 1997 running period the inner region was pre-calibrated using the kinematic peak method, while for the remaining part cosmic muon data were exploited.

The maximum precision of the energy measurement can, however, be achieved only in the physics analysis step. For the cross section measurement it is necessary to equalise the simulated and the real SpaCal energy scales and resolutions. In the framework of this analysis an extensive study of the SpaCal energy measurement has been carried out and a subsequent recalibration using elastic QED Compton events has been performed. Particular attention was payed to the influence of passive material in front of the calorimeter on its performance.

4.6.1 Simulation of Passive Material

Previous H1 analyses [sff98, sta98, mar98] revealed the necessity to improve the H1SIM description of passive material in the backward region of the H1 detector, in order to understand the SpaCal energy scale and resolution and achieve a better agreement between simulated and real data. Therefore the distribution of dead material in the whole region between the nominal vertex position and the SpaCal was investigated and a more accurate and detailed description was implemented into the H1 simulation package. A full list of the introduced changes can be found in [len99].

To estimate the quantity of implemented material, the region between the vertex and forward SpaCal surface is scanned by “geantinos” [es96]. These are pseudo-particles defined within the GEANT framework which record the amount of material they pass through. The scan results obtained for old and new material description are shown in figures 4.22 and 4.23. For comparison a plot of BDC charge in the 1997 data made by the BDC group [sie99] is displayed in figure 4.24. The most essential dead material constellations can be identified on this plot and the corresponding modules stick out on the scan plot for the new material simulation.

The H1SIM version with the new passive material description is employed in the MC simulations used for the present QEDC cross section measurement.

4.6.2 Energy Scale

The new dead material description has been tested using elastic QED Compton events. The study of the SpaCal energy measurement described in this paragraph was a continuation of the work performed in [sff98, sta98]. It was carried out using data of the 1996 run range, before the whole cross section measurement chain was built up. There were however no significant changes of the SpaCal energy scale and resolution between the 1996 and 1997 run ranges, so that the results are applicable to the data of 1997.

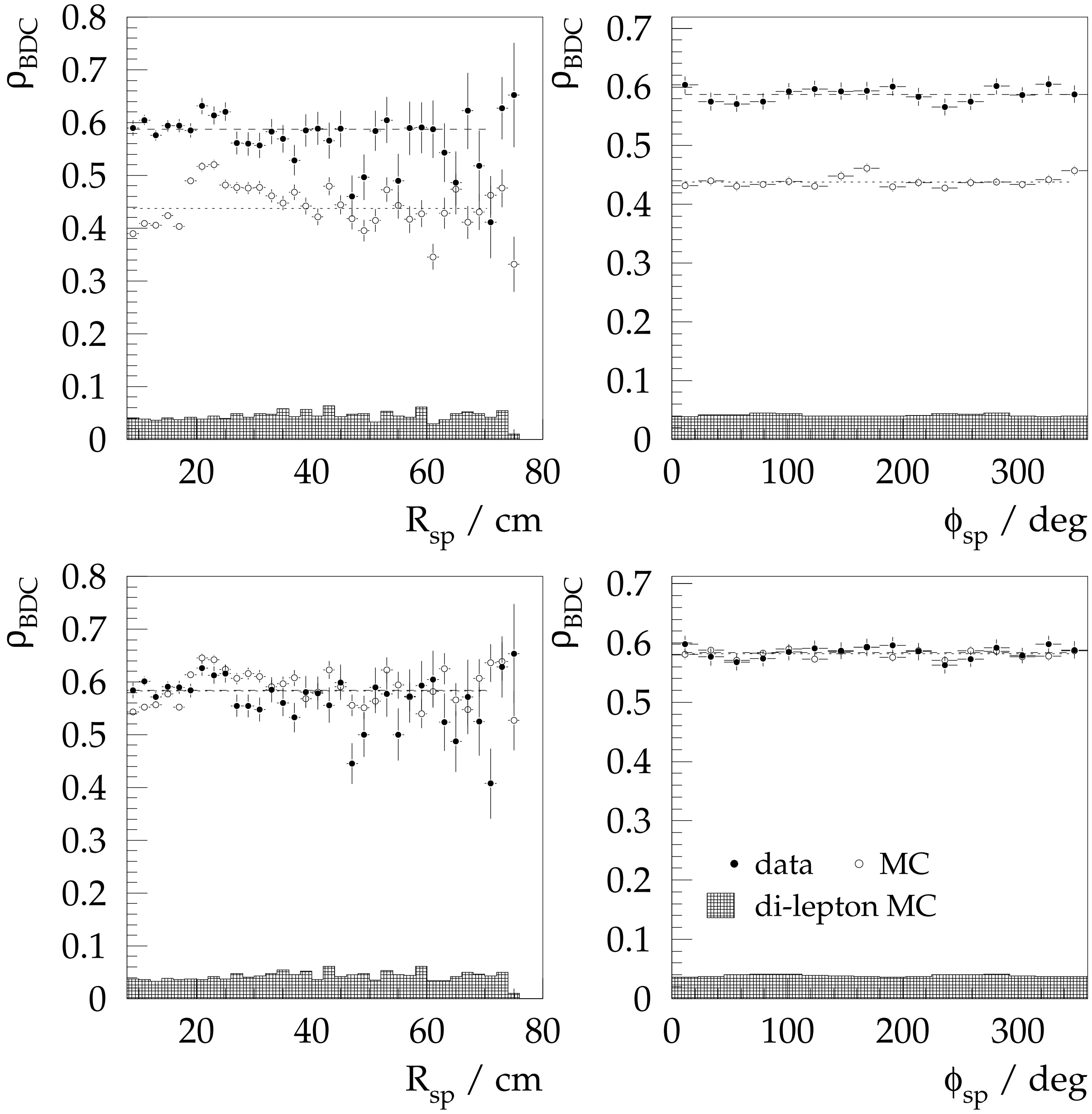

Figure 4.21: *Rate of the photon misidentication in the BDC before the correction (upper plots) and after the correction (lower plots) as a function of the corresponding SpaCal cluster radial position (left plots) and azimuthal position (right plots). Displayed are the real data (closed circles) and sum of all simulated signals (open circles). The dashed and dotted lines demonstrate the average values of the data and simulation rates, respectively. The hatched histogram shows the contribution of simulated dilepton events from the GRAPE and DIFFVM J/ψ samples.*

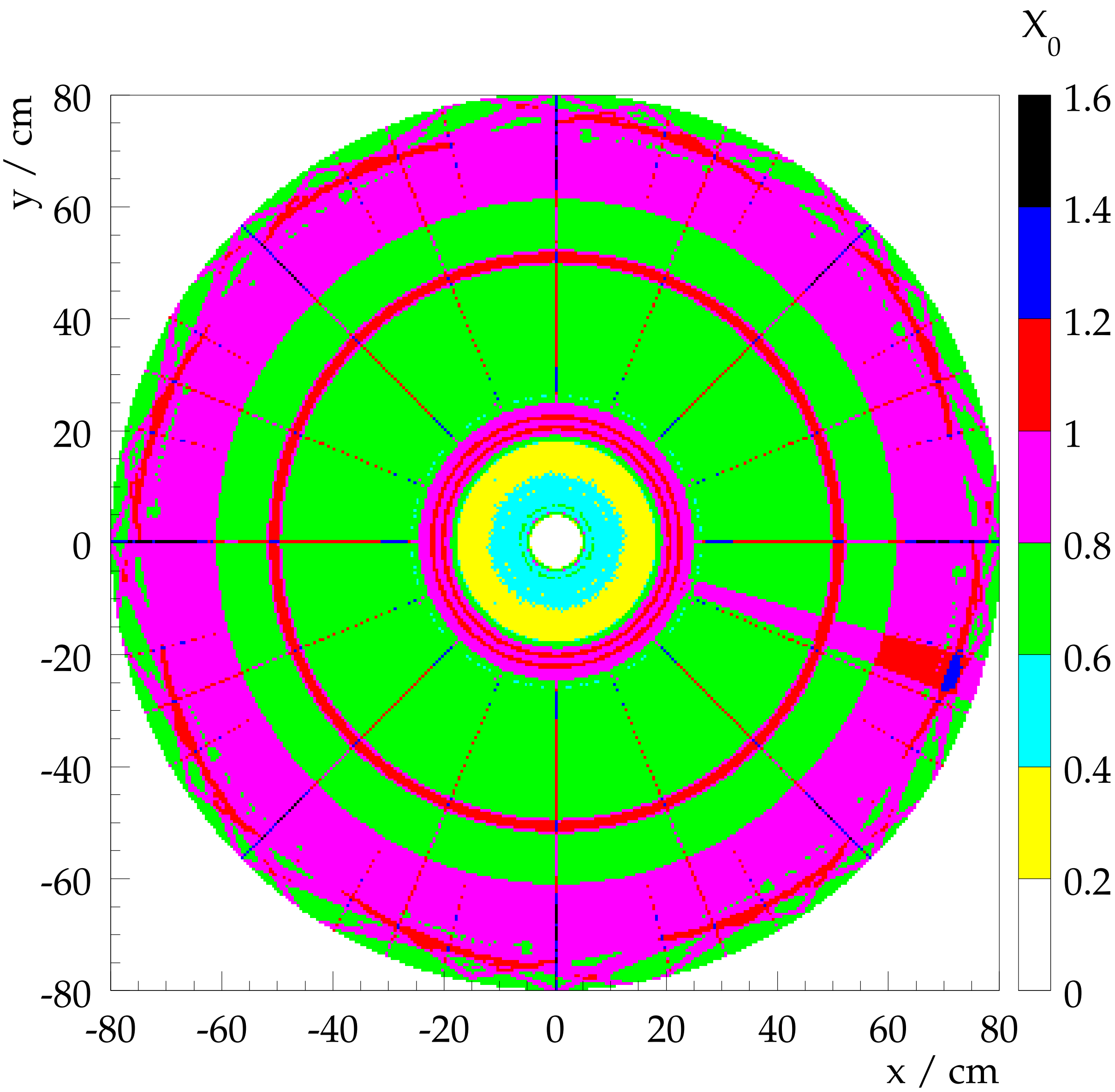

Figure 4.22: *Geantino scan performed from the nominal vertex position up to the SpaCal surface shows the amount of simulated passive material in radiation lengths before the new material implementation.*

For the event selection the basic criteria given in sect. 4.2 are applied. The elastic QEDC events are selected by requiring the total energy in the LAr calorimeter to be smaller than 2 GeV. Although this selection leaves an admixture of inelastic events, it was checked on an elastic MC subsample that it doesn't change the distributions considered in this study. The vertex reconstruction and angle measurement procedure by means of the BST and the CIP is also not performed, but, as will be shown in this paragraph, the badly known vertex position does not affect the relevant distributions.

In order to study the energy scale of a detector, an independent "reference" energy of a particle has to be measured in the same event. In elastic QEDC events it is possible to calculate the energy of both the electron and the photon by measuring their scattering angle. This "double

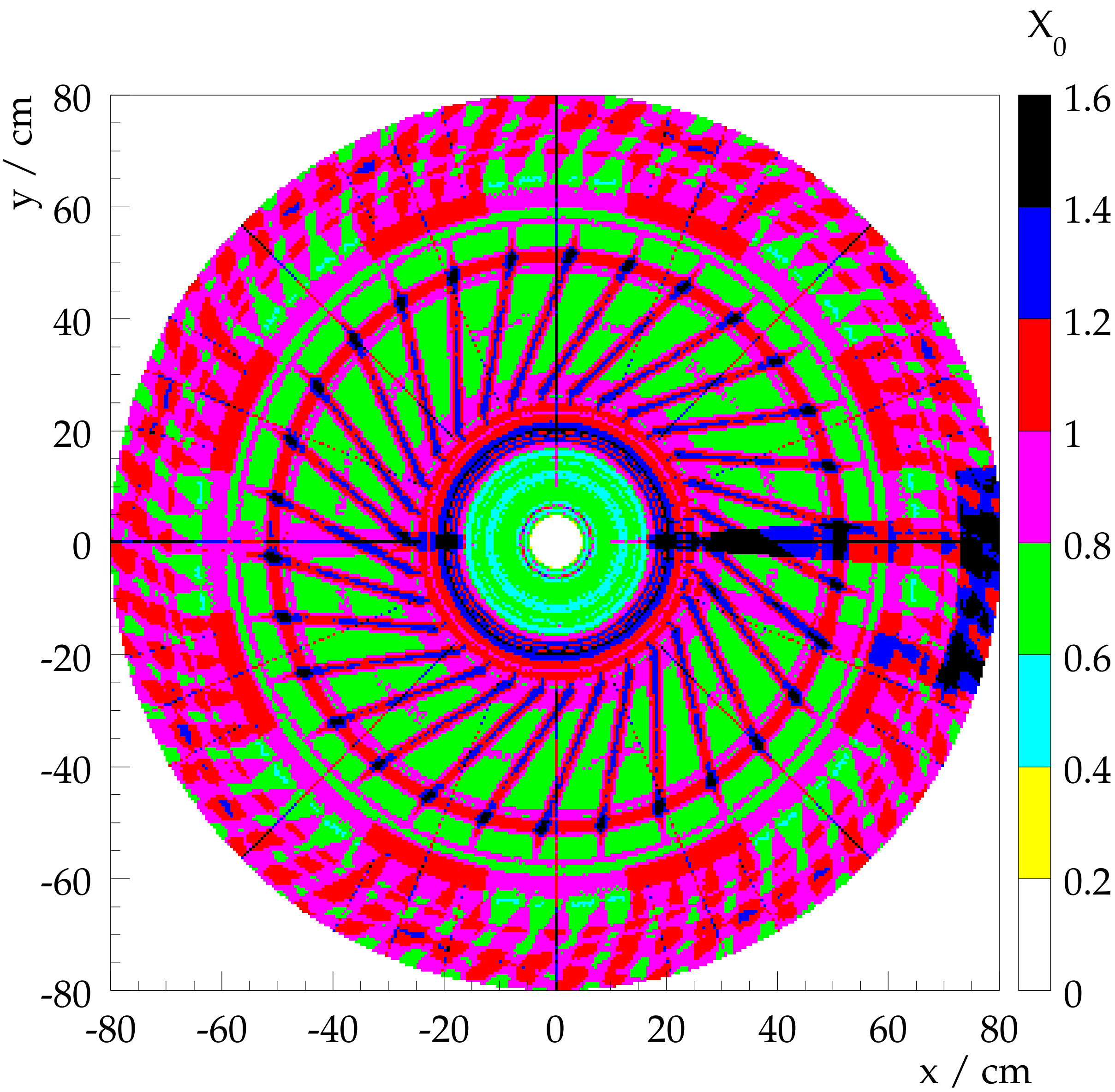

Figure 4.23: *Geantino scan of the new material description introduced into the H1 simulation.*

angle" energy is given by

$$\begin{aligned} E_\gamma\left(\theta_e, \theta_\gamma\right) &= \frac{2E_{e0}\sin\theta_e}{\sin\theta_e + \sin\theta_\gamma - \sin(\theta_e+\theta_\gamma)}, \\ E_e\left(\theta_e, \theta_\gamma\right) &= \frac{2E_{e0}\sin\theta_\gamma}{\sin\theta_e + \sin\theta_\gamma - \sin(\theta_e+\theta_\gamma)}. \end{aligned} \tag{4.36}$$

For the study the deviation from linearity is defined:

$$\Delta L = \frac{E_{\rm m} - E_{\rm da}}{E_{\rm da}}, \tag{4.37}$$

where $E_{\rm m}$ is the energy of each cluster measured by the SpaCal and $E_{\rm da}$ is that derived from the double angle method. Figure 4.25 a shows this quantity in bins of the measured energy and

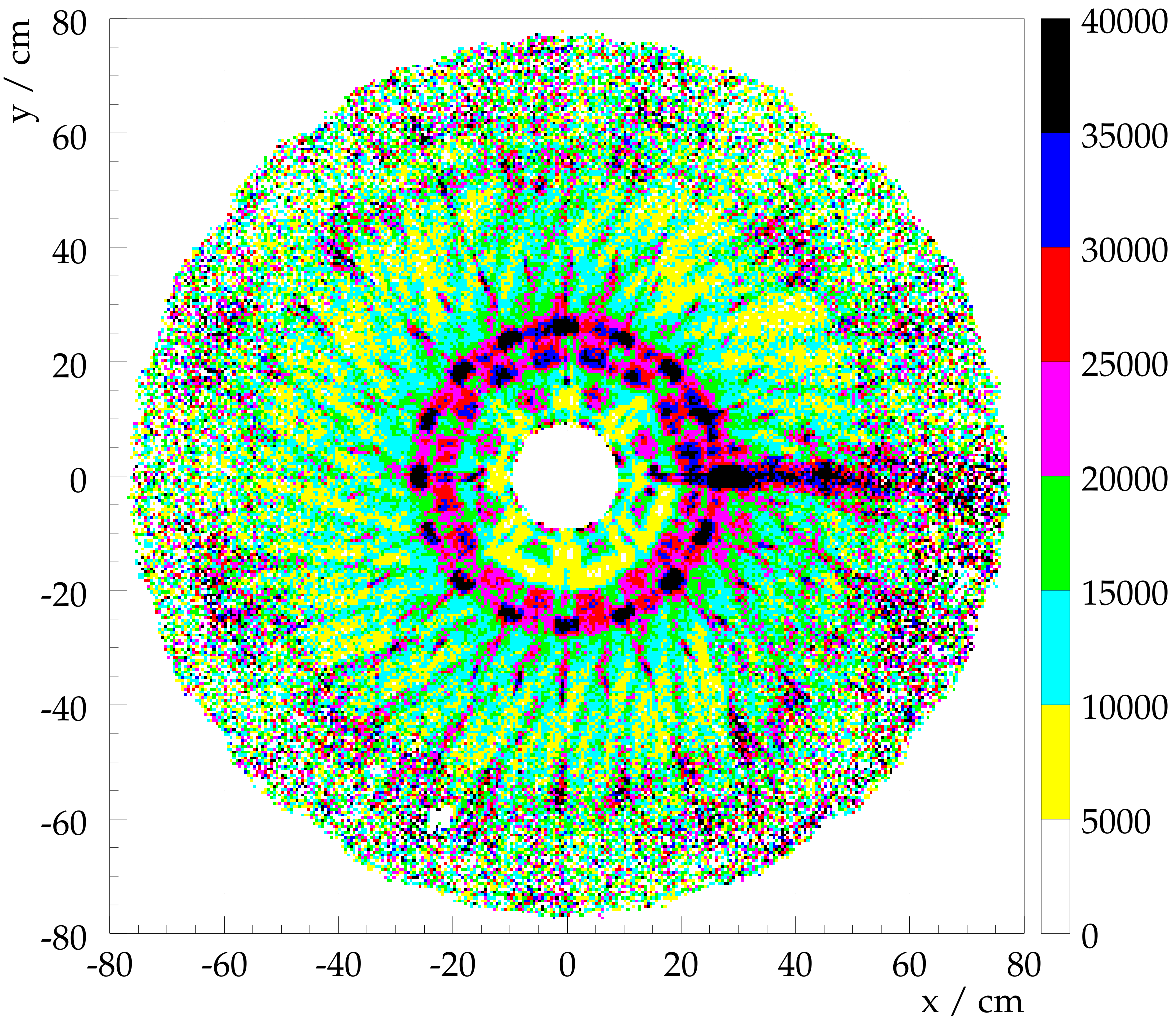

Figure 4.24: *Charge deposited in BDC in average per event in the 1997 data. The charge units are arbitrary. The plot has been made by the BDC group [sie99].*

reproduces fig. 8 from [sff98]. A Monte Carlo simulation using the old material description is represented in this figure. The polar angles are reconstructed using the SpaCal cluster coordinates and the nominal vertex position. One should stress that this plot does not fully reflect the SpaCal energy measurement performance, because several effects influence the distribution.

One of them is a systematic migration near the edges of the QED Compton phase space. Due to the finite SpaCal energy resolution there are events in which the measured energies migrate out of their average bins. But at the phase space limits the effect is not compensated by migration in the opposite direction since the average number of QEDC events per bin drops near the limits. Therefore the points near the higher limit overshoot the general behaviour, while near the lower limit they undershoot it. To cancel the effect, one can use $E_{\rm da}$ for binning, which is much more robust against the migrations. The result is displayed in figure 4.25 b. Only in the last bin minor deviations because of migrations in the opposite direction are visible.

Two features of the $E_{\rm da}$ reconstruction provide its ability to compensate the migrations. At higher energies $E_{\rm da}$ is reconstructed with much better resolution than $E_{\rm m}$. This is depicted in

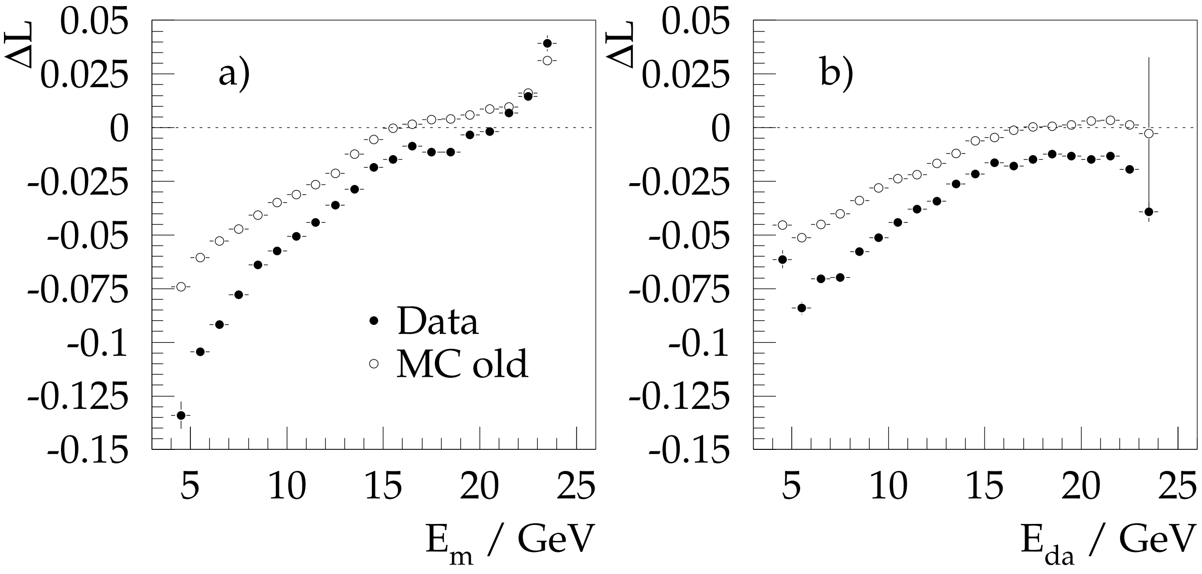

Figure 4.25: *Non-linearity of the SpaCal energy scale for the data and MC with the old material simulation as a function of a) cluster energy and b) energy calculated by the double angle method.*

fig. 4.26 a and b for the example of the bin 21 GeV $< E_g <$ 22 GeV. At lower energies not only a better resolution but also an asymmetric behaviour of the E_{da} reconstruction helps in cancelling the migrations. This can be understood from figures 4.26 c and d, where as an example the bin 5 GeV $< E_g <$ 6 GeV is shown. If one uses E_{da} for the binning, more events migrate to higher energies than to lower energies. This compensates significantly the migrations caused by the rising number of events per bin.

In figure 4.25 b and in all subsequent plots of the non-linearity, in which E_{da} is utilised for the binning, the rise in the first bin is observed that does not follow the general trend of the distribution. This effect is due to the cut on the minimal cluster energy used for the QEDC event selection: $E_m >$ 4 GeV.

To study the influence of dead material on the SpaCal energy measurement, a simulation was performed in which 5.5 times more cables as before were implemented. This implementation corresponds to an additional 0.8 X_0 put as a test between the vertex and the SpaCal. The result is a full agreement between the simulation and the data as depicted in fig. 4.27 a. This underlines the necessity of improving the passive material distribution in the simulation.

In reality it appeared impossible to find so much additional material. As follows from a comparison of figures 4.22 and 4.23, the average amount of simulated passive material in front of the SpaCal was increased by $0.2 - 0.4 X_0$. In fig. 4.27 b the ΔL distributions for the data and the simulation with the new material distribution mentioned in the prior section is shown. The data and Monte Carlo points agree within 0.5% in the range 11 GeV $< E <$ 20 GeV. Below 11 GeV data and MC points start to diverge and leave up to 2.5% disagreement at 4 – 5 GeV.

In fig. 4.28 a the non-linearity $\Delta L'$ with:

$$\Delta L' = \frac{E_m - E_g}{E_g} \tag{4.38}$$

is depicted for simulated events. E_g denotes the generated particle energy. A comparison of this distribution with MC points in fig. 4.27 demonstrates one more important effect influenc-

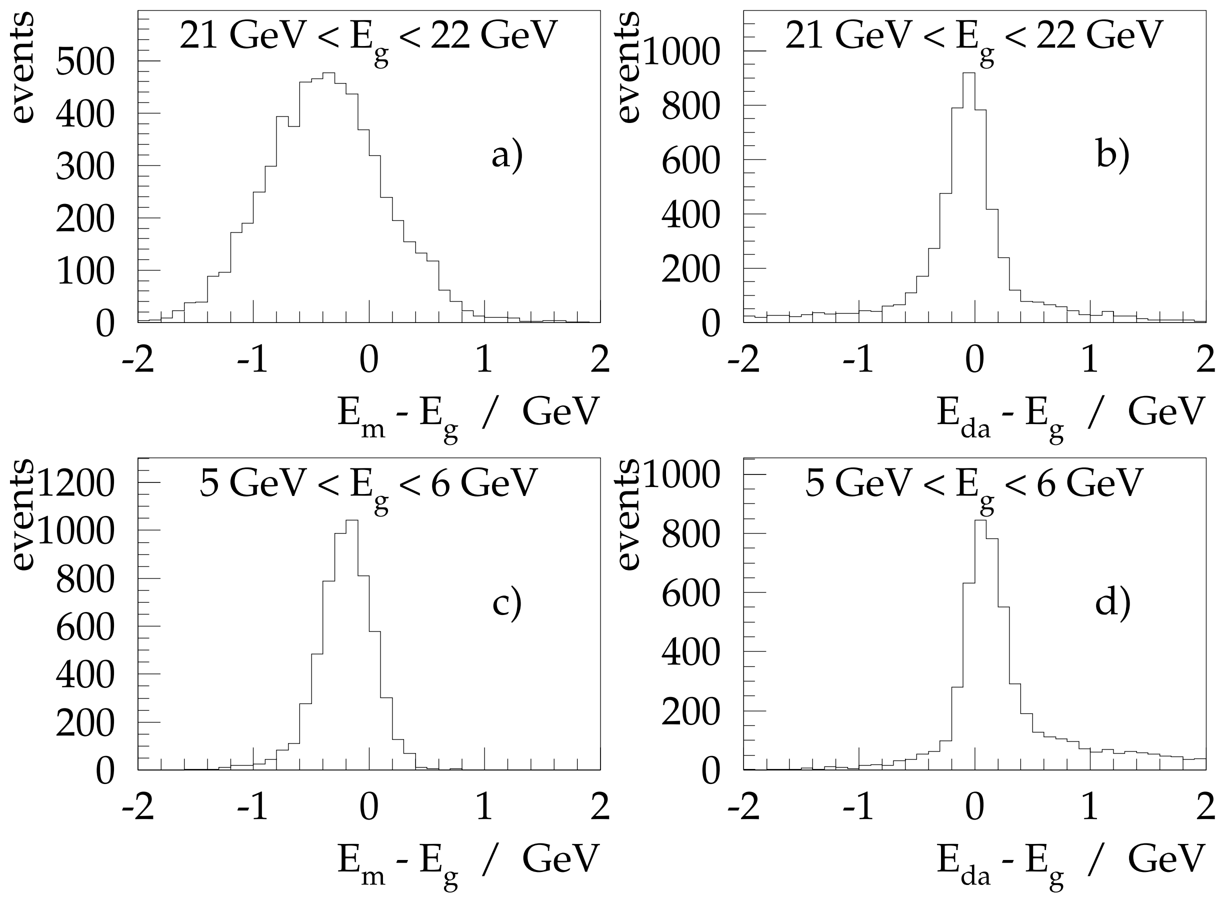

Figure 4.26: *Figures a) and c) display the difference between the cluster energy and the generated energy in MC in two chosen bins of the generated energy. In figures b) and d) the double angle energy is used instead of the cluster energy.*

ing the distribution – a systematic deviation of the double angle energy from the true particle energy. In fig. 4.28 b this deviation:

$$\Delta D = \frac{E_{\text{g}} - E_{\text{da}}}{E_{\text{g}}} \tag{4.39}$$

is displayed for electrons and photons in the simulation.

This study of the energy scale was performed yet without the reconstruction of the event vertex by means of the BST and the CIP. However, it was found that the unmeasured vertex position in QED Compton events does not significantly affect the double angle energy. This follows from fig. 4.29, in which ΔD is plotted again, but using instead of the reconstructed or the nominal vertex z position a constant position of $z_{\text{vtx}} = -5\,\text{cm}$ and $z_{\text{vtx}} = 5\,\text{cm}$. This insensitivity can be easily understood from eq. 4.36 which yields:

$$\begin{aligned} E_\gamma\left(\Theta_e, \Theta_\gamma\right) &\approx E_{e0} \cdot \frac{\Theta_e}{\Theta_e + \Theta_\gamma} \approx E_{e0} \cdot \frac{r_e}{r_e + r_\gamma}\,, \\ E_e\left(\Theta_e, \Theta_\gamma\right) &\approx E_{e0} \cdot \frac{\Theta_\gamma}{\Theta_e + \Theta_\gamma} \approx E_{e0} \cdot \frac{r_\gamma}{r_e + r_\gamma}\,, \end{aligned} \tag{4.40}$$

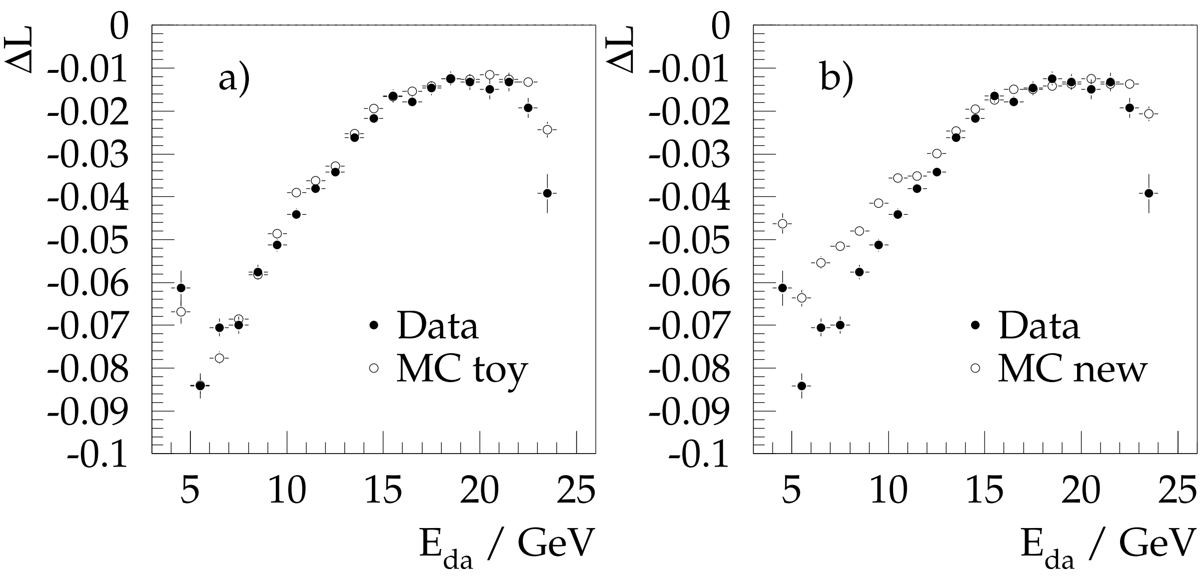

Figure 4.27: *Non-linearity of the SpaCal energy scale for the data and MC including: a) the toy CJC cable simulation and b) the new material simulation.*

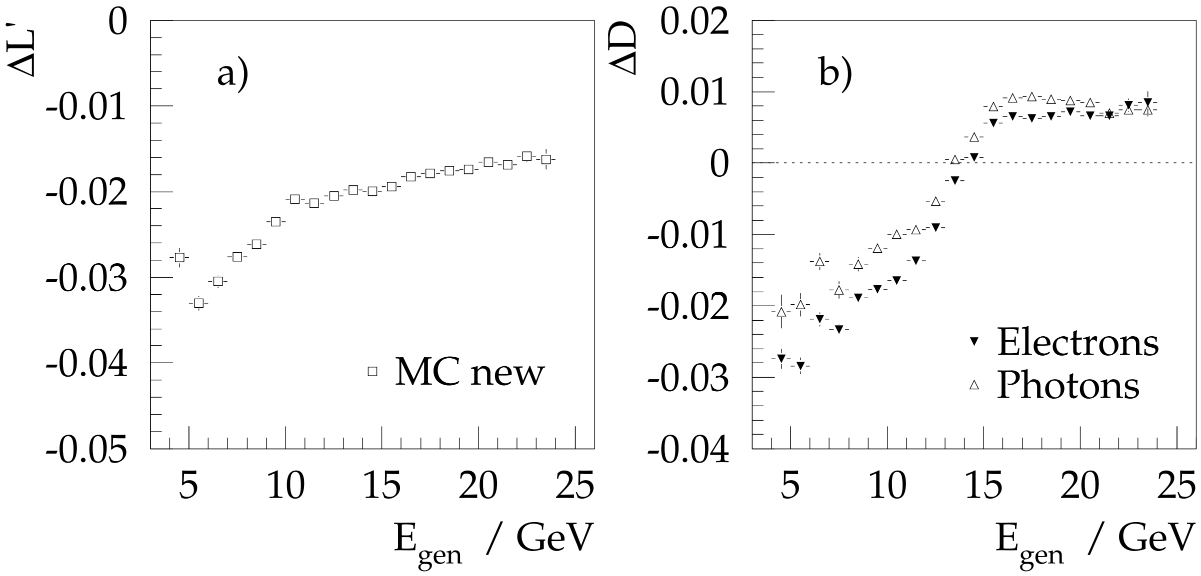

Figure 4.28: *a) non-linearity computed using the generated particle energy in MC; b) difference between the double angle and the generated energy in MC.*

where r_e and r_γ are radial cluster coordinates relative to the vertex position and Θ_e, Θ_γ are the electron and the photon scattering angles measured with respect to the incident electron direction and equal to $\pi - \theta^{\mathrm{H1}}$. Thus, energy calculation with the double angle method does not depend on the distance in z between the cluster and the vertex in first order. Since there is no second order in the expansion of sinus, the correction is at least of third order.

Hence the deviation observed in fig. 4.28 is fully determined by the performance of the SpaCal

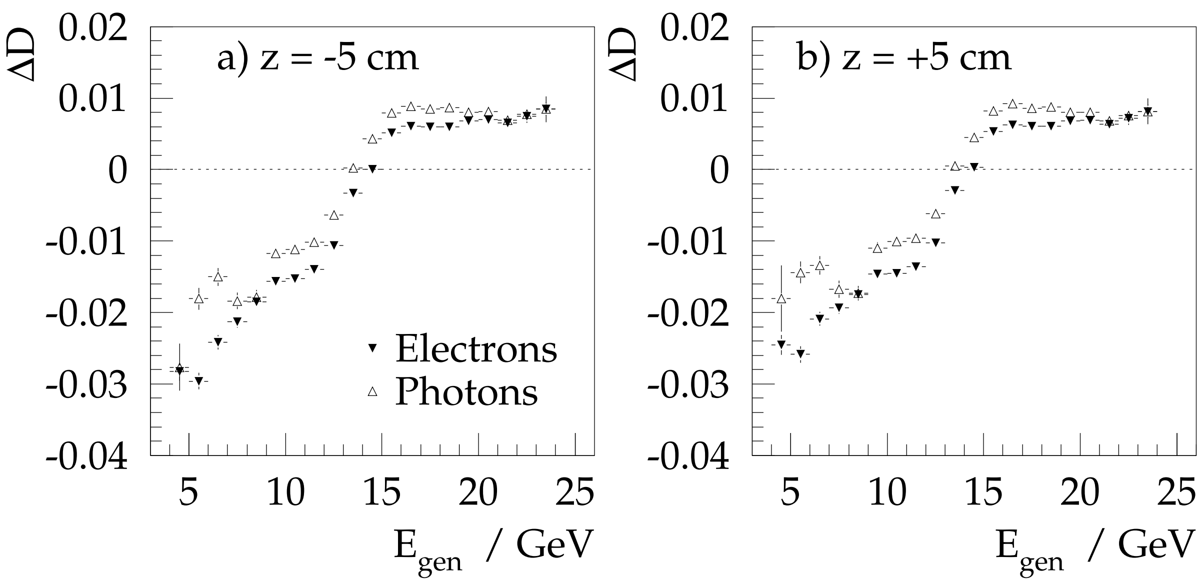

Figure 4.29: *Difference between the double angle and the generated energy in MC is shown. A constant vertex position a)* z_{vtx} *= -5* cm *and b)* z_{vtx} *= 5* cm *is used for the double angle energy calculation.*

angle measurement. It is depicted in fig. 4.30 a as ΔT:

$$\Delta T = \frac{\Theta'_{\mathrm{m}} - \Theta_{\mathrm{g}}}{\Theta_{\mathrm{g}}} \,, \tag{4.41}$$

where Θ_{g} is the generated particle angle and Θ'_{m} is the angle calculated using the SpaCal cluster centre of gravity and the *simulated* vertex position; the angles are also defined relative to the incoming electron direction. Two main effects are visible in the plot:

1. An approximately constant significant difference between the electron and the photon angle measurements;

2. A similar non-linear behaviour of both the electron and the photon ΔT distributions.

The first effect is due to the fact, that the SpaCal cluster z position cannot be measured but just calculated exploiting the results of the longitudinal shower propagation simulation. This calculation has been optimised for electrons and positrons. But a photon, if it is not converted before it reaches the SpaCal, passes roughly $9/7\,X_0$, before it converts to an electron-positron pair (see *e.g.* [kmn89]). Therefore the true cluster z is shifted approximately by $9/7\,X_0 \approx 1.2$ cm deeper in SpaCal. To check this, photons not converted in front of the SpaCal were excluded from the analysis by demanding that both the electron and the photon have associated tracks in the BDC. The distribution of ΔT for such events is depicted in fig. 4.30 b. The constant shift vanishes.

The reason for the second effect is the algorithm of finding the cluster centre of gravity[3]. As can be seen from eq. 4.40, particles with lower energies have larger scattering angles and therefore larger radial coordinates in the SpaCal. It has been shown in an independent analysis [gar00] that the algorithm finding the CoG leads to such radius dependant deviations of the measured angle from its true value.

[3] Logarithmic weighting is used to find the CoG [mur95, poe96].

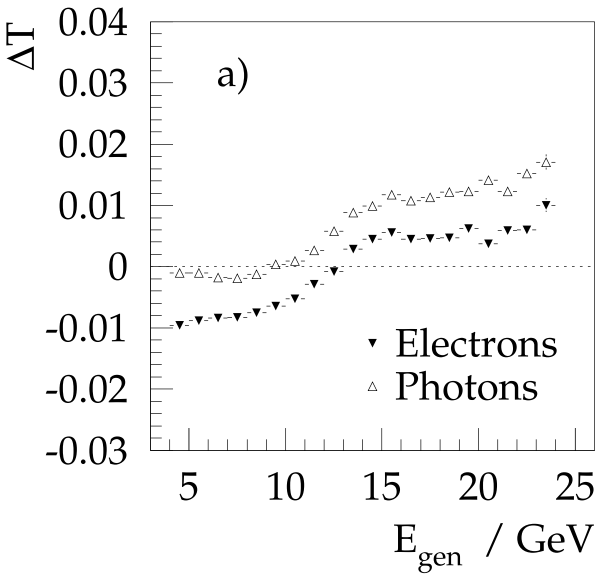

Figure 4.30: *Difference between the generated and reconstructed polar angle in the simulation is depicted a) for all events and b) for events, in which both particles leave tracks in the BDC.*

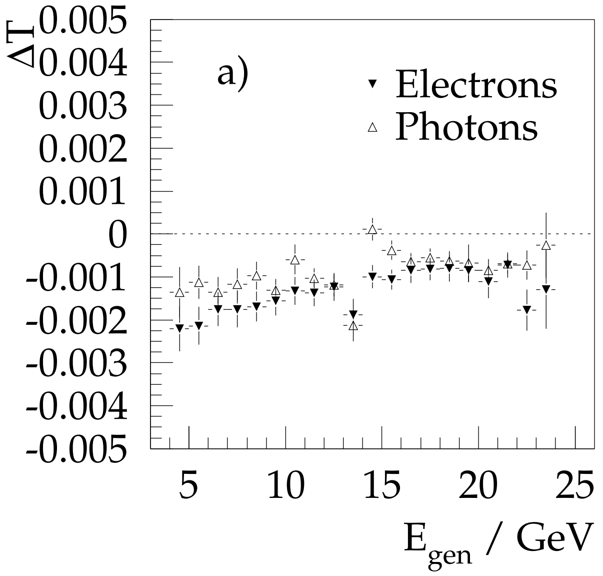

Figure 4.31: *Difference between the generated angle and that reconstructed by the BDC for a) the normal MC simulation and b) the simulation without the magnetic field.*

One way to improve the energy reconstruction with the double angle method is to use BDC track coordinates instead of the cluster CoG. In figure 4.31 a the ΔT is calculated using BDC tracks again demanding that both particles have associated tracks. A tiny deviation from zero of ΔT is due to the magnetic field, which causes a declination of the particle from its original direction resulting in a small shift in θ. Because of showering inside the tracker this shift is larger than that calculated for a single particle and concerns also converted photons. In a simulation without magnetic field the BDC allowes just perfect reconstruction of θ, as displayed

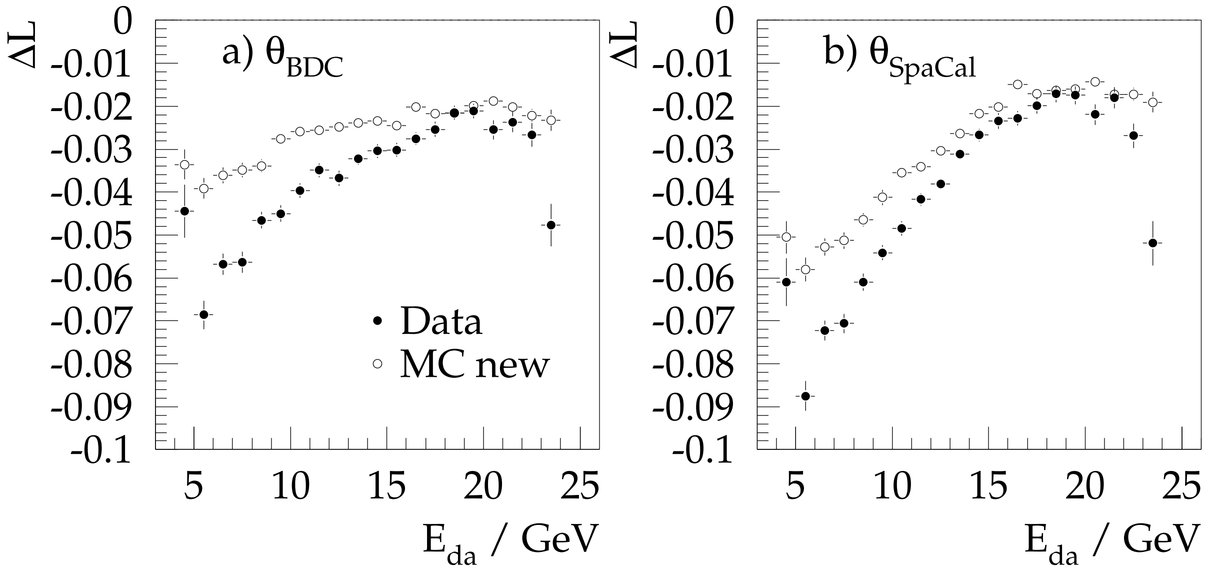

Figure 4.32: *Non-linearity of the energy measurement in the QEDC events, in which both particles left tracks in BDC, obtained using a) BDC and b) SpaCal angle reconstruction for the double angle energy computation.*

in figure 4.31 b.

Figure 4.32 a represents again the energy non-linearity ΔL, but this time with the double angle energy calculated using BDC tracks. A slightly larger difference between the simulation and the data is due to the requirement for both particles to have an associated BDC track, which means that the selection is biased towards particles having more intense interaction with the dead material. Since the inhomogeneity of the dead material is in reality higher, the influence of dead material within this subsample is stronger in the data than in the simulation. In fig. 4.32 b ΔL calculated using the cluster CoG but within the same subsample is plotted. A stronger difference between the data and the simulation is visible, close to that in fig. 4.32 a Since the difference in ΔL between real data and the simulation stays of the same order both using SpaCal cluster CoG and BDC tracks for the double angle energy reconstruction, one can conclude that double angle energy is well described in the simulation.

In order to understand the remaining differences between the simulation and the data, several simulations have been performed with modified H1SIM steering parameters.

One of these parameters is a granularity of geometry definition. Changing the granularity for the central tracker part (H1 GEANT volume "CENT") from default "coarse granularity" to "fine granularity" made no changes in the energy losses.

The next simulation was performed modifying the GEANT energy cut off parameters. These parameters determine, down to which energy particles in showers are simulated. Default H1SIM "GEANT medium cuts" for the shower simulation in the central tracker part are: CUTELE = 10 MeV for the minimum electron energy and CUTGAM = 2 MeV for the minimum photon energy. The new simulation was performed setting "GEANT low cuts" in the volume "CENT": CUTELE = 1 MeV, CUTGAM = 0.2 MeV[4]. The result is displayed in fig 4.33 a. The discrepancy at lower energies remained unchanged in comparison to fig. 4.27.

In another simulation presented in fig. 4.33 b the default "GEANT medium cuts" were kept un-

[4] This simulation consumes approx. 7 times more CPU time than a standard one.

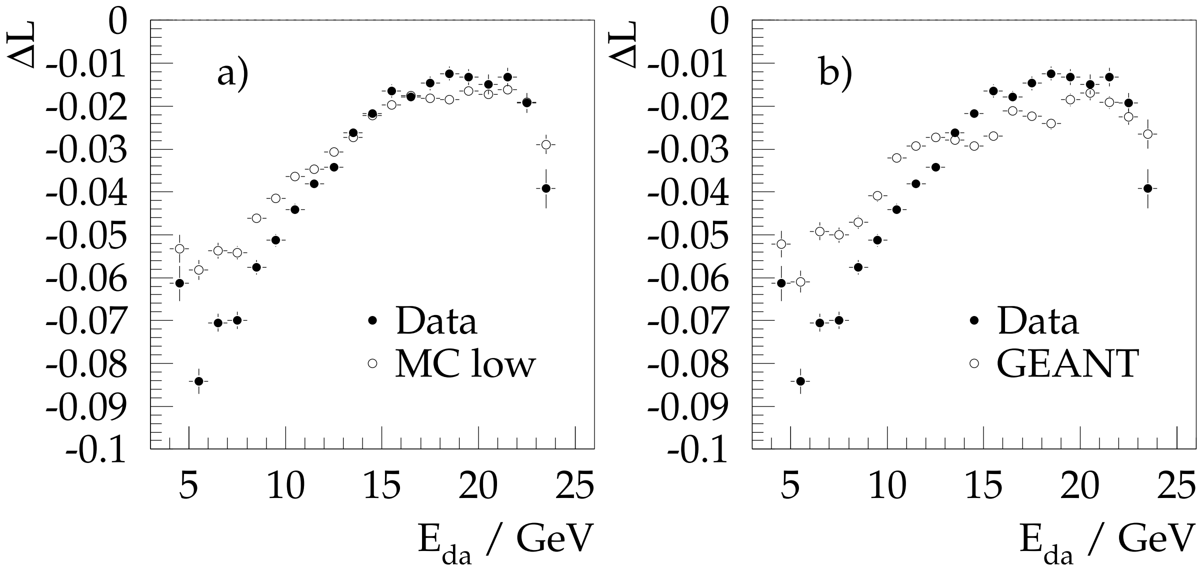

Figure 4.33: *The non-linearity ΔL for special simulations: a) for the simulation with "GEANT low cuts" in the central tracker, b) for the GEANT simulation in the e.m. SpaCal.*

changed in the tracker, but the H1FAST shower parameterisation [gpr90, pha96] was switched off and the full GEANT simulation was enabled in the SpaCal. In this simulation the energy losses at lower energies also remained unchanged.

Thus, the disagreement between real data and the simulation at lower energies remains a mystery and a source of systematic uncertainty. Apart from the studies described here, investigations of possible reasons for this discrepancy were carried out in other analyses [sta98, sie99] but no solution has been found yet. An overview of both studied and not yet investigated effects can be found in [len99].

4.6.3 Corrections of the Polar Angle Reconstruction

For the QEDC cross section measurement a calibration of the SpaCal energy in the 1997 data has been performed. The calibration procedure described in the next paragraph is based on the attained knowledge of the energy scale, whereas the double angle energy is used as a reference scale. For the optimum E_{da} reconstruction it is desirable to reach maximum accuracy of the polar angle measurement for both the electron and the photon. Hence the angle determination procedure, described in sect. 4.5, is employed. This implies also the application of the complete vertex reconstruction algorithm.

In this section several corrections of the systematic shifts occuring in the polar angle measurement are described. These corrections were originally developed on the basis of the above studies of the E_{da} reconstruction, but they are also applied for the QEDC cross section measurement.

In paragraph 4.6.2 it is shown that there is an energy dependent shift of the angle measured using the cluster CoG with respect to the generated angle in MC simulation. In order to make a proper correction both in the data and in the simulation, the relation between the angles

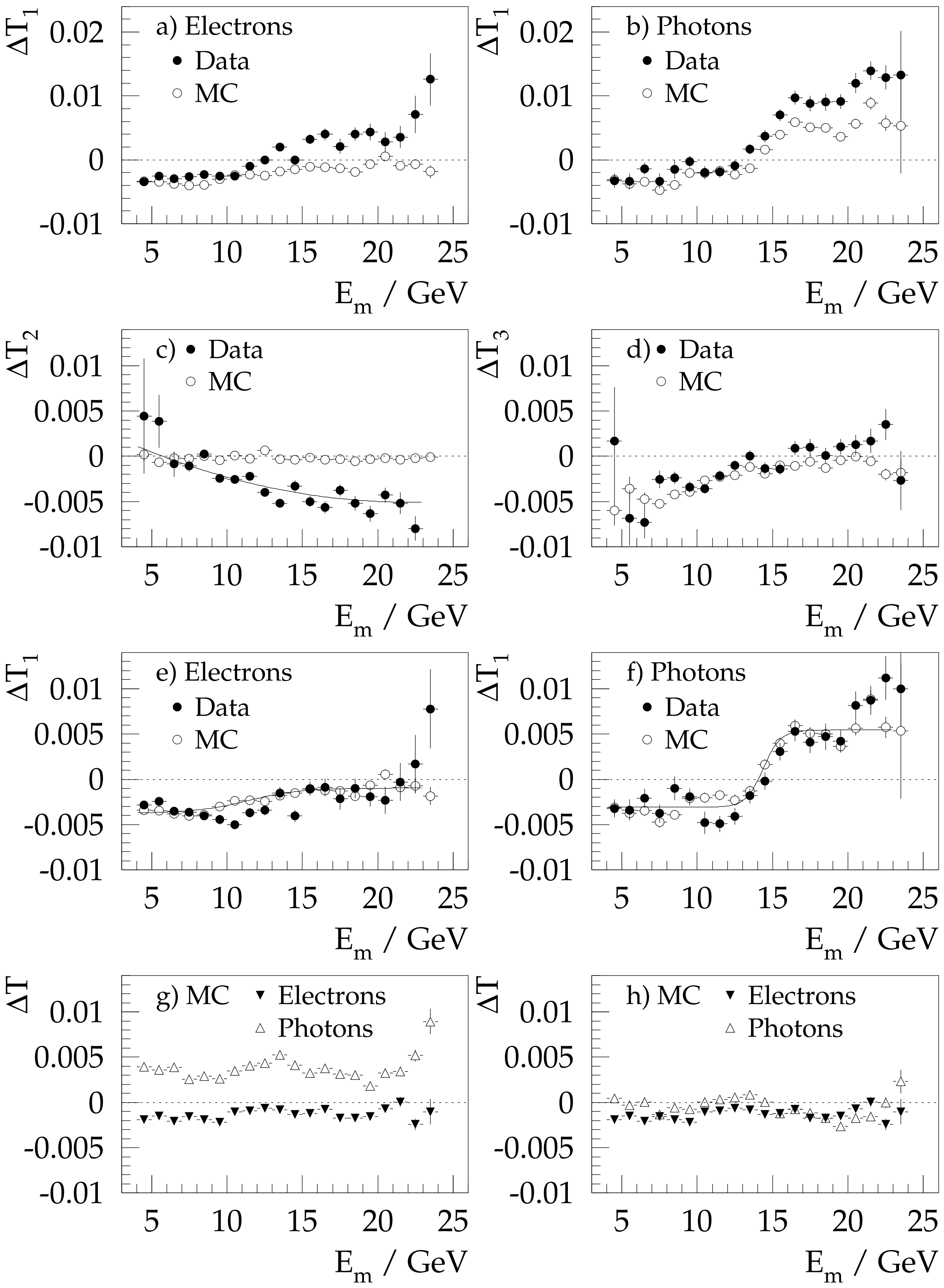

Figure 4.34: *Polar angle reconstruction. See explanation in the text.*

measured by the SpaCal and by the BDC was studied. This relation is given by the quantity

$$\Delta T_1 = \frac{\Theta_{\rm Sp} - \Theta_{\rm BDC}}{\Theta_{\rm Sp}}\,, \tag{4.42}$$

where $\Theta_{\rm Sp} = \pi - \theta_{\rm Sp}$ and $\Theta_{\rm BDC} = \pi - \theta_{\rm BDC}$ are the scattering angles measured relative to the electron beam direction. Like ΔT in paragraph 4.6.2, this quantity is sensitive to transversal shifts rather than to the vertex z position. In fig. 4.34 a and b ΔT_1 is depicted in bins of the cluster energy for the validated electrons and photons, respectively. The photons had to convert in passive material in front of the BDC in order to leave a track in the backward chamber[5].

When comparing these figures to fig. 4.30 one can see that the distributions are slightly different. As pointed out in paragraph 4.6.2 the energy dependence of the SpaCal θ measurement is a consequence of the CoG reconstruction algorithm and of the fact that lower energies correspond to higher radii. Therefore the actual behaviour of the ΔT_1 distribution can vary depending on the radial distribution of particles in the event sample. The sample used in fig. 4.34 contains only events passing the full particle identification procedure, which implies stronger lower limits of the cluster radial coordinate due to the tracker acceptance. The difference between the distributions in fig. 4.34 a and b is due to the same effect, namely, due to different θ spectra of electrons and photons.

A common effect observed in both upper plots of fig. 4.34 is a tiny disagreement between the data and the simulation. In order to understand if it is feature of the BDC or the SpaCal reconstruction, both angles are confronted to the BST θ in the subsample of electrons having a BST track. For the comparison similar quantities are introduced:

$$\Delta T_2 = \frac{\Theta_{\rm BDC} - \Theta_{\rm BST}}{\Theta_{\rm BDC}}\,, \qquad \Delta T_3 = \frac{\Theta_{\rm Sp} - \Theta_{\rm BST}}{\Theta_{\rm Sp}} \tag{4.43}$$

with $\Theta_{\rm BST} = \pi - \theta_{\rm BST}$. These variables are depicted in fig. 4.34 c and d, respectively. From these plots it becomes clear that the discrepancy occurs in the BDC reconstruction. The reason for this deviation is, however, not clear. It was corrected for by parameterising the ΔT_2 distribution with the polynomial fit

$$P^{\rm BDC}(E) = a + bE + cE^2 \tag{4.44}$$

with $a = 4.20 \cdot 10^{-3}$, $b = -8.42 \cdot 10^{-4}\,{\rm GeV}^{-1}$ and $c = 1.92 \cdot 10^{-5}\,{\rm GeV}^{-2}$ and multiplying $\Theta_{\rm BDC}$ by $1 - P^{\rm BDC}$. The fitting function is also shown in fig. 4.34 c.

The ΔT_1 distributions after this correction are displayed in fig. 4.34 e and f. A good agreement between the data and MC points is observed. These distributions were fitted by functions of the form

$$P^{\rm Sp}(E) = \frac{a}{1 + \exp\left[-\frac{E-c}{b}\right]} + d\,, \tag{4.45}$$

as indicated by the solid lines shown in the same plots, with $a = 2.78 \cdot 10^{-3}$, $b = 1.757\,{\rm GeV}$, $c = 11.39\,{\rm GeV}$, $d = -3.74 \cdot 10^{-3}$ for the scattered electrons and with $a = -8.53 \cdot 10^{-3}$, $b = -0.575\,{\rm GeV}$, $c = 14.37\,{\rm GeV}$, $d = 5.44 \cdot 10^{-3}$ for the photons. The angle $\Theta_{\rm Sp}$ was then multiplied by the factor $1 - P^{\rm Sp}$ both in data and in simulation.

[5]On the other hand they must not have converted while passing the central chambers, because otherwise they wouldn't have been validated as photons. The conversion occurs, thus, in the region of the central tracker electronics and cables situated behind the central tracking chambers.

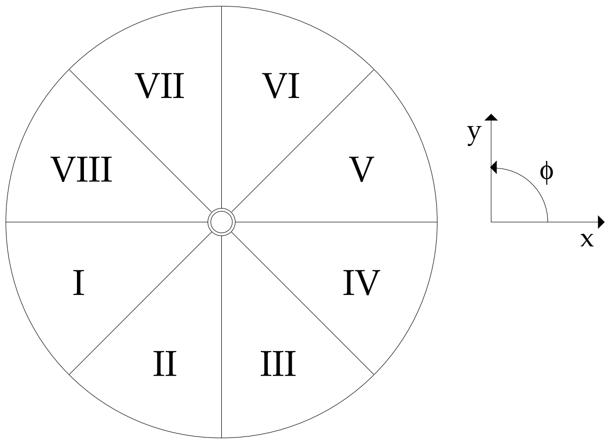

Figure 4.35: *Arrangement of the ϕ octants in the SpaCal, in which the calibration procedure is performed.*

Table 4.5: *Parameters for the SpaCal energy calibration procedure.*

Octant	First Step						Second step		
	Parameters for f^{data}			Parameters for f^{MC}			Parameters for f^{gen}		
#	a, GeV	b, GeV	c, GeV^{-1}	a, GeV	b, GeV	c, GeV^{-1}	a, GeV	b, GeV	c, GeV^{-1}
I	-0.0142	0.0058	0.03594	0.0045	0.0045	0.01196	-0.0116	0.0049	0.03599
II	-0.0203	0.0464	0.20865	-0.0119	0.0727	0.15473	-0.0164	0.0362	0.18487
III	-0.0156	0.0051	0.03594	-0.0200	0.0782	0.23057	-0.0173	0.0787	0.28073
IV	-0.0210	0.0514	0.19917	-0.0173	0.0696	0.14473	-0.0171	0.0297	0.16539
V	-0.0217	0.0563	0.23119	-0.0206	0.1145	0.18549	-0.0176	0.0669	0.29454
VI	-0.0238	0.1289	0.37646	0.0035	0.0042	0.00858	-0.0192	0.1613	0.44058
VII	-0.0190	0.0222	0.13702	0.0203	0.0043	0.00707	-0.0130	0.0041	0.03597
VIII	-0.0226	0.0617	0.25824	-0.0072	0.1357	0.18307	-0.0185	0.0698	0.29311

The last correction was performed for the angle Θ_{Sp} of not converted photons. As explained in paragraph 4.6.2, the z shift of clusters produced by photons leaving no track in the BDC leads to a constant deviation of their reconstructed polar angle from the true one. The last correction consists, thus, in the increase of the absolute value of the z coordinate for such clusters by 1.2 cm.

This effect can be studied in the MC sample only, comparing the generated and the reconstructed polar angle, for there is no other reference angle than Θ_g in MC events. The ΔT distributions before and after the last correction are depicted in fig. 4.34 g and h, respectively, for electrons and photons. A constant discrepancy between both distributions, observed in the first plot vanishes. This correction was again applied for both data and simulation.

4.6.4 Energy Calibration

The energy calibration procedure described below follows, in principle, the algorithm employed in [sff98, sta98] but with improved understanding of the SpaCal energy scale and of the effects influencing the non-linearity distributions. The calibration is performed separately for eight ϕ intervals in the SpaCal, as depicted in fig. 4.35. The ΔL distributions in E_{da} bins are plotted for the octants in fig. 4.36. As before the double angle energy is chosen for the binning, in order to minimise migration effects, as discussed in paragraph 4.6.2.

The calibration procedure involves two iterations. In the first step the SpaCal energy scales in

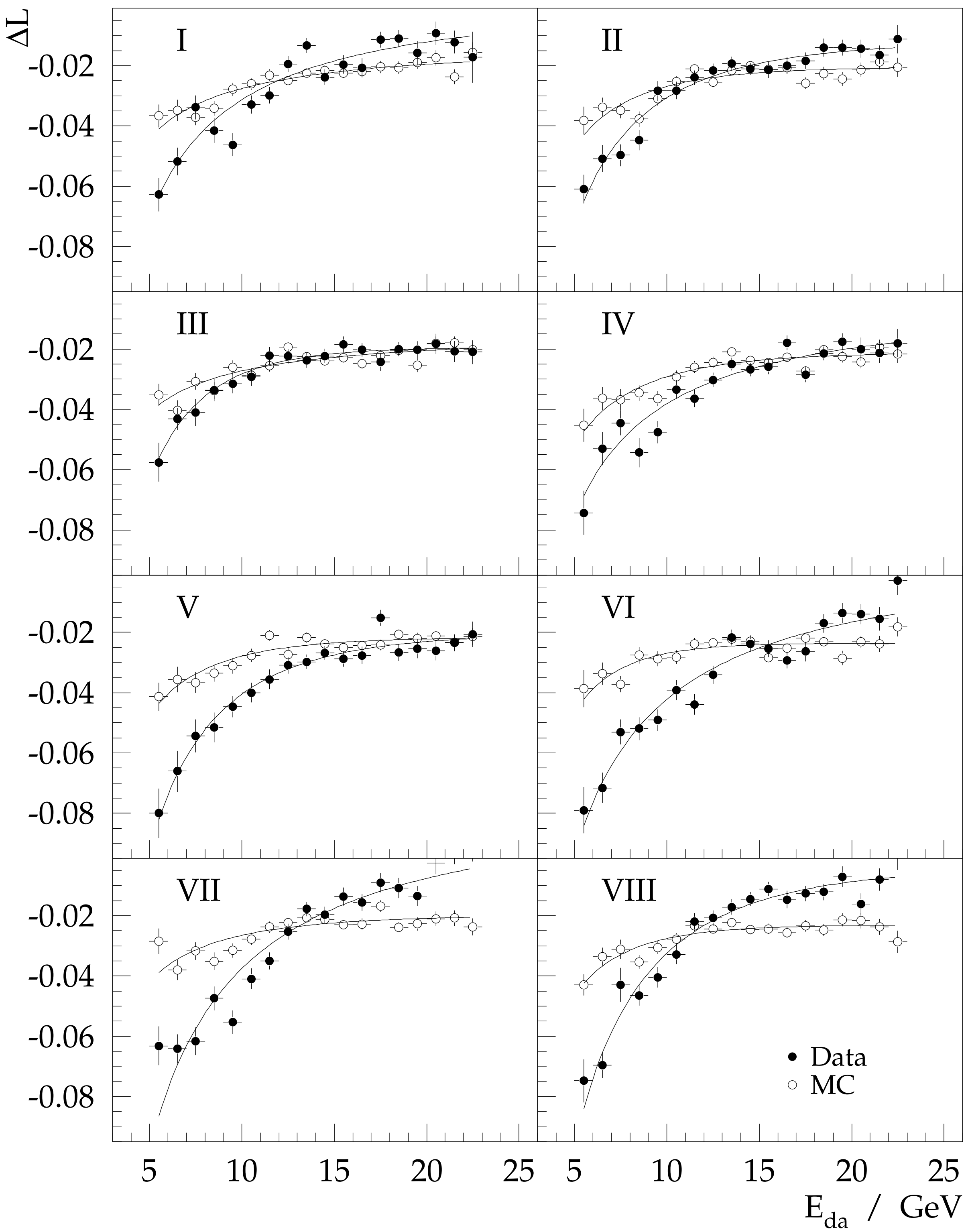

Figure 4.36: *Non-linearity ΔL of the SpaCal energy scale in data and simulation plotted in ϕ octants.*

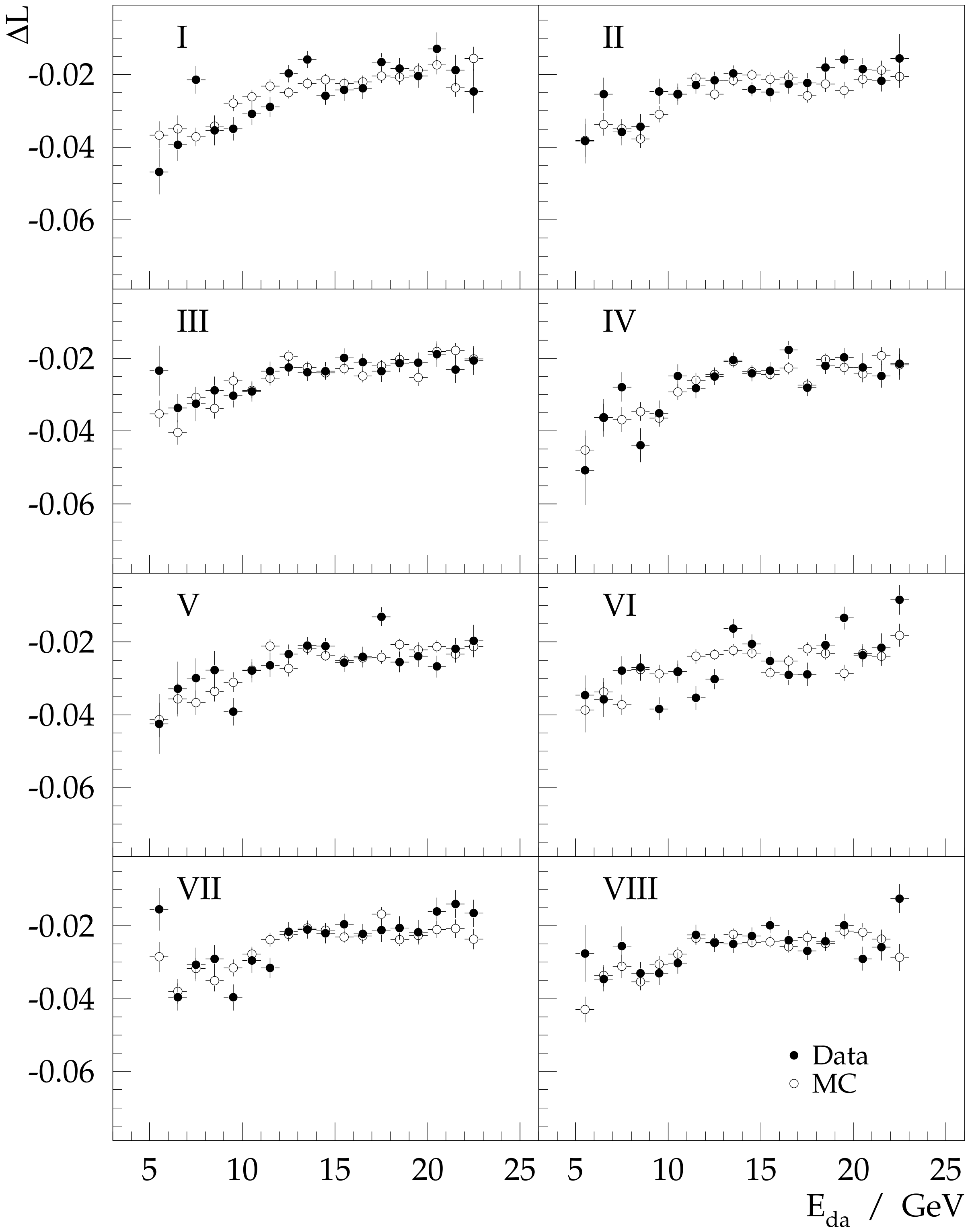

Figure 4.37: *Non-linearity ΔL of the SpaCal energy scale in the data and the simulation after the first calibration step.*

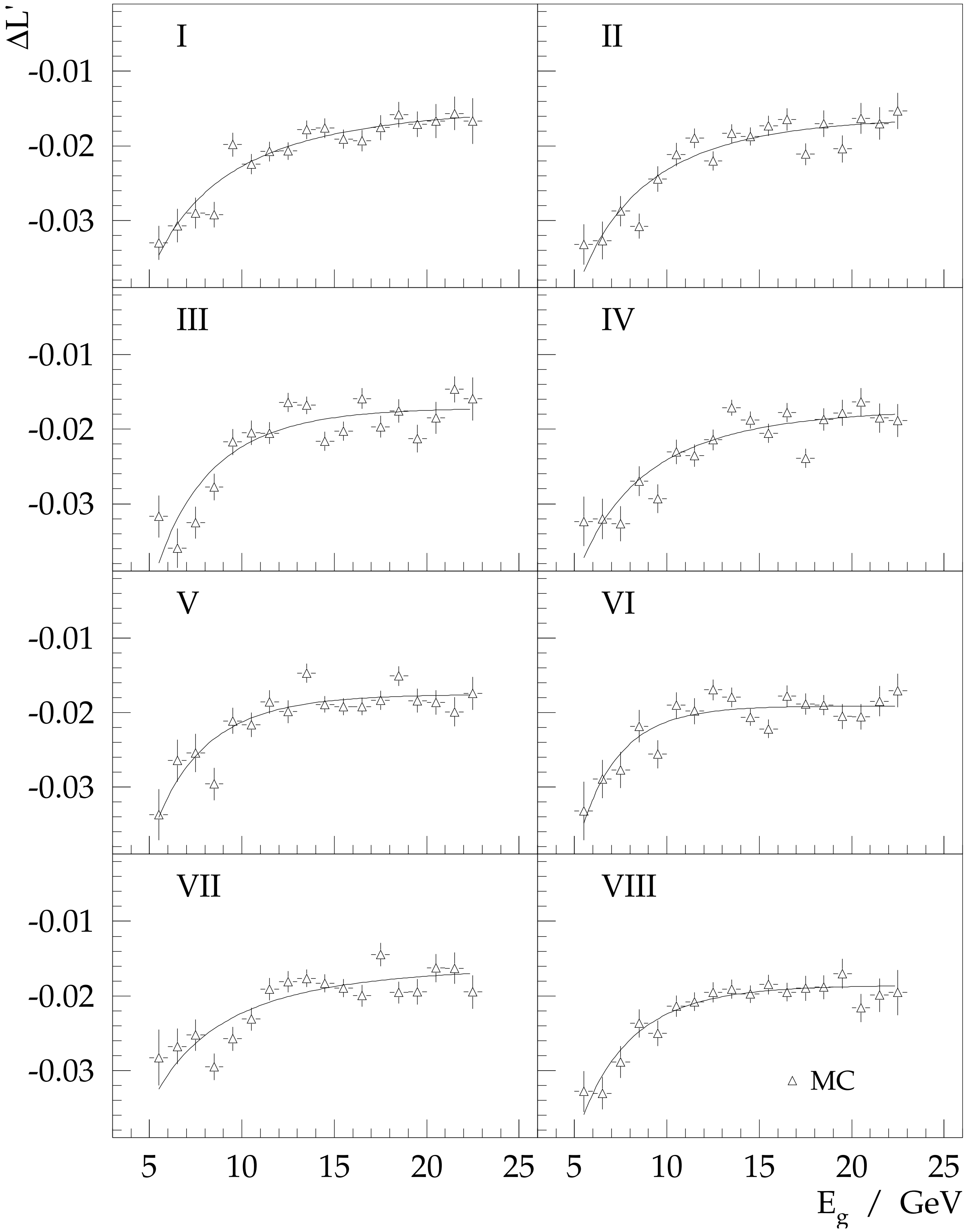

Figure 4.38: *Non-linearity $\Delta L'$ as given by the simulation.*

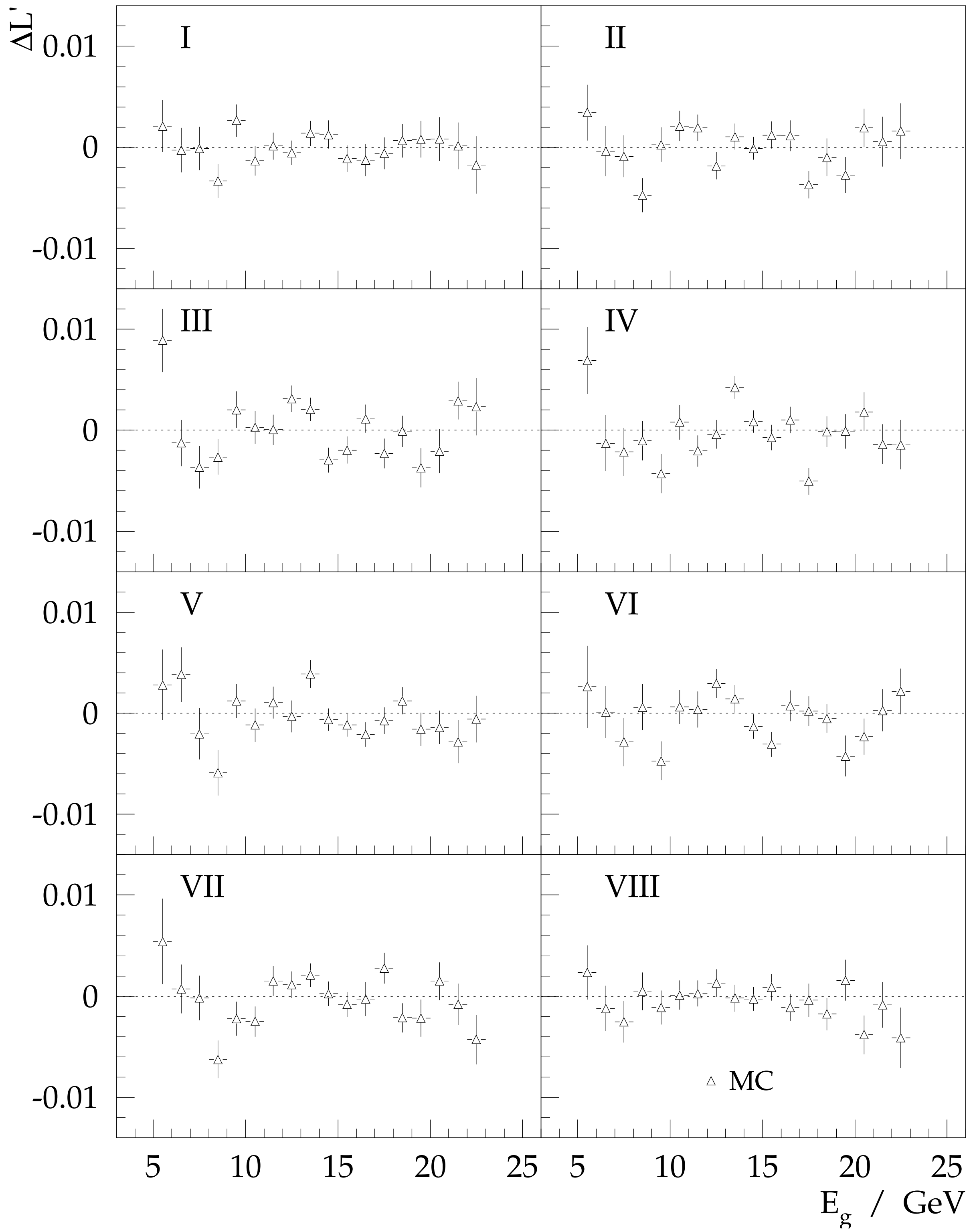

Figure 4.39: *Non-linearity $\Delta L'$ in the simulation after the second calibration step.*

the data and in the simulation are equalised. This is achieved as follows:

1. The non-linearity distributions in the data and the simulation are fitted by functions f^{data} and f^{MC} of the form

$$f(E) = a + \frac{b}{1 - \exp(cE)} \,. \tag{4.46}$$

   The fits are made in the slightly narrowed energy range $5 < E < 21$ GeV, to avoid regions with strong migrations. The fitting functions are displayed together with the ΔL distributions in fig. 4.36 and the fit parameters are listed in table 4.5.

2. The energy E_{m} of each cluster in each event of the data is multiplied by a correction factor, based on the above parameterisations:

$$E'_{\text{m}} = E_{\text{m}} \frac{1 + f^{\text{MC}}(E_{\text{m}})}{1 + f^{\text{data}}(E_{\text{m}})} \,, \tag{4.47}$$

   while the energy scale in the simulation is not changed: $E'_{\text{m}} = E_{\text{m}}$. The result of this recalibration step is presented in fig. 4.37. The data points are now shifted so as to coincide with the Monte Carlo points.

The equalisation of the energy scales is necessary for the cross section measurements with the Monte Carlo method. The calibration procedure involves however also a second iteration, in which both the real and the simulated energy scales are shifted upwards, in order to reproduce, as close as possible, the true energy of the particles. This calibration step does not affect the cross section measurement with the Monte Carlo method, but it may be useful for other H1 analyses, in which the knowledge of the absolute energy scale is required. For the second correction the non-linearity $\Delta L'$, as given by the simulation (see eq. 4.38), is employed. In fig. 4.38 it is depicted in E_g bins for the same ϕ octants. The calibration is then performed as follows:

1. The $\Delta L'$ distributions are parameterised by functions f^{gen} of the same form as above. The fitting functions are also depicted in fig. 4.38, and the fit parararameters are summarised in table 4.5.

2. The final energy scale is computed as

$$E_f = \frac{E'_{\text{m}}}{1 + f^{\text{gen}}(E'_{\text{m}})} \tag{4.48}$$

   from the cluster energy in the simulation and from the cluster energy recalibrated in the first step in the data. The result of this recalibration step in the simulation is depicted in fig. 4.39. The average recalibrated energy is now equal to the original particle energy within 0.5%.

4.6.5 Energy Resolution

It has been shown in [sta98] that there is a discrepancy in the SpaCal energy resolution between MC and data, and that this disagreement can be in principal eliminated by additional dead material put into the simulation. The amount of additional material required to achieve

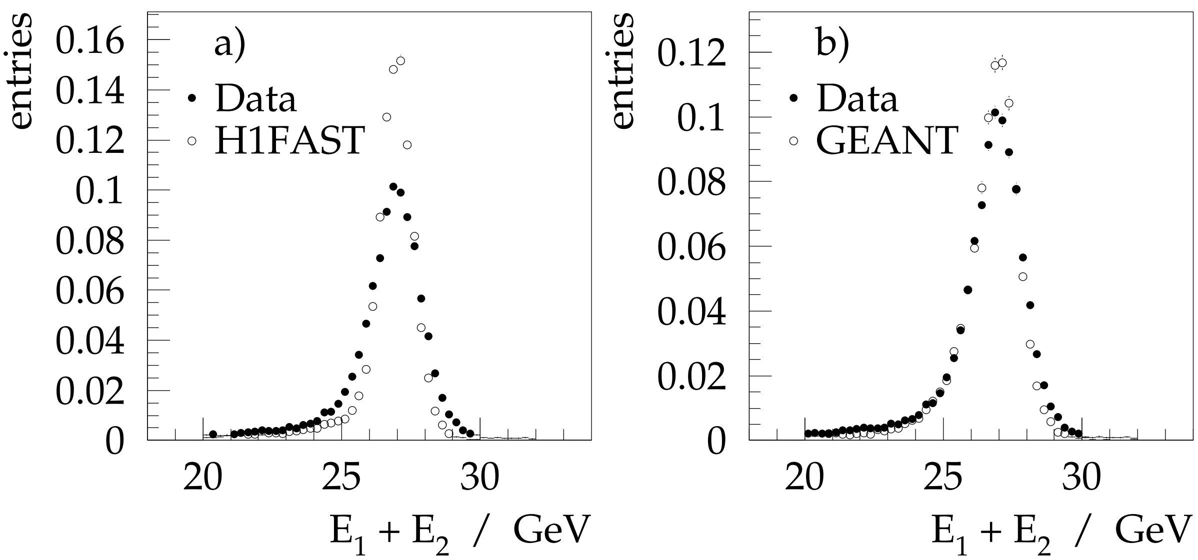

Figure 4.40: *Sum of the two SpaCal cluster energies in the data and MC simulation using a) the H1FAST and b) the GEANT package. Histograms are normalised so as to have equal total content.*

an agreement between MC and data is, however, unrealistically high, and there must be other reasons for the discrepancy. In fig. 4.40 a the sum of cluster energies $E_1 + E_2$ with the new material in the simulation is demonstrated. The width of the distribution is directly correlated with the energy resolution. As in paragraph 4.6.2, the 1996 data are used and the particle identification is not performed. In fig. 4.40 b, in which the GEANT simulation in the SpaCal is presented, a much better agreement between real data and the simulation is visible. Thus, as in the case of the lateral shower profile (see sect. 4.2.4), the observed difference between the measured and simulated energy resolution is mainly due to the rough shower parameterisation employed in the H1FAST program.

For the cross section measurement with the Monte Carlo method the simulated and the real energy resolution must be equalised. This is achieved by an additional Gaussian smearing of the simulated resolution. In doing so an additional effect has to be taken into account, namely, that the real energy resolution of the SpaCal varies significantly for different cells. In particular, the innermost cells have been found to have in average a poorer resolution than the others. After the electron/photon validation and the application of the fiducial cuts on the BST and CIP acceptance, described in paragraph 4.4.4, an additional part of the inner SpaCal is excluded from the analysis. The sum of cluster energies after the complete event selection and particle identification procedure in the 1997 data is depicted in fig. 4.41 a). It can be seen, that the energy resolution of the data in this final sample is better than just after the basic event selection, as shown in fig. 4.40. After an additional smearing of the simulated cluster energy with a factor of 1.5%, full agreement is achieved, as displayed in fig. 4.41 b).

With a closer look at fig. 4.41 b a small shift between both distributions can, however, still be noticed. This shift arises from a tiny difference between the simulated and real electron beam energy E_{e0}. After subtracting E_{e0} from the sum of cluster energies, as depicted in fig. 4.41 c, the agreement between the data and the simulation becomes nearly perfect. To avoid systematic shifts in kinematic distributions, the electron beam energy has been rescaled in all real and simulated events to the constant value of 27.6 GeV. The same rescaling factor has also been

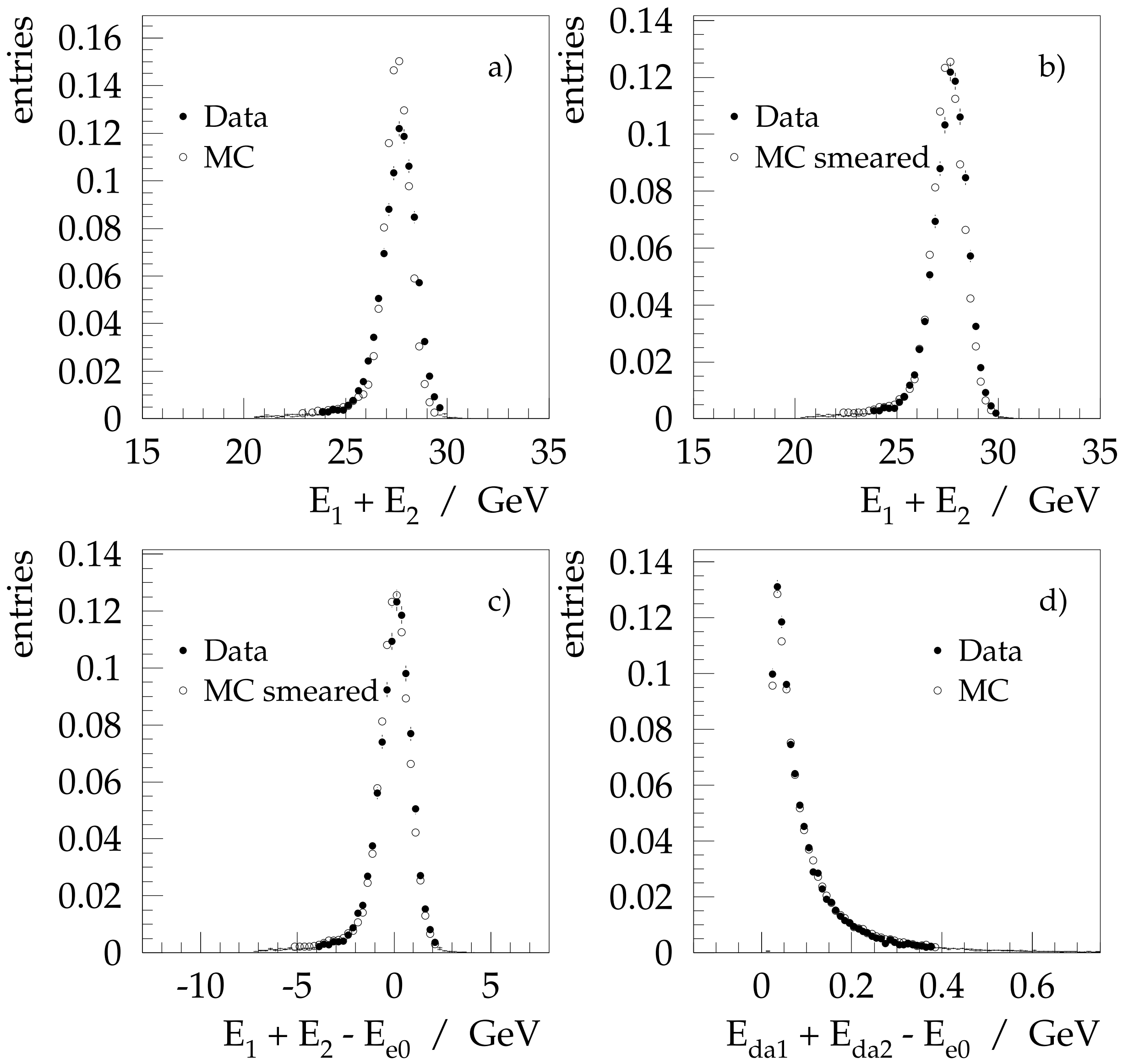

Figure 4.41: *In the upper figures the sum of the two SpaCal cluster energies in the data and MC simulation is plotted a) before and b) after the additional Gaussian smearing. In fig. c) the electron beam energy is subtracted from the cluster energy sum. In fig. d) the double angle energy is plotted instead of that measured by the SpaCal. Histograms are normalised so as to have equal total content.*

applied to the the energies of the final state electron and photon.

For comparison the double angle energies are used instead of the cluster energies in fig. 4.41 d. As mentioned in the previous paragraph the double angle method provides a better resolution than the SpaCal measurement. However, the use of E_{da} for the cross section measurement would lead to migration effects in the inelastic QEDC events. In particular, the tail of the $E_1 + E_2$ distribution below the electron beam energy is not reconstructed at all.

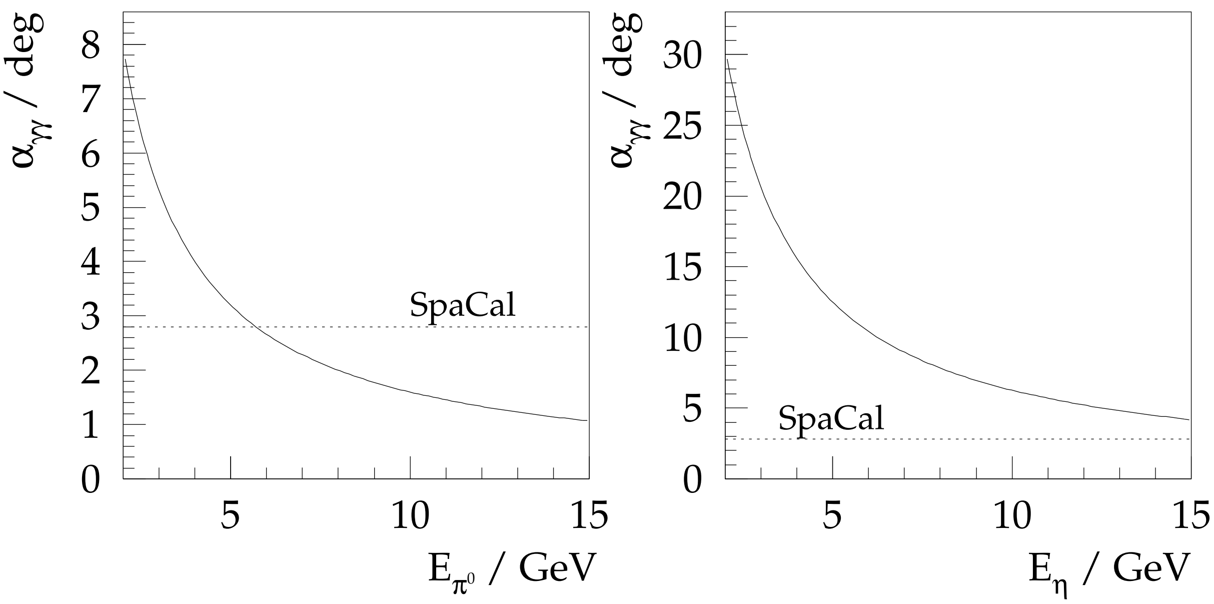

Figure 4.42: *Minimum opening angle of two photons in π^0 (left) and η (right) meson decays. The dotted line corresponds approximately to the minimum angle required for the photons to be separated as two clusters in SpaCal.*

4.7 Study of DIS Background

As mentioned in paragraph 3.2.2 an unexpectedly large number of DIS background events fulfilling QEDC selection criteria has been generated by DJANGO. In more than 90% of these events the second SpaCal cluster is created by one or two photons produced by a single π^0 and the remaining contribution is made by photons resulting from η or ω decays or charged pions. More than 90% of detected π^0 mesons arise directly as a result of the fragmentation of the hadronic final state, which is denoted as a "cluster" or a "string" in the generator output banks. The others are produced in the decay of $\rho^\pm$ or K^0 mesons. In approx. 75% of events no other hadron is generated except for a single π^0, while in the other events there are one or two additional hadrons. Only about 2% of all events have a large hadron multiplicity, which is expected for the hadronic mass range in question.

The unlikely high rate of such events has necessitated a direct determination of their contribution from real data. This was done by two complementary methods: studying three cluster events and by means of shower shapes. Both methods exploit very well known features of π^0 decays. In 98.8% of the cases a neutral pion decays into two photons isotropically in its rest frame. This allow us to compute exactly the distribution of the opening angle between them in the laboratory frame for a given energy of the meson. The minimum angle $\alpha_{\gamma\gamma}$ is plotted in fig. 4.42 a as a function of the π^0 energy. Most photon pairs are produced with an opening angle very close to the minimum one. In the SpaCal the two photons can make one common cluster or two separate clusters depending, first of all, on the opening angle. The cluster separation, which is constrained by the cell size and the clustering algorithm, becomes possible at approx. 8 – 9 cm distance between the cluster CoGs in the xy plane. The angle corresponding to approx. 8 cm is denoted by the dotted line in fig. 4.42 a. It is visible that at energies below 5 – 6 GeV mainly two clusters are produced, while at higher energies both photons merge more often into a single cluster.

A similar plot is shown in fig. 4.42 b for η mesons, which decay with 38.8% branching ratio into two photons. Due to their higher mass the opening angle of the photon pair is, however, larger, therefore the two photons usually produce two clusters in the SpaCal.

Below the two methods of the DIS background estimation are discussed in detail.

4.7.1 Three-Cluster Events

In this investigation events with a third SpaCal cluster, in addition to the electron and the photon cluster candidate, are selected. The idea of the method is to determine the rate of those DIS events, in which one cluster is produced by the scattered electron and the two other clusters are created by the two photons from a π^0 decay. Basically the same event selection and particle validation procedure has been applied as for QEDC events with the following changes:

- A third cluster with the minimum energy of 2 GeV is demanded;
- The residual energy in the SpaCal is redefined as

$$E'_{\mathrm{res}} = E_{\mathrm{Sp}} - E_1 - E_2 - E_3, \tag{4.49}$$

  and the same limit of 1 GeV is imposed on the redefined quantity;
- Both the anti-validated cluster (such a cluster is considered to be the final state photon in the QEDC events) and the third cluster are detected closer in ϕ to each other than to the electron. This requirement is imposed in order to suppress events, in which the third cluster is created by a photon from the FSR tail;
- The acoplanarity limit of 45° is applied on the acoplanarity A' between the electron and the centre of mass of two other particles. If the two other clusters really originate from one meson this cut ensures the same kinematic configuration as is actually in the DIS background events, *i.e.*, in case both photons from the pion decay make a common cluster;
- A minimum distance of 8.5 cm in the xy plane between the anti-validated cluster and the third cluster is demanded, to minimise possible disagreement between the data and the simulation, as discrepancies may occur on the boundary of cluster separation due to different lateral shower profiles.

After applying these requirements the neutral pions are selected according to the invariant mass m_{2c} of the anti-validated and the third cluster, as depicted in fig. 4.43. Two strong peaks, produced by π^0 ($m \approx 135$ MeV) and η ($m \approx 547$ MeV) are visible in the simulated distribution[6]. The data reveal, however, a much smaller rate of π^0 and η mesons. The ratio of simulated to real events near the π^0 peak, equal to 18.6, has been employed to renormalise the DJANGO signal. The renormalised sample has been then used for modelling the DIS background.

The contribution of the DIS background events is thus estimated to be of the order of 1%. In an H1 analysis of the DVCS events [sta01] the same problem occured for events with a final state photon detected in the LAr calorimeter. An analogous estimate by means of three-cluster events yielded a similar result.

[6]Other narrow peaks are produced by single events, and appear due to smaller luminosity of the DJANGO sample compared to the data.

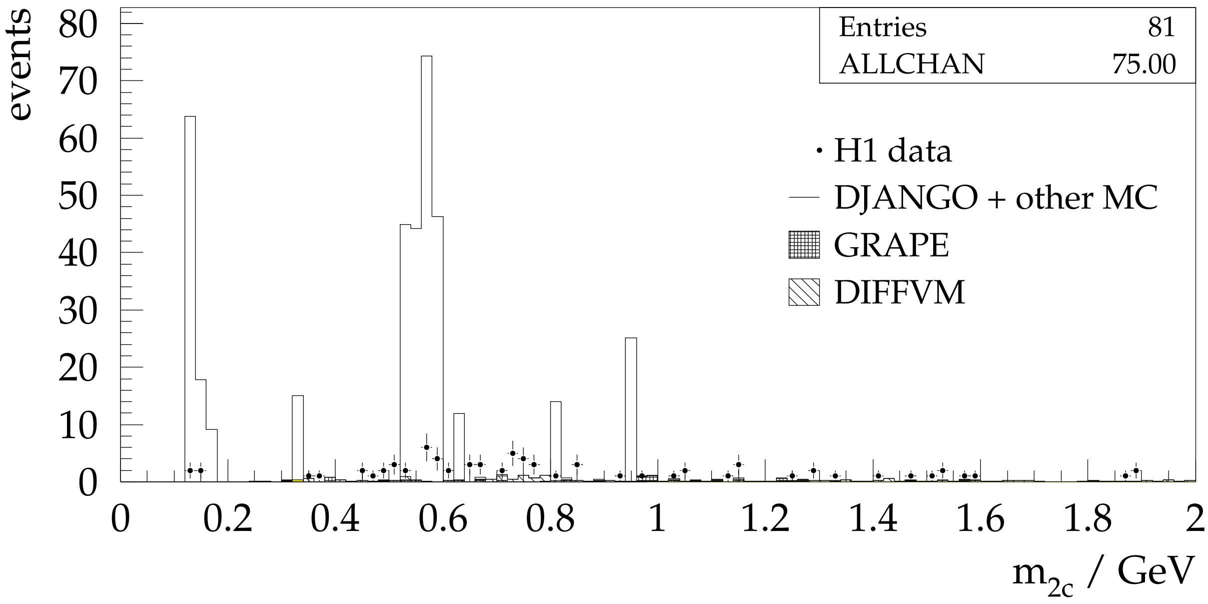

Figure 4.43: *Invariant mass of two particles in events with three selected clusters. The anti-validated cluster and the third energetic cluster are taken for the calculation. The closed circles depict the events of the standard 1997 data sample. The solid line denotes the DJANGO signal with all other simulated signals added. All generated samples are normalised so as to have the same effective luminosity as the data.*

The reason for the wrong DJANGO signal is not clear. One possible explanation is that the JETSET string fragmentation package is optimised for large hadron multiplicities and hence describes only inclusive properties of the hadronic final state but may fail to reproduce exclusive spectra and low multiplicity events. However, other explanations of the incorrect event generation are also possible. In particular, in a previous H1 analysis of QEDC events [mar98] using 1994 data the DIS background generated by DJANGO was found to be negligible. The earlier version of DJANGO, employed in that study, also involved the JETSET fragmentation, but did not use the ARIADNE package for the generation of parton showers.

4.7.2 Shower Shapes

In contrast to the previous approach, this method considers events with two photons originating from a π^0 and producing one common SpaCal cluster. In a calorimeter, in which the cells are stacked so as to point to the vertex position, a single photon would create a cluster of a circular lateral profile, while two photons would produce an oval cluster. The SpaCal cells are stacked parallel to the beam direction, so that a particle coming from the interaction vertex penetrates them under its polar angle θ and therefore a single particle does not make an exactly circular cluster. Nevertheless different shapes for one-particle and two-particle clusters can still be observed.

The shower shapes are described quantitavely by means of the second moments of the energy distribution in the cells of the cluster. The second moments about the cluster's centre of gravity $\hat{x}, \hat{y}$ are defined as (see, for instance, [bra83])

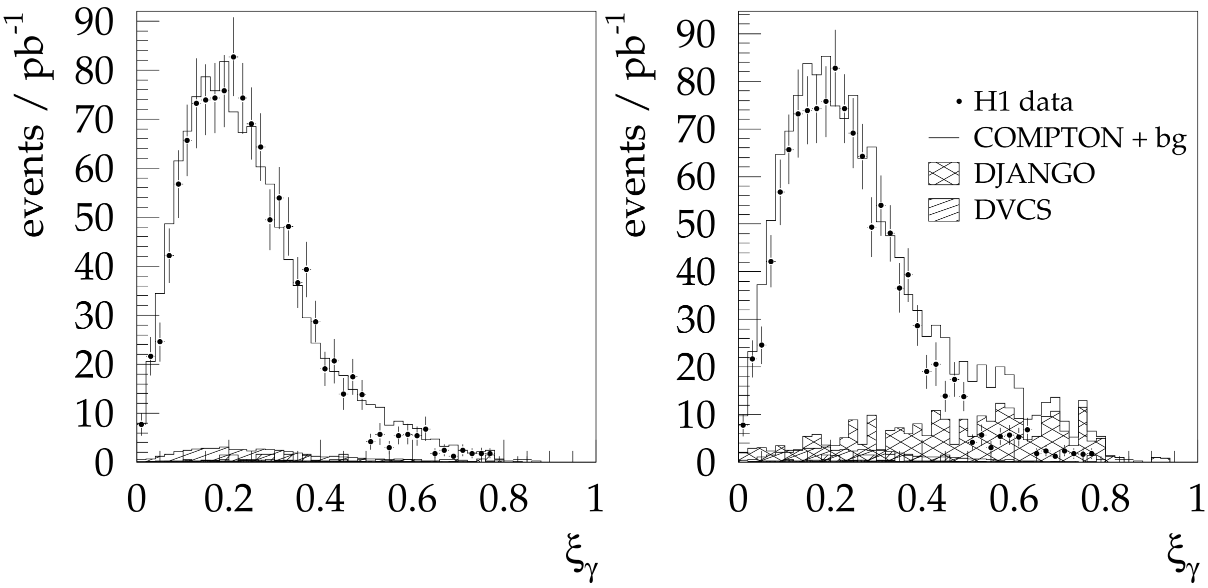

Figure 4.44: *Anti-validated cluster eccentricity. The data (closed circles), the sum of all simulated signals (solid line) and all background contributions are plotted. The renormalised and the original DJANGO signals are depicted in the left and right figure, respectively.*

$$\mu^2_{xx} = \frac{\sum_i w_i (x_i - \hat{x})^2}{\sum_i w_i}\,, \qquad \mu^2_{yy} = \frac{\sum_i w_i (y_i - \hat{y})^2}{\sum_i w_i}\,,$$
$$\mu^2_{xy} = \frac{\sum_i w_i (x_i - \hat{x})(y_i - \hat{y})}{\sum_i w_i} \equiv \mathrm{cov}(x,y)\,, \tag{4.50}$$

where the summations are perfomed over all cells forming the cluster and w_i are energy dependent weighting factors. In this study the logarithimic weighting is used, so that the factors introduced in eq. 4.11 for the definition of the logarithmic cluster radius are employed. The cluster radius can thus be written as: $\mathrm{ECRA}_{\log} = (\mu^2_{xx} + \mu^2_{yy})^{1/2}$.

If the cluster is considered to be an ellipse the main axes of this ellipse a and b have to be found. They define a new coordinate system, which is rotated with respect to the H1 frame of reference by the angle ω given by the expression

$$\tan 2\omega = \frac{2\mu^2_{xy}}{\mu^2_{xx} - \mu^2_{xy}}\,. \tag{4.51}$$

In the new coordinate system the transformed second moments μ^2_{aa}, μ^2_{bb} and μ^2_{ab} can be calculated according to the same eq. 4.50. By this, the covariance μ^2_{ab} is equal to zero, and μ^2_{aa} and μ^2_{bb} define the squared axes of the ellipse. The eccentricity of the ellipse given by

$$\xi = 1 - \frac{\mu^2_{bb}}{\mu^2_{aa}}\,, \qquad 0 \leq \xi \leq 1\,, \tag{4.52}$$

is used as the measure of its form. For a circle $\xi = 0$ holds, and the larger ξ gets, the more stretched the cluster profile becomes.

The distribution of the eccentricity ξ_γ of the anti-validated cluster, *i.e.*, of the cluster identified as the photon, is depicted in fig. 4.44. In the left plot the DJANGO sample renormalised with the three-cluster events is used, while the right plot shows the original DJANGO distribution. It can be seen that the simulation provides a reasonable description of the eccentricity and the data are compatible with the renormalised or even absent DJANGO signal. The original DJANGO signal predicts, however, a large contribution at $\xi_\gamma \gtrsim 0.5$, which is not observed in the data. One should remark, that it would be incorrect to impose a cut on ξ_γ instead of renormalising the DJANGO signal, in order to suppress the DIS background, because the admixture of DJANGO events at lower ξ_γ values would still add a wrong contribution to the cross section.

4.7.3 Limits of Systematic Errors

Although the DJANGO renormalisation factor is determined using three-cluster events, there is a significant statistical uncertainty of the obtained DIS background contribution. Due to the very low number of three-cluster events in the data the systematic error of the normalisation factor is taken to be 100%. However, since the DJANGO signal is found to be generally wrong, one cannot be sure that it is only the question of the common normalisation. The damping factor was determined at low π^0 energies, at which the opening angle of the photon pair is large enough, and it is not clear if it holds also for higher energies. The upper systematic uncertainty for higher energies had, thus, to be estimated from an additional consideration, as described below.

A single pion found in the SpaCal in a DIS event without any other hadrons in the detector represents actually a DIS jet with a particle multiplicity equal to one. Consequently, the probability P_{π^0} to detect such a pion is given by the expression

$$P_{\pi^0} = P_{\text{jet}} \cdot P_{\text{jet}=\pi^0}, \tag{4.53}$$

where P_{jet} is the probability that the centre of mass of the jet falls into the SpaCal acceptance and $P_{\text{jet}=\pi^0}$ is the probability that the jet consists of a single neutral pion. It is obvious that this second quantity cannot rise with the energy of the jet. The most conservative estimation is thus to assume this probability to be equal to its value at low energies, and the upper limit to be given by the inclusive jet distribution.

This distribution is approximately computed as follows. An independent sample of inclusive DIS events generated by DJANGO with the scattered electron falling into the SpaCal acceptance is selected. The simple Quark Parton Model is assumed, and the energy and angle distributions of a "jet" are computed from the electron parameters, as it can be done for the struck quark in the QPM, employing the energy and momentum conservation laws. Finally the events with both the scattered electron and the "jet" falling into the SpaCal acceptance are selected. The "jet" energy and polar angle distributions in these events are depicted by the dashed line in fig. 4.45. The solid line shows the distribution for all generated single π^0 mesons from the original DJANGO sample going into the SpaCal area. The "jet" distribution is normalised so as to coincide with the actually generated π^0 distribution at low energies, at which the DJANGO renormalisation using three-cluster events has been done. It is visible that at higher energies the "jet" distribution runs above the actual π^0 one. The ratio of the two distributions is taken for an estimation of the upper limit for the systematic error on the DIS background. This limit is determined in each x–Q^2 bin and added quadratically to the uncertainty of the common normalisation given above.

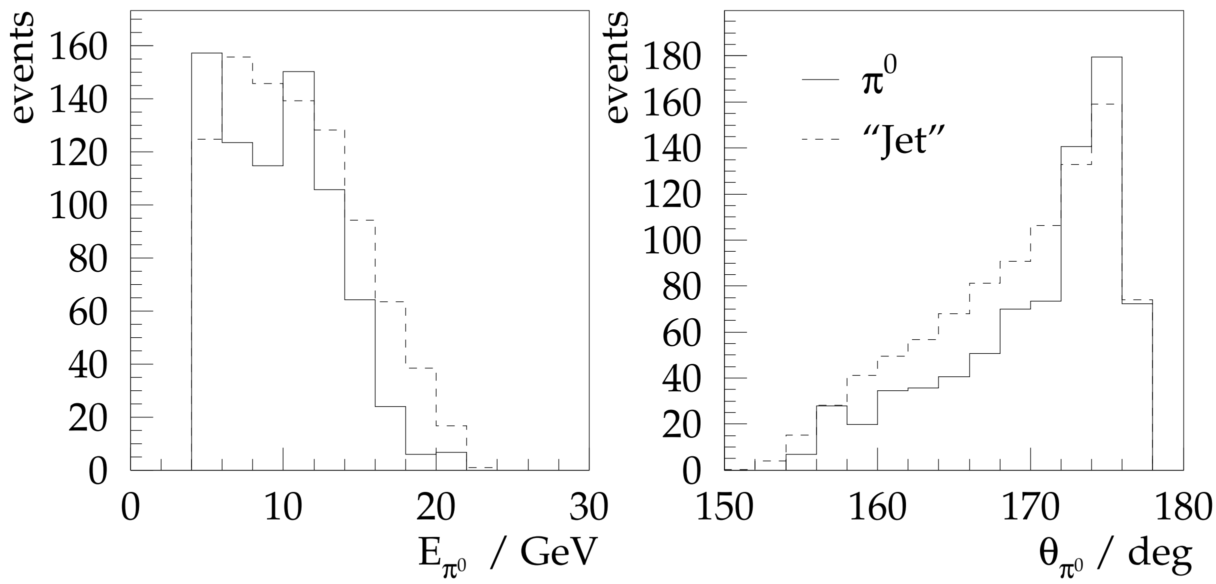

Figure 4.45: *Energy and polar angle distributions of particles falling into the SpaCal acceptance in DIS events. The solid line denotes single π^0 mesons generated by DJANGO, while the dashed line depicts a "jet" (see text). The "jet" distributions is normalised so as to coincide with the π^0 distribution at low energies, at which the renormalisation using three-cluster events has been done.*

4.8 Estimation of Radiative Corrections

As pointed out in sect. 3.3, the most significant radiative correction to the QEDC process, the Initial State Radiation, is generated in the peaking approximation by the COMPTON program. A comparison of cross section values supplied by two COMPTON samples, one of which is generated with radiative correction and the other without them, has shown that the generated effect is of the order of 3 to 5% in most bins. In the intervals with the smallest number of events the difference in the cross section amounts to 8 – 9%. In the present work two cross-checks have been made, in order to understand how well the COMPTON approach describes the real ISR correction.

In the first study QEDC events with an additional signal in the photon detector (PD) of the luminosity system are considered, and the simulated and real energy spectra in the photon detector are compared. To do that, a simulation of the PD response is performed in the analysis chain. The simulation procedure begins with the generation of angular spectra of the ISR photons found in COMPTON events, since in the peaking approximation they are radiated collinear to the electron beam. An approximate polar angle distribution near the ISR peak is produced according to [anl00]

$$\frac{dP}{d\cos\theta} = \frac{1}{1-\beta_{e0}\cos\theta}\,, \tag{4.54}$$

with β_{e0} being the velocity of the electron beam, while the azimuthal angle distribution is assumed to be uniform. In the next step the photon detector acceptance and response are simulated according to the following algorithm [işs01]:

1. The xy coordinates of the photon in the PD plane are determined after applying beam shift and beam tilt corrections[7] ;

2. A Gaussian smearing of the photon xy coordinates is performed;

3. Photons are checked to fall into the PD acceptance and those not fulfilling the acceptance criteria are rejected;

4. The energy resolution of the photon detector given by

$$\frac{d\sigma}{dE} = 1\% + \frac{26\%}{\sqrt{E/\mathrm{GeV}}} \tag{4.55}$$

   is simulated by a Gaussian smearing of the generated photon energy E'_γ.

The energy in the photon detector E_{PD} divided by the electron beam energy is depicted in fig. 4.46 a for data and COMPTON events, simulated as described above. It can be seen that there are much more events in the data than in the simulation. Furthermore, the simulated distribution vanishes at $E_{\mathrm{PD}}/E_{e0} = 0.35$. This kinematic limitation occurs, because the total energy of the two clusters in the SpaCal is required to be larger than 20 GeV (while the electron beam energy is approx. 27.5 GeV) and thus the energy of the ISR photons cannot exceed 8 – 9 GeV, as follows from the $E - P_z$ conservation. Consequently, the entries at higher E_{PD} appear due to an overlap of a QEDC event with another one, most likely with a Bethe–Heitler event. The ISR signal in the data can thus be determined only knowing the spectrum of the pile-up events.

At not very small photon energies but also at energies not too close to the electron beam energy the bremsstrahlung spectrum can be well described by the formula [kpss88]

$$\frac{d\sigma_{\mathrm{BH}}}{dz} \sim \frac{1 - z + 3z^2/4}{z}\left[\ln\frac{4E_{e0}E_{p0}(1-z)}{m_e m_p z} - \frac{1}{2}\right] \tag{4.56}$$

with $z = E'_\gamma/E_{e0}$. At very high energies the above expression does, however, not work, since an overlap with more than one Bethe–Heitler event must be then taken into account. At low energies an additional correction caused by the finite transversal size of the electron and proton beams must be done. In the range between 0.35 and 0.9, in which there can be no admixture of ISR events and in which equation 4.56 can be employed, a fit to the data is performed, as shown by the solid line in fig. 4.46 a. This parameterisation is then extrapolated down to the lower energies as denoted by the dashed line. It can be seen, that the fit curve runs below the data points at low energies, and this difference can be explained by a contribution from the ISR events.

In fig. 4.46 b the sum of the simulated ISR distribution and of the obtained bremsstrahlung spectrum is contrasted to the data. A good agreement at low energies is visible, which serves as a justification of the correctness of the ISR generation procedure employed in the COMPTON program.

A second cross-check performed in the present analysis permits a quantitative estimation of the accuracy of the peaking approximation. This is done by comparing the values of the elastic QEDC scattering cross section $\sigma_{\mathrm{e}}^{\mathrm{el}}$ and $\sigma_{\Sigma}^{\mathrm{el}}$ measured in the x_l–Q_l^2 intervals using the electron

[7] In [işs01] a very detailed run dependent simulation of the beam position in the PD plane is carried out. In the present study such a high precision is not necessary, and one average set of values of the beam coordinates is chosen.

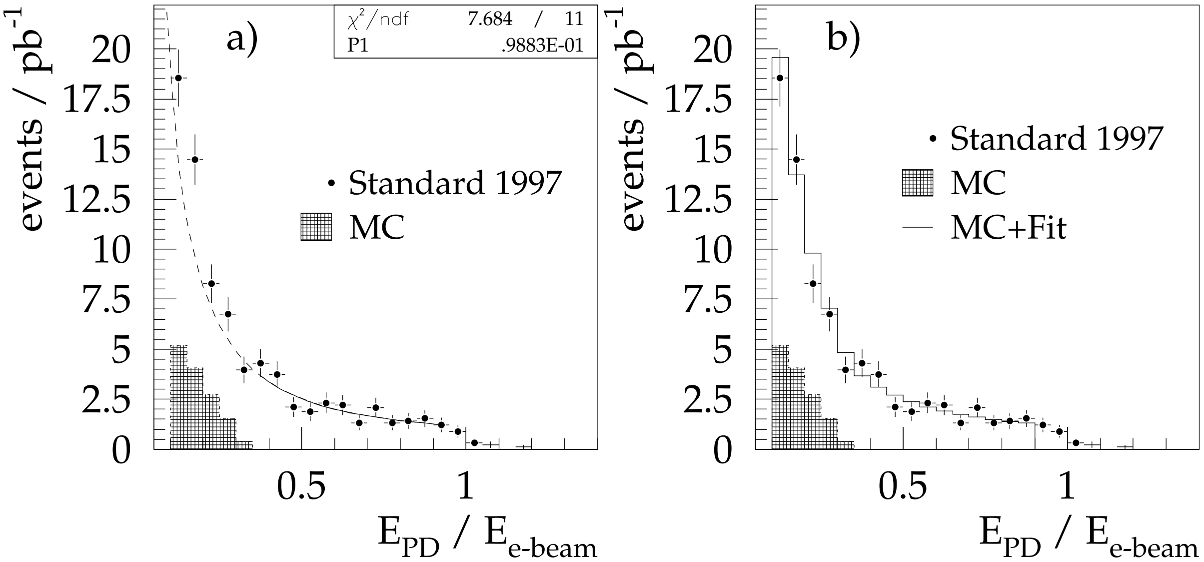

Figure 4.46: *Energy distribution in the photon detector of the luminosity system. Data of the standard 1997 sample are depicted by closed circles, while the hatched histogram shows COMPTON MC events resimulated in the analysis step. The solid line in figure a denotes the fit of the data by the bremsstrahlung spectrum performed between 0.35 and 0.9, and the dashed line displays the extrapolation of the fitting function. The open histogram in figure b represents the sum of the fitting function and the COMPTON signal.*

Q_l^2 bin #	x_l bin # 1	2	3	4
1	-1.1	0.0	2.8	-0.8
2	-1.1	-1.9	-2.7	0.7
3		0.1	-2.2	

Table 4.6: *Relative discrepancy $\delta_{e-\Sigma}$, % of the elastic QEDC cross section in bins of leptonic variables x_l, Q_l^2 reconstructed with the electron and the Sigma method. (See sect. 3.10 for the bin definition.)*

and the Sigma method, respectively. The elastic channel is selected by the same strong acoplanarity cut $A < 4°$, as used, for instance, in the study of the BST efficiency. The elastic selection allows us to avoid possible disagreement, which could occur due to the hadronic final state reconstruction. Actually for the x_l and Q_l^2 reconstruction by the Sigma method in the elastic events the parameters of the outgoing photon (treated as a part of the hadronic final state) are employed. Another advantage of the stronger acoplanarity limit is the additional suppression of several background contributions. The relative discrepancy given by

$$\delta_{e-\Sigma} = \frac{\sigma_e^{el} - \sigma_\Sigma^{el}}{\sigma_\Sigma^{el}} \tag{4.57}$$

is listed for all x_l–Q_l^2 bins in table 4.6. As can be seen, the values are of the order of 1% in average and show no systematic trend. Based on this study, a 1% systematic uncertainty of the description of the radiative corrections near the ISR peak is assumed.

However, an additional uncertainty for the radiative corrections has to be taken into account, which arises from the higher order wide angle bremsstrahlung (WAB). In particular, events with two high energetic photons producing separate clusters in the SpaCal are rejected by the cut on the residual energy $E_{\text{res}} < 1\,\text{GeV}$. The number of such events is expected to be very small, but its direct determination is very difficult. Therefore a conservative estimation of this systematic uncertainty has been performed, namely, that such events can make at most 30 – 40% of the average radiative correction in the ISR peak. As mentioned above, the average ISR correction is of the order of 5%, and, consequently, 2% for the uncertainty due to the wide angle bremsstrahlung are assumed. The total systematic error due to radiative corrections is computed as the quadratic sum of the ISR and WAB uncertainties.

Chapter 5

Results of the Measurement

The results of the conducted analysis are presented in this chapter. In the beginning the systematic uncertainties of the QED Compton cross section measurement are summarised. Afterwards, event rates measured in bins of Q_h^2 and in intervals of leptonic kinematic variables are confronted to the simulated ones. It is shown, that different F_2 parameterisations yield significantly different predictions of the event rates, and that the COMPTON simulation with the ALLM97 fit provides a good description of the data.

A calculation of the leading order differential cross section is required in order to compare the results of the measurement with the analytical models. In the last section of the chapter the extracted cross section values are given and contrasted to the predictions given by the model of De Rújula and Vogelsang. It is shown that this approach fails to describe the data, and possible reasons for the deviations are discussed.

5.1 Summary of Systematic Errors

Systematic effects influencing the measured values were studied either in this work or in other H1 analyses, as discussed earlier. A part of the total systematic error arises from global normalisation uncertainties. These are:

- A 1.5% error due to the uncertainty of the integrated luminosity measurement;
- The global uncertainties of the trigger efficiencies, as discussed in sect. 4.3. They include a 0.5% error for the SpaCal IET and ToF triggers and a 0.5% uncertainty for the L4 filter. Furthermore, a 0.2% uncertainty is assumed for the L2 t18 trigger element in the standard 1997 data sample;
- A 2.2% uncertainty due to radiative corrections, as discussed in sect. 4.8;
- A 0.2% uncertainty for the beam induced background (see paragraph 3.2.7).

In order to estimate the influence of other sources on the measurement results, values of all relevant quantities were varied within their uncertainties in positive and negative direction and the QEDC cross sections in each kinematic bin were recalculated. The deviation of the result from the original value are treated as a systematic uncertainty caused by the particular error source. The total systematic error is computed by the quadratic summation over all error sources. The following uncertainties are taken into account:

1. The uncertainty of the SpaCal energy scale, which affects simultaneously the energies of both clusters in a QEDC event, is estimated from the studies described in sect. 4.6. It is assigned, depending on the cluster energy, to 0.5% at $E > 17$ GeV and 2.5% at $E = 4$ GeV. The error between 4 and 17 GeV is parameterised by a linear function interpolating between the error values at the boundaries;

2. An uncertainty of 0.33 mrad for the electron polar angle reconstruction by the BST and corresponding to it 0.36 cm uncertainty of the vertex reconstruction;
3. An uncertainty of 1 cm for the CIP vertex reconstruction;
4. An uncertainty of 0.6 mrad for the electron and photon polar angle reconstruction by the BDC, which is the quadratic sum of the resolution and the alignment uncertainty. For the particles having no BDC signal the position of the SpaCal cluster were varied within the spatial resolution given in paragraph 2.2.1;
5. Uncertainties of 3% and 1.5% for the electron/photon identification procedures using the BST and the CIP, respectively, (see paragraph 4.4.6);
6. An uncertainty for the common electron/photon identification scheme, as discussed in paragraph 4.4.7;
7. A 4% error for LAr cluster energies. This uncertainty can affect the event rejection due to the θ_{LAr} requirement, since the cluster energy must be larger than 0.5 GeV. Furthermore this uncertainty influences the reconstruction of the kinematic variables with the Sigma method;
8. The errors of the trigger efficiency correction fits for the conditions L1 $\neg\mathrm{DCR}\Phi_{\mathrm{Tc}}$ and L4 LOWMULT in the standard 1997 data sample (see sect.,4.3);
9. The systematic uncertainties for various background contributions, as described in sect. 3.2 and 4.7. The statistical errors of background MC samples are included in the statistical uncertainty of the measurement.

The systematic error contributions of these sources determined in this way are summarised in table 5.1. No dominant error source is observed. The uncertainties of the SpaCal energy, the angle reconstruction and the particle identification are approximately of the same size. The errors of the LAr energy scale and the trigger efficiency correction fits turn out to be negligible. Concerning the background sources, the largest uncertainty is contributed by the DVCS process, while the relative uncertainties brought by dilepton production, photoproduction and vector meson production are practically negligible.

5.2 Sensitivity to the F_2 Parameterisation

The rate of inelastic QED Compton events of the standard 1997 data sample is plotted as a function of Q_h^2 in fig. 5.1. The inelastic channel is singled out from other QEDC events by applying the requirements described in sect. 3.7. The measured rates are contrasted to those simulated by COMPTON using the ALLM97 F_2 fit and the original COMPTON F_2 parameterisation. Good agreement between the simulation with the ALLM97 F_2 and the data is observed. Furthermore it can be seen that the original COMPTON F_2 parameterisation underestimates the data in the measured kinematic region. Thus, the collected statistics of QED Compton events permits a check of the F_2 behaviour in a kinematic domain not accessible in the inclusive DIS measurements at HERA, as described in sect. 1.8.

In fig. 5.2 the total event rate of all QEDC channels in the chosen x_l–Q_l^2 intervals is depicted. One can see that the simulation with the ALLM97 F_2 and the data agree very well also in bins of the leptonic kinematic variables. As shown in sect. 3.10, the higher x_l, the larger is

Table 5.1: *Systematic uncertainties of the QEDC cross section measurement. All values are given in percent. (See sect. 3.10 for the bin definition.)*

x_l bin #	1		2			3			4	
Q_l^2 bin #	1	2	1	2	3	1	2	3	1	2
SpaCal energy scale	2.36	1.93	0.25	0.39	0.38	1.33	2.39	4.39	2.57	2.90
BST $\theta/z_{\rm vtx}$ reconstruction	2.14	1.47	0.12	0.88	0.20	0.78	0.05	0.00	0.13	0.00
CIP $z_{\rm vtx}$ reconstruction	0.00	0.05	0.03	0.32	0.76	0.72	1.89	4.65	2.37	2.63
BDC/SpaCal θ rec.	0.00	0.09	0.05	2.08	1.64	0.31	0.85	1.11	0.88	0.34
Identification in BST	2.64	2.72	2.66	1.39	0.00	1.68	0.05	0.00	0.12	0.00
Identification in CIP	0.00	0.00	0.03	0.66	1.45	0.63	1.43	1.86	1.93	1.36
Identification scheme	0.50	0.50	1.00	0.50	0.50	1.30	1.00	0.60	2.80	1.50
LAr energy scale	0.07	0.14	0.17	0.13	0.10	0.33	0.12	0.07	0.22	0.32
L1 $\neg$DCR$\Phi_{\rm Tc}$ correction	0.05	0.07	0.06	0.06	0.06	0.09	0.08	0.08	0.14	0.16
L4 LOWMULT correction	0.05	0.06	0.06	0.06	0.06	0.08	0.07	0.07	0.11	0.13
DVCS (TINTIN)	3.50	2.76	3.50	1.34	0.54	2.43	0.26	0.34	0.46	0.11
DIS (DJANGO)	1.10	0.85	1.99	0.63	0.26	1.24	0.24	0.18	0.37	0.31
Dilepton (GRAPE)	0.03	0.06	0.04	0.05	0.06	0.04	0.03	0.00	0.03	0.01
γp (PHOJET)	0.62	0.00	0.10	0.77	0.00	0.14	0.00	0.00	0.00	0.00
DIFFVM	0.00	0.10	0.77	0.00	0.14	0.00	0.00	0.00	0.00	0.00

the fraction of continuum inelastic events, therefore the difference between the simulations with the ALLM97 and COMPTON 2.0 F_2 parameterisations becomes more significant with increasing x_l.

The same result is obtained using the minimum bias 1997 event sample, as shown in fig. 5.3. The difference between the two simulated samples is a little larger in this figure. This occurs due to the relaxed cut on the spatial distribution of hadrons, imposed in the analysis of this data set, compared to the standard 1997 data analysis. This cut rejects a smaller fraction of continuum inelastic events making the total QEDC cross section more sensitive to the F_2 choice. This is illustrated in fig. 5.4, in which the cumulative distribution of $\theta_{\rm LAr}$ in simulated events is plotted. Each point of the distribution shows the number of events remaining after imposing the $\theta_{\rm LAr}$ cut at this point. It can be seen that the difference in cross section of the samples produced with different F_2 parameterisations is larger at higher $\theta_{\rm LAr}$ cut values. Nevertheless, although a part of the kinematic range was cut off in the standard 1997 data sample, its high statistics still allows high sensitivity to the F_2 parameterisation.

Good agreement between the data and the COMPTON simulation with the ALLM97 fit is also observed in control distributions of basic measured quantities displayed in fig. 5.5 and 5.6 for the standard and the minimum bias sample, respectively[1]. This justifies the correctness of the data treatment in this analysis.

Since the minimum bias data sample gives nearly the same results as the standard 1997 sample, it is assumed that the hadronic final state is correctly simulated, so that the influence of the $\theta_{\rm LAr}$ cut is the same in the data and the simulation. Therefore the standard 1997 event sample is employed for the cross section measurement providing much smaller statistical errors than the minimum bias data set.

[1] A dip in the polar angle distributions occurs on the boundary of the BST and CIP acceptance. The acoplanarity distribution has already been shown in fig. 4.5.

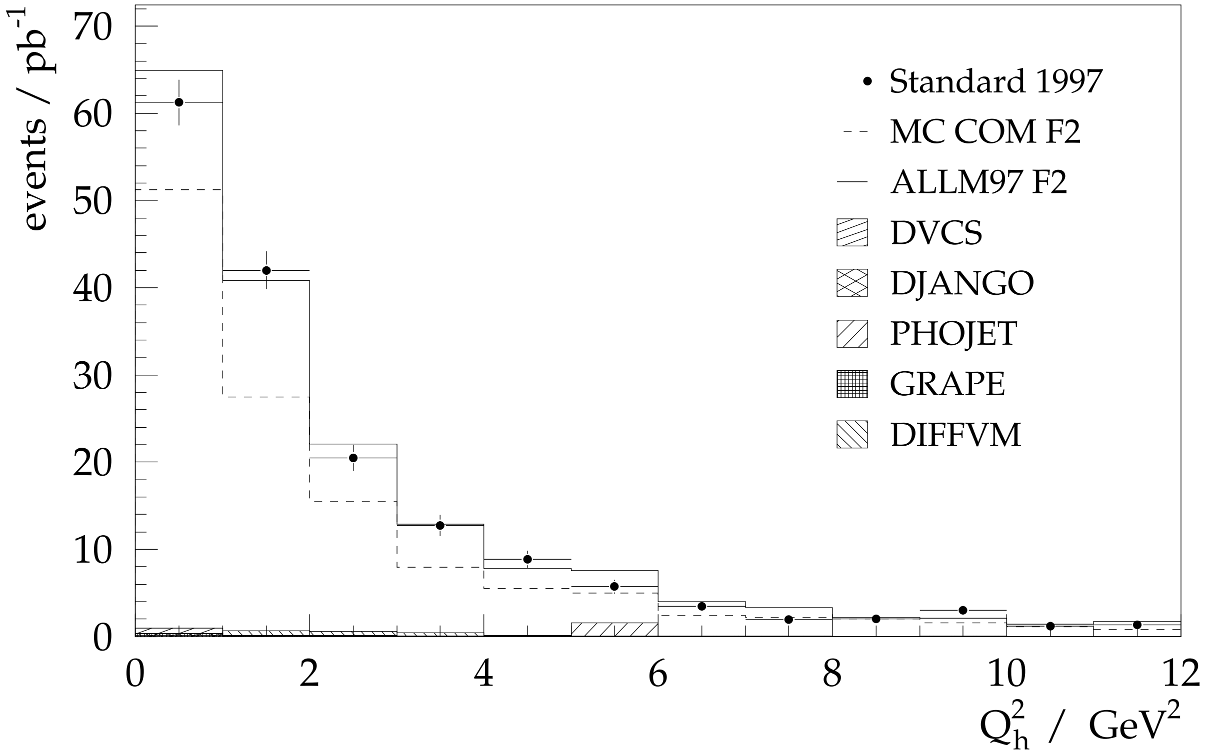

Figure 5.1: *Rate of continuum inelastic QEDC events as a function of Q_h^2 integrated over x_h. The data of the standard 1997 event sample are depicted by closed circles with error bars denoting statistical errors. The solid and dashed lines depict COMPTON MC events with all background contributions added. The solid line stands for the sample generated with the ALLM97 F_2 fit, while the dashed line represents the simulation with the original COMPTON F_2 parameterisation. Simulated background sources are shown by hatched histograms, as denoted in the legend.*

5.3 Comparison to the Model of De Rújula and Vogelsang

The cross section values are extracted from the data by the "Monte Carlo method" described in sect. 3.11. In this technique the leading order cross section used in the MC generator has to be known. In order to compute it, a sample of COMPTON events was generated without radiative corrections. As in the other COMPTON samples, the ALLM97 F_2 parameterisation is used in the continuum region and the fit by Brasse *et al* in the resonance region. The cross section values were calculated after imposing several cuts on the generated quantities in MC events. These limits were chosen so as to correspond approximately to the cuts applied in the measurement, and thus minimise acceptance corrections. The following limits were set:

$$\begin{aligned} &\min(E_e, E_\gamma) > 4\,\mathrm{GeV}\,, \\ &E_e + E_\gamma > 20\,\mathrm{GeV}\,, \\ &0.06 < \theta_e, \theta_\gamma < \pi - 0.06\,, \\ &A < 45^\circ\,. \end{aligned} \tag{5.1}$$

The generated cross section was then calculated in each x_l–Q_l^2 bin by dividing the total num-

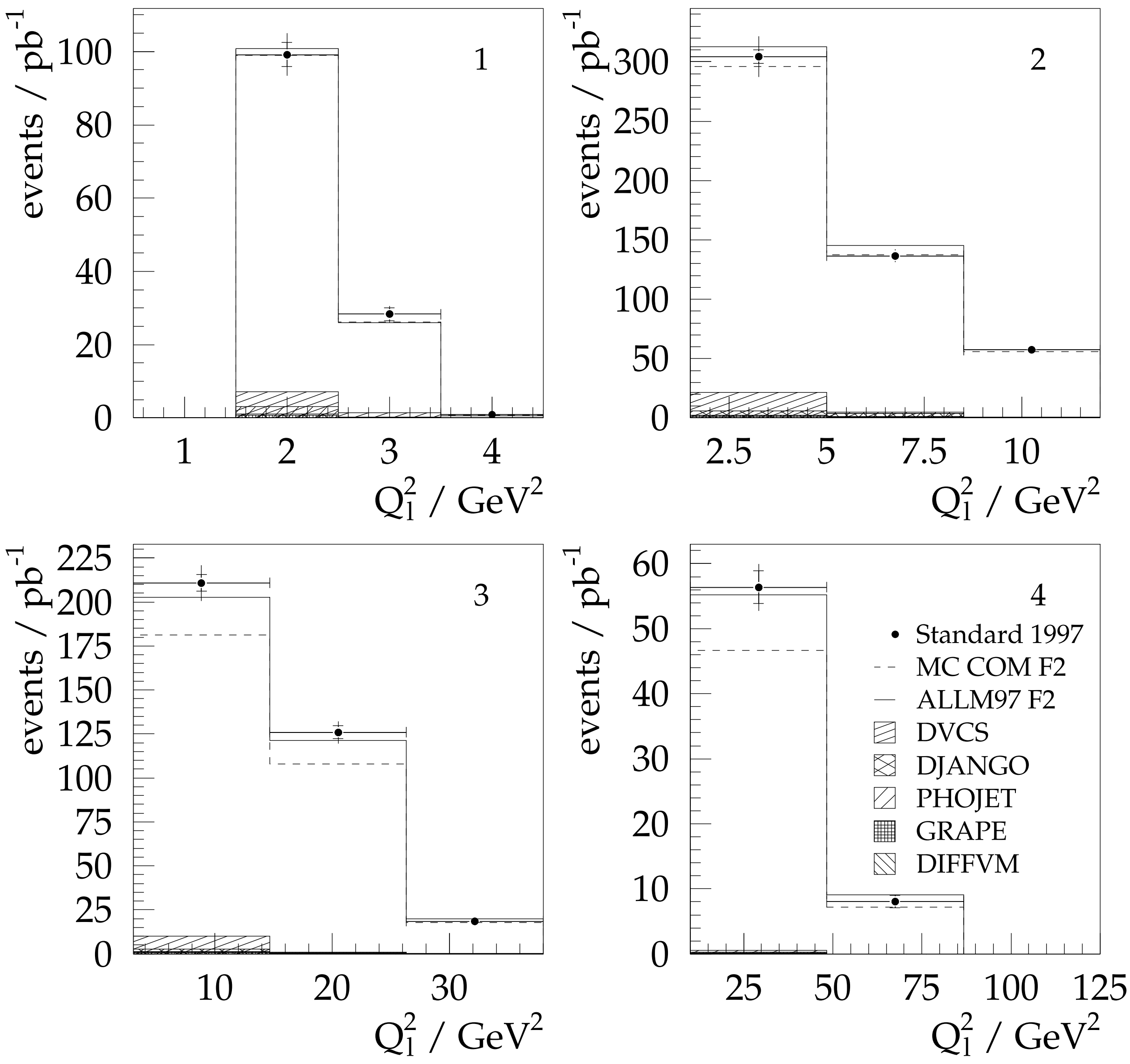

Figure 5.2: *QEDC event rates in bins of leptonic kinematic variables. Each plot is made in a separate x_l bin denoted by its number (see table 3.1). The data of the standard 1997 event sample are depicted by closed circles. The inner error bars denote statistical errors, the outer error bars show statistical and systematic uncertainties added in quadrature. The solid and dashed lines depict COMPTON MC events with all background contributions added. The solid line stands for the sample generated with the ALLM97 F_2 fit in the continuum region, while the dashed line represents the simulation with the original COMPTON F_2 parameterisation. Simulated background sources are shown by hatched histograms, as denoted in the legend.*

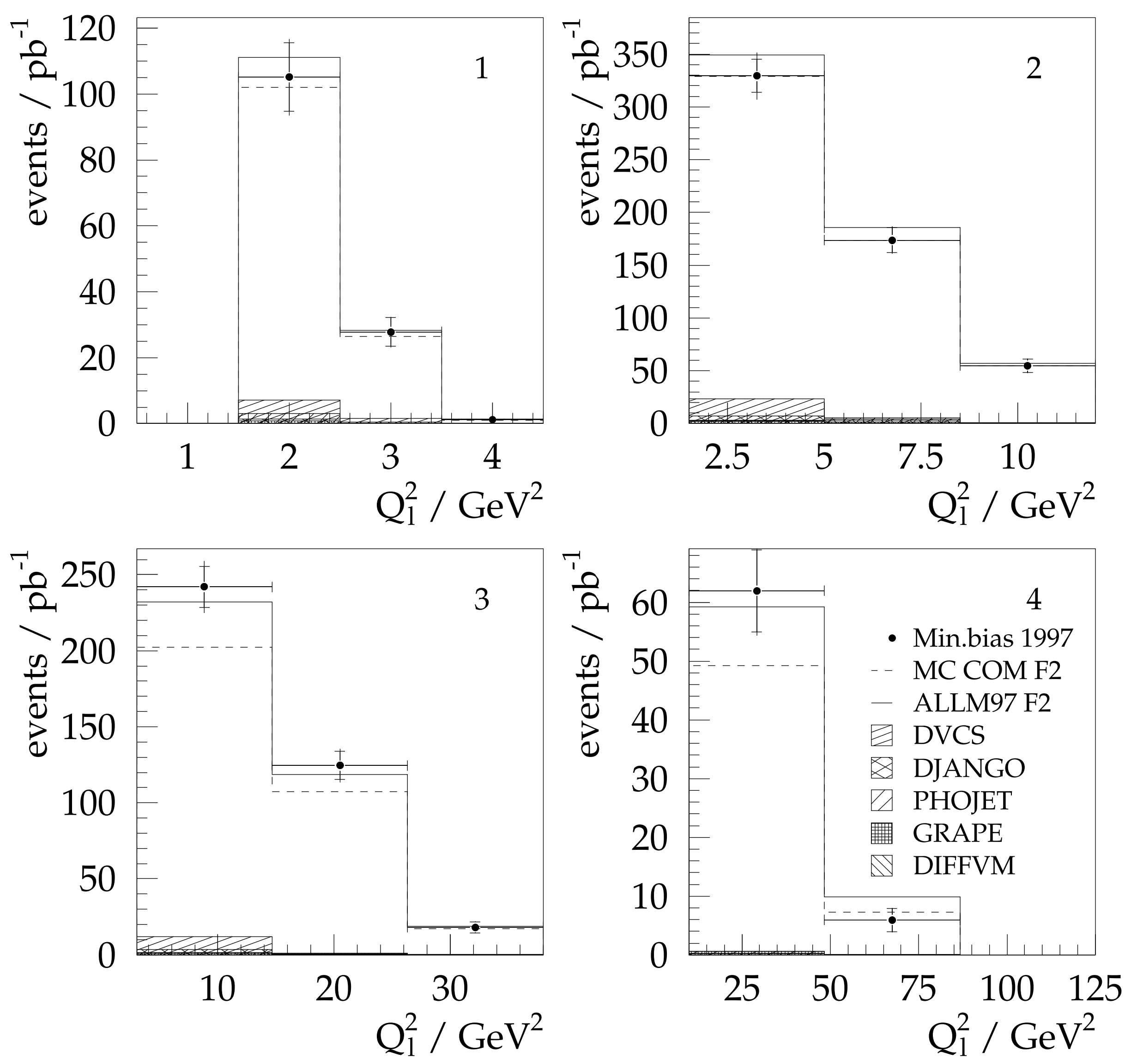

Figure 5.3: *QEDC event rates in the bins of leptonic kinematic variables. Each plot is made in a separate x_l bin denoted by its number (see table 3.1). The data of the minimum bias 1997 event sample are depicted by closed circles. The inner error bars denote statistical errors, the outer error bars show statistical and systematic uncertainties added in quadrature. The solid and dashed lines depict COMPTON MC events with all background contributions added. The solid line stands for the sample generated with the ALLM97 F_2 fit in the continuum region, while the dashed line represents the simulation with the original COMPTON F_2 parameterisation. Simulated background sources are shown by hatched histograms, as denoted in the legend.*

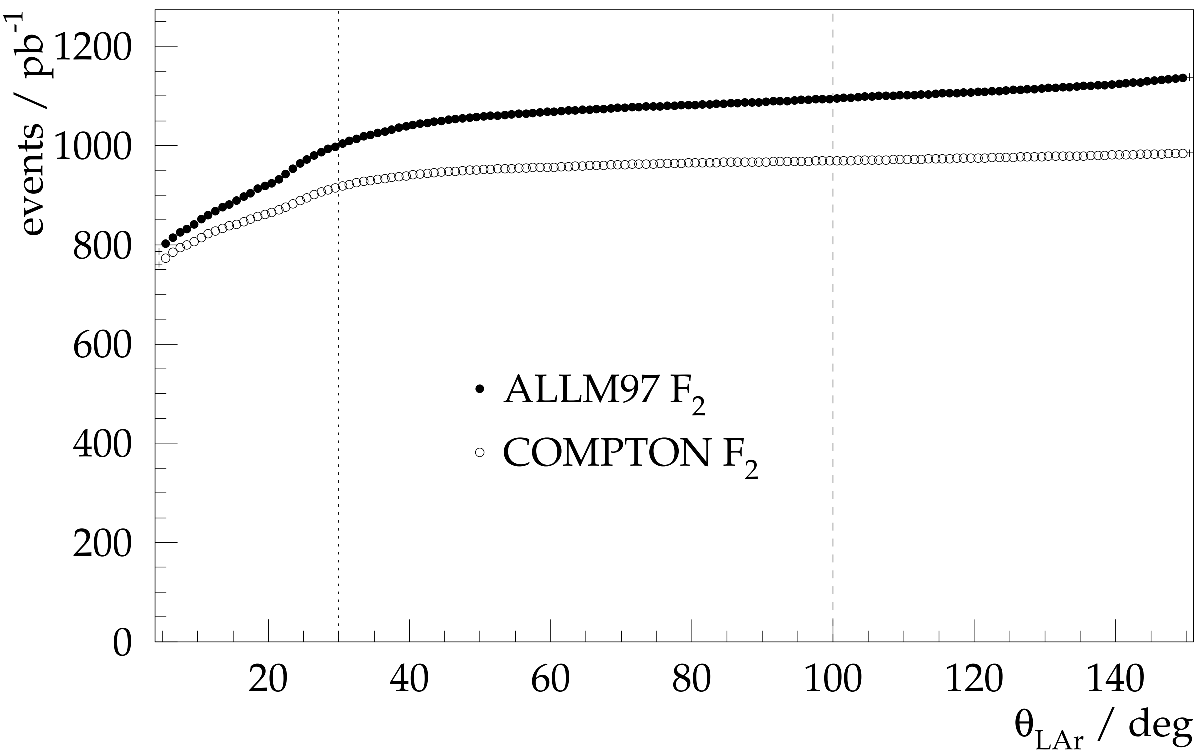

Figure 5.4: *Cumulative distributions of COMPTON events as a function of the highest LAr cluster polar angle $\theta_{\rm LAr}$. Simulations using the ALLM97 F_2 (closed circles) and the original COMPTON F_2 parameterisation (open circles) are employed. Each entry displays the number of events remaining in the sample after imposing the cut on $\theta_{\rm LAr}$ at this point. The $\theta_{\rm LAr}$ values, at which the cuts on the minimum bias and standard 1997 data are made, are denoted by the dashed and dotted line, respectively.*

ber of events fulfilling these selection criteria by the effective luminosity of the MC sample. Afterwards, the cross section in the data was calculated in the measured intervals according to eq. 3.42.

The measured QEDC cross section values together with their statistical and systematic errors are listed in table 5.2. Also given are the generated values with their statistical errors and those calculated analytically by W. Vogelsang [vog01] with the same set of cuts. The error of the analytical calculation is approximately 2% in all bins. All values are plotted in fig. 5.7.

As can be seen in the figure or in the table, there are significant discrepancies in several bins between the measured values and those calculated in the collinear approximation. Hence further investigations were undertaken in order to understand these deviations.

At first, the elastic scattering cross section values generated by COMPTON and computed in the Weizsäcker – Williams approximation were compared. They are also listed in table 5.2. Here one should bear in mind that the same electric and magnetic form factors of the proton have been employed both for the exact treatment in the COMPTON program and for the calculation in the equivalent photon approximation. One can see that the cross section values agree very well in almost all bins. This means that this approximation provides a very good description of the elastic scattering.

The source of the discrepancies is, thus, in the treatment of the inelastic QEDC process. Here

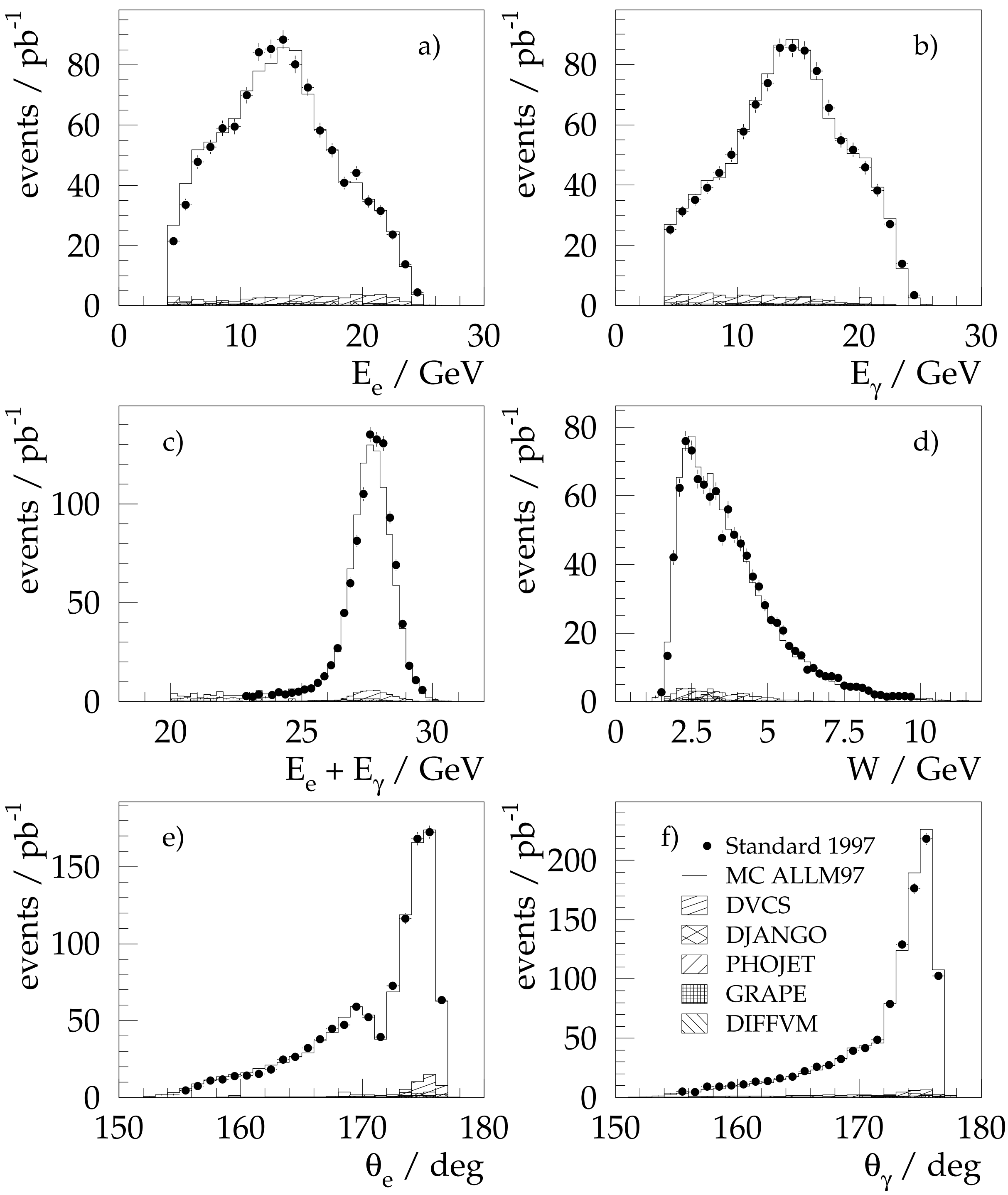

Figure 5.5: *Control distributions of basic measurands. Plotted are the following reconstructed quantities: a) energy of the scattered electron, b) energy of the outgoing photon, c) the sum of both energies, d) the invariant mass of the $e\gamma$ system, e) polar angle of the final electron, f) polar angle of the final photon. The data of the standard 1997 event sample are depicted by closed circles with statistical error bars. The solid line depicts COMPTON MC events with all background contributions added. The sample generated with the ALLM97 F_2 fit in the continuum region is used. Simulated background samples are shown by hatched histograms, as denoted in the legend.*

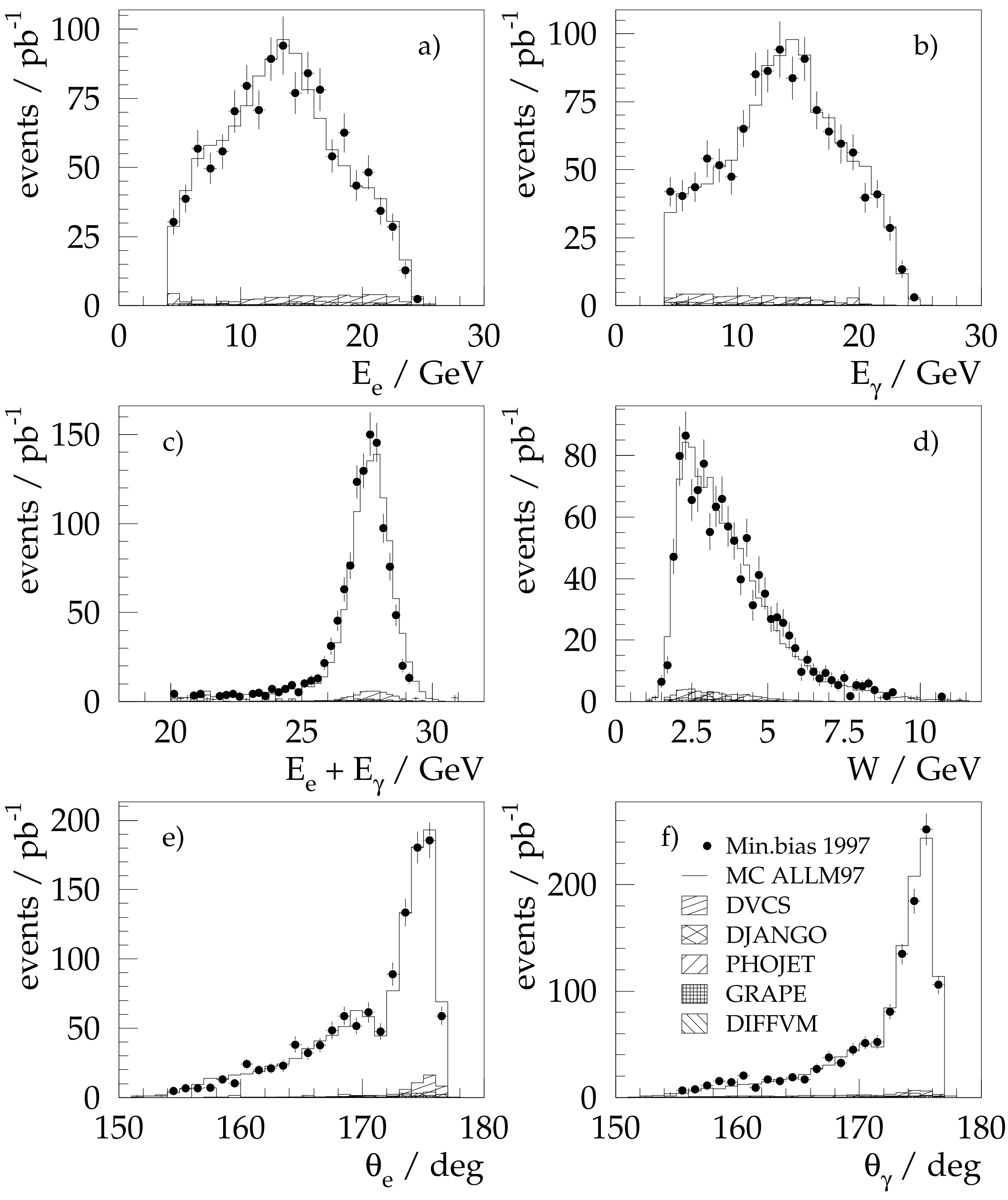

Figure 5.6: *Control distributions of basic measurands. Plotted are the following reconstructed quantities: a) energy of the scattered electron, b) energy of the outgoing photon, c) the sum of both energies, d) the invariant mass of the $e\gamma$ system, e) polar angle of the final electron, f) polar angle of the final photon. The data of the minimum bias 1997 event sample are depicted by closed circles with statistical error bars. The solid line depicts COMPTON MC events with all background contributions added. The sample generated with the ALLM97 F_2 fit in the continuum region is used. Simulated background samples are shown by hatched histograms, as denoted in the legend.*

Table 5.2: *Results of the measurement of the leading order QED Compton scattering cross section. Presented are the cross section values (σ^{data}) measured in x_l–Q_l^2 intervals with the statistical ($\delta\sigma^{\text{data}}_{\text{stat}}$), systematic ($\delta\sigma^{\text{data}}_{\text{syst}}$) and total ($\delta^{\text{data}}_{\sigma}\text{tot}$) errors. Also listed are the values computed from the sample of COMPTON events (σ^{MC}) with their statistical errors ($\delta\sigma^{\text{MC}}_{\text{stat}}$) and the values calculated by W. Vogelsang [vog01] (σ^{RV}) with a 2% uncertainty ($\delta\sigma^{\text{RV}}$). Furthermore, the elastic scattering cross sections calculated from the same COMPTON sample ($\sigma^{\text{MC,el}}$) with their statistical uncertainties ($\delta\sigma^{\text{MC,el}}_{\text{stat}}$) and calculated by W. Vogelsang ($\sigma^{\text{RV,el}}$) also with an uncertainty of 2% are given. All values are expressed in pb. The definition of the kinematic intervals is given in sect. 3.10.*

x_l bin #	Q_l^2 bin #	σ^{data}	$\delta\sigma^{\text{data}}_{\text{stat}}$	$\delta\sigma^{\text{data}}_{\text{syst}}$	$\delta\sigma^{\text{data}}_{\text{tot}}$	σ^{MC}	$\delta\sigma^{\text{MC}}_{\text{stat}}$	σ^{RV}	$\delta\sigma^{\text{RV}}$	$\sigma^{\text{MC,el}}$	$\delta\sigma^{\text{MC,el}}_{\text{stat}}$	$\sigma^{\text{RV,el}}$	$\delta\sigma^{\text{RV,el}}$
1	1	299.6	15.3	18.7	24.2	295.9	3.5	331.3	6.6	234.2	3.2	242.8	4.9
1	2	71.8	5.8	3.9	7.0	67.6	1.7	73.8	1.5	47.1	1.4	51.0	1.0
2	1	749.5	19.5	42.6	46.8	761.5	5.7	771.9	15.4	531.9	4.8	519.7	10.4
2	2	314.9	14.3	13.8	19.8	338.9	3.8	394.4	7.9	232.7	3.2	238.9	4.8
2	3	111.2	6.1	4.5	7.6	112.1	2.2	151.2	3.0	83.2	1.9	85.9	1.7
3	1	453.4	14.0	22.1	26.2	432.3	4.3	352.8	7.1	203.6	2.9	204.5	4.1
3	2	239.1	8.9	11.3	14.4	231.1	3.1	264.2	5.3	138.8	2.4	138.1	2.8
3	3	59.7	5.5	4.5	7.1	64.3	1.6	75.7	1.5	38.6	1.3	37.3	0.7
4	1	165.3	8.9	9.5	13.0	163.5	2.6	116.6	2.3	57.1	1.6	58.8	1.2
4	2	71.6	9.7	3.8	10.4	84.4	1.9	80.3	1.6	38.5	1.3	37.2	0.7
4	3	–	–	–	–	21.60	0.95	23.92	0.48	10.28	0.66	10.63	0.21
5	1	–	–	–	–	67.94	1.70	41.48	0.83	18.77	0.89	18.97	0.38
5	2	–	–	–	–	29.64	1.12	29.24	0.58	12.29	0.72	12.41	0.25
5	3	–	–	–	–	11.78	0.71	14.37	0.29	6.02	0.51	5.91	0.12
6	1	–	–	–	–	20.08	0.92	11.02	0.22	5.76	0.50	4.82	0.10
6	2	–	–	–	–	19.11	0.90	22.93	0.46	9.22	0.63	9.24	0.18
6	3	–	–	–	–	5.25	0.48	6.54	0.13	2.65	0.34	2.58	0.05
7	1	–	–	–	–	3.18	0.37	2.15	0.04	0.68	0.17	0.90	0.02
7	2	–	–	–	–	4.84	0.45	6.24	0.12	2.69	0.34	2.43	0.05
7	3	–	–	–	–	1.43	0.25	1.68	0.03	0.77	0.18	0.64	0.01
8	1	–	–	–	–	0.573	0.155	0.811	0.016	0.427	0.135	0.311	0.006
8	1	–	–	–	–	0.424	0.131	0.661	0.013	0.213	0.095	0.245	0.005
8	1	–	–	–	–	0.043	0.043	0.069	0.001	0.000	0.000	0.025	0.001

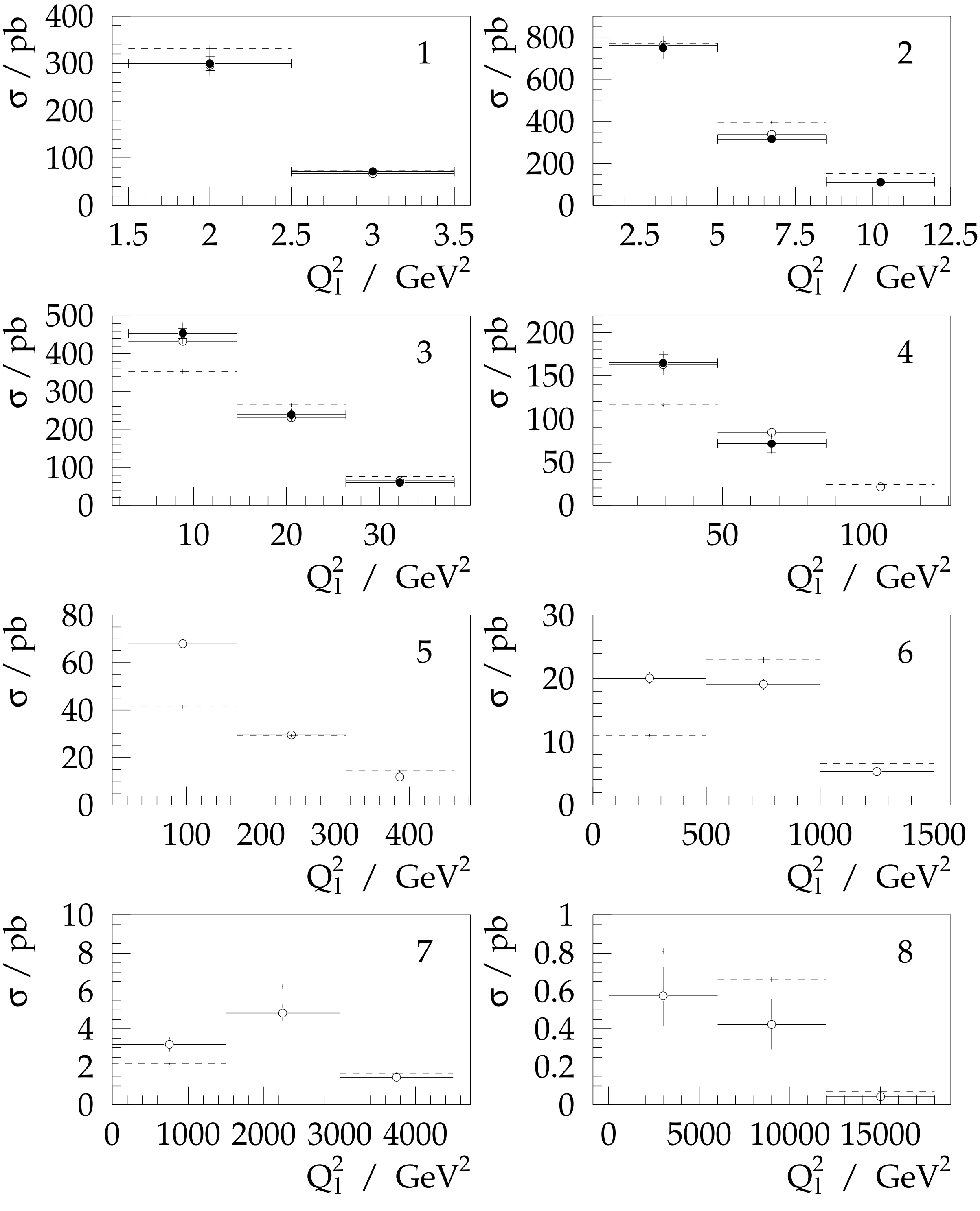

Figure 5.7: *Double differential cross section of QED Compton scattering. The values measured in the standard 1997 data sample are depicted by closed circles with error bars denoting statistical errors (inner bars) and statistical and systematic uncertainties added in quadrature (outer bars). Open circles depict cross section values given by the COMPTON generator with the ALLM97 F_2 fit in the continuum region. The corresponding error bars show statistical errors. The dashed lines denote the values computed by W. Vogelsang.*

two possibilities are considered: either the function $\gamma(x_l, Q_l^2)$ describing real inelastic scattering is different from that calculated by De Rújula and Vogelsang, or the collinear approximation itself is not appropriate to describe the data in this domain.

In the first case, *i.e.*, if the approximative approach is valid, the γ function corresponding to the real data must be determined. Again, in order to calculate it with the Monte Carlo method, the γ function corresponding to the generated MC sample must be known. The COMPTON generator does, however, not employ the collinear approximation, but uses the exact calculation of the cross section. Therefore the corresponding γ function was not known in advance, but was calculated in this work.

The elastic part of the function was calculated as discussed in paragraph 1.9.1 and also done by De Rújula and Vogelsang. In doing so exactly the same values were obtained. The inelastic component was computed according to eq.1.65 by a numerical integration of the F_2 parameterisations, employed in the COMPTON generator. The parameterisations that were to agree with the data in leptonic kinematic bins, as shown in the previous section, were chosen, *i.e.*, the fit by Brasse *et al* for the resonance domain and the ALLM97 fit for the continuum region. The integration over Q_h^2 was performed in all eight x_l bins at the same "central" values $x_{l,c}$ as chosen by De Rújula and Vogelsang.

The result of the calculation is contrasted to the γ function by De Rújula and Vogelsang in fig. 5.8. Both calculations give very close results. The discrepancies between them are less than 4% in all bins. Slight deviations arise from the different F_2 parameterisations (as mentioned in sect. 1.9.2, De Rújula and Vogelsang employed the LO GRV PDF set) and from the choice of the integration start scale $Q^2_{h\,\mathrm{min}}$ in eq.1.65. In the calculation presented here the lower kinematic limit given by eq. 1.57 has been set. This corresponds to reality and is actually employed in COMPTON. De Rújula and Vogelsang have used $0.25\,\mathrm{GeV}^2$ as a start value, as pointed out in sect. 1.9.2.

To test the influence of this parameter, the integration was performed once more, but with the start scale of $0.25\,\mathrm{GeV}^2$. The result is displayed in fig. 5.9. As expected, the γ values have somewhat decreased, but the general Q_l^2 behaviour remained unchanged.

The γ function corresponding to the real data can be in principle calculated using eq. 3.44. Since the data and the simulation agree very well within the quoted uncertainties, the real data γ function should be very close to that corresponding to the simulation. This means that the γ function corresponding to the data should have a Q^2 dependence very close to that predicted by De Rújula and Vogelsang and thus strikingly different from that of the gluon distribution function (see fig. 1.13).

However the extraction of the γ function from the data has not been carried out and, thus, the measurement has not been interpreted as the measurement of the function $\gamma(x_l, Q_l^2)$. The reason for this decision is that apparently the collinear approximation does not supply a sufficient degree of accuracy in the inelastic region. Although the γ functions agree with each other within 4%, the cross sections computed in the collinear approximation exhibit an up to 25% deviation in several bins from those calculated by the exact method in COMPTON and from those measured in the real data (see fig. 5.7). In other words, the factorisation of the cross section given by eq. 1.59 in terms of only two kinematic variables is a too rough approximation of the real QEDC scattering process in the inelastic domain.

In order to understand the reasons for that, a closer look at the QEDC event topology has been taken. In fig 5.10 distributions of several quantities generated by the COMPTON program in events of elastic and inelastic scattering are opposed. The two upper plots show the transverse momentum of the exchanged photon p_{t,γ^*}. In the collinear approximation it is assumed to be

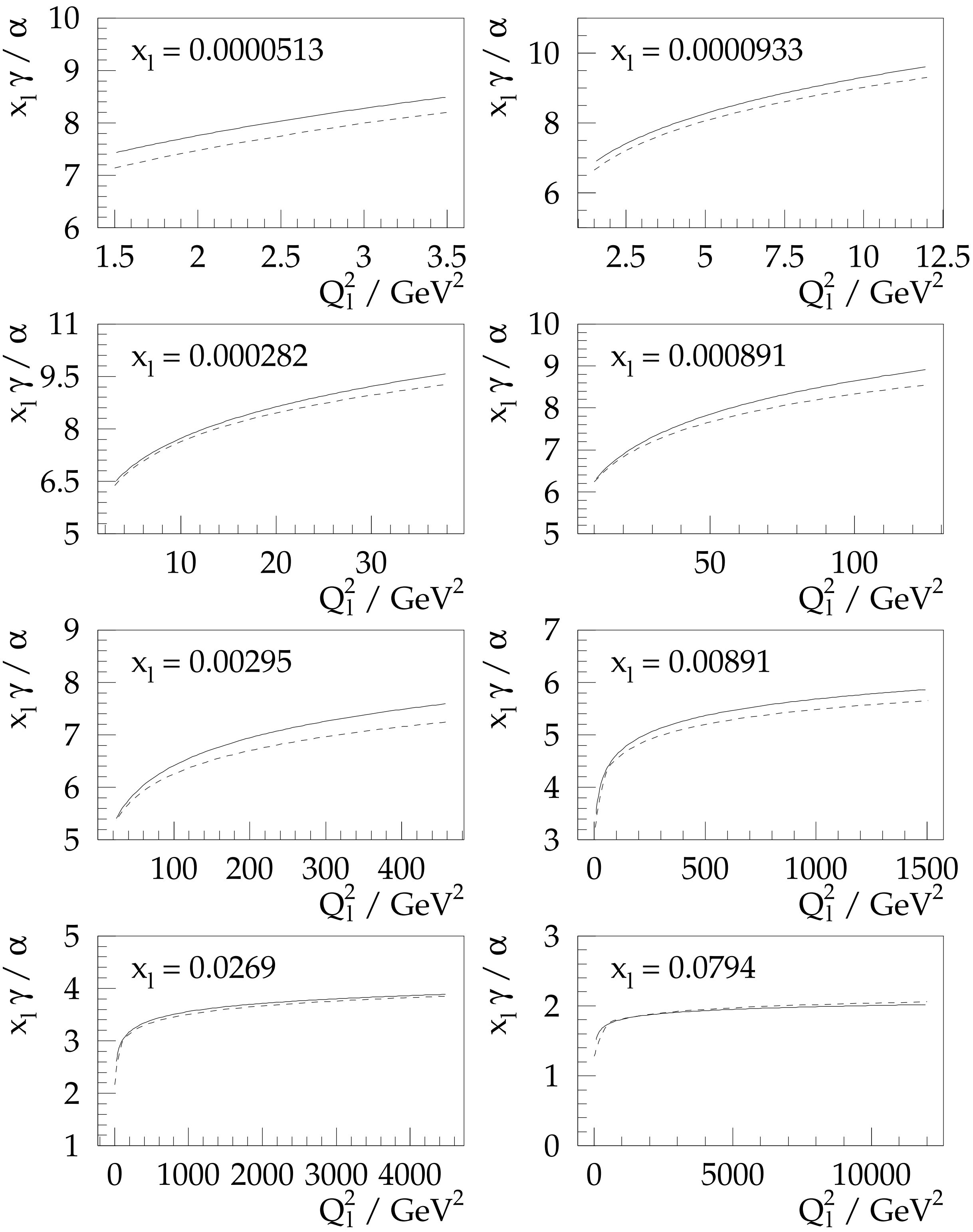

Figure 5.8: *γ function in x_l bins. The solid line depicts the function calculated in this analysis using the ALLM97 F_2 parameterisation in the continuum region and the fit by Brasse et al in the resonance region. The dashed line displays the γ function computed by De Rújula and Vogelsang.*

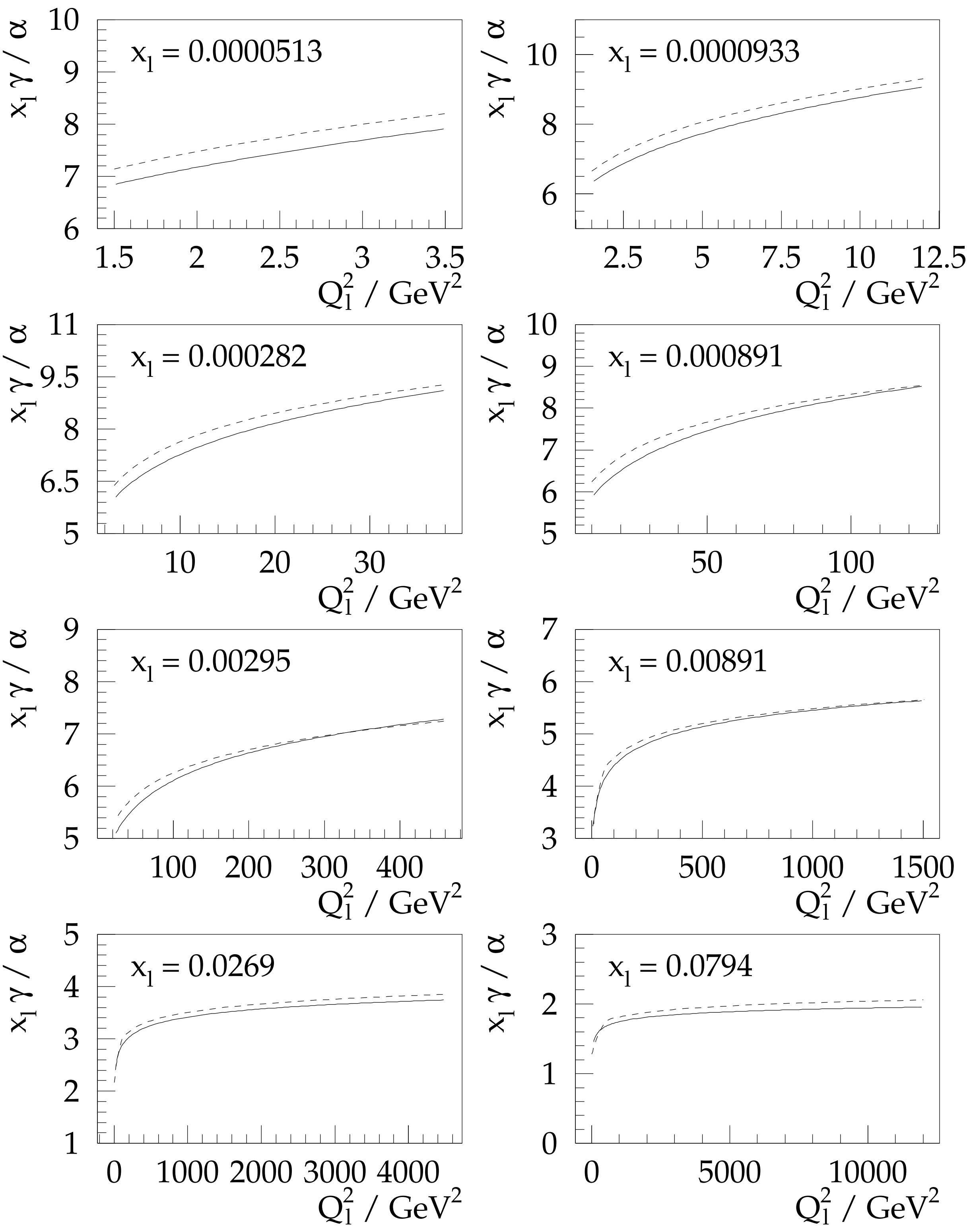

Figure 5.9: *γ function in x_l bins. The solid line depicts the function calculated in this analysis using the ALLM97 F_2 parameterisation in the continuum region and the fit by Brasse et al in the resonance region, where the lower integration limit of the inelastic contribution was set to $Q_0^2 = 0.25\,\mathrm{GeV}^2$. The dashed line displays the γ function computed by De Rújula and Vogelsang.*

zero. One can see, that in elastic events it is really very small. On the contrary, in the inelastic events it is significantly larger. This is directly related to the difference in Q_h^2 ranges of elastic and inelastic events, as discussed in sect. 1.8. Consequently, the collinear approximation may lead to significant migrations of inelastic events between kinematic bins due to not sufficiently accurate calculation of event kinematics.

This is also illustrated in the middle graphs of fig 5.10, in which the two kinematic variables x_l and x_γ are contrasted to each other in elastic and inelastic events. In the collinear approximation these variables are assumed to be identical, as already discussed in sect. 1.9. Again, this assumption holds very well in elastic scattering, but significant deviations are observed in inelastic events.

Apart from migrations, the two other poles of the radiative ep scattering cross section, namely ISR and FSR, and the phase space limits, imposed to stay away from these poles, may cause the discrepancies between the data and the calculus in collinear approximation. To elucidate their influence, the generated $e\gamma$ acoplanarity is plotted in the lower graphs of the same figure. In the collinear approximation the two particles are scattered exactly back-to-back in azimuth, *i.e.*, the acoplanarity is always equal to zero. The criterion $A < 45^\circ$, used throughout this work, is thus fulfilled automatically. As seen in the figure, elastic events are really concentrated near zero in acoplanarity, and the fraction of elastic events rejected by the acoplanarity cut is definitely negligible. On the contrary, inelastic events are characterised by typically larger acoplanarity values[2]. It is visible, that their distribution does not vanish at $A = 45^\circ$, *i.e.*, some fraction of the events, computed in the collinear approximation, is rejected from the measured sample.

The cut at some acoplanarity value is necessary to diminish the contribution of the Final State Radiation peak. For the collinear approximation to work, there must be a sharp topological separation of the QEDC and FSR peaks, *i.e.*, the acoplanarity distribution of inelastic QEDC events must vanish at some point, then a gap in the distribution must occur at larger values, and at even larger values the FSR distribution may begin to rise. This is required, because the collinear approximation describes only the QEDC part of the entire spectrum — the part given by only one of the terms in the complete leading order calculation of the radiative ep scattering.

The distribution at higher acoplanarity values ($A > 45^\circ$) could not be studied with COMPTON due to the internal acoplanarity limit set in the generator. Therefore the distribution in the real data has been viewed, as depicted in fig. 5.11. Data of the minimum bias 1997 sample are plotted, because the QEDC L2 trigger condition in the standard 1997 data does not accept events with high acoplanarity, and because in the minimum bias data treatment a relaxed cut on the angular distribution of hadrons is made. It is also important for the acoplanarity distribution, since at higher acoplanarities one moves into the FSR region, *i.e.*, the region of radiative corrections to DIS, which involves much higher M_X values and much more extensive hadronic activity in the detector. The limit on θ_{LAr}, thus, cuts off a significant part of the phase space in this kinematic region.

The distribution shown in fig. 5.11 is plotted starting not at zero but at some higher acoplanarity value, where the inelastic scattering begins to dominate. As seen from this distribution, there is no point, at which the QEDC contribution would vanish, and there is no gap between QEDC and FSR parts of the spectrum. Both contributions merge around $A \sim 90^\circ$. The FSR part increases with rising A until the electron and the photon begin to merge into the single SpaCal cluster, so that they cannot be separated any more. If one performs an artificial splitting of the total distribution into the sum of FSR and QEDC components, where each component is described by its own term in the complete cross section formula, then imposing a limit on the

[2]This feature has been utilised in this analysis for singling out elastic and inelastic subsamples (see sect. 3.10).

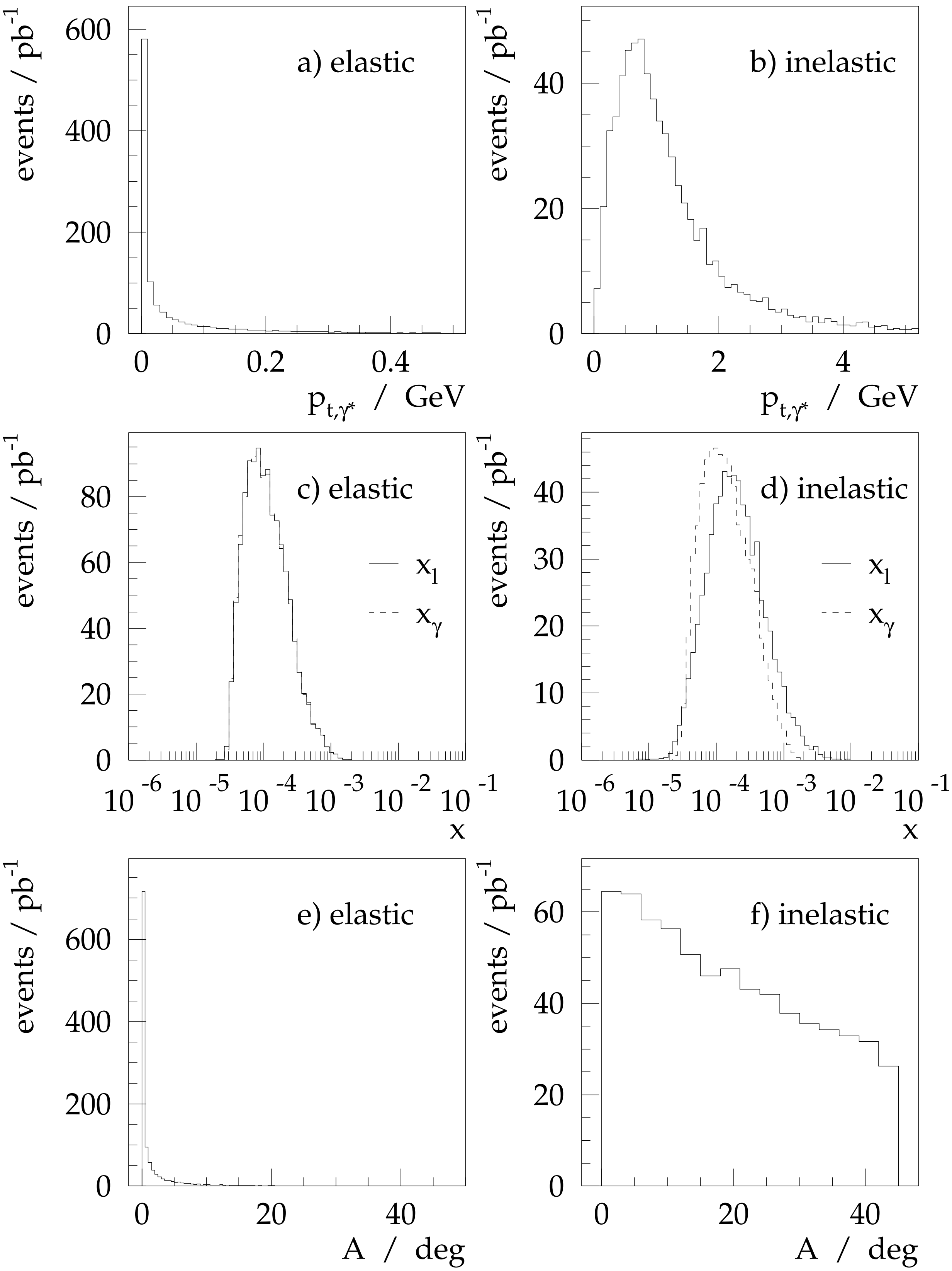

Figure 5.10: *Comparison of elastic events (figures to the left) and inelastic events (figures to the right) generated by COMPTON. Further explanations are given in text.*

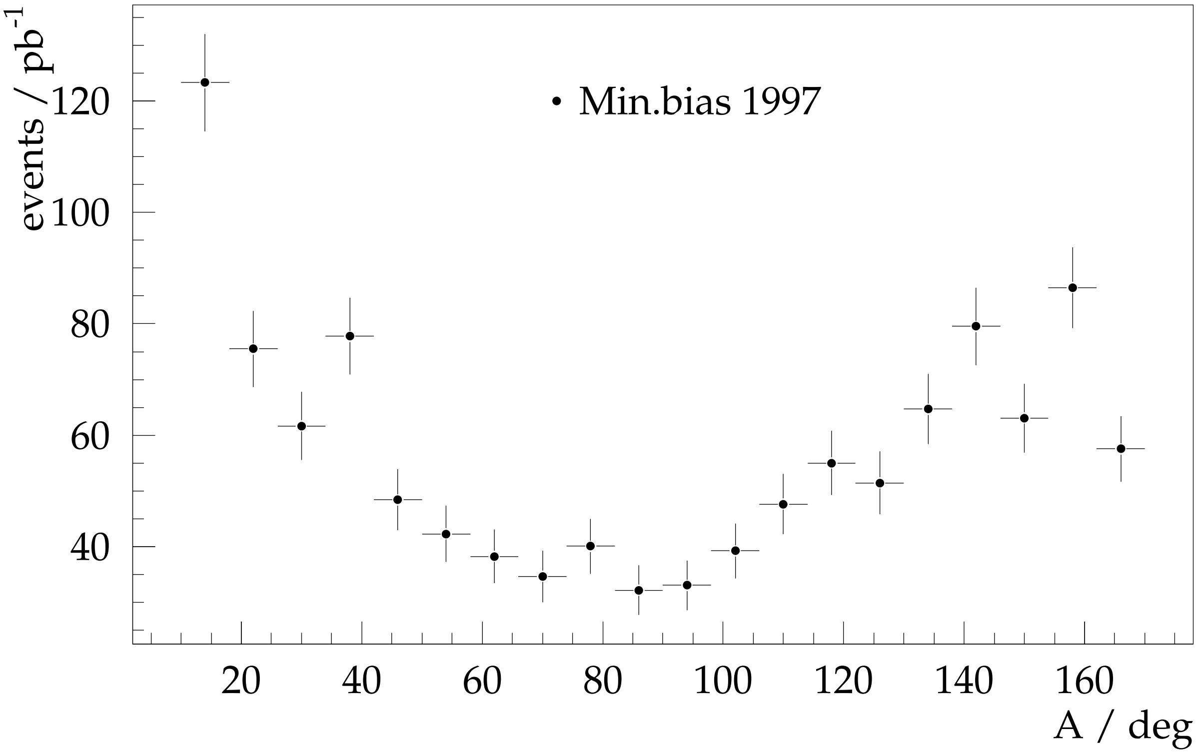

Figure 5.11: *Acoplanarity of two SpaCal clusters in the data after relaxing the cut on it.*

acoplanarity at any point cuts off a tail of the QEDC distribution and on the other hand leaves a tail of the FSR spectrum. Thus, there is no experimental possibility to single out the "pure" QEDC component from the total cross section, and, thus, the event sample, actually used for the measurement, does not correspond exactly to what is treated by the collinear approximation.

A similar situation may happen also with respect to the ISR peak. While calculating the cross section the cut on θ_γ was, in particular, imposed, as pointed out in expression 5.1. This limit is necessary in order to cut off the ISR contribution peaking at $\theta_\gamma = \pi$. It is however not excluded that a similar tail of the ISR spectrum remains in the measured sample.

In order to ensure the validity of the collinear approximation, De Rújula and Vogelsang proposed in [rv98] to apply additional kinematic cuts in the event selection:

$$-\hat{t}, \hat{s} > 1\,\mathrm{GeV}^2 \qquad \text{and} \qquad p_{t,e}, p_{t,\gamma} > 1\,\mathrm{GeV}\,, \tag{5.2}$$

where the momentum scales $\hat{t}$ and $\hat{s}$, defined via

$$\hat{t} = (l-k)^2 \equiv q'^2\,, \qquad \hat{s} = (l-q_h)^2 \equiv q''^2 \equiv W^2\,, \tag{5.3}$$

give the virtualities of the exchanged lepton for the first and second Feynman diagram of the QEDC process, shown in fig. 1.3. Actually, the cuts applied on the transverse momenta $p_{t,e}$ and $p_{t,\gamma}$ have a much stronger effect than those imposed on $\hat{t}$ and $\hat{s}$.

These cuts were applied on the generated variables in COMPTON events and the generated cross section was determined in the same kinematic intervals. The result was again confronted to the corresponding values provided by W. Vogelsang, as shown in fig. 5.12. As before, there are essential discrepancies between the two computations in several bins.

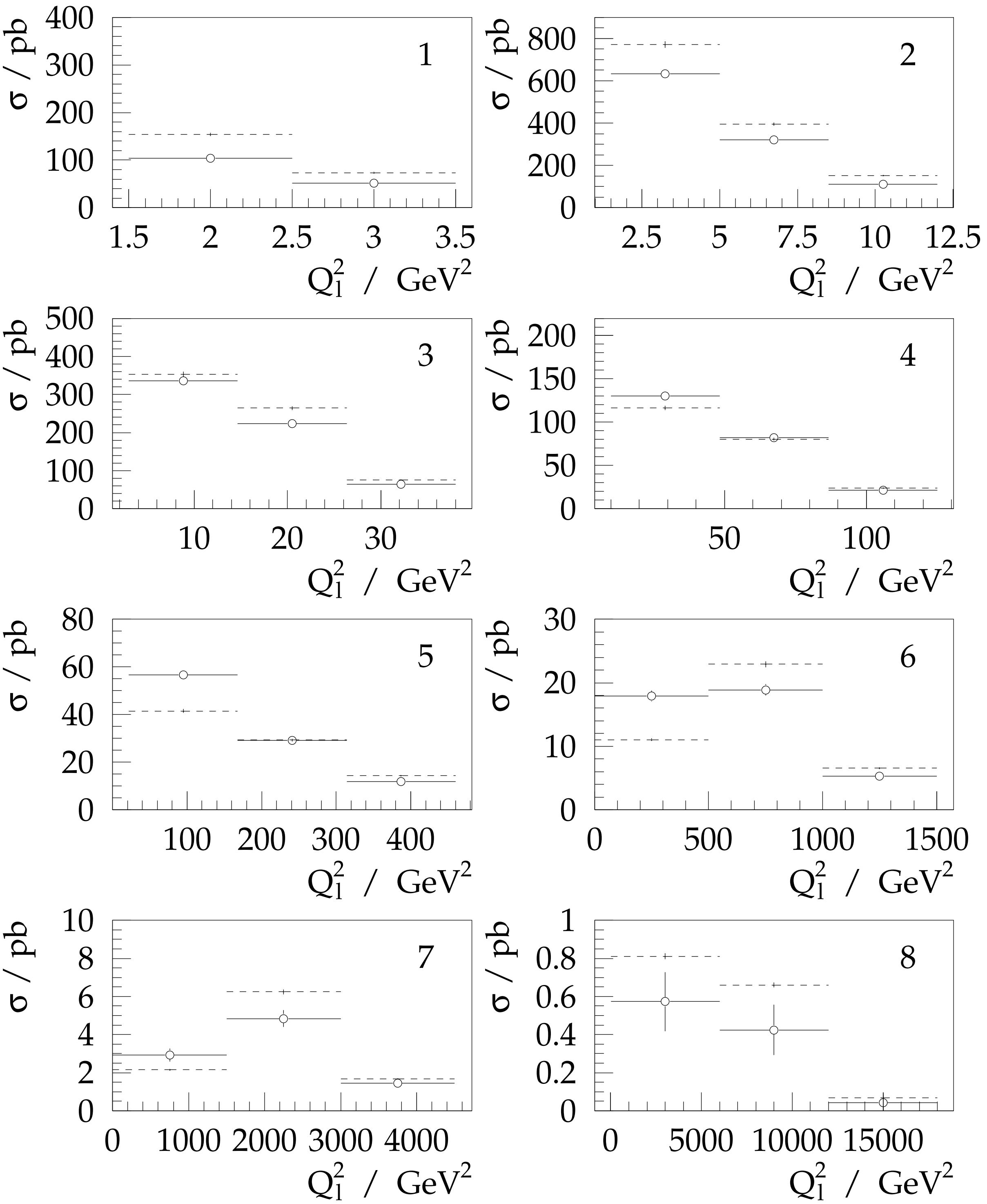

Figure 5.12: *QED Compton scattering cross section after additional kinematic cuts. Open circles depict cross section values given by the COMPTON generator with the ALLM97 F_2 fit in the continuum region. The corresponding error bars show statistical errors. The dashed lines show the values computed by W. Vogelsang.*

This figure supplies a good illustration of the difficulties met by the collinear approximation. To be specific, if one takes a closer look on the lowest Q_l^2 intervals in the x_l bins 2, 3 and 4 and compares the values in these bins to the corresponding ones in fig. 5.7, then one can see that the COMPTON cross section values dropped significantly after applying the additional cuts, while the values computed in the collinear approximation remained unchanged. This occurs, apparently, due to too rough calculation of the event kinematics in the collinear approximation.

It is not ruled out that some carefully chosen cuts on the transverse momenta, polar angles and/or other event quantities may limit the phase space so that the equivalent photon approximation becomes applicable. A determination of such limits remains a task of an additional theoretical analysis.

Summary and Outlook

A comprehensive study of QED Compton events in ep scattering has been performed. For the first time at HERA the double differential cross section of QED Compton scattering has been measured. The measurement was carried out in bins of the leptonic kinematic variables x_l and Q_l^2 in the range $1.8 \cdot 10^{-5} < x_l < 1.8 \cdot 10^{-3}$ and $2\,\mathrm{GeV}^2 < Q_l^2 < 86\,\mathrm{GeV}^2$ using data collected in 1997 by the H1 experiment. The results of the measurement were confronted to the predictions of Monte Carlo simulations performed by the COMPTON event generator [ck92, cckk91] and to the analytical calculation by De Rújula and Vogelsang [rv98].

The measurement was accomplished by building up a complete data analysis chain. The experimental emphasis of this work was put on the following issues:

- Implementation of hadronic final state simulation into the COMPTON program. Three different hadronisation packages were implemented for the low mass regime: EPSOFT, DIFFVM and SOPHIA. In addition, the package based on the quark–parton model followed by the PYTHIA/JETSET fragmentation was implemented for the simulation of hadronic final state at higher M_X and Q_h^2;
- Development of an e/γ separation procedure. The particle identification was performed using the BST and the CIP chambers. The procedure involved a complex chain of resimulation of the electron validation efficiency and the photon misidentification rate;
- Understanding of the DIS background. The background rate was estimated by two complementary methods: using three-cluster events and analysing SpaCal shower shapes;
- Detailed simulation of passive material in front of the backward calorimeter, understanding of the SpaCal energy measurement and its calibration.

Both the statistical and the systematic uncertainties amount to 3 to 8% in most bins.

Continuum inelastic QED Compton events composed previously the worst known part of the cross section and understanding of this channel has been the main purpose of the experimental analysis. The measurement of these events allowed a test of the behaviour of the proton structure function F_2 in the kinematic domain of very small virtualities of exchanged photon Q_h^2 down to 0.05 GeV^2 and wide x_h range between approx. 10^{-4} and 0.5, which is not accessible in inclusive ep scattering at HERA. In a significant part of this domain there has been so far no direct measurement of F_2 in the neutral current lepton–hadron scattering. Comparisons of the experimental data to the simulation performed with different F_2 parameterisations have shown the sensitivity of the measured cross section to the F_2 values in this region. The QEDC cross section measured in the present analysis has been found to be in good agreement with the COMPTON MC simulation involving the ALLM97 F_2 parameterisation [allm97].

The theoretical calculation of De Rújula and Vogelsang has also been confronted to the experimental data. The photon–parton function of a proton $\gamma(x_l, Q_l^2)$ was computed by numerical integration of the ALLM97 F_2 over the kinematic bins of measurement. The obtained function reveals a Q_l^2 dependence very similar to that predicted by the authors. However, in spite of very close γ values, cross sections calculated in the collinear approximation exhibit large deviations from the measured ones in some bins. The reason for that is most probably that this approximation cannot be used in the region of inelastic QEDC scattering. On the contrary, in the elastic scattering domain, which is characterised by much lower Q_h^2 values, the cross sections, computed by the exact method and in collinear approximation, are in a good agreement. Due to bad applicability of this approach in the inelastic scattering regime, the cross section measurement has not been treated as a determination of the γ function.

A natural continuation of this study would be a direct F_2 determination in the continuum inelastic QEDC events by measuring the cross section as a function of the hadronic variables x_h and Q_h^2. The feasibility studies carried on in the present work suggest that the reconstruction of these variables is possible. This measurement may demand a more detailed understanding of the hadronic final state.

Bibliography

[abe99] T. Abe, J. Fujimoto, T. Ishikawa, K. Kato, Y. Kurihara, T. Watanabe, in **Proceedings of the Workshop "Monte Carlo Generators for HERA Physics", Hamburg 1998–1999**, p. 566.

[abe01] T. Abe, private communication.

[ada99] L. Adamszyk, Doctoral Thesis, Krakow, 1999, DESY–THESIS–99–045.

[agis83] B. Andersson, G. Gustafson, G. Ingelman and T. Sjostrand, Phys. Rept. **97** (1983) 31.

[allm91] H. Abramowicz, E. M. Levin, A. Levy and U. Maor, Phys. Lett. B **269** (1991) 465, DESY–91–068.

[allm97] H. Abramowicz and A. Levy, DESY–97–251 (1997), hep–ph/9712415.

[anl00] H. Anlauf, private communication.

[ap77] G. Altarelli and G. Parisi, Nucl. Phys. B **126** (1977) 298.

[ark99] V. Arkadov, private communication.

[ark00] V. Arkadov, Doctoral Thesis, Humboldt University of Berlin, 2000, DESY–THESIS–00–046.

[arn95] C. Arndt, Diploma Thesis, University of Hamburg, 1995.

[awe92] T. C. Awes, F. E. Obenshain, F. Plasil, S. Saini, S. P. Soerensen and G. R. Young, Nucl. Instrum. Meth. A **311** (1992) 130.

[bab94] A. Babaev, H1 internal note 413 (1994).

[bb74] R. Blankenbecler and S. J. Brodsky, Phys. Rev. D **10** (1974) 2973.

[bb95] U. Bassler and G. Bernardi, Nucl. Instrum. Meth. A **361** (1995) 197, hep–ex/9412004, DESY–94–231.

[bbfw98] A. Beglarian, P. Biddulph, M. Fleischer and C. Wissing, H1 internal note 533 (1998).

[bcdms] A. C. Benvenuti *et al.* [BCDMS Collaboration], Phys. Lett. B **223** (1989) 485, CERN–EP/89–06, JINR–E1/89–540.

[ber95] R. Bernet, Doctoral Thesis, ETH Zürich, 1995.

[ber99] E. R. Berger, A. Donnachie, H. G. Dosch, W. Kilian, O. Nachtmann and M. Rueter, Eur. Phys. J. C **9** (1999) 491, hep–ph/9901376.

[bes96] G. Best, Diploma Thesis, University of Dortmund, 1996.

[bg71] E. D. Bloom and F. J. Gilman, Phys. Rev. D **4** (1971) 2901.

[bh34] H. Bethe and W. Heitler, Proc. Roy. Soc. Lond. A **146** (1934) 83.

[biz92] J. C. Bizot *et al.*, H1 internal notes 212 (1992) and 240 (1992).

[bjo68] J. D. Bjorken, Phys. Rev. **179** (1969) 1547.

[bls91] J. Blümlein, G. Levman and H. Spiesberger,
in **Snowmass 1990, Proceedings, Research directions for the decade**, p. 554–556.

[bls93] J. Blümlein, G. Levman and H. Spiesberger, J. Phys. G **19** (1993) 1695.

[bod79] A. Bodek *et al.*, Phys. Rev. D **20** (1979) 1471.

[bor92] K. Borras, Doctoral Thesis, University of Dortmund, 1992.

[bp69] J. D. Bjorken and E. A. Paschos, Phys. Rev. **185** (1969) 1975.

[bra76] F. W. Brasse, W. Flauger, J. Gayler, S. P. Goel, R. Haidan, M. Merkwitz and H. Wriedt, Nucl. Phys. B **110** (1976) 413.

[bra83] S. Brandt, North Holland, Amsterdam, 1983.

[car74] C. Carimalo, G. Cochard, P. Kessler, J. Parisi and B. Roehner,
Phys. Rev. D **10** (1974) 1561.

[cckk91] T. Carli, A. Courau, S. Kermiche and P. Kessler,
in **Proceedings of the Workshop "Physics at HERA", Hamburg, 1991**,
DESY, 1992, Vol. 2, p. 902 and Vol. 3, p. 1468.

[cdr98] A. M. Cooper-Sarkar, R. C. Devenish and A. De Roeck,
Int. J. Mod. Phys. A **13** (1998) 3385, DESY–97–226, hep–ph/9712301.

[cfm62] G. Chew, S. Frautschi and S. Mandelstam, Phys. Rev. **126** (1962) 1202.

[ck92] A. Courau and P. Kessler, Phys. Rev. D **46** (1992) 117.

[ckp76] C. Carimalo, P. Kessler and J. Parisi, Phys. Rev. D **14** (1976) 1819.

[cg69] C. G. Callan and D. J. Gross, Phys. Rev. Lett. **22** (1969) 156.

[coo82] R. L. Cool, K. Goulianos, S. L. Segler, H. Sticker and S. N. White,
Phys. Rev. Lett. **48** (1982) 1451.

[cor01] G. Corcella *et al.*, JHEP **0101** (2001) 010, hep–ph/0011363.

[cstt94] A. Capella, U. Sukhatme, C. Tan and J. Tran Thanh Van, Phys. Rept. **236** (1994) 225.

[desy69] W. Albrecht *et al.*, DESY–69–046 (1969).

[dir96] M. Dirkmann, H1 internal note 477 (1996).

[dl92] A. Donnachie and P. V. Landshoff, Phys. Lett. B **296** (1992) 227,
hep–ph/9209205, CERN–TH/6635–92.

[dl94] A. Donnachie and P. V. Landshoff, Z. Phys. C **61** (1994) 139, hep–ph/9305319.

[dok77] Y. L. Dokshitzer, Sov. Phys. JETP **46** (1977) 641 [Zh. Eksp. Teor. Fiz. **73** (1977) 1216].

[dre71] J. Drees, in *Springer Tracts in Modern Physics*, Springer, 1971, Vol. 60, p. 107.

[e665] M. R. Adams *et al.* [E665 Collaboration], Phys. Rev. D **54** (1996) 3006.

[egl97] S. Egli, E. Elsen, V. Lemaitre, K. Müller, H. Rick and H.-C. Schultz-Coulon, H1 internal note 517 (1997).

[eng96] R. Engel and J. Ranft, Phys. Rev. D **54** (1996) 4244, hep–ph/9509373.

[ept67] E. Etim, G. Pancheri and B. Touschek, Nuovo Cim. B **51S10** (1967) 276.

[es96] V. Efremenko, V. Shekelyan, H1 software note 7 (1990).

[esw96] R. K. Ellis, W. J. Stirling and B. R. Webber, Cambridge Univ. Pr., 1996, *Cambridge monographs on particle physics, nuclear physics and cosmology: 8*.

[fey69] R. P. Feynman, Phys. Rev. Lett. **23** (1969) 1415.

[ffs98] L. Frankfurt, A. Freund and M. Strikman, hep–ph/9806406.

[fgls94] R. S. Fletcher, T. K. Gaisser, P. Lipari and T. Stanev, Phys. Rev. D **50** (1994) 5710.

[fla92] K. Flamm, Diploma Thesis, University of Hamburg, 1992, DESY–FH1K–92–03.

[fm98] L. Favart and R. Maraček, H1 internal note 503 (1996).

[fnal74] D. J. Fox *et al.*, Phys. Rev. Lett. **33** (1974) 1504.

[gar00] F. Garczarek, Diploma thesis, University of Dortmund, 2000.

[gea94] GEANT Team, CERN Program Library Long Writeup W5013.

[gel62] M. Gell-Mann, Phys. Rev. **125** (1962) 1067.

[gel64] M. Gell-Mann, Phys. Lett. **8** (1964) 214.

[gkw98] A. Glazov, M. Klein and R. Wallny, H1 internal note 546 (1998).

[gl72] V. N. Gribov and L. N. Lipatov, Yad. Fiz. **15** (1972) 781 and 1218 [Sov. J. Nucl. Phys. **15** (1972) 438 and 675].

[gl96] N. Gogitidze and S. Levonian, H1 internal note 471 (1996).

[gla98] A. Glazov, Doctoral Thesis, Humboldt University of Berlin, 1998, DESY–THESIS–98–005.

[gou83] K. Goulianos, Phys. Rept. **101** (1983) 169.

[gpr90] G. Grindhammer, M. Rudowicz and S. Peters, Nucl. Instrum. Meth. A **290** (1990) 469, SLAC–PUB–5072.

[gre64] O. W. Greenberg, Phys. Rev. Lett. **13** (1964) 598.

[grv92] M. Glück, E. Reya and A. Vogt, Z. Phys. C **53** (1992) 127, DO–TH–91–07.

[grv98] M. Glück, E. Reya and A. Vogt, Eur. Phys. J. C **5** (1998) 461, hep–ph/9806404.

[gsv95] M. Glück, M. Stratmann and W. Vogelsang, Phys. Lett. B **343** (1995) 399, DO–TH–94–22.

[gun74] J. F. Gunion, Phys. Rev. D **10** (1974) 242.

[gw73] D. J. Gross and F. Wilczek, Phys. Rev. D **8** (1973) 3633.

[h193] I. Abt *et al.* [H1 Collaboration], Nucl. Phys. B **407** (1993) 515, DESY–93–117.

[h197] C. Adloff *et al.* [H1 Collaboration], Nucl. Phys. B **497** (1997) 3, DESY–97–042, hep–ex/9703012.

[h100] C. Adloff *et al.* [H1 Collaboration], submitted to Eur.Phys.J.C, DESY–00–181, hep–ex/0012053.

[h101] C. Adloff *et al.* [H1 Collaboration], Eur. Phys. J. C **19** (2001) 269, DESY–00–187, hep–ex/0012052.

[h1c93] B. Andrieu *et al.* [H1 Calorimeter Group], Nucl. Instrum. Meth. A **336** (1993) 460.

[h1d97] I. Abt *et al.* [H1 Collaboration], Nucl. Instrum. Meth. A **386** (1997) 310 and 348.

[h1d01] C. Adloff *et al.* [H1 Collaboration], hep–ex/0107005.

[h1j99] C. Adloff *et al.* [H1 Collaboration], Eur. Phys. J. C **10** (1999) 373, hep–ex/9903008.

[h1o01] H1 Collaboration, H1prelim–01–117, contributed paper to the International Europhysics Conference on High Energy Physics, Budapest, 2001.

[h1sp] R. D. Appuhn *et al.* [H1 SpaCal Group], Nucl. Instrum. Meth. A **374** (1996) 149, A **382** (1996) 395, A **386** (1997) 397 [DESY–95–165, DESY–95–250, DESY–96–171].

[han63] L. N. Hand, Phys. Rev. **129** (1963) 1834.

[hei99] B. Heinemann, Doctoral Thesis, University of Hamburg, 1999, DESY–THESIS–99–046.

[hf99] D. Hoffmann and L. Favart, IIHE–99–01, in **Proceedings of the Workshop "Monte Carlo Generators for HERA Physics", Hamburg 1998–1999**.

[hn65] M. Y. Han and Y. Nambu, Phys. Rev. **139** (1965) B1006.

[hof56] R. Hofstadter, Rev. Mod. Phys. **28** (1956) 214.

[ing91] R. Ingelman, in **Proceedings of the Workshop "Physics at HERA", Hamburg, 1991**, DESY, 1992, Vol. 3, p. 1366.

[inu01] M. Inuzuka, private communication.

[işs96] Ç. İşsever, Diploma Thesis, University of Dortmund, 1996, DESY–FH1–96–06.

[işs01] Ç. İşsever, Doctoral Thesis, University of Dortmund, 2001, DESY–THESIS–01–032.

[jad75] S. Jadach, Comput. Phys. Commun. **9** (1975) 297.

[jan94] J. Janoth, A. Lindner, A. Walther, D. Wegener, R. D. Appuhn and V. Korbel, Nucl. Instrum. Meth. A **350** (1994) 221.

[jan96] J. Janoth, Doctoral Thesis, Ruprecht Karl University of Heidelberg, 1996.

[jb79] F. Jaquet and A. Blondel, in **Proceedings of the Study "An ep facility for Europe", Hamburg, 1979*.*

[jlnl75] D. Joynson, E. Leader, B. Nicolescu and C. Lopez, Nuovo Cim. A **30** (1975) 345.

[jsm95] J. Janoth, J. Stiewe and A. Meyer, H1 internal note 464 (1995).

[kan98] P. Kandel, Diploma Thesis, RWTH Aachen, 1995.

[kas96] M. Kasprzak, Doctoral Thesis, Warsaw, 1996, DESY–F35D–96–16, and ZEUS internal note 1995–016.

[kat97] J. Katzy, Doctoral Thesis, Ruprecht Karl University of Heidelberg, 1997.

[kel98] N. Keller, J. Marks, P. Sievers, U. Straumann, R. Wallny, T. Wengler, H1 internal note 550 (1998).

[ker94] S. Kermiche, Doctoral Thesis, University of Paris-Sud, LAL Orsay, 1994.

[kmn89] A. N. Kalinovskii, N. V. Mokhov, Yu. P. Nikitin, American Institute of Physics translation series, New York, 1989.

[kn98] W. Kilian and O. Nachtmann, Eur. Phys. J. C **5** (1998) 317, hep–ph/9712371.

[kni91] B. A. Kniehl, Phys. Lett. B **254** (1991) 267.

[kno72] Z. Koba, H. B. Nielsen and P. Olesen, Nucl. Phys. B **40** (1972) 317.

[kob75] M. Kobberling, J. Moritz, K. H. Schmidt, D. Wegener, D. Zeller, J. Bleckwenn and F. H. Heimlich, Nucl. Phys. B **85** (1975) 365.

[kpss88] G. L. Kotkin, S. I. Polityko, A. Schiller and V. G. Serbo, Z. Phys. C **39** (1988) 61.

[kr78] K. Kajantie and R. Raitio, Nucl. Phys. B **139** (1978) 72.

[kr91] C. Kiesling and P. Ribarics, H1 internal note 172 (1991).

[kra98] T. Krämerkämper, Doctoral Thesis, University of Dortmund, 1998.

[kse86] R. Kleiss, W. J. Stirling and S. D. Ellis, Comput. Phys. Commun. **40** (1986) 359.

[ksm92] A. Kwiatkowski, H. Spiesberger and H. J. Mohring, Comput. Phys. Commun. **69** (1992) 155. Also in **Proceedings of the Workshop "Physics at HERA", Hamburg, 1991**, DESY, 1992, Vol. 3, p. 1294.

[kur99] T. Kurca, 1997 run selection on the Web page of the H1 ELAN group: `https://www-h1.desy.de/h1/iww/iwork/ielan/new/97runsel` .

[kw77] K. Koller and T. F. Walsh, Phys. Lett. B **72** (1977) 227 [Erratum-ibid. **73B** (1977) 504].

[lah97] R. Lahmann, BST Operation History for 1997:
`http://www-zeuthen.desy.de/naumann/h1/opera/bst97.html`.

[len99] V. Lenderman, H1 internal note 575 (1999).

[lis93] B. List, Diploma Thesis, Technical University of Berlin, 1993.

[ln73] L. Lukaszuk and B. Nicolescu, Lett. Nuovo Cim. **8** (1973) 405.

[lön92] L. Lönnblad, Comput. Phys. Commun. **71** (1992) 15.

[mah56] R. W. McAllister and R. Hofstadter, Phys. Rev. **102** (1956) 851.

[mar98] R. Maraček, Doctoral Thesis, Inst. of Exp. Physics, Košice, 1998.

[mey96] A. Meyer, H1 internal note 486 (1996).

[muc00] A. Mücke, R. Engel, J. P. Rachen, R. J. Protheroe and T. Stanev,
Comput. Phys. Commun. **124** (2000) 290, astro–ph/9903478.

[mur95] P. Murin, R. Pöschl, S. Schleif, A. Walther, D. Wegener, H1 internal note 461 (1995).

[mw88] G. Marchesini and B. R. Webber, Nucl. Phys. B **310** (1988) 461.

[mt69] L. W. Mo and Y. Tsai, Rev. Mod. Phys. **41** (1969) 205.

[nau98] J. Naumann, Diploma Thesis, University of Dortmund, 1998.

[ned00] M. zur Nedden, private communication, 2000.

[nee61] Y. Ne'eman, Nucl. Phys. **26** (1961) 222.

[nmc97] M. Arneodo *et al.* [New Muon Collaboration], Nucl. Phys. B **483** (1997) 3,
hep–ph/9610231.

[pan68] W. K. Panofsky, SLAC–PUB–0502,
14th Int. Conf. on High Energy Physics, Vienna, Aug 1968.

[pan69] G. Pancheri, Nuovo Cim. B **60S10** (1969) 321.

[pan96] A. Panitch, Doctoral Thesis, Free University of Brussels, 1996.

[pdg00] D. E. Groom *et al.* [Particle Data Group], Eur. Phys. J. C **15** (2000) 1.

[per75] D. H. Perkins,
Symposium On Lepton and Photon Interactions At High Energies, Stanford, 1975.

[pha96] J. P. Pharabod, A. Semenov, V. Shekelyan, D. Vandenplas, A. Walther and A. Zhokin,
H1 internal note 474 (1996).

[plo95] H. Plothow-Besch, Int. J. Mod. Phys. A **10** (1995) 2901,
CERN Program Library Long Writeup, W5051.

[pm93] A. Panitch and P. Marage, H1 internal note 297 (1993).

[pol73] H. D. Politzer, Phys. Rev. Lett. **30** (1973) 1346.

[poe96] R. Pöschl, Diploma Thesis, University of Dortmund, 1996.

[poe00] R. Pöschl, Doctoral Thesis, University of Dortmund, 2000, DESY–THESIS–00–057.

[pro95] R. Prosi, H1 internal note 433 (1995).

[reg59] T. Regge, Nuovo Cim. **14** (1959) 951 and **18** (1960) 947.

[rgp77] A. De Rújula, H. Georgi and H. D. Politzer, Phys. Lett. B **64** (1977) 428.

[ros50] M. N. Rosenbluth, Rhys. Rev. **79** (1950) 615.

[rv98] A. De Rújula and W. Vogelsang, Phys. Lett. B **451** (1999) 437, CERN–TH/98–377, hep–ph/9812231.

[sc99] H.-C. Schultz-Coulon, E. Elsen, T. Nicholls, J. Coughlan and H. Rick, IEEE Trans. Nucl. Sci. **46** (1999) 915.

[sch96] B. Schwab, Doctoral Thesis, Ruprecht Karl University of Heidelberg, 1996.

[sch00] D. Schmidt, private communication.

[sff98] R. Stamen, M. Fleischer, L. Favart, H1 internal note 554 (1998).

[sie99] P. Sievers, Diploma Thesis, Ruprecht Karl University of Heidelberg, 1999.

[sjo94] T. Sjostrand, Comput. Phys. Commun. **82** (1994) 74, CERN–TH/7111–93.

[slac69] E. D. Bloom *et al.* [SLAC–MIT collaboration], Phys. Rev. Lett. **23** (1969) 930.

[slac73] P. N. Kirk *et al.*, Phys. Rev. D **8** (1973) 63 and references therein.

[slac92] P. Bosted *et al.*, Phys. Rev. Lett. **68** (1992) 3841 and references therein.

[spi91] H. Spiesberger *et al*, in **Proceedings of the Workshop "Physics at HERA", Hamburg, 1991**, DESY, 1992, Vol. 2, p. 798.

[ss91] G. A. Schuler and H. Spiesberger, in **Proceedings of the Workshop "Physics at HERA", Hamburg, 1991**, DESY, 1992, Vol. 3, p. 1419.

[sta97] RACO QEDC data quality checks done by R. Stamen. Talks given in the H1 data quality meetings: C. Issever on 22.04.1997, 06.05.1997 and 19.08.1997, R. Stamen on 27.05.1997.

[sta98] R. Stamen, Diploma Thesis, University of Dortmund, 1998.

[sta01] R. Stamen, Doctoral Thesis, University of Dortmund, 2001.

[tay69] R. E. Taylor, C69–09–14.26, SLAC–PUB–0677, in **Proc. of the 4th Int. Symp. on Electron and Photon Interactions at High Energies, Liverpool, 1969**, Daresbury Nuclear Physics Lab, 1969, p. 251–260.

[ua587] G. J. Alner *et al.* [UA5 Collaboration], Nucl. Phys. B **291** (1987) 445.

[vog01] V. Vogelsang, private communication.

[vw94] G. A. Voss and B. H. Wiik, Ann. Rev. Nucl. Part. Sci. **44** (1994) 413.

[wal97] ELAN data quality checks done by R. Wallny.
Talks given in the H1 data quality meetings:
R. Wallny on 14.10.1997 and 25.11.1997, J. Olsson on 16.12.1997.

[wal99] R. Wallny, private communication.

[wei34] C. F. von Weizsäcker, Z. Phys. **88** (1934) 612.

[wel94] H. P. Wellisch *et al.*, H1 internal note 346 (1994).

[whi92] L. W. Whitlow, E. M. Riordan, S. Dasu, S. Rock and A. Bodek,
Phys. Lett. B **282** (1992) 475, SLAC–PUB–5442.

[wil34] E. J. Williams, Phys. Rev. **45** (1934) 729.

[wis98] C. Wissing, Diploma Thesis, University of Dortmund, 1998.

[yh58] M. Yearian and R. Hofstadter, Phys. Rev. **110** (1958) 552.

[zbpt00] J. Breitweg *et al.* [ZEUS Collaboration], Phys. Lett. B **487** (2000) 53, hep–ex/0005018.

[zeus93] M. Derrick *et al.* [ZEUS Collaboration], Phys. Lett. B **316** (1993) 412, DESY–93–110.

[zeus96] M. Derrick *et al.* [ZEUS Collaboration], Z. Phys. C **69** (1996) 607, hep–ex/9510009.

[zeus00] J. Breitweg *et al.* [ZEUS Collaboration], hep–ex/0006013, DESY–00–084.

[zeus01] S. Chekanov *et al.* [ZEUS Collaboration], Eur. Phys. J. C **21** (2001) 443,
hep–ex/0105090.

[zho99] A. Zhokin, private communication.

[zwe64] G. Zweig, CERN–TH/401, CERN–TH/412.

Acknowledgements

This work has been accomplished with the support of many people. I thank all of them, though it is impossible to name them all here. I wish to express my gratefulness to

- Prof. Dietrich Wegener for giving me the possibility of working in his group and for the permanent guidance and encouragement during my time as a graduate student;
- Prof. Peter Buchholz, who kindly accepted to be the co-referee of this work;
- Hans-Christian Schultz-Coulon for the critical reading of this thesis, for the guidance and support during the last two years and for the tremendous help in publicity and presentation issues;
- Klaus Wacker, who has carefully read this manuscript and whose great professional experience and almost unlimited patience I shamelessly exploited during the whole work;
- Laurent Favart, who directed my attention to the DICS paper, helped me at several steps of the analysis and made important comments to this thesis;
- Manfred Fleischer, who introduced me into the H1 environment and initiated the study of passive material;
- Çigdem İşsever, Roman Pöschl and Rainer Stamen, who shared so much of their analysis experience and software with me;
- Dieter Lüke for the help with Monte Carlo production and many other things;
- Werner Vogelsang for the friendly cooperation in the DICS study;
- Vladimir Arkadov, Rainer Wallny and Alexander Zhokin, who enlightened me about many important details of the F_2 analysis;
- Nicolas Keller for the useful discussions of the QEDC analysis issues;
- Harald Anlauf for the discussion of radiative corrections;
- all members of the H1 collaboration and, in particular, of the RACO and ELAN working groups for a friendly and truly collaborative atmosphere;
- Miguel Mondragon, Jürgen Naumann and Christoph Wissing for their hospitality in those occasions, when there was no free place in the DESY guest houses;
- all colleagues from EV for a pleasant working atmosphere;

and my special gratitude belongs to my parents and Julia for their support, patience and love.

This work was supported by the Graduate College "Production and Decays of Elementary Particles" and by the Federal Ministry for Education, Science, Research and Technology, FRG, under contract number 05 H1 1PEA/6.